Air-sea Exchanges at the Oceanic Mesoscale

A driver of ocean circulation?

Sophia Moreton

A thesis presented for the degree of

Doctor of Philosophy

Department of Meteorology

University of Reading

October 2021

Abstract

The exchange of heat and momentum between the oceanic mesoscale and the atmosphere, and its impact on the local and large-scale ocean and atmosphere, presents a relatively new field. Its explicit representation or parameterization remain absent in most of the current generation of CMIP6 climate models. Using a state-of-the-art coupled climate model, it is shown that 1/12° and 1/4° resolution oceans generate 63% and 40% of the eddies found in observations respectively. Improvements in 1/12° are likely to be due to a better representation of the mean state in eddy-energetic regions with many more, smaller eddies being represented. However, eddy survival rates are biased high in the 1/12°, especially in the Southern Ocean.

The first estimate of the turbulent heat flux feedback over coherent mesoscale eddies is provided, using a high-resolution coupled model. However, the ocean-to-atmosphere regridding of sea surface temperature (SST) may underestimate the feedback by between 20 to 80%. Importantly, the underestimate increases for models with larger ratios between atmospheric and ocean resolutions, implying that eddy SST anomalies are not dampened enough in such setups.

Finally, by parameterizing the mesoscale heat flux feedback and SST-wind stress feedback in an ocean-only model, I was able to isolate and compare their effects. It is shown that the two feedbacks drive opposite meridional shifts of the western boundary current separation, suggesting they could partially cancel one another in the real ocean.

The results of this thesis hold implications for future model development, highlight biases in the current observational altimeter dataset and guide the future pa-

rameterization of mesoscale air-sea feedbacks in climate models. Both the ocean and atmospheric resolutions are critical to represent the oceanic mesoscale and its interaction with the atmosphere, with uncoordinated increase in the ocean and atmosphere resolutions having a potential detrimental impact on the quality of the solutions.

Declaration

I confirm that this is my own work and the use of all material from other sources has been properly and fully acknowledged.

Data Availability statement

The dataset of the tracked mesoscale eddies, and their properties, is freely available in a University of Reading repository, under a Creative Commons Attribution 4.0 International Licence:

https://creativecommons.org/licenses/by/4.0/ (Moreton and Roberts, 2021).

The HighResMIP model data used in this thesis is freely available from the Earth System Grid Federation (ESGF) at:

https://esgf-index1.ceda.ac.uk/search/primavera-ceda/.

- The N512-12 configuration datasets (HadGEM3-GC31-HH) are freely available at Roberts (2018).
- The N216-12 configuration datasets (HadGEM3-GC31-MH) are free available at Roberts (2017a).
- The N216-025 configuration datasets (HadGEM3-GC31-MM) are freely available at Roberts (2017b).

Sophia Moreton

Acknowledgements

I thank my supervisors, David Ferreira, Malcolm Roberts and Helene Hewitt, and many other impressive scientists I have met along the way, for their supportive guidance, critical feedback and above all, inspiration during this project.

I am grateful to my family and friends, especially to Rachael Bryom, for their continuous unwavering support, and, above all, to Joseph and Lily Rose Moreton.

Thank you to NERC and the Met Office for funding this enjoyable project and many stimulating conferences and summer schools.

Contents

List of Figures

Chapter 1

Introduction

Air-sea exchanges at the oceanic mesoscale present a new frontier to understanding the coupled climate system. The oceanic mesoscale comprises of a highly turbulent field, encompassing a range of features such as quasi-stationary fronts, meanders, jets and coherent geostrophic eddies, with a spatial resolution between 10 to 1000 km (Fig. 1.1). The role of the eddies in oceanic heat, volume and nutrient transport, and carbon uptake, is well established (Munday et al., 2013; Griffies et al., 2015; von Storch et al., 2016; Munday et al., 2014; Abernathey et al., 2011; Gnanadesikan et al., 2015). Instead, the exchange of heat, momentum and freshwater between the oceanic mesoscale and the atmosphere presents a relatively new field. These mesoscale air-sea exchanges impact both the local and large-scale atmosphere and ocean, and thus influence Earth's climate (Minobe et al., 2008; Czaja et al., 2019; Putrasahan et al., 2021; Ma et al., 2017; Kirtman et al., 2012; Zhou et al., 2015; Sugimoto et al., 2017). In comparison to the atmospheric response, research into feedback on the large-scale ocean receives far less attention (Hogg et al., 2009; Renault et al., 2019b; Bishop et al., 2017; Ma et al., 2016). The lack of research promotes a fundamental question; to what extent do mesoscale air-sea exchanges impact large scale ocean circulation? Here, this thesis aims to improve our understanding of mesoscale eddies, their interaction with the atmosphere, and

feedback on the local and large-scale ocean.

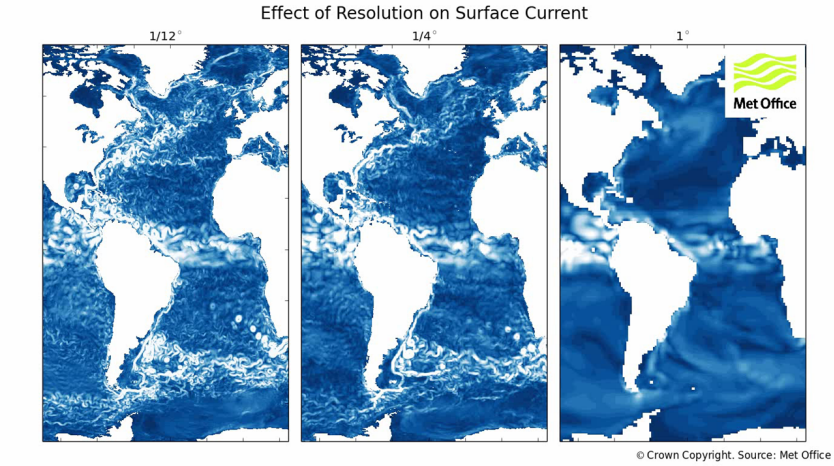

Figure 1.1: *Ocean surface currents (shown in white) for different resolutions of ocean component of the coupled climate model, HadGEM3-GC3.1: either 1/12° (left), 1/4° (middle) or 1° (right). Met Office*

The thesis aim aligns closely with the ability of climate models to represent, not only mesoscale eddies but also, their interaction with the atmosphere. Today, in coupled climate models within the next international Climate Model Intercomparison Project (CMIP6), most ocean components still have a horizontal grid resolution of 1° (Fig. 1.1, right) (Hewitt et al., 2020; Bishop and Bryan, 2013). This coarse resolution results from the high computational expense needed for long climate prediction runs (Roberts et al., 2019; Czaja et al., 2019). At this resolution the ability to resolve mesoscale eddies is limited, as they typically possess a radius between 10 to 100 km. Instead, the widely-used Gent-McWilliams eddy parameterization scheme represents the role of eddies in tracer transports, but the role of eddies in air-sea exchanges remains absent in these models (Munday et al., 2013; McWilliams et al., 1990; Gent and McWilliams, 1990; Marshall and Radko, 2003; Zanna et al., 2020; Taylor et al., 2012; Hewitt et al., 2017; Kjellsson and Zanna, 2017). Despite this, it is widely agreed that increasing model resolution reduces systematic biases found in coarser resolution climate models (Roberts et al., 2019; Hewitt et al., 2017; Griffies et al., 2015). Recently, both high-resolution global ob-

servations and state-of-the-art climate models, with an ocean component of either 1/12° or 1/4°, provide the opportunity, and accessibility to study mesoscale air-sea exchanges like never before (Fig. 1.1 left, middle) (Haarsma et al., 2016, 2019; Roberts et al., 2019; Chang et al., 2020). Therefore whilst evaluating our scientific objectives, a prominent theme which runs throughout this thesis is the importance of representing mesoscale air-sea exchanges in climate models. This theme matches an on-going discussion in climate science today, with a dedicated CLIVAR working group, formed in 2019, called: 'Mesoscale and Frontal-Scale Ocean-Atmosphere Interactions and Influence on Large-Scale Climate' (Hewitt et al., 2020).

First, this thesis introduction reviews the current evidence for defining the oceanic mesoscale (section 1.1) and how it impacts the local atmosphere (section 1.2). Next, this review provides a critical analysis of the latest studies comparing how mesoscale air-sea exchanges feedback onto both local eddy dynamics and the large-scale ocean (section 1.3). Section 1.4 discusses how well current state-of-the-art climate models represent mesoscale eddies, and their air-sea exchanges. Finally, section 1.5 summarises key gaps found in current literature and highlights research priorities. These priorities form the three principle objectives, and three scientific Chapters 3, 4 and 5, of this thesis.

1.1 The oceanic mesoscale

Ocean mesoscale research has come a long way from early studies in the 1950s. Previous conjectures assumed the ocean as laminar and steady, so small-scale features were thought to play little, if any, role in large-scale ocean circulation; instead the mesoscale was largely presented as small-scale noise (Sverdrup, 1947; Stommel, 1948; Munk, 1950; Luyten et al., 1983; Wunsch, 2002). Later, localised ship measurements and small aircrafts provided the first recordings of individual eddies and their interaction with the atmosphere (Dewar and Flierl, 1987; Stern, 1965; Sweet et al., 1981; Wallace et al., 1989; Hayes et al., 1989; White and Bernstein, R., 1979; Guymer et al., 1983). These measurements were sparse and poorly constrained. In

the 1970s, the increased availability of high speed computers prompted investigations into turbulent geophysical flows, but it was the advent of satellites in the 1990s, which provided the first opportunity for global coverage of surface topography, currents and geostrophic eddies (Klein et al., 2019; Wunsch, 2002). Despite being coarse in spatial resolution relative to today's satellite products, this breakthrough in observational data from localised ship-based measurements launched the field of global mesoscale air-sea exchange research (Chelton and Schlax, 1996, 2003).

Globally, strong mesoscale activity concentrates in specific regions, such as the Gulf Stream, Kuroshio Current Extension, the Agulhas current retroflection and the Antarctic Circumpolar Current, as indicated in Fig. 1.1 by an increased in surface current activity in these regions (Ferrari and Wunsch, 2009). These regions of high ocean intrinsic variability possess a stratified water column and strong horizontal temperature gradients, or fronts, which provide the ideal conditions for the largest mesoscale eddies to form. As the fronts become turbulent and unstable, available potential energy, which is stored in the time-mean front induced by wind forcing, transfers into eddy potential energy and eddy kinetic energy (EKE) via barotropic and baroclinic instability (Gill et al., 1974; Bryden, 1979; Marshall et al., 2002; Yang et al., 2019a). High values of EKE characterize 'eddy-rich' regions, which can be up to 10 times higher than the background KE (Fig. 1.2) (Ferrari and Wunsch, 2009), which are partially controlled by the strong mesoscale air-sea exchanges also found in these regions which is explained further in section 2.1 (Renault et al., 2019c; Ma et al., 2016). Often, EKE magnitude diagnoses how well a model represents mesoscale eddy activity, and its interaction with the atmosphere (Jullien et al., 2020). Outside of these 'eddy-rich' regions (e.g. in the open ocean), smaller eddies are formed by the tilting of isopycnal surfaces through baroclinic instability, and largely depend on the Rossby radius of deformation (Eady, 1949).

Most early studies of mesoscale air-sea exchanges evaluate the whole oceanic mesoscale field, which extends up to 1000 km, as a result of coarse resolution observational and model data available at the time, with White and Annis (2003) being the exception by examining mesoscale eddies (Chelton and Schlax, 2003; O'Neill et al.,

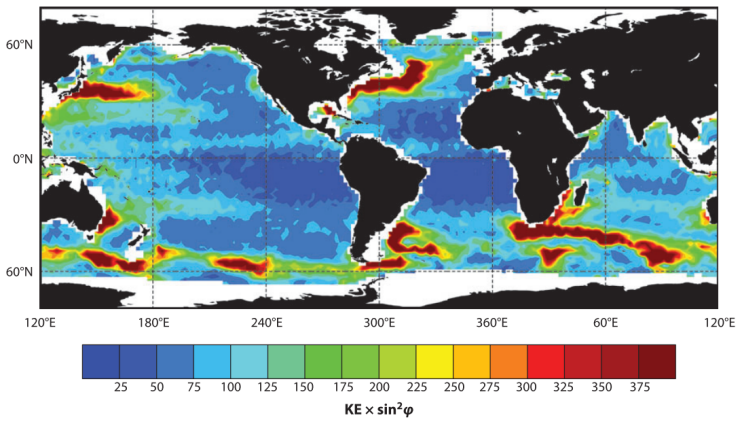

Figure 1.2: *An early global estimate of surface geostrophic kinetic energy (KE) (cm^2 s^{-2}) multiplied by sin 2 ϕ (ϕ is latitude) to reduce noise at the equator. Geostrophic KE is energy contained in geostrophic features such as mesoscale eddies. The plot is adapted by Ferrari and Wunsch (2009) and originates in Wunsch (1999).*

2003, 2004; Chelton et al., 2004). While in more recent work, the increased spatial resolution provides the opportunity to isolate individual coherent eddies (with spatial scales of 10 to 100 km) from the mesoscale field (Frenger et al., 2013; Villas Bôas et al., 2015; Hausmann and Czaja, 2012; Tarshish et al., 2018). We highlight the distinction between the mesoscale field and eddies because first, they encompass different spatial scales and second, the quantity of mesoscale energy contained within closed coherent eddies is not obvious (Bishop and Bryan, 2013; Bishop et al., 2020). Although the mesoscale field composes mainly of eddies (up to 20-60 %), some recent studies argue the relative percentage of EKE relative to the total kinetic energy (KE) in coherent mesoscale eddies is small, in comparison to smaller eddies and meanders (Braby et al., 2020; Martínez-Moreno et al., 2019; Laurindo et al., 2018; Yang et al., 2018; Ferrari and Wunsch, 2009). The discrepancy in energy between the KE field and coherent mesoscale eddies is interesting, and advocates an area of active research (Bishop et al., 2020). Due to high resolution data availability, this thesis begins by focusing on individual coherent eddies, rather than mesoscale fronts or jets, and aims to extend previous research to even smaller spatial scales (ap-

proximately 10 km), which starts to approach sub-mesoscales (McWilliams, 2016; Thomas et al., 2008).

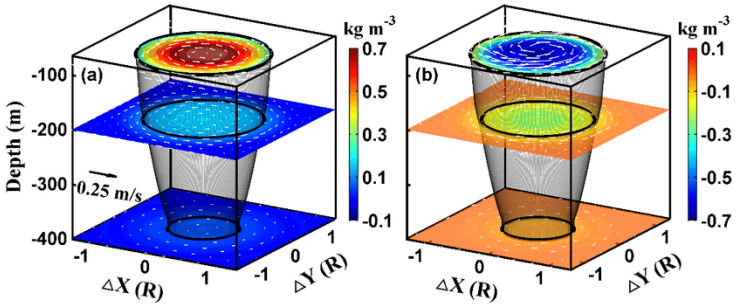

Figure 1.3: *A 3-D structure of either an anti-cyclonic (left) or cyclonic (right) eddy. The background colour represents a potential density anomaly (kg m^{-3}) and the white vectors indicate geostrophic current anomaly (m s^{-1}) (Sun et al., 2018).*

Individual coherent eddies are observed almost in geostrophic balance, where deviations from geostrophic flow (i.e. ageostrophic perturbations) cause vertical and horizontal motion. The motion generates vorticity in the flow by stretching or compressing the fluid column. Therefore, mesoscale transient eddies are typically characterised by localised regions of increased vorticity and anomalies of SSH and large ocean surface current velocities compared to the background field (as shown in Fig 1.3 for potential density anomalies) (Sun et al., 2018). Anti-cyclonic eddies have a 'warm-core', a positive sea surface temperature (SST) anomaly and clockwise-rotating geostrophic flow in the Northern Hemisphere (Fig. 1.3). Anti-clockwise cyclonic eddies have a 'cold-core' or a negative SST anomaly. The direction of rotation is opposite in the Southern hemisphere, due to a negative Coriolis parameter. As eddies rotate, they induce either a local convergence of water through upwelling within an eddy structure, or a local divergence of water and downwelling (Gaube et al., 2015). Generally, in 'warm-core' eddies, the upwelled water is associated with a locally raised SSH, relative to its surroundings, whilst the downwelled water from the sea surface produces a local dip in the SSH in 'cold-core' eddies. These small-scale SSH anomalies are fundamental for air-sea exchanges and feedback on the ocean; the polarity of the SST anomaly, and the strength of the surface

current anomaly can both determine the atmospheric response.

1.2 Impact on local atmospheric variability

To understand feedback on the ocean from mesoscale air-sea exchanges, first we need to evaluate the local atmospheric response. Although the oceanic mesoscale can impact the atmosphere beyond the boundary layer for example, by shifting storm tracks positions, it is the sea surface - boundary layer interactions which play the dominant role in feeding back onto the ocean (Czaja et al., 2019; Ma et al., 2017). This section describes how, and at which spatial scales, the oceanic mesoscale induces local atmospheric variability. Current research compares the different mechanisms and isolates three main air-sea relationships at the oceanic mesoscale. Finally, this section indicates limitations and gaps in this research.

Today, research widely establishes that at mesoscales intrinsic ocean variability can drive changes in the ABL, through the exchange of momentum, freshwater and turbulent (i.e. latent and sensible) heat fluxes [i.e. Small et al. (2020); Cayan (1992); Frankignoul (1985); Bishop et al. (2017); Li et al. (2017); Smirnov et al. (2014); Minobe et al. (2008); Frenger et al. (2013); Laurindo et al. (2018); Putrasahan et al. (2017)]. This contrasts with the traditional negative correlation observed at basin-wide scales where atmospheric variability forces the ocean, mainly by wind stress and turbulent heat fluxes (Charnock, 1955; Bjerknes, 1964; Bretherton, 1982; Ma et al., 2020). It is argued the transition between the two occurs at the atmospheric baroclinic Rossby radius of deformation (R_d) at 1000 km, i.e. roughly 10 times the oceanic R_d (Laurindo et al., 2018). In contrast, Bishop et al. (2017) demonstrate this transitional scale occurs at about 500 km, and is dependent on the time scale of the coupling, while Bellucci et al. (2021) suggest the transition occurs at about 400 km in high resolution coupled models within the High Resolution Model Intercomparison Project (HighResMIP). All these proposed scales are much larger than the scale of mesoscale eddies.

Although mesoscale ocean variability drives atmospheric changes, early research debates the specific mechanisms by which mesoscale SST anomalies impact the local atmosphere; Small et al. (2008) provide a thorough summary. Today, most

studies agree different mechanisms occur depending on the strength and scale of the SST gradient relative to the wind speed (Small et al., 2008; Spall, 2007b; Putrasahan et al., 2013; Byrne et al., 2015). For example, for strong SST gradients approaching 1000 km (at the very edge of the mesoscale) the 'pressure adjustment' mechanism dominates (Lindzen and Nigam, 1987; Putrasahan et al., 2013; Minobe et al., 2008). Warm SST anomalies at the mesoscale induce low sea level pressure (SLP) anomalies which cause surface wind convergence from the hydrostatic adjustment of the atmospheric boundary layer, ABL (Lindzen and Nigam, 1987). While cold SST anomalies induce a high SLP anomaly and wind divergence. It is through this mechanism Minobe et al. (2008) indicates ocean anomalies can influence beyond the local atmosphere, into the troposphere. This significant study precedes numerous more, promoting the importance of the ocean on large-scale atmospheric variability and weather patterns, such as Czaja et al. (2019); Ma et al. (2015, 2017); Sheldon et al. (2017); Zhang et al. (2019); Zhou et al. (2015). In addition, the 'pressure adjustment' mechanism, and Coriolis parameter, become important towards the equator where the wind strength is weak and the ABL is shallow (Byrne et al., 2015; Spall, 2007b). Distinguishing the different atmospheric responses remains important as the wind stress response determines the ocean feedback.

At smaller scale SST gradients, i.e. over eddies, the frequently used 'vertical mixing' mechanism illustrates how the local atmosphere responds to the oceanic mesoscale (Wallace et al., 1989; Hayes et al., 1989; Putrasahan et al., 2013). A warm mesoscale SST anomaly transfers heat through turbulent heat fluxes into the ABL. This heat addition increases local vertical mixing, reduces stability and extends the height of the ABL. The increase in mixing encourages the transfer of momentum downwards and strengthens surface winds, cloud cover and rainfall. The opposite occurs over a cold SST anomaly, where vertical mixing increases the ABL stability. Surface winds decouple from stronger flows above and weaken, in association with a reduction in cloud cover and rainfall. This mechanism was first formed by Chelton et al. (2001) for Tropical Instability Waves in the Pacific, but research since widely confirms its occurrence at much smaller mesoscales as well (Byrne

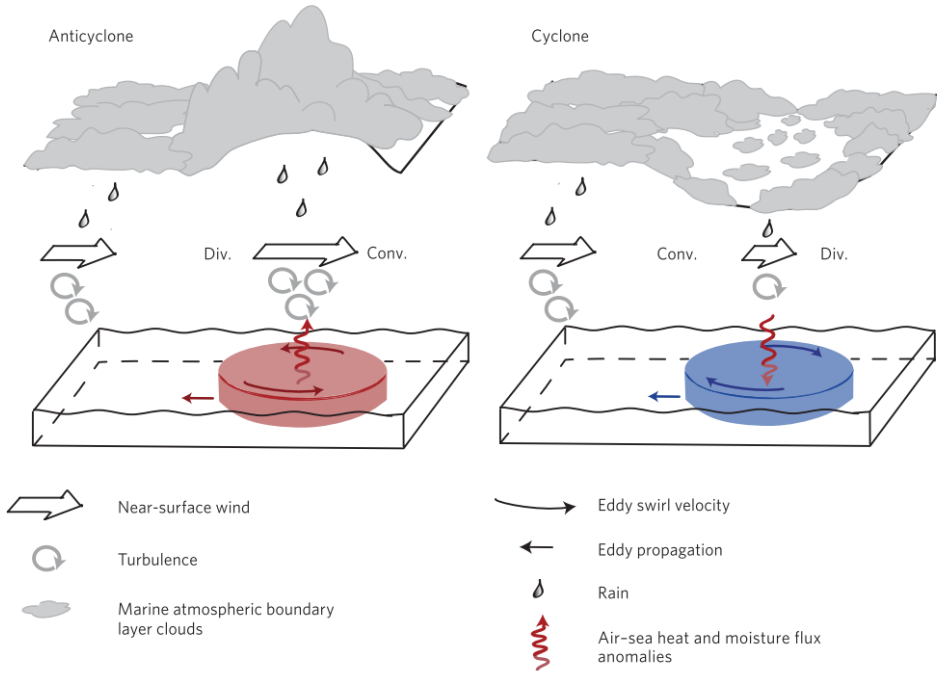

Figure 1.4: *A schematic of the 'vertical mixing mechanism' over individually tracked warm-core anti-cyclonic (left) and cold-core cyclonic (right) eddies in the Southern Ocean (Frenger et al., 2013).*

et al., 2015; Kilpatrick et al., 2014; Xie, 2004; Samelson et al., 2006; Chelton and Xie, 2010). Frenger et al. (2013) supply a clear, commonly-used schematic of this mechanism over individually tracked eddies in the Southern Ocean, as demonstrated in Fig. 1.4. The study highlights the importance of the strong background wind in that region, to generate this particular atmospheric response.

Two fundamental air-sea relationships at the mesoscale can be isolated from this 'vertical mixing' mechanism alone: first, mesoscale SST- wind stress exchanges and second, mesoscale SST - turbulent heat fluxes (THFs). Originally, the positive linear regression between mesoscale SST and wind stress anomalies typically diagnose mesoscale air-sea exchanges, as shown in Fig. 1.5 from Chelton and Xie (2010) (O'Neill et al., 2012; Chelton et al., 2004; Small et al., 2008; O'Neill et al., 2012; Chelton and Xie, 2010; O'Neill et al., 2010; Xie, 2004; Chelton et al., 2001; Bryan et al., 2010; Wei et al., 2019; Lin et al., 2019; Samelson et al., 2020). The

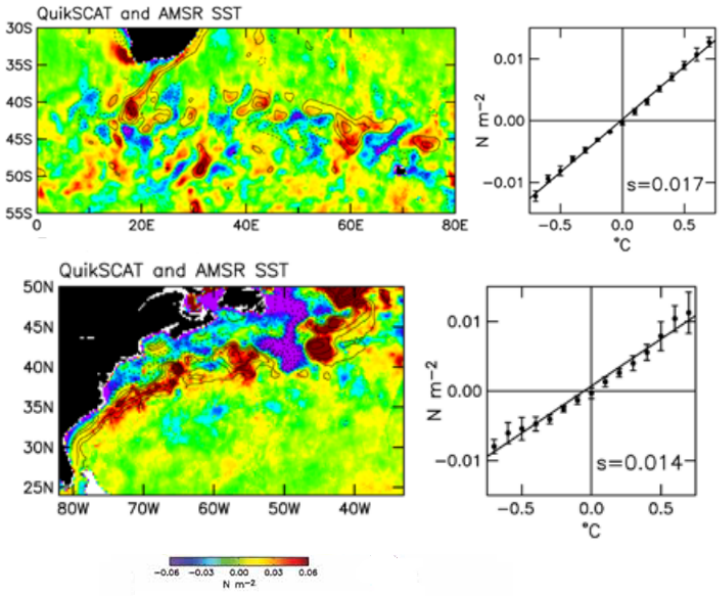

Figure 1.5: *Maps and binned scatter plots for two-month averages (January–February 2008) of spatially high-pass filtered observed SST (lines, °C) and wind stress magnitude (colour, N m^{-2}), in the Agulhas Current retroflection (upper subplot) and the Gulf Stream (lower). The data is from QuikSCAT observations of wind stress and AMSR-E observations of SST. Note the dotted lines indicate negative SST, and the contours have an interval of 1°C (with no zero contours displayed). The binned scatter plots represent the overall average (black circle) and the standard deviation (error bars) of the individual binned averages over eight January–February time periods (Chelton and Xie, 2010).*

wind direction relative to the SST gradient is important, as shown in the schematic in Fig. 1.6 from Kilpatrick et al. (2014). A cross-wind SST gradient induces wind stress curl, when wind passes 90° to the SST gradient (blue area in the schematic). While a down-wind SST gradient induces wind stress divergence (red area), when the wind direction and the SST gradient are the same i.e. in the Antarctic Circumpolar Current. Typically, a down-wind SST gradient induces a larger atmospheric response, because air temperature has time to adjust as the wind passes over the gradient (O'Neill et al., 2010). Both wind stress curl and divergence alter the feedback on the local ocean, depending where the wind anomaly is situated relative to

the SST anomaly (Frenger et al., 2013).

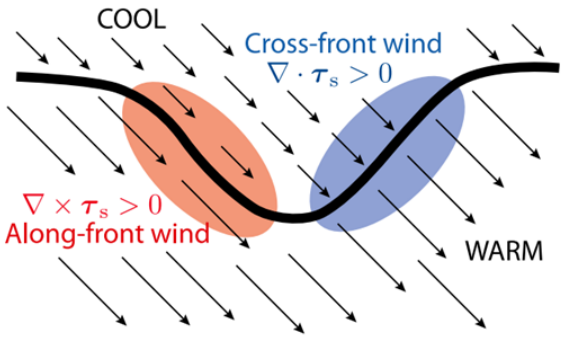

Figure 1.6: *A commonly used schematic to demonstrate how wind stress generates either wind stress curl (blue area) or divergence (red area), depending on its relation to a meandering SST gradient (thick black line). (Kilpatrick et al., 2014).*

Second, the positive correlation between SST and THF anomalies presents another impact from mesoscale SST anomalies on the atmosphere (Hausmann and Czaja, 2012; Hausmann et al., 2017; Liu et al., 2020; Putrasahan et al., 2017; Bretherton, 1982; Bishop et al., 2017; Li et al., 2017; Ma et al., 2016). Note that a positive THF represents an upward flux into the atmosphere. Both frontal regions and individual coherent eddies exhibit the correlation, with a good example shown for individually tracked eddies in the South Atlantic by Villas Bôas et al. (2015). Up to 20% of THF variance is associated with mesoscale eddies in the South Atlantic (Villas Bôas et al., 2015). Although Leyba et al. (2016) contrast their study, arguing positive THFs can be associated with cold-core eddies in the Brazil-Malvinas confluence, depending on the eddy's position on an existing front. THFs over eddies in the South China Sea present similar characteristics (Liu et al., 2020). These results suggest the correlation of SST and THF will vary regionally. Research into isolating mesoscale SST and THF anomalies from wind stress is growing, as a result of improvements in observational air-sea flux datasets (Cronin et al., 2019). However, current research limit their results to regional studies with larger spatial scales, so a quantification of the mesoscale SST-THF relationship over individual eddies has

yet to be undertaken globally (Ma et al., 2016; Hausmann et al., 2016, 2017).

In addition to SST gradients, surface current anomalies typically characterise the oceanic mesoscale, as seen from Fig. 1.1. The relationship between the surface current and wind stress facilitates another commonly-used physical mechanism to examine the local atmospheric response. (Renault et al., 2016b, 2017a, 2019a; Xu et al., 2016; Renault et al., 2019d). The wind direction and magnitude relative to the ocean surface current controls the net surface stress, and can partially re-energize the atmosphere, by transferring energy from the ocean into the ABL (Abel et al., 2017). Important studies by Renault et al. (2016b, 2019a) prompt the inclusion of this re-energization as a parametrization in atmosphere-only and coupled climate models. The imprint of the surface current on the atmosphere only occurs at the mesoscale, for example on average, global wind stress variability induced by surface currents is very small at 1% (Jullien et al., 2020; Renault et al., 2016b; Kelly et al., 2001).

To date, very few studies explore mesoscale air-sea freshwater fluxes, and some argue it is negligible (Yang et al., 2019a). Apart from in the Tropics, the impact of freshwater fluxes on the atmosphere is far smaller than heat or momentum fluxes, and freshwater fluxes are far less efficient at changing density than heat fluxes (Von Storch et al., 2012; Bishop et al., 2020; Small et al., 2008)). Therefore despite being an important air-sea flux, this review does not consider further variability induced by freshwater fluxes at the mesoscale.

Most of the early studies discussed above highlight two crucial limitations; first, the lack of high resolution spatial and temporal observational data of both the local atmosphere and ocean and second, the spatial filtering method used to isolate mesoscale anomalies. First, initial research in the early 2000s highlights the very small sample of data available, which only begins to resolve the mesoscale at 1000 km horizontal scales, and for a short time period e.g. for a few months, such as Fig. 1.5 (Chelton et al., 2001; White and Annis, 2003; O'Neill et al., 2003; Chelton et al., 2004; Xie et al., 1998). In addition, observational air-sea flux datasets are forced to use reanalyses, where SST anomalies are not always aligned to atmo-

spheric features. The subsequent interpolation and averaging of coarse resolution data, into a reanalysis dataset, results in an incorrect quantification of mesoscale air-sea exchange magnitudes (O'Neill et al., 2003; White and Annis, 2003; Rouault et al., 2014). For example, an abrupt increase in mesoscale SST-THF coupling is found between 2001-2002 as the SST dataset changes (Li et al., 2017). Finally, QuikSCAT scatterometers measure wind speeds with a spatial resolution of approximately 1/4°, although rainfall biases their estimates (Laurindo et al., 2018). In 2014, a study of only 6 eddies in the Agulhas region had 20% of wind speed data missing due to partial global coverage of the scatterometer (Rouault et al., 2014). Note, in the early 2000s most coupled numerical models were unable to provide high enough resolution either.

Today, mesoscale air-sea exchanges are much better quantified in modern satellite datasets. Global SST satellite products provide a spatial resolution of 1/4° (Laurindo et al., 2018). Theoretically, this resolution should capture some mesoscale eddies, although the actual resolution is likely to be much larger, due to the interpolation undertaken to achieve a gridded observational product (Wei et al., 2019; Chelton et al., 2011; Reynolds et al., 2007; Banzon et al., 2016). Air-sea flux reanalyses are starting to resolve 1/4° spatial resolutions to resolve the atmospheric impact from mesoscale eddies (Small et al., 2020; Li et al., 2017; Liu et al., 2020). Even today, depending on how wind speed and stress are calculated, some scatterometers cannot observe the mesoscale surface current - wind stress relationship (Renault et al., 2019d). Although numerical models provide much higher resolutions to analyse mesoscale exchanges, a realistic benchmark is not available. Satellite and in-situ observations are still too sparse (Yang et al., 2019a). The future looks brighter. Scheduled to launch in 2022, the Surface Water Ocean Topography (SWOT) altimeter predicts higher spatial resolutions (about 10 km) of sea surface height, which will greatly improve our ability to capture small scale eddies (Carrier et al., 2016).

More recent work at higher resolution provides the opportunity to evaluate smaller scale features, however this introduces the second main limitation; there is no uni-

fied spatial filtering cut off to isolate mesoscale anomalies, such as SST, from the background field (Laurindo et al., 2018; Abel et al., 2017; Jullien et al., 2020). The width of the filtering cut off determines the strength of the remaining anomaly, and therefore the coupling coefficient e.g. between SST and wind stress. Therefore, differences in the filtering cut off could explain, in part, the large variations between studies. Essentially, the spatial, and also temporal, scales of mesoscale SST-wind stress coupling lack definition (Laurindo et al., 2018). To resolve this, some studies perform a spectral analysis of frequency and wave number space, to study the SST-wind stress relationships e.g. Small et al. (2005); O'Neill et al. (2012). These studies encompass a range of spatial and temporal scales, and argue that, unsurprisingly, quasi-stationary fronts have a much greater impact on the atmosphere than mesoscale eddies. More recently, Laurindo et al. (2018) extend these regional cross-spectral studies to a much larger domain (55°S–60°N) with spatial scales from 100 to 1000 km. Despite aiming to evaluate the role of mesoscale eddies, it is surprising the spatial scale of the spectral analysis appears to exclude spatial scales smaller than 100 km, typical of most mesoscale eddies (Laurindo et al., 2018).

To summarize, at spatial scales below approximately 500-1000 km, ocean intrinsic variability drives local atmospheric changes, particularly through three principle relationships: SST-wind stress, surface current-wind stress and SST-turbulent heat flux exchanges. The strength and direction of the SST gradients and surface current anomalies, compared to the wind stress both determine the atmospheric response. Limitations of observational data, and filtering cut offs have been raised. An outstanding research gap is the global quantification of mesoscale SST-THF exchanges over individual coherent eddies. Key questions which now arise are as following. How do mesoscale SST-THF exchanges feedback on the local and large-scale ocean? And how do they compare to mesoscale SST-wind stress or surface current-wind stress induced feedbacks? Finally, how well are these relationships and feedbacks on the ocean, represented in current state-of-the-art climate models?

1.3 Impact on local and large-scale ocean circulation

The previous section identified a gap in quantifying SST-THF exchanges over individual mesoscale eddies. The importance of mesoscale SST-THF exchanges alongside the more well-known relationships involving wind stress is only starting to be evaluated in current research, especially regarding feedback on the ocean. Whether mesoscale SST-THF exchanges have a comparative feedback on local eddy dynamics and large-scale ocean circulation, relative to wind stress exchanges (and therefore whether they need to be parameterized into numerical models) remains unclear.

Western boundary currents (WBCs) are among the world's strongest currents and are critical to global climate and European weather, due to both their strong coupling with the atmosphere and dominant role in ocean heat transport (Moreno-Chamarro, E., L.-P. Caron, P. Ortega, S. L. Tomas, 2020). In this section all three mesoscale air-sea exchanges are shown to feedback onto both the local and large-scale ocean circulation, altering the strength of WBCs. This relatively new, perhaps previously controversial, area of research contrasts with the traditional view. In the 1950s classical wind-driven ocean circulation theory, small scale variability is not expected to drive large scale ocean circulation, and time-averaging simply removes small scale eddy fluctuations (Sverdrup, 1947; Munk, 1950; Stommel, 1948). This section is segmented into three mesoscale feedbacks, and concludes with a comparison of which feedback dominates in different locations and why. Gaps in the current research are identified.

1.3.1 Surface current - wind stress

The feedback from mesoscale surface current- wind stress exchanges on the local and large-scale ocean is widely appreciated, and is beginning to be parameterized in ocean-only models, starting with NEMO, by adding a simplified slab ABL component (Lemarié et al., 2020; Renault et al., 2019c). The wind direction and magnitude relative to the ocean surface current control the net surface stress. The change in the

curl of this surface stress induces Ekman pumping velocities which oppose the eddy surface vorticity, and induce eddy dampening or, commonly termed, 'eddy killing' (Gaube et al., 2015; Renault et al., 2016b). A global map of surface current-induced Ekman pumping vertical velocities is shown in Fig. 1.7a. Depending on the region, feedback on Ekman pumping anomalies induced by mesoscale surface current-wind stress coupling causes a large reduction, or 'oceanic sink', of EKE between 10-55%, as energy transfers from the ocean to the atmosphere (Renault et al., 2019b,d,a; Shan et al., 2020b; Renault et al., 2016b; Seo et al., 2016; Oerder et al., 2018; Jullien et al., 2020; Xu et al., 2016). As EKE reduces, eddy amplitude and rotational speed weaken. In other words, without mesoscale surface current feedback EKE is artificially high, as the oceanic sink of energy to the atmosphere is missing (Seo, 2017).

This reduction in EKE from mesoscale surface current-wind stress exchanges controls and stabilizes western boundary currents and Agulhas retroflection Renault et al. (2016a, 2017b, 2019b). (Renault et al., 2019b) argue mesoscale air-sea feedback dampens eddy activity, and reduces interactions between eddies and the mean flow. Normally, eddies transfer energy into the mean flow through the inverse cascade of energy, although this energy transfer is not currently resolved or parameterized in current CMIP climate models (Arbic et al., 2013; Small et al., 2020). With dampened eddy activity, less energy is transferred, which stabilises the mean flow (Renault et al., 2019b).

1.3.2 Sea surface temperature - wind stress

Mesoscale SST-wind stress exchanges feedback and dampen eddy activity, by altering Ekman pumping vertical velocities i.e. the upwelling or downwelling within an eddy interior (O'Neill et al., 2003, 2012). A global map of SST-induced Ekman pumping vertical velocities are shown in Fig. 1.7b. Over eddies (when the 'vertical mixing' mechanism is present) mesoscale SST gradients generate a distinctive non-linear dipole of SST, due to the dominant relationship between the downwind

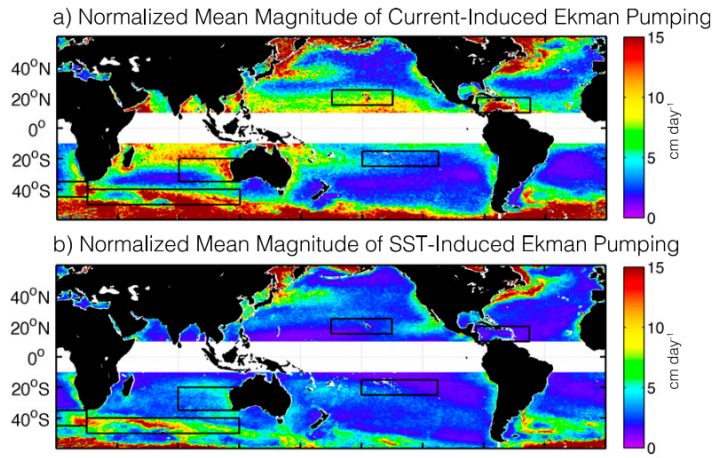

Figure 1.7: *Global 1/4° maps of surface current-induced (upper subplot) and SST-induced (lower) Ekman pumping vertical velocities, averaged over a 7.5-yr period. Data is masked to only include observations within the interiors of mesoscale eddies (Gaube et al., 2015).*

SST gradient and wind divergence over the eddy, introduced in section 1.2 (Gaube et al., 2015). Over larger mesoscale SST anomalies (when the 'pressure adjustment' mechanism dominates) a linear monopole is generated (Byrne et al., 2016; Gaube et al., 2015; Hausmann and Czaja, 2012). Within the monopole or dipole, the upwelling or downwelling slows the rotational speed, reduces eddy amplitude (or SSH anomaly) and dampens the eddy SST anomaly (Dewar and Flierl, 1987; Gaube et al., 2015). Vertical velocities from the upwelling or downwelling of water often determine the strength of the dampening feedback on an eddy.

In contrast to surface current-induced feedback, Seo et al. (2016) argue SST-wind stress feedback has no impact on EKE. Some studies debate this statement within eastern boundary upwelling systems and in the South Atlantic, depending on the wind gradient (Jin et al., 2009; Byrne et al., 2016). For example in the South Atlantic, Byrne et al. (2016) propose a new theory; strong background wind stress allows SST-wind stress feedback to contribute up to 10% of mesoscale kinetic energy, and to outweigh EKE dampening from surface current feedback of about 3%. As this study focuses on a small region, it is unclear whether this source of

energy can be replicated across the whole Southern Ocean, or in western boundary currents.

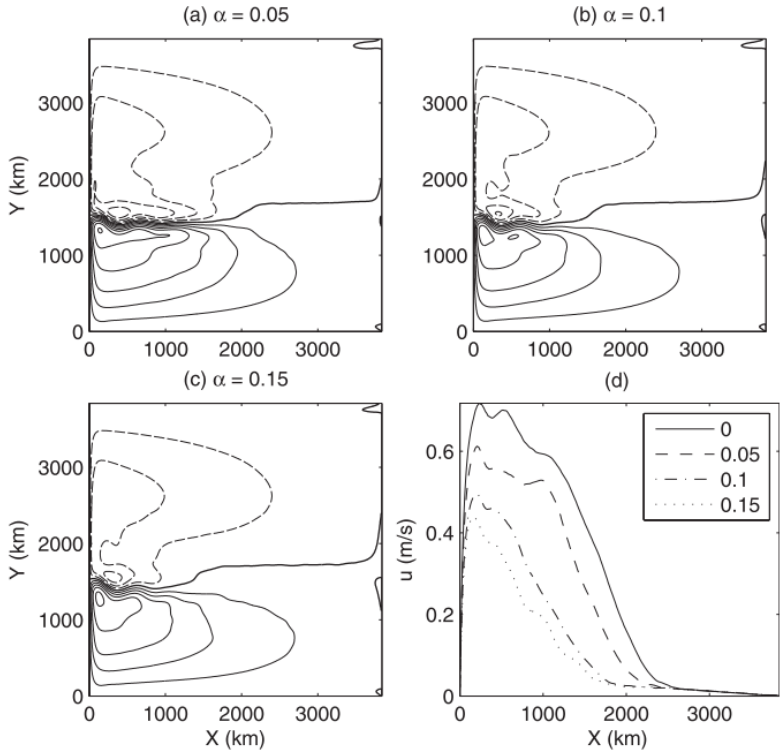

Figure 1.8: *Mean upper-layer stream-function when the coupled coefficient (α) between mesoscale SST-wind stress increases from 0.05 to 0.15 (a-c). (d) shows the maximum zonal velocity as a function of x along the jet core for each experiment (Hogg et al., 2009).*

Despite having debated impact on surface EKE, SST-wind stress feedback does impact large-scale gyre circulation, as shown by early studies, [e.g. Spall (2007a) and Hogg et al. (2009)] using idealized numerical models. Unlike observational data, numerical models provide the opportunity to control and isolate mesoscale air-sea exchanges and investigate how they alter the large-scale. Spall (2007a) claim mesoscale SST-wind stress exchanges influence the growth of baroclinic waves, e.g. the growth rate enhances, when surface winds pass a cold SST anomaly, or reduces, when passing a warm SST anomaly. Although, this theory is only marginally important in mid-latitude WBCs i.e. regions of intense mesoscale activity. Instead,

Hogg et al. (2009) present a much stronger argument for how mesoscale SST-wind stress exchanges regulate transient eddy-induced Ekman pumping anomalies, and reduce mid-latitude gyre circulation. The circulation reduces by 30 to 40%, when mesoscale SST-wind stress coupling is included, causing an associated reduction in zonal jet velocity (Fig. 1.8). This experiment uses a simple parameterization of mesoscale SST-wind stress coupling. However, unlike Spall (2007a), the study by Hogg et al. (2009) use a quasi-geostrophic model, with only three ocean layers and a single atmospheric mixed layer. Whether the same reduction in gyre circulation is found in a more advanced primitive equation model remains unknown.

In disagreement, Renault et al. (2019c) argue coupled simulations with or without mesoscale SST-wind stress feedback present a very similar mean circulation. They argue this is because no ocean-to-atmosphere energy transfers exist, and mesoscale SST-wind stress feedback only influences eddy propagation and not eddy magnitude, as discussed in section 1.3.1 (Seo et al., 2016). Even in 'eddy-rich' regions (WBCs and the Agulhas retroflection) this research argues that SST-wind stress feedback is much weaker than surface current-wind stress feedback at the mesoscale. However, the study itself highlights mesoscale eddy wind work is spatially filtered, unlike the SST field. This will undoubtedly alter the relationship between mesoscale SST-wind stress coupling. In summary, the importance of mesoscale SST-wind stress feedback for large-scale flows remains unclear. Furthermore, the work by Renault et al. (2019c) fails to consider variations in surface EKE from mesoscale SST-THF feedback.

1.3.3 Sea surface temperature - turbulent heat flux

A few recent studies begin to highlight the importance of mesoscale SST- turbulent heat flux (THF) exchanges on local EKE dampening and large-scale ocean circulation.

Besides wind stress induced feedbacks, mesoscale air-sea THF feedback has a fundamental role in the dampening timescale of mesoscale SST anomalies, through

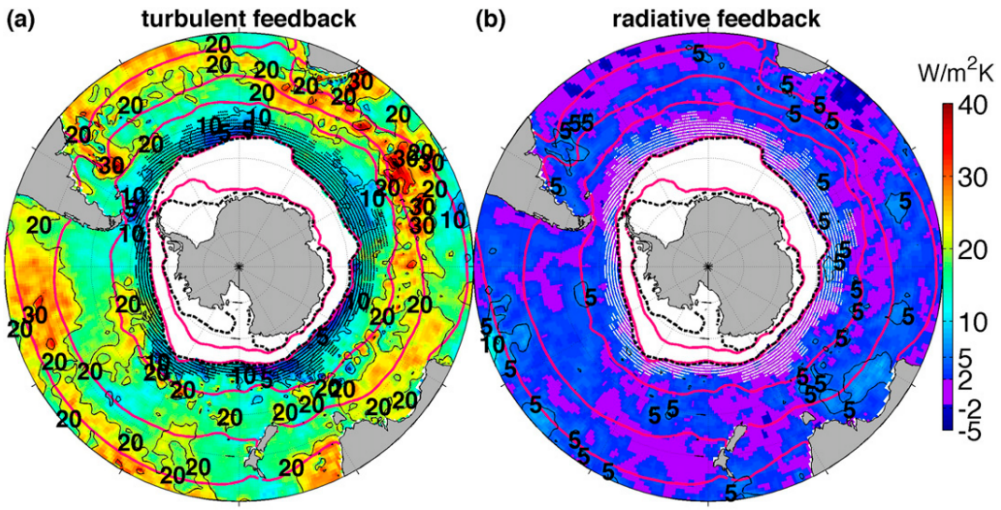

Figure 1.9: *SST - (a) turbulent or (b) radiative heat flux feedback strength (W m^{-2} K^{-1}) in the Southern Ocean, estimated from ERA-I data (Hausmann et al., 2016).*

negative feedback (Hausmann and Czaja, 2012; Hausmann et al., 2016, 2017; Bishop and Bryan, 2013; Frankignoul, 1985). SST-THF feedback acts as a crucial mechanism in setting SST both on basin-wide scales, which stabilizes the thermohaline circulation, and at smaller mesoscales (Frankignoul, 1985; Rahmstorf and Willebrand, 1995). Estimated turbulent feedback values between 5-25 W m^{-2} K^{-1} are shown in Fig. 1.9a for the Southern Ocean, with the lowest feedback found at the sea ice edge (Hausmann et al., 2016). Comparably, feedback from radiative long-wave heat fluxes is small (Fig. 1.9b). Despite indications that SST-THF feedback depends on the spatial scale of the SST anomaly, the minimum spatial scale analysed to date is approximately 100 km, which excludes most mesoscale eddies (Chelton et al., 2011; Hausmann et al., 2017; Li et al., 2017). Furthermore, studies so far only focus on specific areas, such as the Kuroshio Extension, or isolate 'eddy-rich' and 'eddy-quiet' regions. To date, no quantification of mesoscale SST-THF feedback exists globally. These research gaps heighten our aim of quantifying mesoscale SST-THF exchanges, and their feedback on the local ocean, over individual mesoscale eddies, as first suggested in section 1.2.

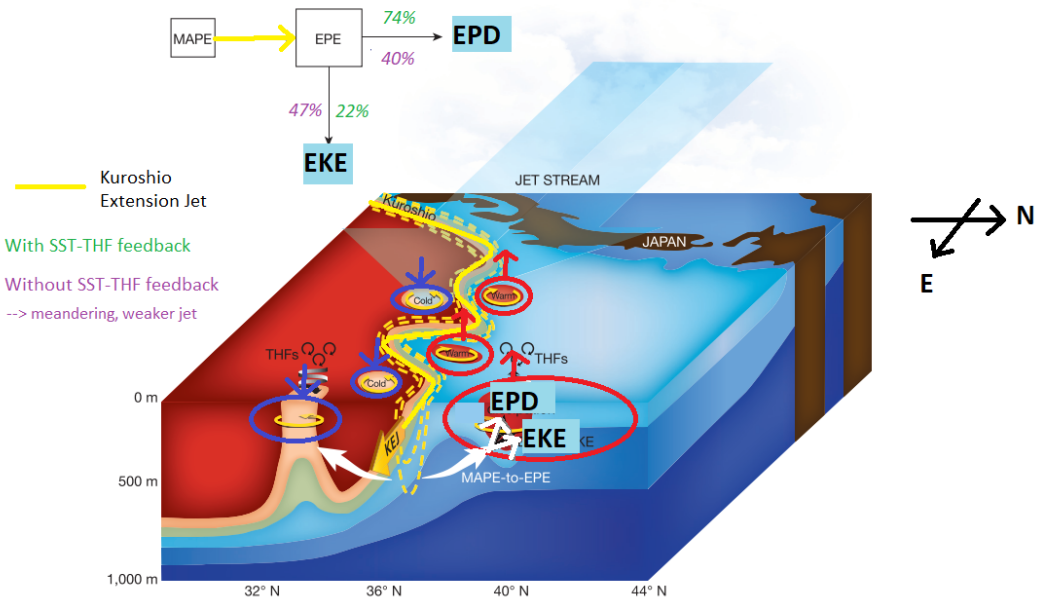

Figure 1.10: *A simplified schematic of the impact of mesoscale SST-THF feedback on energy pathways in the Kuroshio Extension region. The mean jet (yellow), cold-core eddies (blue), warm-core eddies (red) and energy pathways (white arrows) are shown. The mean available potential energy (MAPE) in the jet releases eddy potential energy (EPE) into either eddy potential dissipation (EPD) or eddy kinetic energy (EKE). SST-THF feedback dominates EPE dissipation into EPD (74%, green text), while only 22% is left for eddy activity. Suppressing the feedback causes only 40% EPD (purple text), more eddy activity and a weaker meandering jet. Adapted from Ma et al. (2016).*

A cutting-edge study by Ma et al. (2016) highlights the importance of mesoscale SST-THF feedback on large-scale ocean circulation, due to its dampening of EKE (similarly to surface current-wind stress feedback) (Yang et al., 2019a; Bishop et al., 2017; Li et al., 2017). In the Kuroshio Extension region mesoscale SST-THF feedback increases the dissipation of eddy potential energy, EPE, which importantly reduces the conversion of EPE into EKE, reducing eddy activity. This energy pathway is demonstrated in Fig. 1.10 with an adapted schematic from Ma et al. (2016) (Shan et al., 2020a; Ma et al., 2016; Yang et al., 2018; Bishop et al., 2020; Yang

et al., 2019a). In 'eddy-rich' regions mesoscale air-sea exchanges provide a sink of EPE, by increasing its dissipation. Without considering the mesoscale field, more EPE would be converted into EKE. Using a regional coupled model, mesoscale SST-THF feedback is shown to strengthen the western boundary current by 20 to 40%, in comparison to the same model run with suppressed SST anomalies (Ma et al., 2016). Inflated EKE would have produced a meandering current and more mesoscale eddies. Instead, EPE is dissipated, or released, into the atmosphere and most of the kinetic energy resides within the time-mean current.

An advantage of selecting the Kuroshio Extension region is the western boundary current extension is not shaped by topography and extends freely into the subtropical gyre, unlike the Gulf Stream. This makes it a useful 'eddy-rich' region to examine the effect of mesoscale air-sea exchanges on the mean jet. Although Renault et al. (2019c) argue the spatial box-car filter width of 1000 km from the study by Ma et al. (2016) is too large to isolate mesoscale anomalies from eddies; this wide filter cutoff provides the opportunity to replicate the study by Ma et al. (2016) at smaller spatial scales. In summary, although both mesoscale surface current-wind stress and SST-THF feedback alter energy transfers, how mesoscale SST-THF feedback alters the large-scale jet strength, in direct comparison to SST-wind stress feedback, remains unexplained.

In contrast to the study by Ma et al. (2016), Von Storch et al. (2012) argue eddy terms (here 'eddy' is defined as deviations from the mean state) can be a source of EPE, rather than a sink. However, the seasonal cycle is not considered in this conclusion (Von Storch et al., 2012). The latest study by Bishop et al. (2020) resolve this controversy by explaining regions with a large seasonal cycle generate EPE, which outweighs EPE sinks from mesoscale activity. In summary, the importance of mesoscale SST-THF feedback on energy transfers is an area of active research.

In 2020, the latest studies continue work from Ma et al. (2016) using a regional coupled model in the Kuroshio Extension region, by evaluating the impact of mesoscale SST-THF exchanges on thermal stratification and upper ocean cooling (Fig. 1.8) (Shan et al., 2020a). They argue mesoscale SST-THF exchanges weaken

thermal stratification and eddy-induced re-stratification flux in upper ocean, which promotes sea surface cooling, through the efficient dissipation of EPE, first proposed by Ma et al. (2016) (Shan et al., 2020a). Indeed these mesoscale SST-THF feedbacks regulate 'eddy temperature variance' providing up to 36% of the total dissipation in the surface layer (upper 350 m) (Yang et al., 2019a).

1.3.4 Which mesoscale air-sea feedback dominates?

Which feedback dominates in different regions and why remains unclear. Here two regions are isolated: 'eddy-rich' (typically mid-latitudes WBCs) and the 'eddy-quiet' open ocean. Isolating and understanding whether mesoscale SST-THF or wind stress-induced feedbacks dominate in different regions could be fundamental to improving knowledge on eddy energy dissipation, one of the significant challenges in ocean science today (Yang et al., 2018; Ma et al., 2016; Ferrari and Wunsch, 2009; Wunsch and Ferrari, 2004; Zanna et al., 2020; Zhai et al., 2010; Fox-Kemper et al., 2019).

Contrary to expectation, a recent study by Jullien et al. (2020) predicts the control of mesoscale surface current-wind stress feedback on EKE magnitude is actually relatively larger in 'eddy-quiet' regions, as shown in Fig. 1.11. This occurs despite the largest air-sea energy transfers occurring in 'eddy-rich' regions, due to stronger wind stress, and a lack of eddy activity in 'eddy-quiet' regions due to reduced baroclinic and barotropic instabilities here (Zhai et al., 2010). In a high resolution coupled model, the mesoscale surface current-induced dampening rate in 'eddy-quiet' regions of 40% halves to 20% in 'eddy-rich' regions. Jullien et al. (2020) claim the reason why the impact of mesoscale surface currents remains relatively small in 'eddy-rich' regions is owing to the high magnitude of EKE found here. In these regions, enhanced ocean intrinsic variability increases EKE through barotropic and baroclinic instabilities, i.e. the generation of eddy energy outweighs the mesoscale surface current- induced dampening. The restriction of oceanic spatial scales to above 100 km, i.e. larger than most mesoscale eddies, is a limitation to

this result (Jullien et al., 2020; Chelton et al., 2011). In addition, this study leaves the relative importance of surface current-induced feedback, compared to mesoscale SST-THF induced, unanswered.

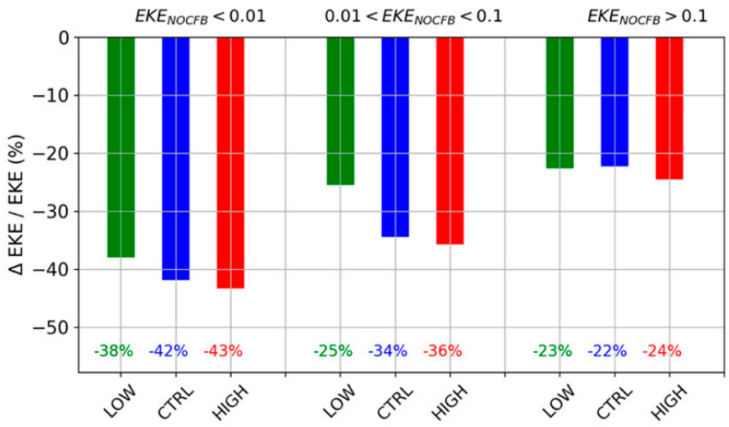

Figure 1.11: *Percentage of EKE decrease due to surface current-induced feedback averaged over regions characterized by their EKE level ($m^2\ s^{-2}$) in the simulation where current feedback is removed (labelled NOCFB). 'Eddy-quiet' regions are defined by EKE <0.01 $m^2\ s^{-2}$, and 'eddy-rich' regions by EKE >0.1 $m^2\ s^{-2}$. The LOW resolution (1/4° in ocean and atmosphere), control (CTRL, 1/12° in ocean and 1/4° atmosphere) and HIGH resolution (1/12° in ocean and atmosphere) are compared. In the HIGH resolution configuration, EKE reduces by 43% in 'eddy-quiet' regions but only by 24% in 'eddy-rich' regions (Jullien et al., 2020).*

Strong temperature gradients characterise 'eddy-rich' regions, increasing the importance of mesoscale SST-induced feedbacks (Bishop et al., 2017). Gaube et al. (2015) argue in 'eddy-rich' regions the relative importance of mesoscale SST-induced feedback on Ekman pumping velocities is comparable to the surface current-induced feedback, otherwise surface current feedback dominates over most of the ocean, as seen earlier from Fig. 1.7 (Dewar and Flierl, 1987; Seo et al., 2016).

Furthermore, mesoscale SST-THF feedback is likely to be strong in 'eddy-rich' regions, due to intensified air-sea heat fluxes (Bishop et al., 2017; Small et al., 2019). If we follow Jullien et al. (2020), wind stress-induced feedback on EKE variability is relatively weaker in these 'eddy-rich' regions. Does mesoscale SST-THF feed-

back then dominate in 'eddy-rich' regions, over wind stress-induced feedbacks? Yang et al. (2019a) argue it does at least in terms of the impact on sub-surface EKE dissipation down to 350m in the Kuroshio Extension. However this study does not appear to isolate mesoscale SST-wind stress coupling from surface current-wind stress coupling. There is ample reason to extend the study by Yang et al. (2019a) to investigate the impact of the dominance of mesoscale SST-THF feedback on the ocean in 'eddy-rich' western boundary current regions, compared to SST-wind stress exchanges to improve its representation in climate models.

Most studies above show the importance of isolating each mesoscale air-sea feedback, however the method to do this is nontrivial. Generally, previous studies use either one of three methods: first, to analyse fully coupled model runs including or excluding mesoscale air-sea exchanges, by smoothing the SST, e.g. Renault et al. (2019d); Jullien et al. (2020) or second, to compare an ocean-only model to a fully-coupled system, e.g. Yang et al. (2018, 2019a) or third, compare a fully coupled run to an uncoupled atmospheric model forced with smoothed SST from the coupled run e.g. Putrasahan et al. (2013). The first option is more complex, but effective, and involves filtering out mesoscale SST or surface current anomalies before the fields pass to the atmosphere in the coupled model (Jullien et al., 2020; Ma et al., 2016). Ma et al. (2016) is one of the first studies to introduce this new method, which remains frequently used to evaluate the impact of mesoscale air-sea exchanges on the large-scale (Renault et al., 2019b). The second option has limitations, each model type has different initial conditions, so the mesoscale ocean could be different, and mesoscale feedback could be overestimated in ocean-only models from a lack of feedback from the atmosphere (Yang et al., 2019a). In contrast, the advantage of an ocean-only model is it allows air-sea momentum and thermal feedbacks to be easily isolated from each other, which becomes difficult in the fully-coupled model where SST, wind stress and THF are all inter-related. Finally, the third method focuses on evaluating local atmospheric impacts, rather than feedback on the ocean.

To summarise this section, the importance of mesoscale SST-wind stress feedback on the local ocean was previously debated, and its impact on the large scale

ocean has only been quantified using an idealized quasi-geostrophic model, rather than a full primitive equation model. Mesoscale SST-THF feedback remains ambiguous over individual eddies. Finally, how mesoscale SST-THF feedback on the large-scale ocean compares to SST-wind stress feedback remains to be quantified in a single study and using the same model. Therefore, after identifying mesoscale SST-THF feedback over individual coherent eddies, this thesis focuses on the comparison of mesoscale SST-wind stress and SST-THF feedback, in a region resembling the Kuroshio Extension.

Many of the limitations of the studies in this section draw similarities to limitations discussed in sections 1.2 e.g. constraints on data, size of the domain studied, filtering cut offs and the method to isolate each mesoscale feedback. Additional considerations are the type and ability of the numerical model used, i.e. how well a model realistically resolves both mesoscale interactions, and large scale circulation. Subsequently, this is a topic we address in section 1.4. It is crucial to investigate how well mesoscale air-sea exchanges are represented in current state-of-the-art climate models to perform investigations into how they impact large scale ocean circulation.

1.4 Representation in current climate models

So far this review emphasises the importance of three principle mesoscale air-sea exchanges for both atmospheric boundary layer (ABL) variability (section 1.2), and feedback on local mesoscale activity and the large-scale ocean circulation (section 1.3). These mesoscale exchanges are fundamental to further our understanding of the coupled earth system. Most current research uses either observations (with their limitations discussed in section 1.2) or regional coupled models. This final section of the review discusses the current representation of mesoscale air-sea exchanges in both state-of-the-art high-resolution climate models (e.g. HighResMIP), and in coarser resolution climate models typical of CMIP6 and finally, this section highlights the future of ocean modelling. This discussion aligns with a wider area of active research: what resolution is required, in both the atmosphere and ocean, within climate models to realistically resolve key processes within our earth system?

The ability to resolve mesoscale air-sea exchanges globally relies on the following three key factors:

- the representation of mesoscale activity i.e. the ocean grid resolution relative to the baroclinic Rossby radius of deformation (Hallberg, 2013; Fox-Kemper et al., 2019; Hewitt et al., 2017, 2020)
- the representation of ABL processes i.e. the corresponding atmospheric resolution, particularly vertical mixing processes, pressure gradients and surface wind (Yang et al., 2018, 2019a; Song et al., 2009; Renault et al., 2019b)
- and the ratio of ocean to atmosphere resolution (Laurindo et al., 2018; Jullien et al., 2020).

The first baroclinic Rossby radius of deformation (R_d) is a fundamental scale, where rotational effects become as important as stratification, which acts to determine the size of eddies able to be represented, i.e. about 30 km at mid-latitude boundary currents (Chelton et al., 1998). The Rossby radius (R_d) reduces at higher

latitudes (to about 10 km) making it harder to resolve mesoscale eddies here. Therefore unsurprisingly, there are inter-model differences in the ability to represent mesoscale air-sea exchanges, which are largely dependent on differences in oceanic and atmospheric resolution (Yang et al., 2018).

Typically, state-of-the-art climate models possess either a 1/4° (eddy-present) or 1/12° (eddy rich) ocean component, and a minimum atmospheric component of 25 km at mid-latitudes (Haarsma et al., 2016). Although 25 km - 1/10° climate models are gradually being able to perform the full length Coupled Model Intercomparison Project (CMIP) runs, e.g. Chang et al. (2020), the vast majority of CMIP6 models possess an ocean component of 1°, meaning almost no mesoscale activity is explicitly resolved. Evidently at these coarse resolutions most of the small-scale air-sea heat and momentum variability and feedback on the ocean and atmosphere is not able to be resolved, and the ocean simply passively responds to the atmosphere in mid- and high- latitudes (Small et al., 2019).

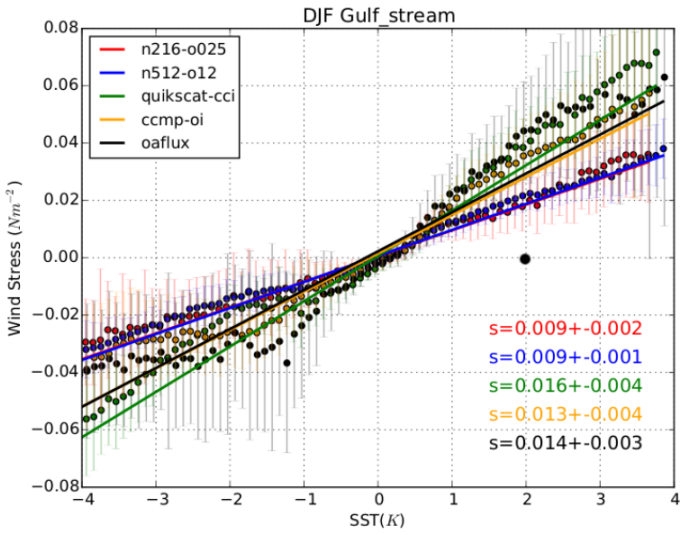

Figure 1.12: *Binned scatter plots of high pass filtered SST and wind stress over the Gulf Stream region with the linear regression coefficient indicated. There are three pairs of observational-based data (green, yellow and black). The Met Office GC3 climate model (HadGEM) data is plotted in blue for ∼ 25 km atmosphere, 1/12° ocean and in red for ∼ 60 km atmosphere, 1/4° ocean (Roberts et al., 2016).*

Despite overly strong spatial and temporal filtering of SST, Maloney and Chelton (2006) present one of the first studies to highlight that a coarse-resolution 1° ocean model reduces mesoscale ($\sim$ 1000 km) SST-wind stress coupling by half. Even with an eddy-rich ocean resolution of about 1/10°, coupled models still generally under predict realistic mesoscale SST-wind stress exchanges (Bryan et al., 2010; Laurindo et al., 2018; Lin et al., 2019). An exception to this under-prediction is found in the extra tropics within the Community Earth System Model (CESM). The CESM instead artificially enlarges mesoscale SST variance, causing mesoscale air-sea exchanges to be too strong (Laurindo et al., 2018). Bellucci et al. (2021) suggest 1/4° ocean resolution, in HighResMIP simulations, overestimates the covariance (or coupling strength), but improves the spatial structure, of mesoscale SST-sensible heat flux coupling in the Gulf Stream. In summary, despite a more eddy-energetic field, increasing ocean resolution from 1/4° to 1/12° does not necessarily improve the representation of mesoscale SST-wind stress coupling. For example, once mesoscale eddies are resolved, Roberts et al. (2016) argue model resolution doesn't change the mesoscale SST-wind stress coupling in the Gulf Stream (as shown in Fig. 1.12 where blue is $\sim$ 25 km atmosphere, 1/12° ocean and red is $\sim$ 60 km atmosphere, 1/4° ocean).

As a result of the high ocean and atmosphere resolution needed in coupled climate models, the representation of mesoscale air-sea interactions creates a great challenge for model development. For example, a 1/12° ocean component coupled to a $\sim$ 25 km atmosphere (as shown in Fig. 1.12) has a larger computational cost by a factor of about 10, compared to a 1/4° ocean, with a $\sim$ 60 km atmosphere (Fig.1.13) (Hewitt et al., 2016). The 1/4° ocean component typically lies in the 'grey zone' where some, but not all, mesoscale activity is resolved (and no adequate eddy parameterizations exist). The advantage of the increased computational cost of a 1/12° ocean, compared to a 1/4°, remains debated. Essentially, how well a 1/4° ocean represents realistic mesoscale eddy properties is yet to be quantified.

A higher resolution 1/12° ocean component is argued to improve the representation of the ocean mean state i.e. in the Atlantic Meridional Overturning Circulation

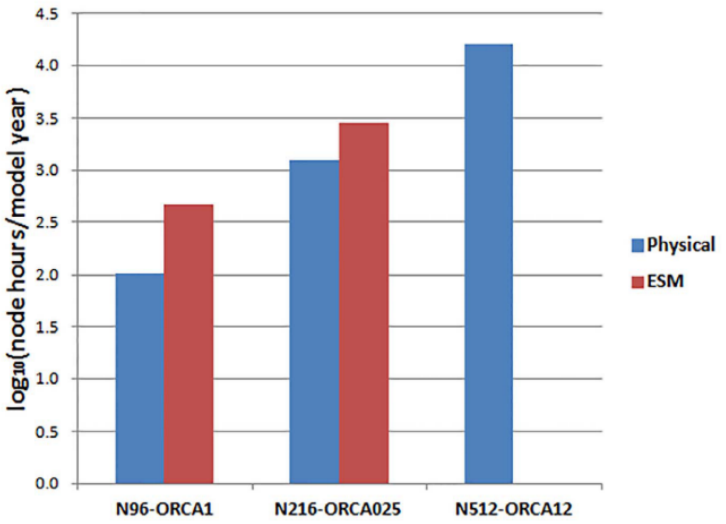

Figure 1.13: *Node hours per model year (shown as log_{10}) for coupled configurations of varying resolution from the Met Office GC3 climate model (HadGEM), either for the physical model only (blue) and the inclusion of the Earth System Model (ESM) components (red). N96, N216 and N512 are atmosphere resolutions of $\sim$ 150, 60 and 25 km respectively. ORCA1, ORCA025 and ORCA12 are ocean resolutions of 1°, 1/4° and 1/12° respectively (Hewitt et al., 2017).*

and the Southern Ocean (Chassignet and Marshall, 2008; McWilliams, 2008; Hewitt et al., 2017, 2020; Marshall et al., 2017; Munday et al., 2013). Although, whether a higher 1/12° ocean resolution improves the representation of WBC separation, through mesoscale air-sea exchanges, is unknown. Recent research suggests state-of-the-art coupled climate models still consistently fail to realistically represent WBCs and their separation, even with realistic topography, higher ocean resolution and near-global representation of mesoscale eddies (Ma et al., 2016; McWilliams, 2008; Chaigneau et al., 2008; Renault et al., 2019b; Hewitt et al., 2017). For example, although the high ocean-atmosphere resolution of 1/12° - 25 km shifts the Gulf Stream separation southward, compared to all other CMIP models, it is not necessarily an improvement from coarser resolution coupled simulations, as shown in Fig. 1.14 (Grist et al., 2021; Chassignet and Xu, 2017). Could this failure to represent WBCs in current models be because mesoscale air-sea exchanges are not

properly represented ?

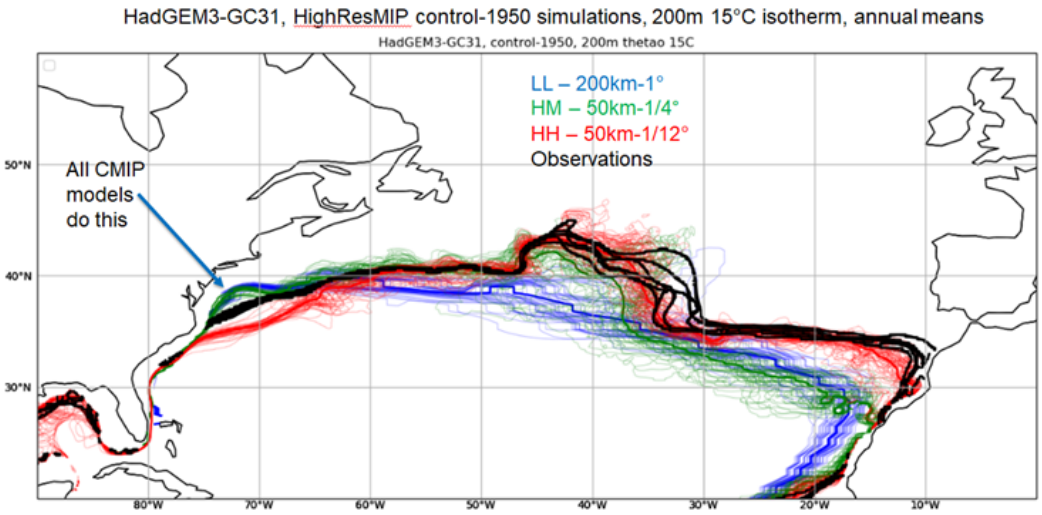

Figure 1.14: *Annual means of the 200 m 15°C isotherm for different resolutions of HadGEM3-GC3.1, as part of HighResMIP. Figure from personal communication with Malcolm Roberts.*

So far this section focuses on evaluating differences in ocean resolution to realistically represent mesoscale exchanges. There is a substantial lack of research in current literature discussing the corresponding atmospheric resolution needed to simulate the atmospheric response. The atmospheric grid resolution typically remains much coarser than the ocean, and each component is nearly always at different resolutions (Laurindo et al., 2018; Czaja et al., 2019; Maloney and Chelton, 2006). A comparison of high-resolution atmosphere-only models demonstrate a low resolution ($\sim$ 130 km) atmosphere cannot correctly capture turbulent heat fluxes in regions of strong SST gradients in mid-high latitudes, and simulates weaker surface winds than found at higher resolutions ($\sim$ 25 km) (Wu et al., 2019). High-resolution coupled models are not necessarily better at representing mesoscale air-sea exchanges due to the difference between the ocean-atmosphere grids (Wu et al., 2019). Compensating errors can be present and if the ratio of ocean-atmosphere resolution is high, small-scale features will be averaged out (Yang et al., 2018; Jullien et al., 2020).

In contrast, Jullien et al. (2020) argue an increase of atmospheric resolution only (from 1/4° to 1/12° with the same ocean) does not impact energy transfer induced by mesoscale surface current-induced feedback. This study uses a coupled model $46°N - S$ around the equator, although the effects of this change in resolution on mesoscale SST-induced coupling are unexplored (Jullien et al., 2020). To date there is no quantification of the ocean to atmosphere resolution ratio needed in coupled models for resolving mesoscale SST-induced air-sea coupling.

Looking at the future of ocean modelling can help to highlight research priorities. In the next decade (2020-2030) a study by Fox-Kemper et al. (2019) predicts finer ocean resolutions to 1/12° or 1/10 ° oceans will become more commonplace, unstructured grids and nested regional down-scaling so resolution can change regionally, increased use of high-resolution ocean and coupled models, better parameterizations and numerical and resolution improvements to air-sea coupling. One of the future goals of ocean modelling is the ability to represent submesoscales, particularly to improve the representation of mesoscale eddies (Schubert et al., 2019; Hewitt et al., 2020). As future ocean and atmospheric resolution increases, it is vital to understand what climate models can represent, regarding mesoscale exchanges and feedback on the ocean and what is missing, in order to guide future research.

There is a strong argument for parameterization of mesoscale air-sea exchanges in climate models (Bishop et al., 2020). Parameterizations are still required at the resolutions that will be affordable for at least the next several decades in most modeling inter-comparison projects. In the next version of the ocean NEMO model, both mesoscale surface current-wind stress, and SST-wind stress, feedback on the ocean will be parameterized by including a slab ABL to replace a full atmospheric model at a much cheaper computational expense (e.g. 10% extra to the ocean run) and to provide a better framework to test the model (Lemarié et al., 2020). This notable advance in the field of mesoscale air-sea research leaves room for the parameterization of mesoscale SST-THF exchanges as well, as promoted by Bishop et al. (2020).

In summary, two principle gaps in the representation of mesoscale activity in

current climate models are highlighted: first, whether a 1/4° or 1/12° ocean component is needed to realistically represent mesoscale eddy properties and second, what is the impact of changing the ratio of ocean to atmosphere grid resolution on mesoscale air-sea exchanges, particularly SST-THF exchanges. Implications for parameterization of mesoscale air-sea exchanges in coarser ocean resolutions are highlighted as a future research priority.

1.5 Conclusions and research priorities

The overarching aim of this thesis is to better understand feedback on the local and large-scale ocean from mesoscale air-sea exchanges. Within this, we aim to evaluate how well high resolution models can represent mesoscale eddies and their interaction with the atmosphere.

This literature review has highlighted key gaps in the current research. First, a quantification of mesoscale SST-THF feedback over individual coherent mesoscale eddies, globally and at smaller spatial resolutions than previously analysed, is outstanding. As an important contributor to mesoscale air-sea exchanges, at least in terms of energy transfers, this needs to be addressed. Second, how well mesoscale eddies, and their properties, are represented in 1/4° or 1/12° ocean resolutions in coupled models is yet to be quantified. The corresponding atmospheric horizontal resolution needed to accurately represent mesoscale air-sea exchanges is unclear. Finally, whether mesoscale SST-heat flux or SST-wind stress exchanges dominate in controlling large scale gyre circulation, using a primitive equation ocean model is yet to be evaluated in a single study.

This thesis provides an original contribution to science to address these current research gaps. The knowledge gaps form the following three research priorities, and the three corresponding scientific chapters of this thesis.

- How does the representation of coherent mesoscale eddy properties change with increased model ocean resolution ? (Chapter 3)
- What is the SST-THF feedback over coherent mesoscale eddies globally in coupled climate models, and is it dependant on the ratio of ocean-atmosphere grid resolution ? (Chapter 4)
- How do mesoscale SST-induced air-sea exchanges (SST-wind stress and SST-heat fluxes) impact mid-latitude gyre circulation ? (Chapter 5)

A discussion is provided in Chapter 6 to summarise the key results, answer-

ing the three thesis objectives, and how they improve our wider understanding of mesoscale air-sea exchanges, and their representation in current climate models, to move the field forward. The thesis concludes by examining the sensitivity of the results to the dataset and method used, and provides an outlook for future research.

In the following chapter, we first review the datasets and computational tools used through the thesis to address the three research objectives.

Chapter 2

Data and Computational Tools

2.1 Satellite altimeter data

This section introduces first, why this study chooses to use an observational dataset of sea surface height (SSH) to study mesoscale eddies and second, how SSH is observed including the benefits and limitations of this dataset.

2.1.1 Why do we choose SSH?

Chapter 1 states our objective to investigate the representation of coherent mesoscale eddies in numerical models, compared to reality. To achieve this aim, individual mesoscale eddy anomalies need to be identified. SSH provides a useful, reliable variable to accurately identify and analyse mesoscale eddies within the turbulent mesoscale field, due to the relation of surface height anomalies to geostrophic flow.

Transient eddies are observed both in hydrostatic balance, where the momentum equations reduce so the vertical pressure gradient balances the gravitational force (equation 2.1) and in geostrophic balance, where horizontally the pressure gradient balances the Coriolis acceleration (equations 2.2 and 2.3) as following (Vallis, 2019).

$$\frac{\partial p}{\partial z} = -\rho g \tag{2.1}$$

$$f\ u_g = -\frac{1}{\rho}\frac{\partial p}{\partial y} \tag{2.2}$$

$$f\ v_g = \frac{1}{\rho}\frac{\partial p}{\partial x} \tag{2.3}$$

where ρ is density, g is gravitational acceleration, f is the Coriolis parameter, u_g and v_g are the zonal and meridional surface geostrophic velocities respectively and $\frac{\partial p}{\partial x}$ and $\frac{\partial p}{\partial y}$ are the horizontal pressure gradients in the x- and y- direction respectively. $\frac{\partial p}{\partial z}$ is the vertical pressure gradient.

The vertical momentum equation reduces to hydrostatic balance when friction and the vertical acceleration are assumed negligible i.e. there is no (or very little) vertical motion. This is a balance between gravity and the vertical pressure gradient and is one of the most fundamental approximations made in ocean dynamics. Because of the hydrostatic relation, pressure can be computed at all depth levels by a single level, if density is known. The hydrostatic approximation is used because horizontal scales are much larger than the vertical, as typical of the ocean.

The balance of geostrophic forces is illustrated in Fig. 2.1 in vector form where on the left, pressure slopes downwards from the high pressure anomaly at the centre of the anomaly (or eddy) to the outside perimeter, and consequently the Coriolis term is directed towards the centre. The horizontal geostrophic flow **u** (a vector comprising of u_g and v_g) is perpendicular to the pressure gradient ∇p (i.e. $\frac{\partial p}{\partial x}$ or $\frac{\partial p}{\partial y}$). The flow is deflected to the right as a result of the Coriolis force in the Northern Hemisphere, or to the left in the Southern Hemisphere. The opposite occurs for a low pressure anomaly, where the Δp is in the opposite direction as shown in Fig. 2.1, right.

The tilt in the free surface, provided by the horizontal pressure gradient, means ocean surface structure and geostrophic flow can be calculated by knowing sea surface height η (Marshall and Plumb, 2008). Integrating the hydrostatic balance equa-

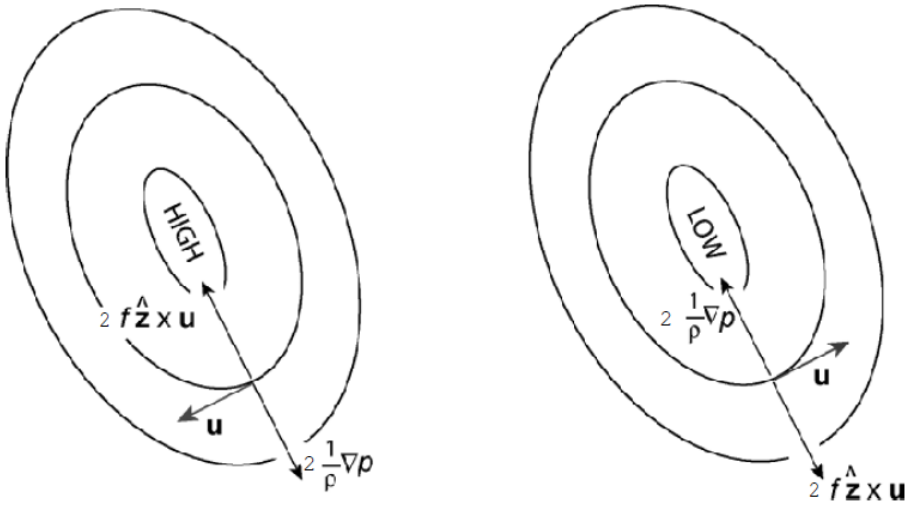

Figure 2.1: *A schematic of geostrophic balance over an anomaly of either high (left) or low (right) pressure.* ***u*** *represents a vector comprising of* u_g *and* v_g*,* f *is the Coriolis parameter in the vertical direction* $\hat{\mathbf{z}}$*,* ρ *is density and* ∇p *is the horizontal pressure gradient (Marshall and Plumb, 2008).*

tion from a constant depth (z) upwards to the free surface where $z = \eta$, assuming depth variations are much larger than density variations (i.e. $\rho = \rho_{ref}$) and by neglecting daily variations of atmospheric pressure, the pressure gradient equates to surface elevation η as following.

$$u_g = -\frac{g}{f}\frac{\partial \eta}{\partial y} \tag{2.4}$$

$$v_g = \frac{g}{f}\frac{\partial \eta}{\partial x} \tag{2.5}$$

where η is SSH.

The Rossby number ($R_o = \frac{\mathbf{u}}{f\ L}$) determines the importance of rotation in a fluid: it is a ratio of the acceleration of a fluid parcel compared to the Coriolis term, where L is the horizontal length scale. If the Coriolis term is large, the Rossby number is very small meaning the flow forms geostrophic balance.

2.1.2 How SSH is observed globally

In the 1990s, near-global gridded observational altimeter datasets of SSH first provided the opportunity to identify transient mesoscale anomalies within the highly turbulent oceans e.g. Chelton et al. (2011), and to compute the surface geostrophic flow associated with mesoscale eddies. Since then, an increased number of satellites with higher spatial and temporal resolutions have provided a long-term dataset to isolate mesoscale eddies from westward propagating Rossby waves.

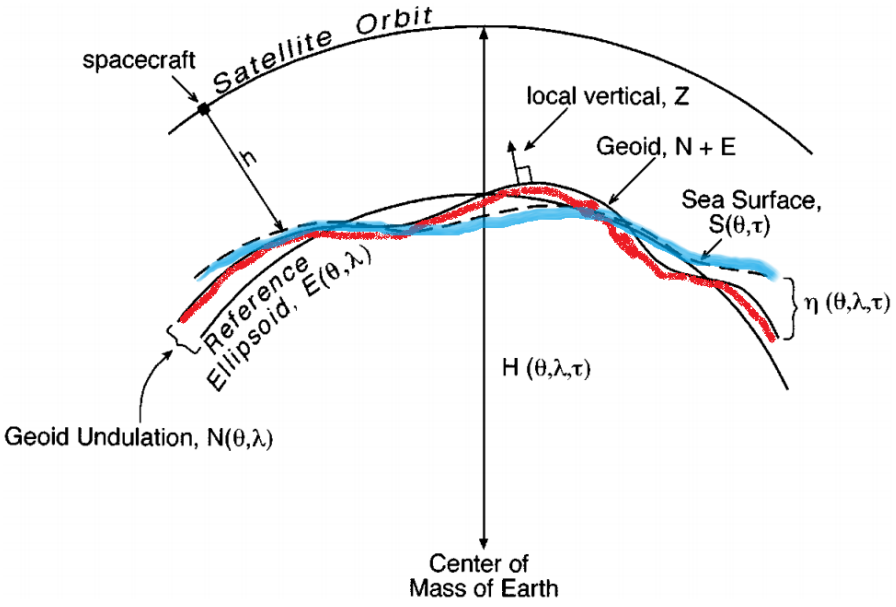

Figure 2.2: *A schematic showing the variables involved in the calculation of SSH (η). The free sea surface (S) is highlighted in blue and the geoid (reference ellipsoid plus geoid undulation) is highlighted in red. Variables vary with latitude θ, longitude λ and time t as indicated Wunsch and Stammer (1998).*

SSH (η) is the deviation of the ocean free surface (denoted as S and highlighted in blue in Fig. 2.2) relative to the geoid, as shown in red. The geoid is an estimate of the ocean surface if the ocean were at rest, i.e. no forces were acting on it (Wunsch and Stammer, 1998). The geoid is calculated by the addition of the reference ellipsoid of our planet (E in the figure) plus the geoid undulation (N) i.e. local variations in gravity. Satellite altimeters provide the opportunity to estimate the sea

surface (S) using radar by flying at a constant distance relative to the earth's centre, at a height H in the figure (Wunsch and Stammer, 1998). The distance (h) between the spacecraft and the physical sea surface is calculated using radar e.g. the travel time a pulse is emitted and received back to the spacecraft. Assuming E is included in the geoid height (N), as is commonly done, SSH can be computed as:

$$\eta(\theta, \lambda, t) = H(\theta, \lambda, t) - N(\theta, \lambda, t) - h(\theta, \lambda, t) \tag{2.6}$$

where θ, λ and t are latitude, longitude and time respectively.

The 20-year (1993-2014) SSH gridded dataset used in this thesis uses the highest global spatial (1/4°) and temporal (daily) resolution altimeter product available to date. The global multi-satellite Ssalto/DUACS (Developing the Use of Altimetry for Climate Studies) delayed-time altimeter products were produced and distributed by AVISO (Archiving, Validation and Interpolating of Satellite Oceanographic Data, 2014), and now by the Copernicus Marine and Environment Monitoring Service (CMEMS) (Ducet et al., 2000). The data used in this study was accessed in October 2016.

The long-term 20-year time mean is removed from the along-track altimeter product (SSH) to provide a global, gridded dataset (L4) of sea level anomalies (SLA). The time mean is the mean sea surface (MSS) along ground tracks i.e. the temporal mean of SSH (above the ellipsoid and including the geoid) as following (Mertz et al., 2017).

$$SLA = SSH - MSS_t \tag{2.7}$$

over a time period t. The anomalies are computed with an optimal and centered computation time window, by AVISO. The gridded field is generated through filtering out residual noise, sub-sampling, cross-calibration and optimal interpolation from the delayed-time merging of multiple satellites. All the missions are homogenized with respect to a reference mission (currently OSTM/Jason-2). This product processes data from all altimeter missions: Jason-3, Sentinel-3A, HY-2A,

Saral/AltiKa, Cryosat-2, Jason-2, Jason-1, TOPEX/Poseidon, ENVISAT, GFO, ERS1/2.

Although it is the highest global resolution currently available, at least until the new Surface Water Ocean Topography SWOT satellite is launched in the future, there are limitations to using this observational product, especially regarding the identification of mesoscale eddies (Carrier et al., 2016). The small-scale features identified in the along-track altimeter dataset can be smoothed out in the gridded map, except perhaps when these features are located at the crossover between ascending and descending ground tracks (Chelton et al., 2011; Archer et al., 2020). These reduces the effective resolution of the SSH dataset, and this is explored further in Chapter 3. Chelton et al. (2011) argue only features larger than 0.4° can be fully resolved by the gridded dataset. Using a new mapping method using 2D variational analysis (2DVAR) the space-time resolution of the AVISO SSH gridded product can be increased (Archer et al., 2020). Unfortunately we were not aware of this recent technique prior to performing the analysis in this study. A daily snapshot of the SSH dataset is given in section 2.4 when describing the post-processing.

2.2 A high-resolution coupled climate model: HadGEM3-GC3.1

As discussed in Chapter 1, the representation of mesoscale eddies, and corresponding small-scale air-sea exchanges, creates a great challenge for model development, as a result of the high ocean and atmospheric resolution required. To achieve the objectives of this thesis (Chapters 3 and 4) we rely on recent high-resolution fully coupled outputs from the UK Met Office climate model: HadGEM3-GC3.1.

HadGEM3-GC3.1 comprises of a GA7.1/GL7.1 global atmosphere/ land configuration based on the Met Office Unified Model (UM) and JULES components (Walters et al., 2019), a GO6 ocean (Storkey et al., 2018) based on the NEMO3.6 (Nucleus for European Modelling of the Ocean) ocean with a tri-polar grid (Madec, 2008) and a GSI sea ice component based on CICE (Ridley et al., 2018). The configurations form part of the coupled CMIP6 HighResMIP, a protocol especially designed for high-resolution models, as described further in Roberts et al. (2019) and Haarsma et al. (2016). For further information about the model set-up, the reader is referred to Hewitt et al. (2016), Williams et al. (2018) and Storkey et al. (2018).

The three high-resolution model configurations of HadGEM3-GC3.1 used in this thesis are as follows. At these high resolutions, no eddy parameterizations (i.e.Gent and McWilliams (1990); Munday et al. (2013)) exist in these configurations, but parameterizations of isopycnal mixing are present.

- N512-12 (model ID: u-al500) with an approximate 25 km atmospheric resolution (at mid-latitudes) and an ORCA12 (1/12°) ocean
- N216-12 (u-aj393): 60 km atmosphere, ORCA12 ocean
- N216-025 (u-aj368): 60 km atmosphere, ORCA025 (1/4°) ocean

The number of vertical layers in the ocean is 75 and in the atmosphere is 85. The top 10 m of the ocean has 1 m vertical resolution. Output from the different configurations is available here (Roberts, 2017a,b, 2018) through the Earth System Grid

Federation (ESGF). Chapter 3 uses the N216-12 and N216-025 configurations for 20 years of SSH output to isolate mesoscale eddies, whilst Chapter 4 uses one year of output, for a range of variables such as sea surface and air temperature, turbulent heat fluxes and surface wind speeds, from all three configurations. Model outputs are obtained after a 20 year spin-up. Although the large-scale climate continues to drift, it is likely to have a negligible effect on the results of this study.

2.2.1 Benefits of increasing resolution

Recent literature emphasises the benefits of increasing ocean resolution in a coupled climate model, despite its large computational expense, beyond the local representation of transient eddies and increased eddy kinetic energy to larger scale impacts (Hewitt et al., 2020, 2017; Thoppil et al., 2011). Due to the reduction in the diffusivity and viscosity permitted at higher ocean resolutions, an improvement in both the strength and position in quasi-stationary boundary currents occurs alongside improved large-scale ocean heat budgets and mean surface temperature biases (Kirtman et al., 2012; Chassignet and Xu, 2017; Roberts et al., 2020a; Marzocchi et al., 2015a; Griffies et al., 2015). In addition, improvements in the representation of the Agulhas Leakage and (generally) an increased strength in the Atlantic Meridional Overturning Circulation (AMOC) and transport exists, the latter a result of enhanced Labrador Sea convection (Roberts et al., 2020b). These improvements in the ocean mean state directly impact atmospheric variability, e.g. blocking and the North Atlantic Oscillation, and sub-seasonal weather forecasting (Roberts et al., 2020a). Finer resolution bathymetry (Fig. 2.3) improves the representation of small-scale topographic features, which act to steer currents and fronts and increase baroclinic instability and eddy formation (Hurlburt et al., 2008).

2.2.2 The representation of air-sea fluxes

The representation of air-sea fluxes of heat and momentum in models are vital for controlling the strength of mesoscale eddy anomalies. Turbulent (latent and sensi-

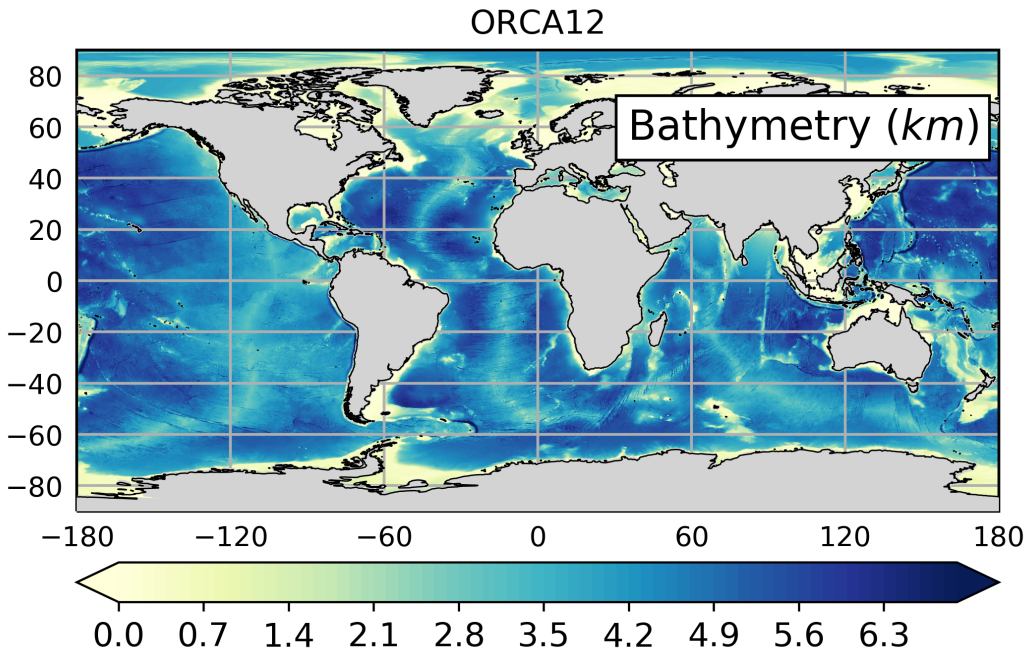

Figure 2.3: *ORCA12 bathymetry*

ble) heat fluxes are implemented in HadGEM3-GC3.1 by bulk formulae from Large and Yeager (2004), as following.

$$Q_S = C_p \, \rho_{air} \, C_H \, U_{10} \, (SST - T_{air}) \tag{2.8}$$

$$Q_L = L \, \rho_{air} \, C_E \, U_{10} \, (Q_{sat} - Q_{air}) \tag{2.9}$$

where Q_{air} is the specific air humidity, Q_{sat} is the saturation specific humidity, SST is the sea surface temperature, T_{air} is air temperature at 1.5 m. C_p is the specific heat capacity of air, ρ_{air} is air density, C_H is the sensible heat flux coefficient (Stanton number), U_{10} is the surface wind speed at 10 m, relative to the ocean current, L is the latent heat of evaporation and C_E is the latent heat flux coefficient (Dalton number).

The calculation of heat air-sea fluxes in HadGEM3-GC3.1 relies on hourly 'fully parallel' OASIS3-MCT coupling (a reduction from 3-hourly in GC2 to reduce ocean-atmosphere time lags, although still a long time for SST changes) (Valcke, 2013; Valcke et al., 2015; Craig et al., 2017; Hewitt et al., 2011; Williams

et al., 2018). To calculate latent and sensible heat fluxes, the OASIS coupler passes ocean fields (e.g. SST) to the atmosphere, where the heat fluxes are then calculated (Williams et al., 2018). This regridding occurs spatially and temporally, using first order conservative interpolation (Jones and Division, 1998). Conservative interpolation applies corrections to the decomposed mapped field to conserve area-integrated field magnitudes (Craig et al., 2017).

- Temporally, atmospheric fields are calculated more frequently compared to the ocean fields. Therefore, ocean fields are instantaneously passed to the atmosphere, and atmospheric fields are time-averaged to 1 hour, to match the ocean fields, to ensure heat and energy conservation. This is accurate to 10^{-4} W m^{-2} (Williams et al., 2018).

- When the atmospheric spatial resolution is noticeably coarser than the ocean resolution (i.e. N216-12), there is an atmospheric imprint onto the ocean during the spatial interpolation (Williams et al., 2018). Changing to second order conservative interpolation can improve this by smoothing the ocean data before it is passed to the OASIS coupler, however only existing relatively smooth fields can use second order interpolation (Jones and Division, 1998). Currently it is only used for evaporation and the net heat flux in HadGEM3 (Williams et al., 2018). It is not currently possible to generate the second order weights needed for turbulent heat fluxes because of the high spatial resolutions involved. At lower resolutions, second order interpolation is performed.

Chapter 4 further explores the impact of the ratio of grid resolution on small-scale air-sea heat fluxes.

2.3 The MITgcm

To address our final thesis objective (Chapter 5), we require a highly configurable scalable ocean model to resolve a turbulent mesoscale field and to relatively easily modify air-sea fluxes. The coupled climate model, HadGEM3-GC3.1, described in the previous section is too complex. The outputs are very computationally expensive and have already been run. Besides, using a fully coupled model allows many secondary feedbacks to exist, which are difficult to control (e.g. in the atmospheric boundary layer). Instead, the MIT general circulation model (MITgcm, Marshall et al. (1997)) provides a numerically efficient, simplified alternative to investigate the impact of the mesoscale field on the large-scale ocean. The following section provides an overview of some of the key features of the MITgcm configuration used in Chapter 5. Further adaptations of the set up (i.e. surface forcing, domain size, etc.) are supplied in Chapter 5.

In our set up, there is no atmospheric component coupled to the ocean model, therefore air-sea heat and momentum fluxes are parameterized and easily isolated from one another. The lack of atmosphere means surface temperature is restored to a defined temperature with a meridional gradient to mimic air temperature, using a restoring timescale: this temperature restoring acts as the air-sea heat flux.

The model uses spherical coordinates, which means the Cartesian coordinates (x, y and z) translate to unit vectors **i,j,k** where longitude is denoted as λ, latitude by ϑ and depth by z.

To simplify the full momentum equations the MITgcm, like many other ocean models including NEMO, solves the hydrostatic primitive equations as following for horizontal velocities (u and v) (Vallis, 2019; Marshall and Plumb, 2008; Madec, 2008; Marshall et al., 1997). Note the viscous and diffusion terms are omitted here for simplicity.

$$\frac{Du}{Dt} - f\ v + \frac{u\ v \tan\vartheta}{a} = -\frac{1}{\rho a \cos\vartheta}\frac{\partial p}{\partial \lambda} \tag{2.10}$$

$$\frac{Dv}{Dt} + f\ u + \frac{u^2 \tan\vartheta}{a} = -\frac{1}{\rho a}\frac{\partial p}{\partial \vartheta} \tag{2.11}$$

The vertical momentum equation reduces to hydrostatic balance (equation 2.1), the Coriolis term is approximate and the shallow water approximation can be made (Marshall et al., 1997). The shallow water approximation means vertical velocity (w) is neglected when it appears alongside a horizontal velocity (u, v), as vertical depths are comparatively much smaller, and by assuming the distance to the Earth's centre is constant. In the model, the additional of viscous and diffusive terms to the momentum equation provide viscous dissipation for momentum and diffusive sub-grid scale closure for temperature.

2.3.1 Model grid

We use an idealized baroclinic double gyre set up with 1/10° horizontal resolution. This resolution provides an active eddying field across the domain, whilst simulating an idealized western boundary current separating a subpolar and subtropical gyre, similarly to the Gulf Stream or Kuroshio Current regions.

The MITgcm uses a Arakawa C-grid. Fig. 2.4 indicates the position for the key variables: temperature, current velocities and vorticity. Knowing the location of each variable on the grid is fundamental for further calculations made throughout this thesis for example, for 'Brunt-Vaisala' buoyancy frequency (introduced in section 2.7), eddy kinetic energy or vorticity. It is also used to understand the numerical advection scheme used, as described in Chapter 5.

2.3.2 Vertical mixing parameterization

Finally, an important addition to the model in this study is the non-local 'kpp' parameterization of small-scale vertical mixing in the ocean surface boundary layer (OSBL). The OSBL is the layer between highly-turbulent atmospheric forcing (from wind and buoyancy stresses) and the slowly varying ocean interior, which acts to control air-sea fluxes of heat and momentum (Large et al., 1994). Turbulent mixing

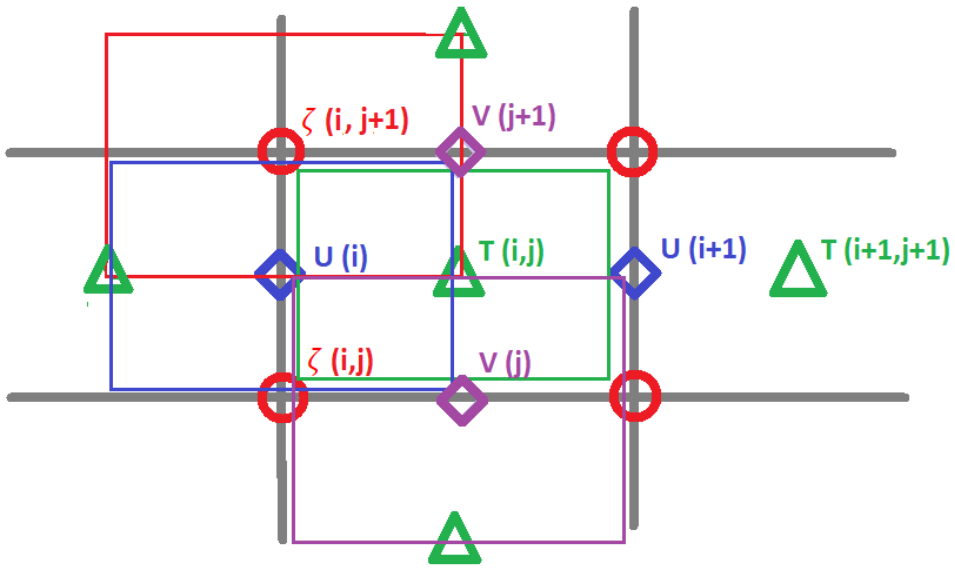

Figure 2.4: *A sample of the Arakawa C-grid used in the MITgcm, showing the position of model variables. The background grid is shown by the grey lines. The centre of the grid box for temperature (T) is positioned at the green triangle, for U- (blue) and V- (lilac) velocities at the diamond shapes, and for vorticity (ζ) at the red circle. The area covered in the grid box by each variable is shown in the large coloured boxes, by the corresponding colour.*

competes against restratification (or stabilization) from surface forcing to control the depth of the OSBL i.e. the vertical limit eddies can mix properties. Through the parameterization scheme, this depth is set by the 'boundary layer height': a critical value based on the Richardson number (Ri). The Richardson number is a ratio of buoyancy ($\frac{\partial \rho}{\partial z}$) to flow shear ($\frac{\partial u}{\partial z}$) terms as shown:

$$Ri = \frac{g}{\rho} \frac{\partial \rho}{\partial z} \left(\frac{\partial u}{\partial z}\right)^{-2} \tag{2.12}$$

Without this vertical mixing parameterization scheme, important boundary layer physics is excluded from the model. For example, a key advantage of including this scheme is formation of the mixed layer and increased surface mixing, which allows the extension of the boundary layer to penetrate into a stable thermocline. As this study will explore and alter air-sea interactions (Chapter 5), a more realistic impact

on mixing in the boundary layer and penetration into the ocean interior needs to be included.

2.4 Grid point dependent spatial filtering

There are a variety of methods to isolate mesoscale anomalies from the background large-scale field: a long-term mean is removed to isolate the mesoscale in HadGEM3-GC3.1 (20-yrs) and in observations, while a monthly mean is removed interactively as the model runs in the MITgcm.

When using output from the HadGEM3-GC3.1, and observational data, we can relatively easily perform a spatial high-pass filtering technique, on both the observational dataset and the model configurations, to remove large-scale variability and seasonality present in the background field. This study adopts a commonly-used efficient approach to remove a low-pass or 'smoothed' field to isolate the mesoscale anomalies, through low-pass Gaussian filtering. Although, it is too computational expensive to run this filtering interactively in MITgcm. Many previous studies successfully spatial filter the field to isolate mesoscale anomalies, such as Hausmann and Czaja (2012) who remove variability greater than 150 km, Villas Bôas et al. (2015) greater than 600 km, and Gaube et al. (2015) greater than 2°.

Although, a limitation of removing a low-pass filtered field is the choice of the spatial filtering width can influence the strength of the remaining high-pass filtered anomalies. Many different studies use different filtering widths. Since the work in this thesis was performed, the use of statistical analysis has gained popularity to avoid high-pass filtering (Laurindo et al., 2018; Li et al., 2017). Laurindo et al. (2018) argue cross-spectral analysis can be used to evaluate SST-wind speed coupling at spatial scales larger than 100 km, while Li et al. (2017) use spectral regression to evaluate the continuous scale dependence of SST-turbulent heat flux coupling in the Kuroshio region from 150 - 4000 km scales. Although these techniques can give reasonable estimates, the spatial scales in these previous studies are too large for comparison to our work.

Chelton et al. (2011) provide a commonly used eddy tracking dataset, which filters observational SSH anomalies by removing a low-pass Gaussian filtered (smoothed) field of $20° \times 10°$. For continuity this study uses the same filtering widths. Details

of how the low-pass Gaussian filtering works, and how it is adapted to work using either ocean or atmospheric model grid resolutions, or the observational gridded dataset, is described below. Despite differences found in the strength of the filtering between previous studies, most importantly for this work, a consistent strength of filtering is maintained across resolutions and variables by applying grid point-dependent filtering as following.

- First, a daily climatological mean is created: either over 20 years for the eddy tracking, or 10 years for the compositing data, due to data availability. A long-term mean has already been removed from the daily data in AVISO observations in the creation of the dataset (see section 2.1).
- Second, for eddy tracking the SSH extremes are removed in both the daily data and the long-term mean dataset. This removes very large values associated with coastlines (tides), lakes and inland seas.
- Third, the land in the model is set to zero, i.e. a land mask is added.
- Finally, both the observational and model daily data is high-pass filtered, by removing a low-pass Gaussian filtered field of $20^{\circ} \times 10^{\circ}$.

The multi-dimensional low-pass Gaussian filter assumes a normal distribution of the variable, then computes a sequence of 1 D Gaussian convolution kernel filters along each axis (as shown in equation 2.13).

$$G(x, \sigma) = \frac{1}{\sqrt{2\pi\sigma^2}} \exp^{-\frac{x^2}{2\sigma^2}} \tag{2.13}$$

where σ determines the width of the Gaussian kernel, or its standard deviation, for each given axis and σ^2 is the variance. The term $\frac{1}{\sqrt{2\pi\sigma^2}}$ normalizes the kernel, so increases in σ values reduces the amplitude and increases the width of the filter. In other words, increases in σ blur or smooth the data.

Evidently the different ocean and atmospheric variables need the same strength of spatial filtering. Therefore this method is named 'grid-point dependent' filtering

to account for the different number of grid boxes in either the ocean or atmospheric grids for each spatial scale (km). The filtering is implemented using the SciPy module in Python: scipy.ndimage.gaussian_filter and the source code can be found in Verveer (2005). Following Verveer (2005), the radius of the filter (w) is given in grid points as following.

$$w = 2 \times (t_{trun}\ \sigma + 0.5) + 1 \tag{2.14}$$

where t_{trun} truncates (or shortens) the filter at this many standard deviations. The default value of 4 is used for t_{trun}. The data is truncated to preserve the main features of the normal distribution and removes extreme values i.e. it can be used to make the range of the data finite at both ends.

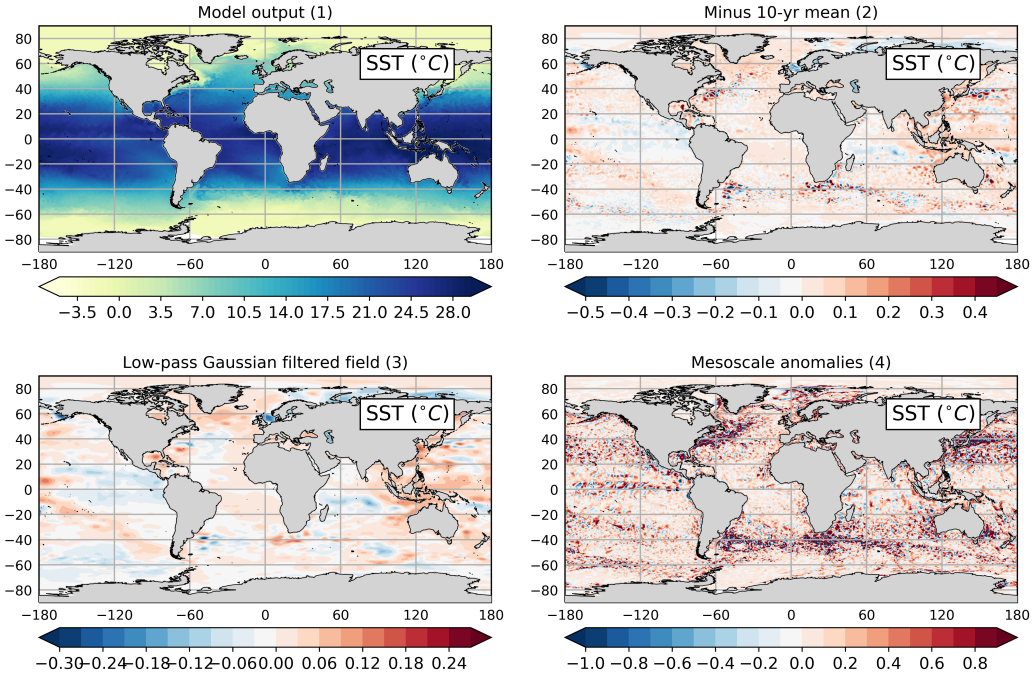

Figure 2.5: *The transition of the original model output (1), to the removal of the 10 year mean (2), to the creation of the low-pass Gaussian filtered field (3) and finally, to the difference between (2) and (3) to isolate the mesoscale anomalies (4). As an example, a daily snapshot of SST (°C) is plotted from N512-12. This process was repeated for all variables, all model configurations and in observational SSH data.*

Using equation 2.14, we can estimate the σ values needed in x- and y- direc-

Data	Grid resolution	$dx\ (km)$	$dy\ (km)$	σ_x	σ_y
AVISO	1/4°			10	5
ORCA12	$\sim$ 1/12°	$\sim$ 9 (max)	$\sim$ 9 (max)	30	15
ORCA025	$\sim$ 1/4°	$\sim$ 28 (max)	$\sim$ 28 (max)	10	5
N216	$\sim$ 1/2°	$\sim$ 93 (max)	62	3	2
N512	$\sim$ 1/4°	$\sim$ 39 (max)	26	7	5

Table 2.1: *Grid resolution (in $^\circ$ and km) and σ_x and σ_y values (rounded to an integer) needed to create a low-pass Gaussian filtered field of 20° zonally $\times$ 10° meridionally, for AVISO observations and each ocean (ORCA025 and ORCA12) and atmospheric (N216 and N512) resolution. The maximum values, as indicated by 'max', are found at the equator.*

tions to achieve a low-pass filter of approximately 20° zonally (in longitude) $\times 10^\circ$ meridionally (in latitude) in either an ocean or atmospheric grid. For example, to filter an ORCA12 (1/12° ocean) variable (such as SST) by 20°$\times$ 10°, this equates to approximately 240 grid boxes (w) in longitude and 120 grid boxes in latitude i.e. there are 120 grid boxes of size 1/12° in a 10° box. Rearranging equation 2.14 and substituting finds σ as approximately: σ_x = 30 and σ_y = 15. The sigma values, for each x- and y- direction, and the grid resolutions are shown in Table 2.1.

The ocean grid changes in dx (longitude) and dy (latitude), and the sigma values for the filtering are constant global estimates based on either 1/12° or 1/4° i.e. at the poles the filtering is not strong enough (as the sigma values are not high enough). The same is true for dx within the atmospheric grid, while dy is constant. The sigma values are calculated by the grid box size in km, rather than degrees.

A series of panels in Fig. 2.5 illustrate the processing of an example SST snapshot from the original data (1), to the removal of the long-term mean (2), the creation of the low-pass Gaussian filtered field (3) to its removal and the subsequent isolation of mesoscale anomalies (4). This transition is repeated for the absolute 10 m

wind speed (= $\sqrt{(u^2 + v^2)}$) and sensible heat flux in Fig. 2.6, and for a snapshot of daily SSH, halfway through the time series, in Fig. 2.7. The global distribution of the high-pass filtered SSH anomalies is shown in Fig. 2.7 for both observations and the two model resolutions prior to tracking mesoscale eddies (section 2.5). At first glance, the SSH anomalies display a similar strength and spatial distribution between the model and observations.

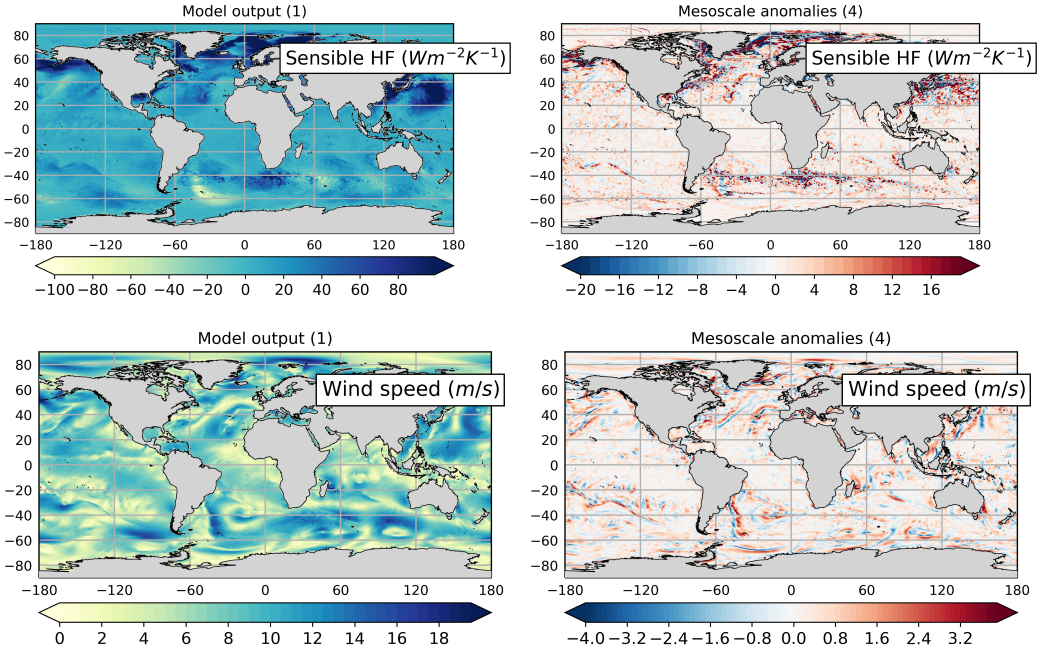

Figure 2.6: *The transition of the original dataset (1) to the creation of mesoscale anomalies (4) for a snapshot of the sensible heat flux (upper subplots) and the absolute 10 m wind speed (= $\sqrt{(u^2 + v^2)}$) from N512-12.*

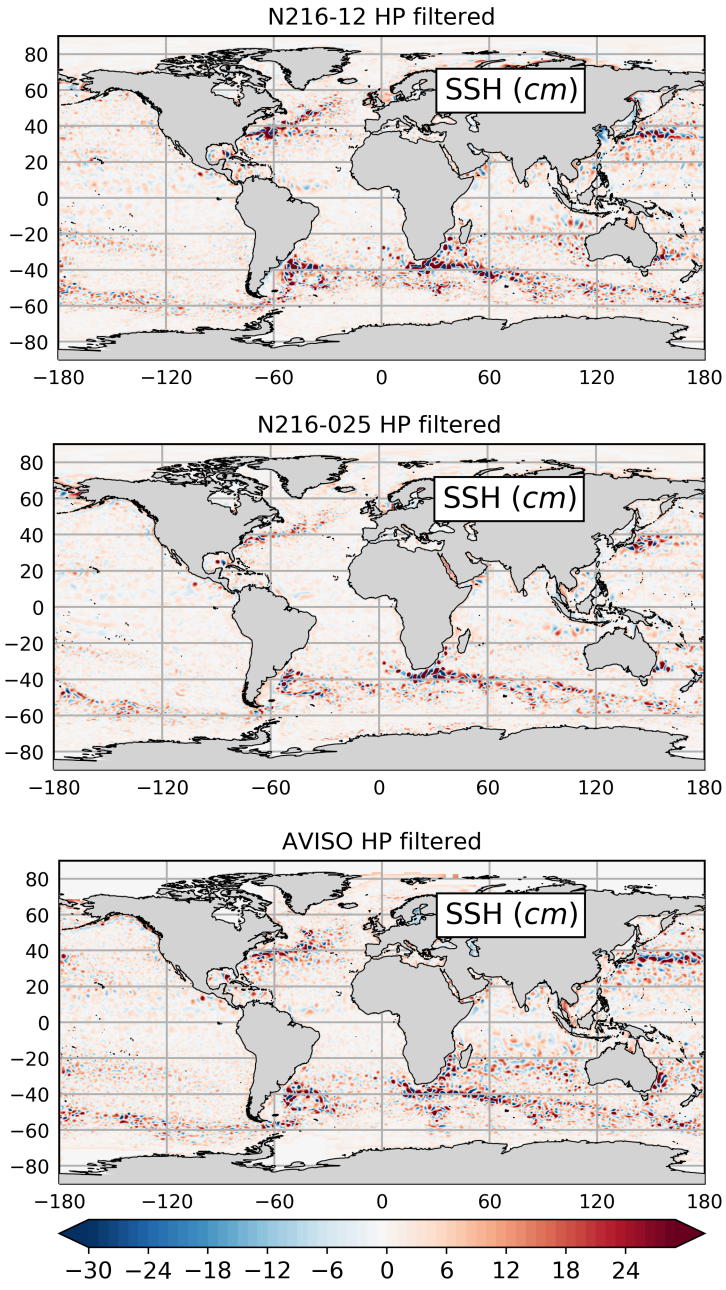

Figure 2.7: *SSH anomalies after high-pass filtering, by removing a low-pass Gaussian filtered field, for N216-12, N216-025 and observations: a snapshot taken halfway through the time series (10 years in).*

2.5 Eddy detection algorithm

Both Chapter 3 and 4 use closed coherent mesoscale eddies, isolated and tracked globally using a SSH-based eddy detection algorithm. There are numerous eddy detection algorithms available in the literature, differing by either the metric used for eddy identification (such as vorticity, Okubo-Weiss parameter or Lagrangian particle tracking), high-pass filtering or the tracking technique (for example to include the merging and splitting of eddy trajectories) (Chelton et al., 2011; Chaigneau et al., 2008). Each method has its own advantages and limitations, and the basis of our algorithm is physically-based and has been heavily tested and used in literature. Crucially, in this thesis, the same eddy detection algorithm is used on all datasets, both climate model outputs (section 2.2) and altimeter observations (section 2.1), to eliminate differences arising from different detection algorithms.

For this work, an SSH-based eddy detection algorithm is adapted from Mason et al. (2014) (itself based on Chelton et al. (2011), where differences are discussed in Mason et al. (2014)). Eddies are identified and tracked as closed coherent vortexes detected through successive closed contours of SSH anomalies, and subject to various tests as shown in Fig. 2.8 (left) for a region around the Canary Islands using observational data. The closed contours are shown in green, identified eddy centres are shown in white and the eddy trajectories over time are shown as either red (for anti-cyclonic eddies) or blue (cyclonic) lines. The background colour represents SSH in cm. How the eddy identification and tracking algorithm works, its criteria and the adaptations from Mason et al. (2014) are listed below.

After the SSH anomalies are isolated from the background and high-pass filtered (section 2.4) a global map of SSH contours is computed from 100 cm to -100 cm with an interval/ step of 0.3 cm, as shown for a sample region in Fig. 2.8, left. Starting from a SSH minimum (cyclone) or maximum (anti-cyclone), the algorithm then loops outwards over successive closed contours of SSH (Fig. 2.8 right, grey lines). The various criteria needed to save the identified anomaly are:

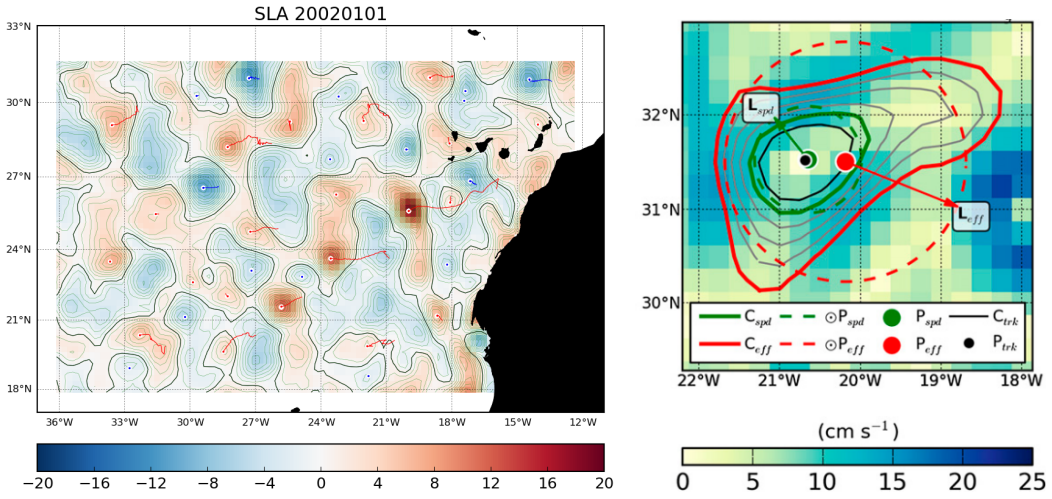

Figure 2.8: *(left) A sample region near the Canary Islands of SSH anomalies (cm, colour), the contour lines used for eddy identification (green), the identification of an eddy centre (white dot) and the tracked eddy trajectory (red lines for anti-cyclonic warm-core eddies) using AVISO observational data. (right) A schematic of a single eddy from Mason et al. (2014) used to explain eddy identification and tracking. Contours of SSH (grey) overlay the surface current velocity (colour). Two eddy radii are introduced: the speed-based radius (denoted as L_{spd}) which is the radius of a circle (green dotted line) fitted to the SSH contour found at the maximum rotational velocity (green solid line) and second, the effective radius (L_{eff}) which is the radius of a circle (red dotted) fitted to the outermost closed SSH contour (red solid). Eddies are tracked using the centre of the L_{spd} circle (black dot), rather than the centre of the L_{eff} (red dot). The black circle indicates the minimum pixel limit of 8.*

.

- A 'shape test' is undertaken based on Kurian et al. (2011) i.e. how circular the anomaly is to exclude filaments. If the error set to high, more irregular shapes can be identified. This is maintained at 55% error from Mason et al. (2014).

- Positive SSH values are required for an anti-cyclonic eddy (and negative for

cyclonic).

- The anomaly must contain a single maximum (or minimum) peak of SSH anomaly (unlike (Chelton et al., 2011) which allows multiple anomalies).
- A minimum amplitude is set to 1 cm and a minimum pixel count of 8 is required.

There is no set minimum or maximum eddy radius; instead an eddy's size is limited by its pixel range, as demonstrated by the black circle in Fig. 2.8 (right). For an eddy to be successfully identified, each closed contour of SSH needs to lie within a specific pixel range of 8 and 10,000. Therefore when increasing the grid resolution the same minimum pixel number of 8 allow smaller eddies to be detected compared to a coarser resolution.

As shown in Fig. 2.8 (right) two eddy radii are created during the identification of an eddy: first, the speed-based radius (denoted as L_{spd}) which is the radius of a circle fitted to the SSH contour found at the maximum rotational velocity and second, the effective radius (L_{eff}) which is the radius of a circle fitted to the outermost SSH contour. These two radii are shown in green and red respectively in Fig. 2.8 (right). After identification, eddies are then tracked using the centre of the L_{spd} circle, following Mason et al. (2014), unlike Chelton et al. (2011) who use the centre of the L_{eff} (red dot).

Identified eddies are tracked (or joined together) by forming an elongated ellipse in the x-direction (west-east) around the eddy, and using this ellipse to search for the next identified eddy. Previously, the ellipse was based on the Rossby wave speed (see section 2.7). This was updated in 2017 by D.Chelton and AVISO when providing a new dataset of tracked eddies directly from AVISO (Chelton et al., 2017). The update provided an improvement in the unrealistic 'jumping' of eddy tracks by changing the search ellipse and applying a cost function, as described in Altimetry (2017), page 5. This improvement in the eddy tracking was incorporated into our eddy tracking algorithm. Two further adaptations we made from (Mason et al., 2014) are listed below:

- The identification and tracking components of the algorithm were split so global identification at each daily timestep is run in parallel to increase computational efficiency. For a chosen region and time period, eddies can be tracked from the already identified eddy centres. All eddy tracks (and their associated properties) are stored and for eddies left 'active' (not masked), their tracks are able to be resumed for future tracking.

- The algorithm is adapted for use with the irregular NEMO ocean grid. A remaining limitation to our method is the ability to wrap tracks across the irregular NEMO grid divide at approximately 73°E. This slight jump in tracks is assumed to not have a large consequence on global statistics and there is no obvious increase in eddy birth and death frequency either side of this divide. This can be observed in Chapter 3: Figs. 3.2 and 3.14.

An example of the filtered SSH anomalies with the identified and tracked mesoscale eddies is given for a sample region, including the Agulhas Current and Brazil-Malvinas Confluence, in Fig. 2.9. This is a zoomed in snapshot of SSH anomalies from Fig. 2.7 to illustrate the result of the tracking algorithm for both anti-cyclonic and cyclonic eddies.

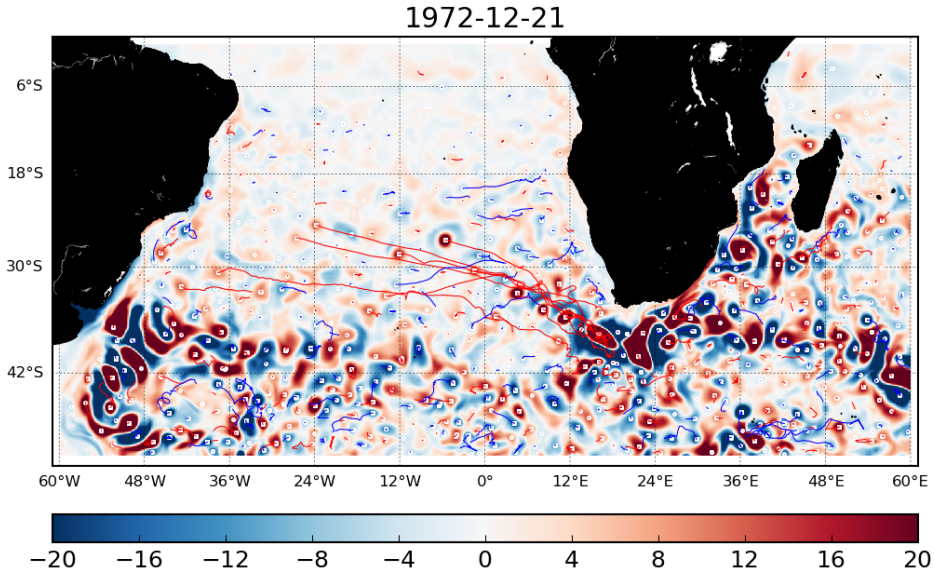

Figure 2.9: *A random daily snapshot of filtered SSH anomalies (cm, colour) overlaid with identified eddies (white dots) and eddy trajectories for either anti-cyclonic (red lines) or cyclonic (blue) eddies in the Agulhas Retroflection in N216-12.*

2.6 Eddy composite averaging

Using the dataset of globally tracked mesoscale eddies, we examine air-sea exchanges of heat and momentum, associated with them e.g. SST, air-sea heat fluxes and wind speed. A technique termed 'composite-averaging' is an efficient and frequently used way to show mean signatures on ocean and atmospheric variables from individual time-varying mesoscale eddies, and to effectively remove variability associated with changing oceanic and atmospheric conditions e.g. weather (Hausmann and Czaja, 2012; Villas Bôas et al., 2015; Frenger et al., 2013; Gaube et al., 2015).

The 'composite averaging' technique used in Chapter 4 is illustrated in Figure 2.10 and described as following.

- First, a region is identified around the tracked mesoscale eddy centre in the chosen high-pass filtered variable, SSH in this example (left subplot). The reader is referred to section 2.4 for details of the filtering. The nearest grid point to the eddy centre is used.

- Second, the region is normalized to the effective radius L_{eff} (plotted as a white circle in the next subplot). L_{eff} is defined as the radius of a fitted circle with the same area as the outermost closed SSH contour in each tracked eddy. The whole region is now 2.8 $\times$ L_{eff} in both directions from the eddy centre (i.e. 5.6 $\times$ L_{eff} in the zonal and meridional directions). A magnitude of 2.8 was arbitrarily chosen to include the surrounding impact of the eddy without the region being too large.

- Third, the region is either rotated to align with a westerly wind (third subplot), or rotated so the pole is northwards and equator is southwards. Essentially if the eddy is in the Southern Hemisphere, the region is flipped in the meridional direction (not shown in the figure). This produces a consistent background northward SST gradient, irrespective of which hemisphere the eddy was originally situated in.

- Finally, the fourth subplot shows the region is interpolated onto a high-resolution regular grid of size 2.8 $\times$ L_{eff}. For ocean variables, this interpolation converts the normalized region from an irregular NEMO grid to a regular grid.

Figures 2.11 and 2.12 repeat this process over the same tracked eddy for SST (on the ocean grid) and wind speed (on the atmospheric grid). The final subplot is then averaged over all eddies globally in 1-year to achieve a mean composite. All eddies globally are averaged for one year in the following three model configurations: year 1955 in N216-025, year 1954 in N512-12 and year 1975 in N216-12. The year chosen is either 4 or 5 years into the eddy tracking; the results are independent of the year chosen.

For the SST and turbulent heat flux anomalies used in the published work in Chapter 4, rotating the snapshots to align with the wind direction before composite averaging made little difference. This rotation becomes important when evaluating mesoscale SST-wind stress relationships (Gaube et al., 2015). Instead, the SST and turbulent heat flux composites were rotated so the pole is northwards and equator is southwards.

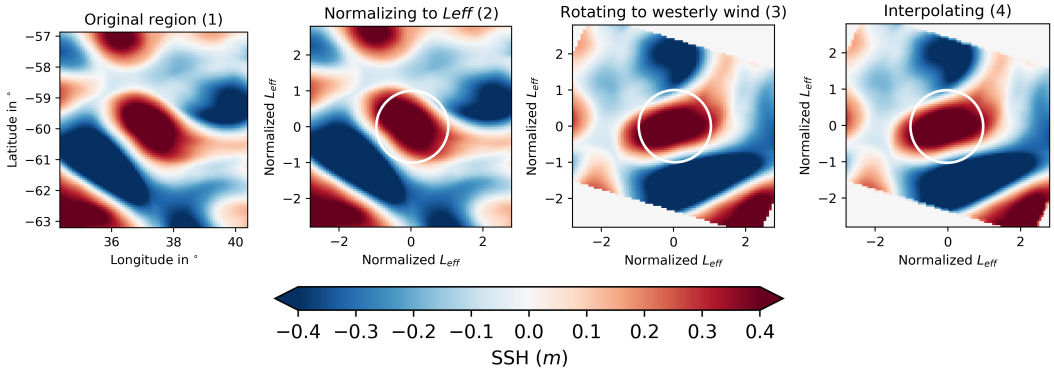

Figure 2.10: *A 1-day snapshot of SSH associated with a single large-amplitude (binned between 34±6 cm) anti-cyclonic eddy in N512-12.*

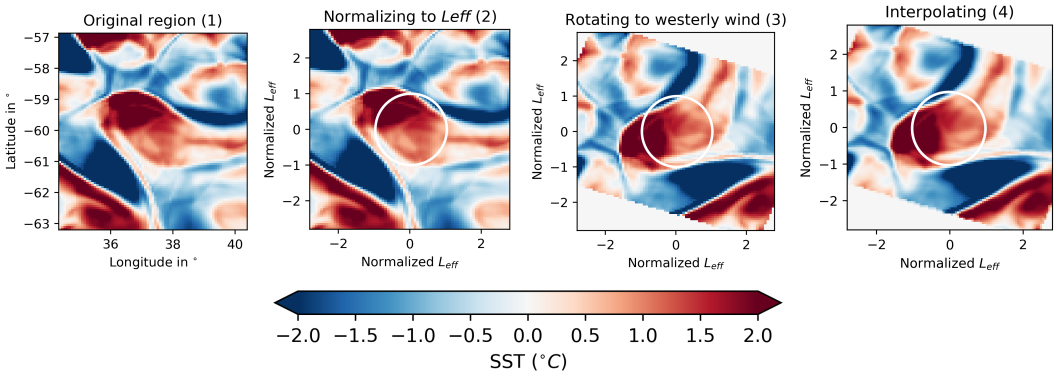

Figure 2.11: *A 1-day snapshot of SST associated with the same large-amplitude (binned between 34±6 cm) anti-cyclonic eddy in N512-12.*

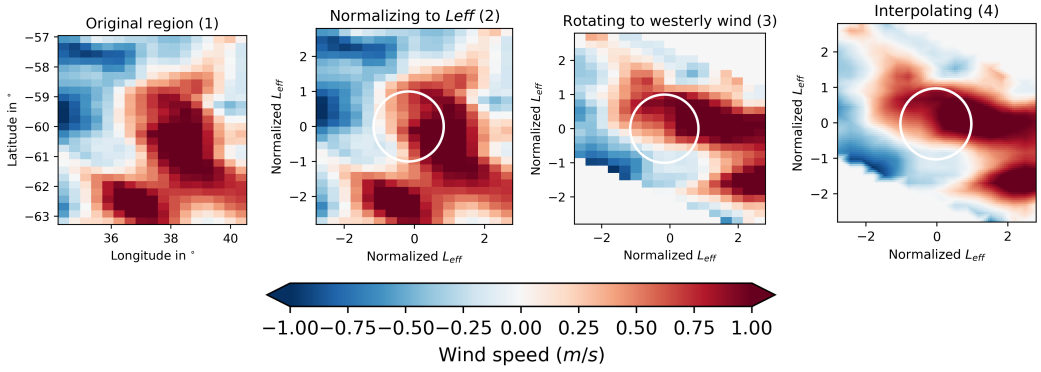

Figure 2.12: *A 1-day snapshot of wind speed associated with the same large-amplitude (binned between 34±6 cm) anti-cyclonic eddy in N512-12.*

2.7 Rossby radius of deformation

The oceanic baroclinic Rossby radius of deformation (denoted as R_d) is a fundamental parameter for determining where mesoscale eddies can be resolved in the oceans, i.e. the length scale which permits baroclinic instability to occur, as first introduced in Chapter 1. Put simply, R_d is the length scale where the effects of rotation (such as within a coherent eddy) become comparable with effects of stratification, and can be approximated by the ratio between the two:

$$R_d = \frac{NH}{f} \tag{2.15}$$

where N^2 measures ocean stratification: the 'Brunt-Vaisala' buoyancy frequency, H is water depth and f is the Coriolis parameter (Vallis, 2019).

In both Chapter 3 and 5, following Chelton et al. (1998) based on the WKB approximation and assuming one baroclinic mode, R_d is computed from the phase speed of long mode gravity waves (C_{ph}) outside the Tropics ($> 5°N/S$). Unlike R_d, C_{ph} is a function of solely stratification and water depth as shown in equation 2.16. A key assumption when calculating R_d from the gravity wave phase speed is the temporal variability of stratification is neglected, because we can assume the seasonal variation of R_d at any given location is small (Chelton et al., 1998).

$$C_{ph} \approx C_{ph}^{WKB} = \frac{1}{\pi} \int_0^H N(z)\, dz \tag{2.16}$$

where $N = \sqrt{N^2}$ as follows:

$$N^2 = -\frac{g}{\rho_{ref}} \frac{d\rho}{dz} \tag{2.17}$$

where ρ is density and $\rho_{ref} = 1000\ kg\ m^{-3}$. For the climate model HadGEM3-GC3.1 density variations are a function of both temperature and salinity, whilst in the MITgcm model density is dependent solely on temperature (see section 2.3). In the models $\frac{d\rho}{dz}$ is situated at the grid cell centre (i.e. at the yellow triangles in Fig. 2.4).

The gravity wave phase speed C_{ph} is isotropic, due to the square root of N, so the absolute value of C_{ph} in both directions is the same.

R_d is then simply:

$$R_d = \frac{C_{ph}}{f} \tag{2.18}$$

An example of the calculated R_d in the coupled climate model HadGEM3-GC3.1 is shown in Fig. 2.13 for the ORCA025 global ocean. As shown, spatial variations of R_d follow changes in latitude (f), with maximum values of about 100 km found towards the equator, and minimum values of about 10 km towards the poles, as found in observations with spatial resolution of 1° (Chelton et al., 1998). Some more subtle variations in R_d are shown, associated with variations in internal density stratification.

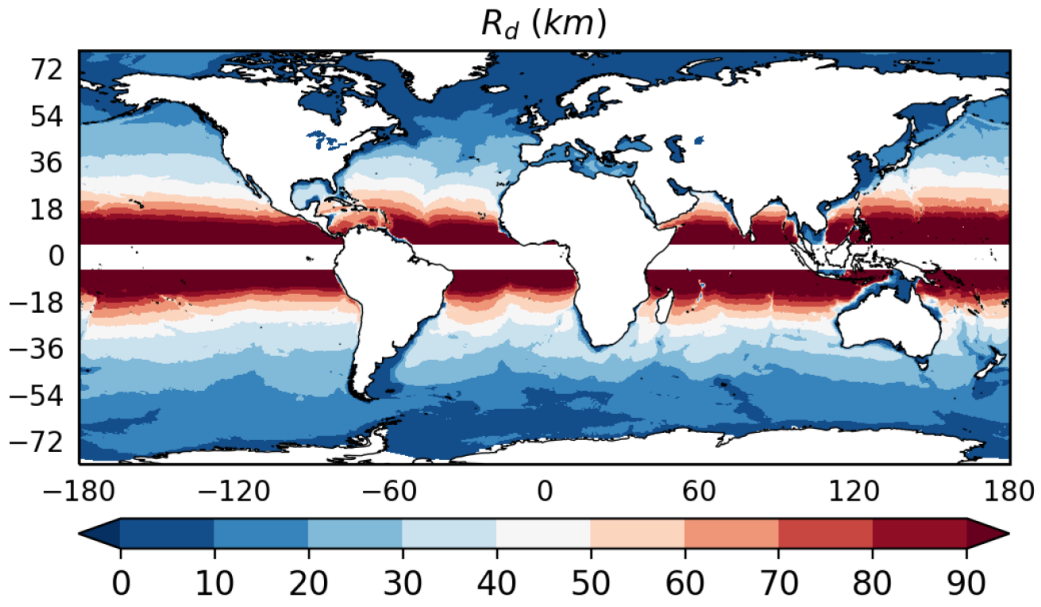

Figure 2.13: *A daily snapshot of the Rossby radius of deformation (R_d, km) in N216-025.*

The Rossby radius of deformation is then used to calculate the long-wave baroclinic Rossby wave phase speed (C_g) for comparison to the propagation speed of mesoscale eddies in Chapter 3, as shown in equation 2.19. We assume Rossby waves propagate westward at a speed similar to mesoscale eddies.

$$C_g = -\beta \, R_d^2 \tag{2.19}$$

where β is the latitudinal variation of the Coriolis parameter, calculated as $\beta = \frac{2\Omega}{R} \cos\theta$. Ω is earth's rotational rate, R is its radius and θ is latitude (Chelton et al., 1998).

2.8 Summary of key points

This chapter has introduced the numerical tools and datasets, which provide the opportunity for the analysis to come in Chapters 3, 4 and 5. An explanation is given of why either a observational or model dataset, or a particular tool, was chosen by discussing its benefits and limitations.

Chapter 3

Evaluating surface eddy properties in coupled climate simulations with 'eddy-present' and 'eddy-rich' ocean resolution

The chapter is structured as follows. Sections 3.1 to 3.5.4 present the published paper (Moreton et al., 2020), and additional complementary unpublished results are given in section 3.6. Section 3.7 concludes the chapter.

The publication details are: Moreton S., Ferreira D.,Roberts M.J., and Hewitt H.T., Evaluating surface eddy properties in coupled climate simulations with 'eddy-present' and 'eddy-rich' ocean resolution. Ocean Modelling, 147, 2020. ISSN 14635003. doi:10.1016/j.ocemod.2020.101567

3.1 Abstract

As climate models move towards higher resolution, their ocean components are now able to explicitly resolve mesoscale eddies. High resolution for ocean models

is roughly classified into eddy-present (EP, $\sim$ 1/4°) and eddy-rich (ER, $\sim$ 1/12°) resolution. The cost-benefit of ER resolution over EP resolution remains debated. To inform this discussion, we quantify and compare the surface properties of coherent mesoscale eddies in high-resolution versions of the HadGEM3-GC3.1 coupled climate model, using an eddy tracking algorithm. The modelled properties are compared to altimeter observations. Relative to EP, ER resolution simulates more (+60%) and longer-lasting (+23%) eddies globally, in better agreement with observations. The representation of eddies in Western Boundary Currents (WBC) and the Southern Ocean compares well with observations at both resolutions. However a common deficiency in the models is the low eddy population in subtropical gyre interiors, which reflects model biases at the Eastern Boundary Upwelling Systems (EBUS) and at the Indonesian outflow, where most of these eddies are generated in observations. Despite a grid spacing larger than the Rossby radius of deformation at high-latitudes, EP resolution does allow for eddy growth in these regions, although at a lower rate than seen in observations and ER resolution. A key finding of our analysis is the large differences in eddy size across the two resolutions and observations: the median speed-based radius increases from 14 km at ER resolution to 32 km at EP resolution, compared with 48 km in observations. It is likely that observed radii are biased high by the effective resolution of the gridded altimeter dataset due to post-processing. Our results highlight the limitations of the altimeter products and the required caution when employed for understanding eddy dynamics and developing eddy parameterizations.

3.2 Highlights

- Eddy-rich (ER) has smaller and longer-lasting eddies than eddy-present (EP)
- EP captures 40% of eddies in observations even at high latitudes (ER captures 63%)
- Both model resolutions have a low eddy count in the EBUS and gyre interiors

- Eddy radii scale well with the smaller of the Rossby radius or the Rhines Scale

3.3 Introduction

Mesoscale ocean eddies, generated from baroclinic and barotropic instabilities of the mean flow, are ubiquitous in the world oceans (Chelton and Xie, 2010). Ocean eddies are important for a number of local processes such as air-sea exchanges of momentum, freshwater and heat fluxes (Renault et al., 2016a,b; Gordon and Giulivi, 2014; Villas Bôas et al., 2015) and the upwelling of nutrients, which promotes biological activity (Gaube et al., 2017; Brannigan, 2016). Mesoscale eddies have a major influence on the large-scale circulation, controlling its mean state in the Antarctic Circumpolar Current (Marshall and Radko, 2003), as well as its response to climate change (e.g. Abernathey et al., 2011; Munday et al., 2013; Griffies et al., 2015).

Over the last decade or so, many climate modelling groups have sought to increase the resolution of ocean models (e.g. McClean et al., 2011; Griffies et al., 2015; Sein et al., 2017). The primary aim has been to improve the representation of key mesoscale features such as eddies, boundary currents and narrow sills (for dense overflows), and hence improve the mean-state and variability of the coupled climate system (Roberts et al., 2016; Minobe et al., 2008; Marzocchi et al., 2015b). It remains unclear whether the improved model fidelity in higher resolution models is primarily a result of an improved mean state via these key frontal features, or a consequence of the improved representation of the eddies themselves. The computational expense of a high-resolution ocean component in a coupled climate model is high and the benefits of increased computational cost need to be clearly identified.

In this context, the ”high resolution” ocean component often refers to two types of resolutions: eddy-present (EP, $\sim$ 1/4 °) and eddy-rich (ER, $\sim$ 1/12°) (Fox-kemper and Bachman, 2014). Although not strictly defined, EP denotes resolutions which permit some mesoscale eddies to be captured in the low and mid-latitudes, while

ER refers to resolution for which eddies are present at most latitudes (excluding the Arctic basin and the continental shelf around Antarctica). The distribution of mesoscale features in a model mainly depends on the ratio of its horizontal grid resolution, Δx, to the Rossby radius of deformation, R_d. Barotropic and baroclinic instability processes are only expected to be properly resolved when the grid point spacing Δx is several times smaller than R_d, although a minimal criteria of 2 times smaller has sometimes been used (Hallberg, 2013).

Although coupled models with a high-resolution ocean component are increasingly available, many modelling centres have not yet developed an operational version of their climate models with a high-resolution ocean component. Coupled Model Inter-comparison Projects (CMIP) will encompass models across a range of resolutions, including EP and ER resolutions (CMIP6 HighResMIP) as well as eddy-parameterising models (Eyring et al., 2016; Haarsma et al., 2016). The cost-benefit balance of ER versus EP resolution is still being examined. While EP offers a lower computational cost than ER resolution, it sits in the so-called 'grey-zone' where the benefits of removing eddy parameterization and resolving some (but not all) mesoscale eddies and eddy fluxes are not obviously superior to a coarser resolution ocean with full eddy parameterization (Hewitt et al., 2017). Although the mesoscale field comprises more than just coherent eddies, evaluating the representation of coherent eddies at EP and ER resolutions can inform the choice of resolution in future model development (Hewitt et al., 2017; Torres et al., 2018).

Understanding the properties of eddies is also essential for their parameterization in coarse ocean models (Gent and McWilliams, 1990). For example, the eddy scale (estimated from either observations or models) often explicitly enters eddy parameterization schemes through mixing length arguments e.g.(Eden and Greatbatch, 2008; Bates et al., 2014). The size of coherent mesoscale eddies is often used as an indicator of scale for the whole mesoscale field and is a fundamental measure employed in numerous studies of eddy dynamics, notably to distinguish dynamical regimes (Tulloch et al., 2009, 2011; Eden, 2007; Theiss, 2004; Klocker and Marshall, 2014).

While ocean models are not perfect tools to provide estimates of eddy properties, the robustness of the spatial and temporal eddy scales from satellite altimetry has been questioned (Chelton and Schlax, 2003; Chelton et al., 2011; Cipollini et al., 1997; Eden, 2007). Distortion of the data can occur through the smoothing and interpolation required to generate a gridded product from raw satellite measurements. Whilst high-resolution altimeters are currently being developed e.g. the future Surface Water Ocean Topography (SWOT) mission, numerical simulations can allow us to evaluate eddy properties at a much higher resolution than currently possible through observations (Klein et al., 2019; Ubelmann et al., 2015).

To date eddy properties have been studied in (coupled or ocean-only) high-resolution models at a regional scale. Particular regions of interest include the Agulhas eddy pathways, important for heat transfer into the South Atlantic (McClean et al., 2011), and the Californian Current System where eddies play a role in the transfer of heat and nutrients from upwelling systems into the open ocean (Kurian et al., 2011; Frenger et al., 2018). Here we present a first global assessment of mesoscale eddy properties (e.g. distribution, size, speed and lifetime) in two versions of the coupled model HadGEM3-GC3.1 with EP and ER ocean resolution. Our study focuses on the field of coherent mesoscale vortices, defined by closed sea surface height (SSH) contours, rather than the general mesoscale field comprising filaments and unclosed structures. The characteristics (e.g. eddy kinetic energy, heat transport) of the two fields likely differs (e.g. Tarshish et al., 2018; Su and Ingersoll, 2016). We will address three central questions in this study: 1. As ocean resolution in coupled models is increased, how does the representation of eddies and their properties change? 2. How do modelled eddies and their properties compare to observations? 3. How do modelled eddies compare to theoretical predictions?

This Chapter is organised as follows. Section 3.4 describes the eddy detection algorithm, and the model outputs and observational datasets used. Section 3.5 presents published results of global eddy counts and properties, and section 3.6 presents additional unpublished results. Section 3.7 concludes and discusses the wider implications of the results, including which metrics are important for

mesoscale air-sea feedbacks in Chapter 4.

3.4 Method and Data

3.4.1 Eddy detection algorithm

In this study, we use an eddy detection algorithm adapted from Mason et al. (2014) (itself based on Chelton et al. (2011)). Eddies are identified and tracked as closed coherent vortices detected through successive closed contours of SSH anomalies, subject to various tests. The SSH field has a long-term 20 year mean removed. Large-scale SSH variability is removed using a Gaussian filter with widths of $20^\circ \times 10^\circ$ (zonal$\times$meridional). The differences between this algorithm and the original eddy detection algorithm of Chelton et al. (2011) are discussed in Mason et al. (2014). For example, this algorithm uses interpolated SSH contours instead of raw SSH pixels, it includes a 'shape test' (to test how circular the closed contour of SSH is), a test for one local SSH minimum or maximum per closed SSH contour and Chelton et al. (2011) use a minimum lifetime of 4 weeks. Although the elongation of eddy shape can play a role in the strength and extent of Western Boundary Currents (WBC), it is excluded from this study. Details of the scheme, criteria and tracking along with our adaptations of the filtering and detection algorithm are further discussed in Chapter 2.4 and 2.5.

For both models and observations, the eddies are tracked globally using 20 years of daily SSH anomalies. We only consider eddies with a minimum lifetime of 7 days. To minimize noise, the maps and probability density functions (pdfs) of eddy statistics shown below only use eddies lasting longer than 1 month (unless otherwise specified). Eddy properties considered in this study are as follows (Chelton et al., 2011; Mason et al., 2014). The effective radius, L_{eff}, is defined as the radius of a circle with the same area as the area within the outermost closed SSH contour (satisfying all other criteria). The speed-based radius, L_{spd}, is taken as the radius of a circle similarly fitted to the SSH contour with maximum averaged geostrophic

velocity, U. By definition, L_{spd} is smaller than L_{eff} and (Chelton et al., 2011) found that typically $L_{spd} \simeq 0.7 L_{eff}$. Eddy amplitude, A, is the absolute difference between the maximum (for anti-cyclones) or minimum (cyclones) SSH within the eddy and the SSH value of the outermost closed SSH contour (same contour as that used to define L_{eff}). The propagation velocity C_g^{eddy} is computed from the daily displacements of the eddy center (defined as the center of a fitted circle to the smallest SSH contours). Here, we focus on the zonal component of C_g^{eddy} computed from the zonal displacements only. Finally, a measure of eddy non-linearity is the ratio of the eddy rotational velocity to the eddy propagation velocity, $r = U/C_g^{eddy}$. A value of r greater than 1 suggests that fluid parcels are trapped within an eddy (Chelton et al., 2011).

There are numerous eddy detection algorithms available in the literature (Wolfram and Ringler, 2017; Sun et al., 2017; Li et al., 2016; Abernathey and Haller, 2018; Chelton et al., 2007; Fang and Morrow, 2003; Frenger et al., 2013; Oerder et al., 2018). They differ by the metric used for eddy identification (such as vorticity, Okubo-Weiss parameter or Lagrangian particle tracking), filtering or the tracking technique (for example to include the merging and splitting of eddy trajectories). Each method has its own advantages and limitations. The basis of this algorithm is physically-based and has been heavily tested and used in literature (Chelton et al., 2011). In comparison to Lagrangian methods for example, Eulerian tracking methods (such as closed SSH contours employed here) tend to over-estimate material conservation and transport, see (Chelton et al., 2011; Abernathey and Haller, 2018; Tarshish et al., 2018). However, a comparison of surface eddy properties is carried out here instead of a quantification of eddy transport and energy. Crucially, in this study, the same eddy detection algorithm is used on all datasets (model outputs and altimeter observations) to eliminate differences arising from different detection algorithms.

3.4.2 Coupled model configuration and outputs

Outputs are analysed from the coupled high-resolution global climate model HadGEM3-GC3.1 (Williams et al., 2018). This model comprises a GA7.1/GL7.1 atmosphere/land configuration based on the MetUM and JULES (Walters et al., 2017), a GO6 ocean (Storkey et al., 2018) based on NEMO (Madec, 2008) and GSI8 sea ice based on CICE (Ridley et al., 2018). Two resolutions of the ocean component, both coupled to the same atmospheric component (labelled N216, with a resolution of $\sim$ 60 km at mid-latitudes) are compared: ORCA025 ($\sim$ 1/4 °, hereafter EP_{sim}) and ORCA12 ($\sim$ 1/12°, hereafter ER_{sim}). The ocean components do not employ any eddy parameterizations other than a small amount of isopycnal mixing to control grid-scale noise. For further information about the model set-up, the reader is referred to Hewitt et al. (2016); Williams et al. (2018); Storkey et al. (2018).

The model simulations follow the CMIP6 HighResMIP protocol (Haarsma et al., 2016) with implementation described in Roberts et al. (2019). Model outputs (20 years of daily mean SSH) are obtained after a 20 year spin-up. Although the large-scale continues to drift, it is likely that this has a negligible effect on eddy statistics, as changes in the background state are relatively small. To facilitate the comparison between versions of the coupled model, the eddy detection algorithm is also applied to 10 years of ER_{sim} SSH output re-gridded onto the EP_{sim} grid ($\sim$ 1/4°) (hereafter $ER_{sim}regrid$). The re-gridding was performed by bilinear interpolation, using an Earth System Modelling Framework (ESMF) (Esmf Joint Specification Team: et al., 2018), to generate conservative remapping of surface ocean variables (such as SSH) (Hewitt et al., 2016; Jones and Division, 1998).

3.4.3 Observational data

Observational SSH is taken from the gridded AVISO altimeter dataset (Archiving, Validation and Interpolating of Satellite Oceanographic Data, 2014; (Ducet et al., 2000)). The Ssalto/Duacs altimeter products were produced and distributed by the Copernicus Marine and Environment Monitoring Service (CMEMS) http://www.marine.copernicus.eu.

The dataset provides daily SSH anomalies at $\sim$ 1/4° resolution after the removal of a 20-yr mean. The gridded SSH field is generated through optimal interpolation from the delayed-time merging of multiple satellites. Note that, because we use an updated gridded altimeter product as well as a modified eddy tracking algorithm, our observed eddy statistics will differ from those published by (Chelton et al., 2011).

Comparison of the raw daily SSH variances reveals differences before applying any filtering or eddy tracking, notably between observations and EP_{sim}. Although it captures the observed pattern correctly, EP_{sim} underestimates the magnitude of the observed variance, notably in WBC (not shown). ER_{sim}, however, compares reasonably well with observations on a global scale. Similar conclusions are obtained when comparing surface Eddy Kinetic Energy (not shown).

3.5 Results

We re-emphasize that the eddies detected in both observations and the model mostly consist of non-linear mesoscale coherent vortices in geostrophic balance. Most eddies in the ER_{sim}, EP_{sim} and observations have a small Rossby number R_o $(= \frac{U}{fL_{spd}})$: only 0.5, 0.06 and 0.09% of eddies in ER_{sim}, EP_{sim} and observations, respectively, have a Rossby number larger than 0.1 (Fig. 3.1, right). That is, none of the detected eddies, in the models or observations, are in submesoscale range (here we follow McWilliams (2016); Thomas et al. (2008) who define submesoscale as features with a Rossby number of order 1, among other criteria; this contrasts with other works which define submesoscales as smaller than 50 km (Su et al., 2018)). Finally, as shown in Fig. 3.1 (left, note the logarithmic scale), most eddies have a non-linearity parameter $r = U/C_g^{eddy}$ larger than 1.

3.5.1 Eddy genesis and lifetime

We start by comparing the rate and location of eddy genesis. Here, "eddy genesis" effectively refers the first time an eddy is identified. Although this is not the exact

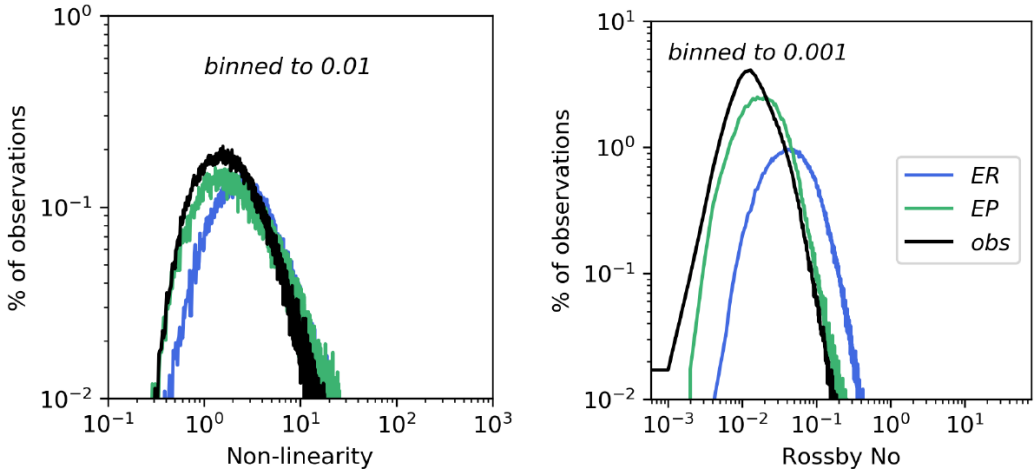

Figure 3.1: *Probability density functions of the non-linearity parameter r (left) and the Rossby number R_o (right) .*

time when an eddy is born, this is a reasonable proxy. Fig. 3.2 shows maps of eddy genesis as the averaged frequency of first eddy detection in each 1° grid box per year. Note that eddies require a minimum lifetime of 1 week to be identified by the detection algorithm. Differences between models and observations are not sensitive to this choice – see the eddy genesis maps for eddies lasting longer than 1 month in Fig. 3.3.

As expected eddies are not born homogeneously across the global ocean. Large genesis rates are found in the vicinity of intense currents such as the Antarctic Circumpolar Current (ACC) and boundary currents. Genesis rates are low in the open oceans, typically a factor of 4 smaller than in energetic regions. Model and observations share broadly similar distributions of eddy genesis although the modelled rates are significantly lower, notably in EP_{sim}. As a result, genesis rates in the gyre interiors of EP_{sim} approach zero. In addition closer inspection reveals that genesis rates in EP_{sim} at Eastern Boundary Currents (EBCs) are very weak compared to observations and ER_{sim}. This is particularly noticeable along the west coasts of Australia, Africa and South America around 20-30°S. In contrast, ER_{sim} is able to capture these hot-spots of eddy genesis, as well as generate as many eddies in the Southern Ocean as found in observations. This can be attributed to improve-

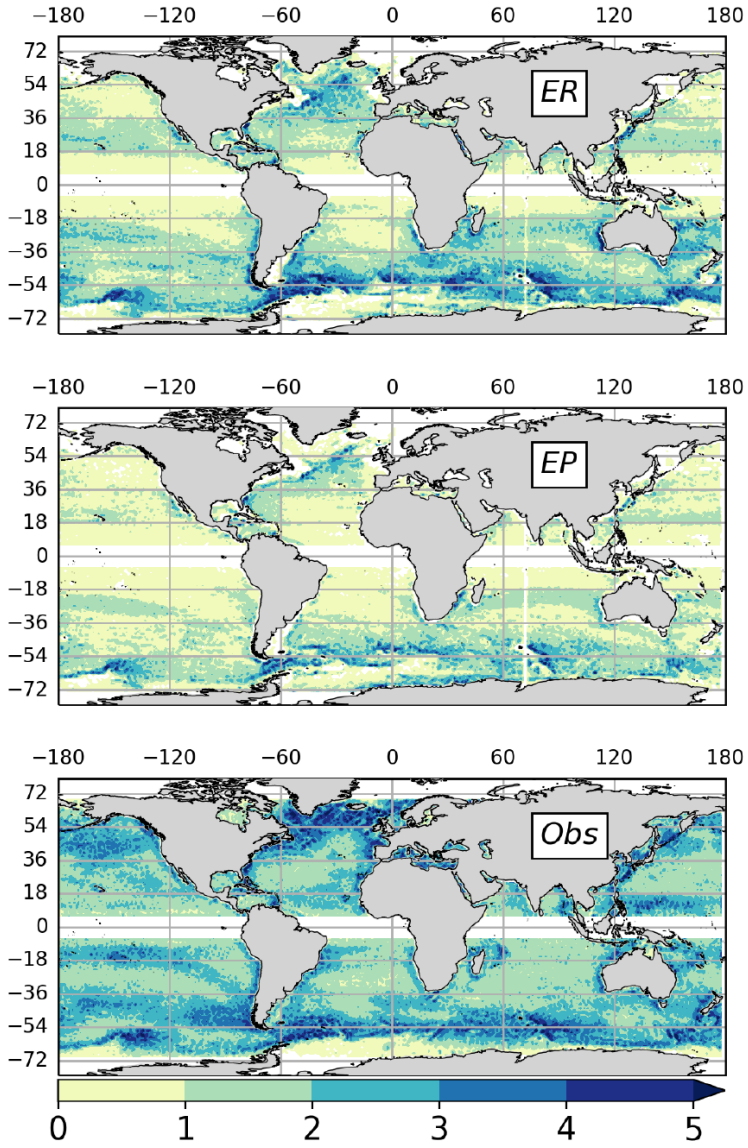

Figure 3.2: *Eddy genesis (number of eddies per year) for eddies lasting longer than 1 week (binned to 1°× 1° boxes) scaled to 10 years.*

ments in the representation of ocean currents and outflows in ER_{sim}, partly through improved topography, which provides a source of frontal shear for eddies to form (Deremble et al., 2016). For example improvements in ER_{sim} are found in the Mediterranean outflow, EBCs, the ACC and the Drake passage, as well as in the East Australian and Leeuwin currents around Australia (Holt et al., 2017). However, ER_{sim} fails to capture the high genesis rates of the North Atlantic and North

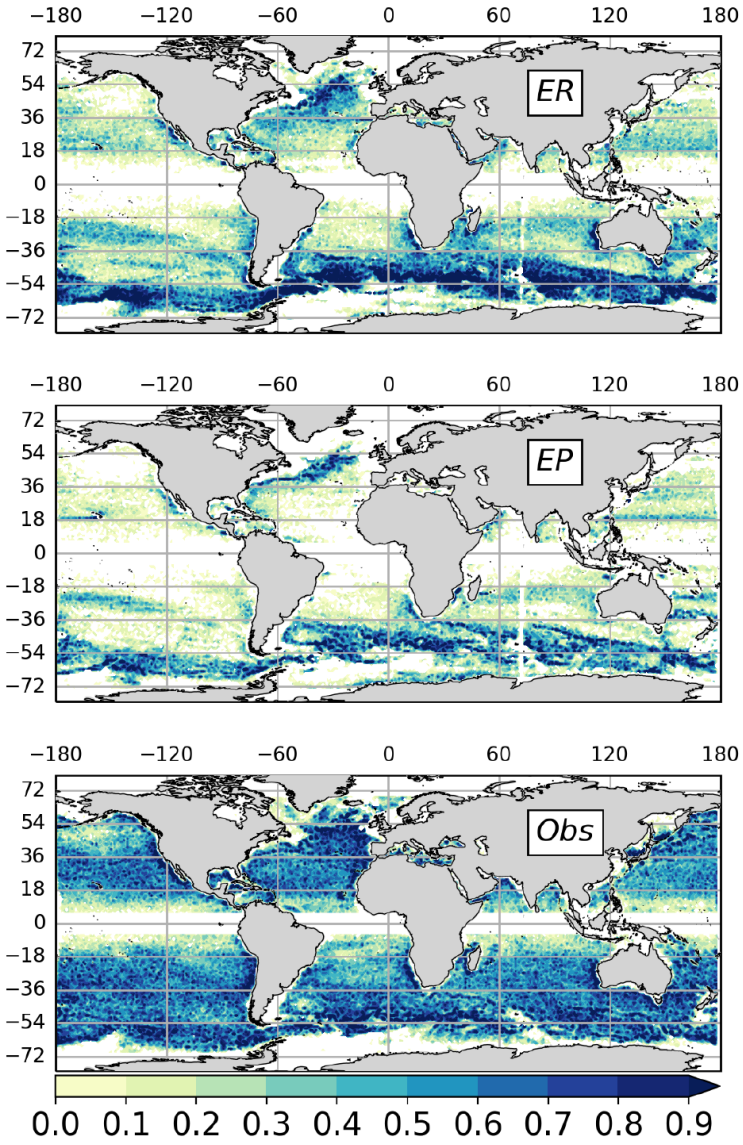

Figure 3.3: *Eddy genesis (number of eddies per year) for eddies lasting longer than 1 month (binned to 1°× 1° grid boxes).*

Pacific sub-polar gyres as well as the long-lived (> 6 months) cyclonic eddies from the Leeuwin Current and Tasman Outflow around Australia found in observations (see Fig. 3.5 below).

Table 3.1 and Fig. 3.4 show the total number of eddies detected that last more than one week, as a crude measure of the global eddy genesis. In all data sets the genesis rate are similar for cyclonic and anti-cyclonic eddies. However consistent

	Type	>1 wk	>4 wks	>16wks	>26wks	>40wks	>52wks	>78wks
EP	A	143,944	29,721	2,099	495	96	41	13
	C	135,892	24,943	1,744	378	58	13	1
			19.5%	*1.4%*	*0.31%*	*0.06%*	*0.02%*	*0.005%*
ER	A	202,639	45,595	4,412	1,333	386	190	82
	C	205,633	41,642	4,003	1,240	346	155	33
			21.4%	*2.1%*	*0.63%*	*0.18%*	*0.08%*	*0.03%*
Obs	A	355,221	73,683	5,021	1,276	306	115	32
	C	334,599	64,064	3,874	933	206	70	11
			20.0%	*1.3%*	*0.3%*	*0.07%*	*0.03%*	*0.006%*

Table 3.1: *Number of eddies detected with lifetimes longer than 1, 4, 16, 26, 40, 52 and 78 weeks for the eddy-permitting simulation EP_{sim}, the eddy-resolving simulation ER_{sim}, and the AVISO gridded satellite altimetry product (Obs). The counts are scaled to 10 years and separated for cyclonic (C) and anti-cyclonic (A) eddies. For each data set, the third line (in italic) indicates the survival rate, i.e. the ratio (expressed in %) between the total number of eddies with a given lifetime and the total number of eddies with lifetime longer than 1 week.*

with Fig. 3.2, genesis rates are significantly lower in the models than in observations: ER_{sim} and EP_{sim} generate only about 63% and 40% respectively of eddies found in observations. These biases in genesis rate are reflected in the eddy counts for eddies with lifetimes longer than 4 weeks (even for eddies living more than 16 weeks in EP_{sim}). For longer time-scales, other effects are playing a role (see below). These differences in eddy genesis between the ER_{sim} and observations indicate that the ER resolution may still be too coarse to generate mesoscale (coherent) eddies realistically. This may reflect that 1/12° (and 1/4°) resolution fails to capture some smaller scale processes (e.g submesoscale activity, convection) that act as 'seeding' mechanisms for the mesoscale activity through an inverse cascade

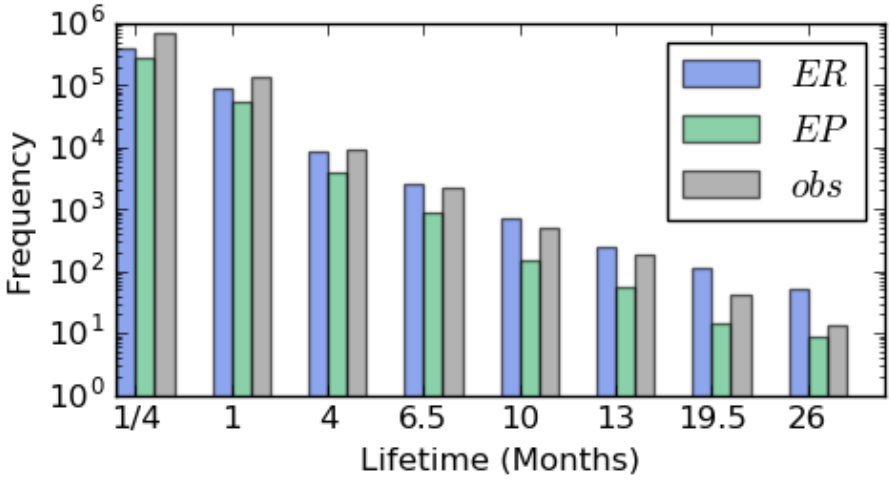

Figure 3.4: *Eddy genesis (total number of eddies) for eddies lasting longer than 1 week for the EP_{sim}, ER_{sim} and observations, scaled to 10 years*

of energy (Sasaki et al., 2014; Callies and Ferrari, 2017; McWilliams, 2016; Brannigan et al., 2017).

Consistent with the genesis rates, the density of eddy tracks is larger in ER_{sim} and observations than in EP_{sim} especially in eddy-energetic regions such as the Southern Ocean and WBCs (Fig. 3.5). For readability only eddy trajectories lasting longer than 6 months are shown (the trajectories for all eddies lasting more than 2 months cover most of the ocean as shown in Fig. 3.6 and in Fig. 3.7 at the Poles). Eddy trajectories lasting longer than 1 year are shown in Fig. 3.8.

Eddies lasting longer than 6 months are concentrated in the subtropical gyres between 20° and 50° latitude. They originate mainly from EBCs and to some extent from WBCs, notably from the Gulf Stream and North Atlantic drift. Overall, the EP_{sim} significantly under-estimates the number of long lasting eddies although anti-cyclonic eddies from the Agulhas current retroflection ('Agulhas rings') are relatively well represented. These trajectories form an important component of the meridional overturning circulation by controlling the quantity of heat and salt entering the North Atlantic (Biastoch et al., 2008). However in other locations an

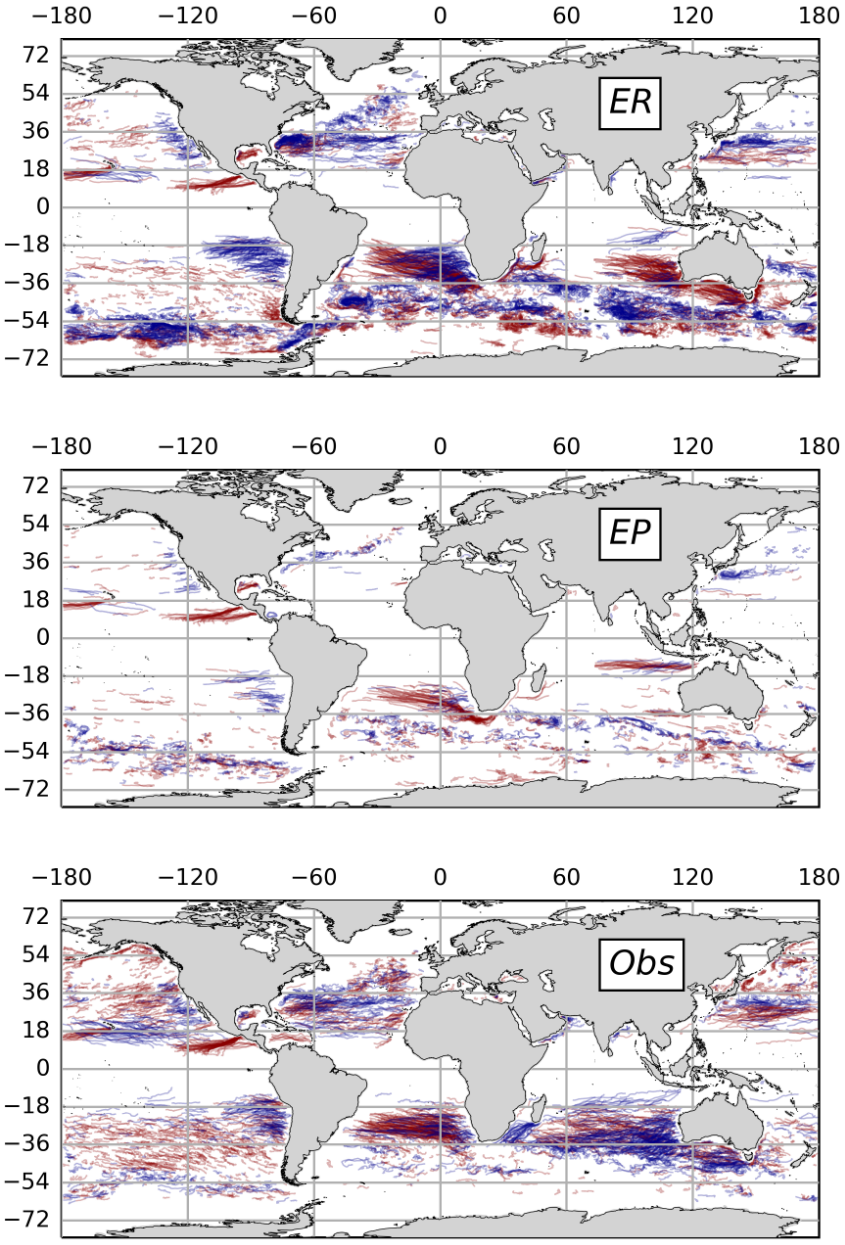

Figure 3.5: *Eddy trajectories lasting longer than 6 months over 20 years. Anticyclonic (cyclonic) eddies are shown in red (blue).*

artificially high number of eddy trajectories is found in the EP_{sim}, for example west of the Indonesian outflow (which may affect the Agulhas leakage (Bars et al., 2014)). A striking feature of observations is the absence of long lived eddies within and south of the ACC path, which may be due to insufficient resolution in the ob-

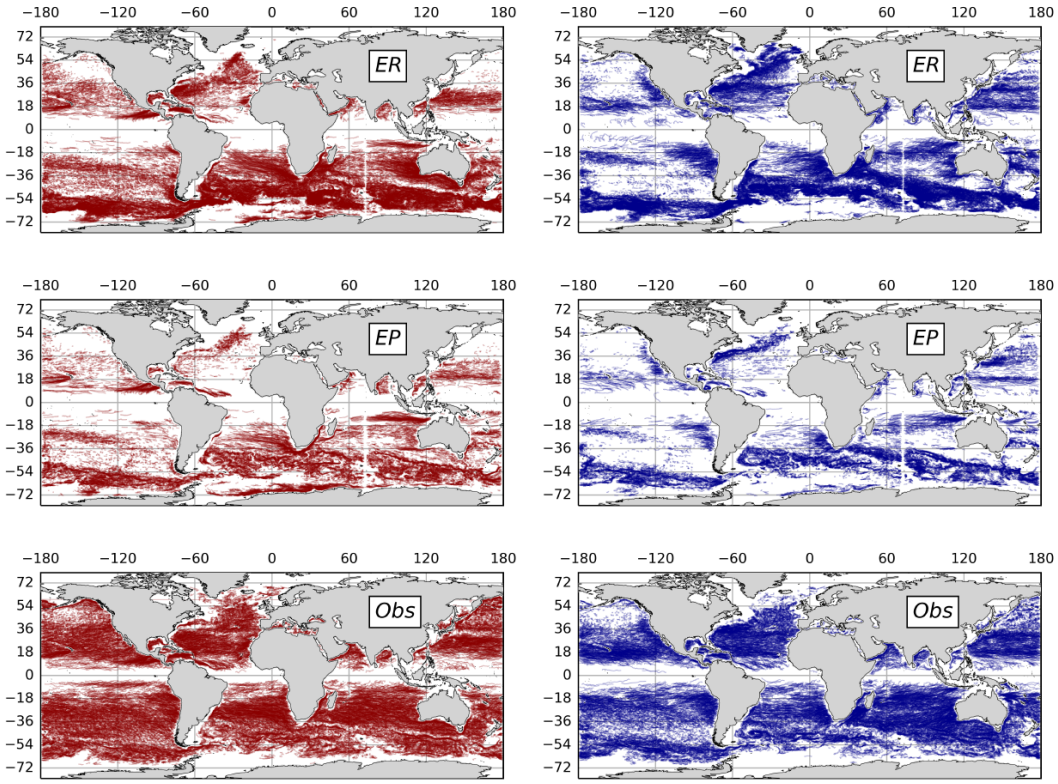

Figure 3.6: *Eddy trajectories lasting longer than 2 months over 20 years. Anticyclonic eddies (left) are shown in red and cyclonic eddies (right) are in blue.*

servational dataset (note that eddies are detected as far as 70°S, see Fig. 3.6). In contrast, in EP_{sim} and most notably in ER_{sim}, the ACC path is highlighted by the presence of numerous long-lived eddies.

These differences between the ER_{sim}, EP_{sim} and observations are reflected in the statistics of eddy lifetime (Fig. 3.9). On average eddies in EP_{sim} and observations have shorter lifetimes than in ER_{sim}. The (normalized) probability density distributions of the eddy lifetimes are similar for EP_{sim} and observations but exhibit lower values than ER_{sim} for lifetimes of 6 months and longer (Fig. 3.9, left).

Geographically, models and observations exhibit similar distributions of eddy lifetimes although, as expected from Fig. 3.5 and 3.9, values in ER_{sim} are larger, with a global mean lifetime of 2 months compared to 1.8 months in EP_{sim} and observations (Fig. 3.10). Eddy lifetimes are large in mid-latitudes (20-50°) in all

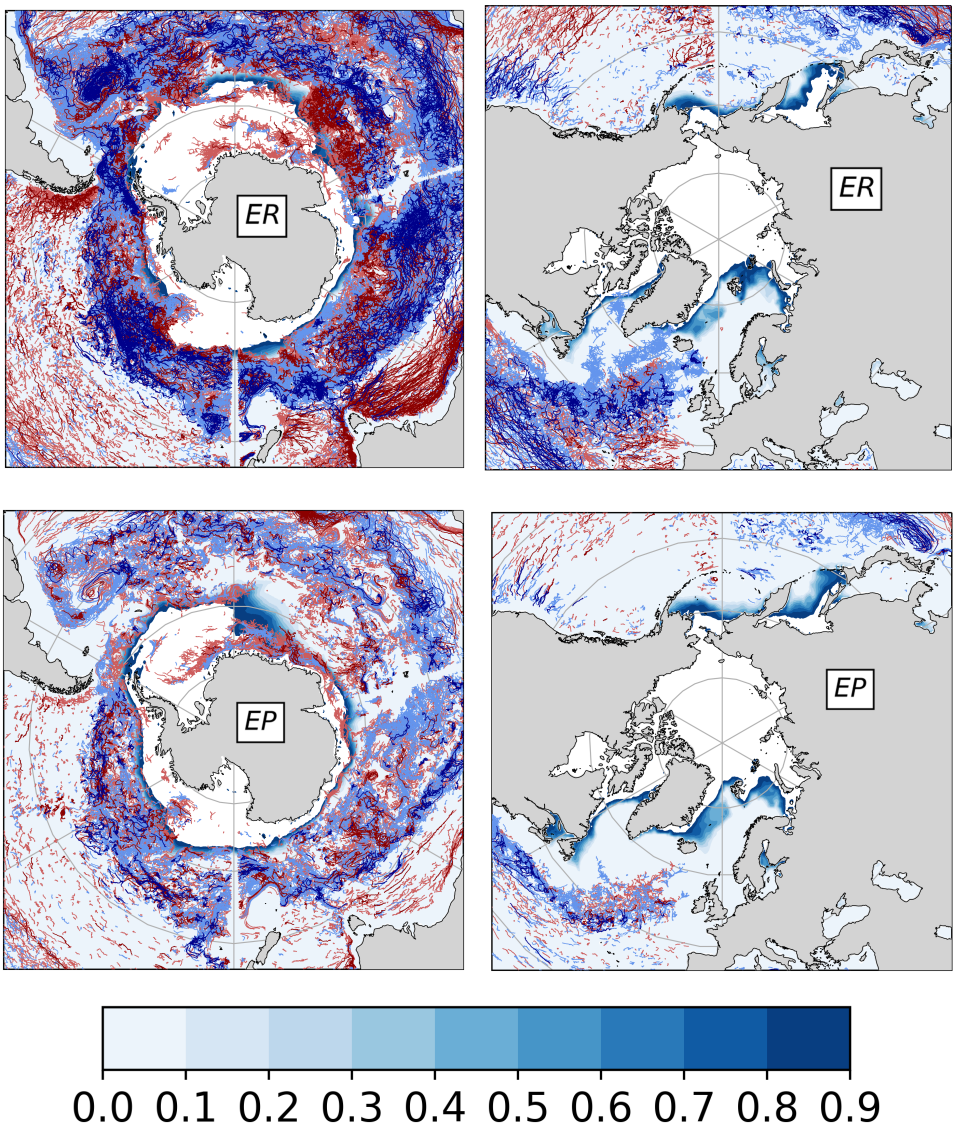

Figure 3.7: *Eddy trajectories lasting longer than 2 months over 20 years at the Poles for the ER_{sim} (top two subplots) and EP_{sim} (bottom). Trajectories lasting longer than 6 months are overlaid in darker colours. Anti-cyclonic eddies are shown in red and cyclonic eddies are in blue. The background colour is the 10 year climatological monthly mean of the percentage of sea ice area at the end of winter (March in the Arctic and September in the Antarctic). Dark blue represents a high % of sea ice cover. The region in white is complete sea ice cover.*

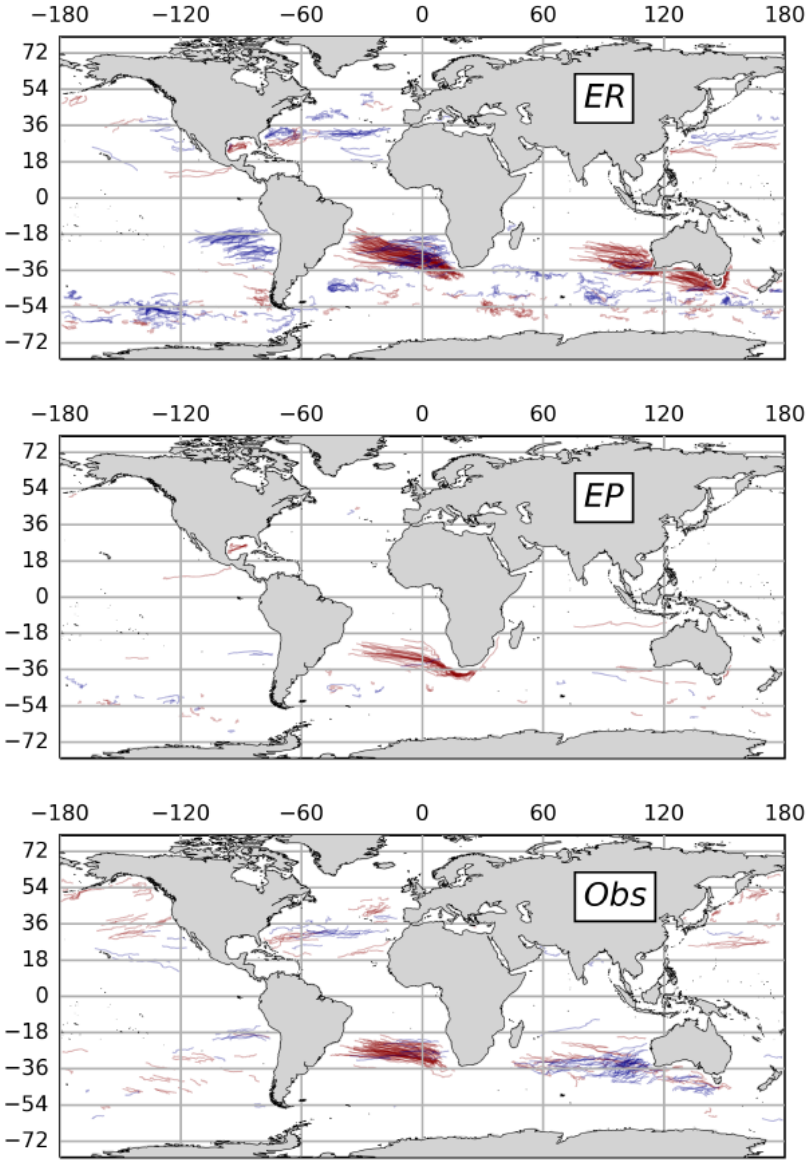

Figure 3.8: *Eddy trajectories lasting longer than 1 year. Anti-cyclonic eddies are shown in red and cyclonic eddies are in blue.*

data sets, and large along the ACC pathway, notably in the Pacific sector in models. As highlighted by the zonal average (Fig. 3.9b), eddy lifetimes reach typically 2.2-2.4 months near 30-40°S and fall to about 1.4-1.6 months at high latitudes and in the tropics. While models and observations show remarkable agreement in the Northern Hemisphere (Fig. 3.9b and Fig. 3.10), lifetimes in the models are consistently longer than in observations south of $\sim$ 40°S. Near 60°S, zonally averaged

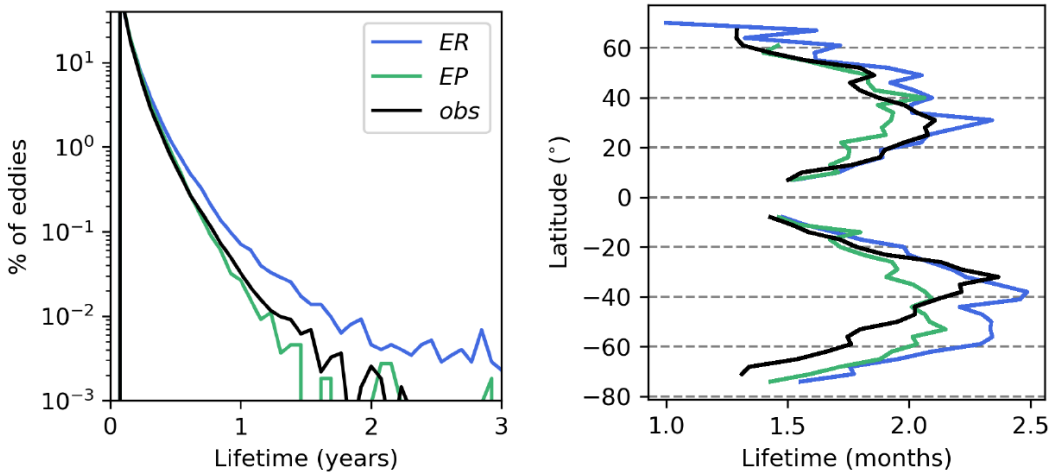

Figure 3.9: *Probability density function of eddy lifetime (left) and zonal average of eddy lifetime (right). Both plots use eddies with lifetimes longer than 1 month.*

eddy lifetimes in EP_{sim} and ER_{sim} are (respectively) $\sim$ 1.2 and $\sim$ 1.4 times longer than in observations. At the highest latitudes, the presence of sea ice may partly explain the discrepancy as AVISO does not provide SSH data under sea while the models do 3.7 (Hewitt et al., 2016). However, the contrast between modelled and observed lifetimes is also clear in the core of the ACC which is ice-free all year long, suggesting other issues (see discussion below).

It is remarkable that, globally, the ER_{sim} simulates as many eddies with lifetimes $>$ 16 weeks as seen in observations (Table 3.1) despite a significantly lower genesis rate (by 37%). This implies that the "survival rate" of eddies is much larger in ER_{sim} than in observations (and EP_{sim}) (Table 3.1). The survival rate up to 4 weeks is quite similar across the three data sets. However it is 1.5 times larger in ER_{sim} than in observations at 16 weeks and up to 3 times larger at 1 year. It is noteworthy that the survival rates of observations and EP_{sim} are very similar.

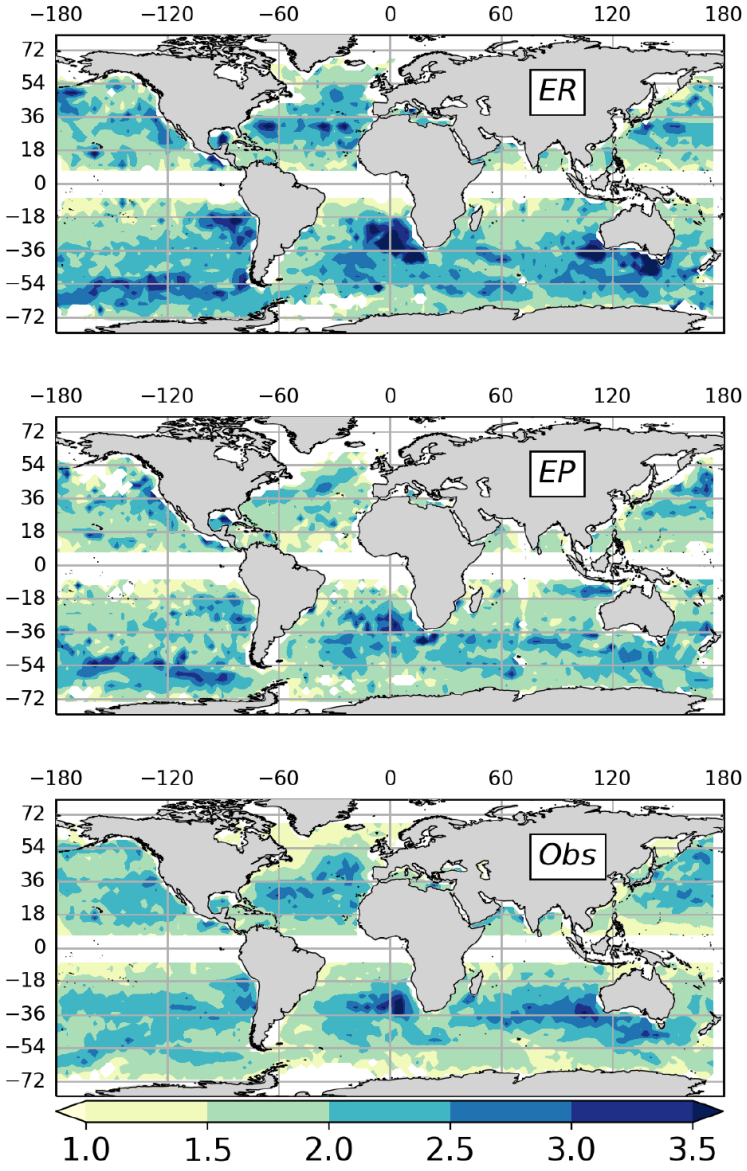

Figure 3.10: *Eddy lifetimes (in months) mapped to genesis location and binned to* $3^\circ \times 3^\circ$ *grid boxes. All plots use eddies with lifetimes longer than 1 month.*

3.5.2 Propagation

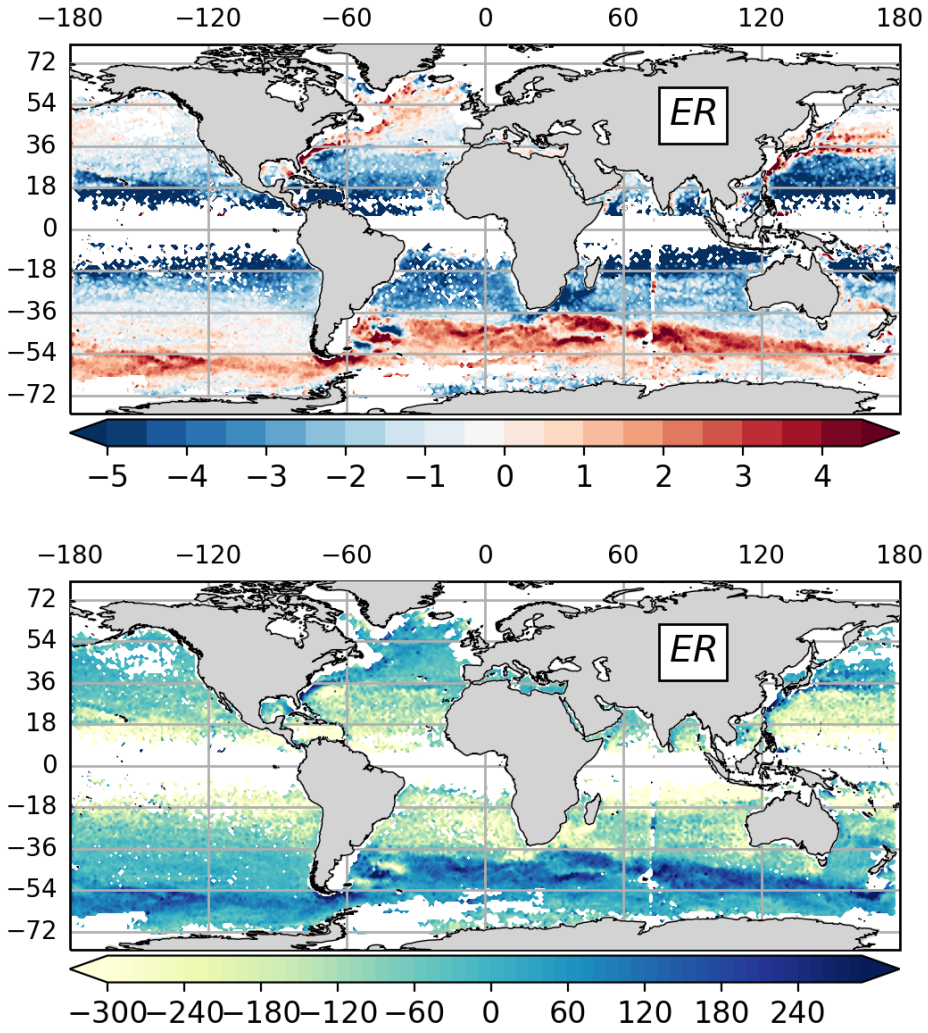

Figure 3.11: *Global maps of the zonal propagation speed (cm s^{-1}, upper subplot) and distance travelled (km, lower subplot) in the ER_{sim}, binned to 1°× 1° boxes. (If the direction is westwards, the speed and distance are negative.)*

Away from boundary currents and topography, eddies travel mainly in the zonal direction (Fig. 3.5, 3.11). Theoretical predictions suggest that non-linear mesoscale eddies propagate westward with a velocity close to that of non-dispersive long baroclinic Rossby waves (Cushman-Roisin et al., 1990). The theoretical Rossby wave phase speed in the long wave limit is given by $C_g^t = -\beta R_d^2$ where R_d

is the Rossby radius of deformation. In the models, R_d is computed as $R_d = \int_{-H}^{0} \frac{N}{|f|\pi} dz$ where $N(z) = \sqrt{-\frac{g}{\rho_o}\frac{d\rho}{dz}}$ (Brunt-Vaisala frequency) and f is the Coriolis parameter. For observations, we use the Rossby radius from Chelton et al. (1998). As found in previous studies (e.g. Chelton and Schlax, 1996; Klocker and Marshall, 2014), the observed propagation speed of eddies, C_g^{eddy}, closely matches the Rossby wave speed, C_g^t, outside of the ACC (Fig. 3.12). Note that Fig. 3.12 shows C_g^t computed for the observed and modelled climatologies. At high-latitudes, the eddy propagation speed, C_g^{eddy}, approaches zero but increases towards the equator up to $\sim$ 10-12 cm s^{-1} (westward). In the Southern Ocean however, eddies are carried eastward by the barotropic component of the ACC, resulting in a net eastward propagation speed of $\sim$ 1 cm s^{-1} Klocker and Marshall (2014). Modelled zonal eddy propagation speed, C_g^{eddy}, in both ER_{sim} and EP_{sim} shows very good agreement with observations, including in the ACC (Fig. 3.12). This reflects the good climatology of the models (also evidenced by the similarity of the modelled and observed Rossby radius, not shown) as well as a good representation of the barotropic ACC in both models.

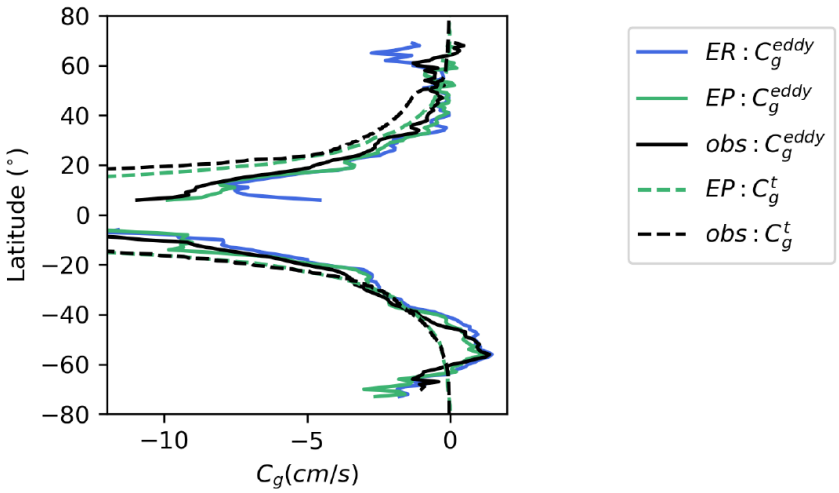

Figure 3.12: *Zonal average of zonal propagation velocity (cm s^{-1}) from tracked eddies, C_g^{eddy}. Dotted lines are the theoretical long-wave baroclinic Rossby Wave speed C_g^t for observations (black) and EP_{sim}/ER_{sim} (green).*

The co-location of global westward-propagating eddy trajectories longer than

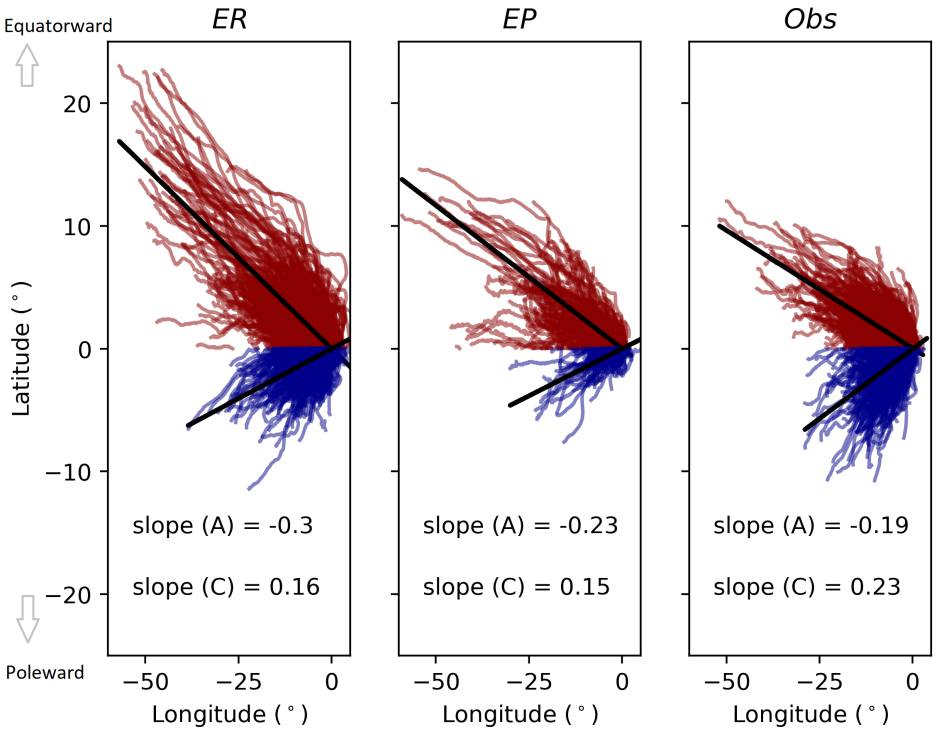

Figure 3.13: *Co-located trajectories of westward-propagating eddies lasting longer than 6 months for ER, EP and observations. Anti-cyclonic eddies (A) are plotted in red, cyclonic eddies (C) are in blue and the regression coefficients for each are given on each subplot. Note the x- and y- axis are degrees of latitude and longitude, where positive latitudes indicate eddies move equator-ward, and negative latitudes indicate eddies move pole-ward. Please refer to Fig.3.2 to evaluate where globally the most eddies are located.*

6 months reveals the small equator-ward drift of anticyclonic and pole-ward drift of cyclonic eddies (Fig. 3.13). Figure 3.13 flips the direction of propagation for NH and SH eddies so the positive latitudes are equator-ward and the negative latitudes are pole-ward. For anti-cyclones (red), this meridional displacement increases from observations to EP_{sim}, and to ER_{sim}: the regression coefficients are 0.19, 0.23 and 0.3°/° for observations, the EP_{sim} and ER_{sim} with R^2 values of 69%, 82% and 78% respectively. This means that anti-cyclonic eddies in the ER_{sim} are displaced by about 15° latitude for every 50° longitude travelled, whilst they are

only displaced $\sim 10^{\circ}$ latitude in observations. The cyclonic eddies mainly originate in the eastern boundary upwelling systems, while most of these long-lasting anti-cyclonic trajectories form part of the Agulhas rings. Compared to observations, a larger north-westward displacement of the Agulhas rings is also present in the stand-alone ocean component (Parallel Ocean program) of the Community Earth System Model, but this bias is reduced in the coupled simulations (McClean et al., 2011; Small et al., 2014). This suggests that the representation of air-sea feedback over mesoscale eddies may influence their meridional migration, by increasing eddy dampening and reducing an eddy's lifetime.

Although a similar number of eddies are plotted in Fig. 3.13, differences also partly reflect the longer eddy-lifetime found in the models (Fig. 3.5 and 3.9) with longer-lasting anti-cyclonic eddies found in the ER_{sim} compared to observations (and EP_{sim}). In ER_{sim} and EP_{sim}, the meridional drift is smaller for cyclones than anti-cyclones with regression coefficients of 0.16 $^{\circ}/^{\circ}$ and 0.15 $^{\circ}/^{\circ}$ respectively (Fig. 3.13). However in observations, the meridional displacement is larger in cyclones (0.23 $^{\circ}/^{\circ}$) than anti-cyclones (0.19 $^{\circ}/^{\circ}$), and the displacement for each polarity is more symmetric than in the models. Many of these observed cyclonic trajectories are found in the Indian Ocean. These trajectories are absent from the models and may explain the asymmetric behavior found.

A simple measure of how "stationary" eddy are is given by the ratio $D/\overline{L_{eff}}$, where D is the absolute net zonal distance of propagation of an eddy and $\overline{L_{eff}}$ is its lifetime-averaged effective radius (Fig. 3.14). This ratio is simply a measure of the zonal displacement of eddies in units of "eddy radius". Maps of $D/\overline{L_{eff}}$ (Fig. 3.14) reveal that on average eddies are relatively stationary, moving by 3 or 4 times their radius. This is in contrast with the impression given by Figs. 3.5 and 3.13, which only include eddies longer than 6 months. Fig. 3.14 reflects that overwhelmingly eddies are short-lived with lifetimes of about 2 months, which may be easier to parameterize (see Fig. 3.9). $D/\overline{L_{eff}}$ varies mainly in the meridional direction, decreasing from 6-7 in the Tropics down to 1-2 at high latitudes, which primarily reflect variations of the propagation speed C_g^{eddy}. The 10 fold change in propaga-

tion speed between Tropics and high-latitudes (Fig. 3.12) is somewhat reduced in $D/\overline{L_{eff}}$ due to the counter acting effect of changes in L_{eff} (decreasing from the tropics to high latitudes, see below). Interestingly, the pattern of $D/\overline{L_{eff}}$ in ER_{sim} is less zonally symmetric than in EP_{sim} or observations, with enhanced values of $D/\overline{L_{eff}}$ in eddy-energetic regions such as the Agulhas Current Retroflection, WBCs and along the ACC path. The latter feature notably is absent from observations, and reflects the smaller eddies detected in the ACC of ER_{sim}, which are not found in observations (see below). In the EP_{sim}, eddies are effectively more stationary than in ER_{sim} or observations almost everywhere. This bias may affect the ability of eddies at this resolution to transport and mix properties in the zonal direction along the ACC.

3.5.3 Eddy amplitude, rotational velocity and radius

Distributions of eddy amplitude and rotational velocity are very similar between the three datasets although there is a hint that the distribution of amplitudes in ER_{sim} is narrower than in EP_{sim} and observations (Fig. 3.15a). Most eddies have amplitudes A between 1 and 5 cm with a median values of 2 cm.

Differences in rotational velocity U are more noticeable, although models and observations share similar distributions (Fig. 3.15b). The peak of the distribution is displaced toward larger values in ER_{sim} (6 cm s^{-1}) compared with observations and EP_{sim} (4 cm s^{-1}). In the ER_{sim}, 19% of eddies have a velocity faster than 14 cm s^{-1} (dotted line in Fig.. 3.15b), whilst 14% do in the EP_{sim} and 13% in observations. In addition the fastest eddies (increased rotational velocity) in the EP_{sim}, at about 80 cm s^{-1}, are noticeably weaker than in the ER_{sim} and observations at 120-140 cm s^{-1} (not shown).

The largest differences between the models and observations can be found when inspecting the radius of eddies (Fig. 3.16). Distributions are shown for both the speed-based L_{spd} and effective radii L_{eff}. The three distributions of eddy radius L_{spd} are very distinct, with median values of 48, 32 and 14 km for observations,

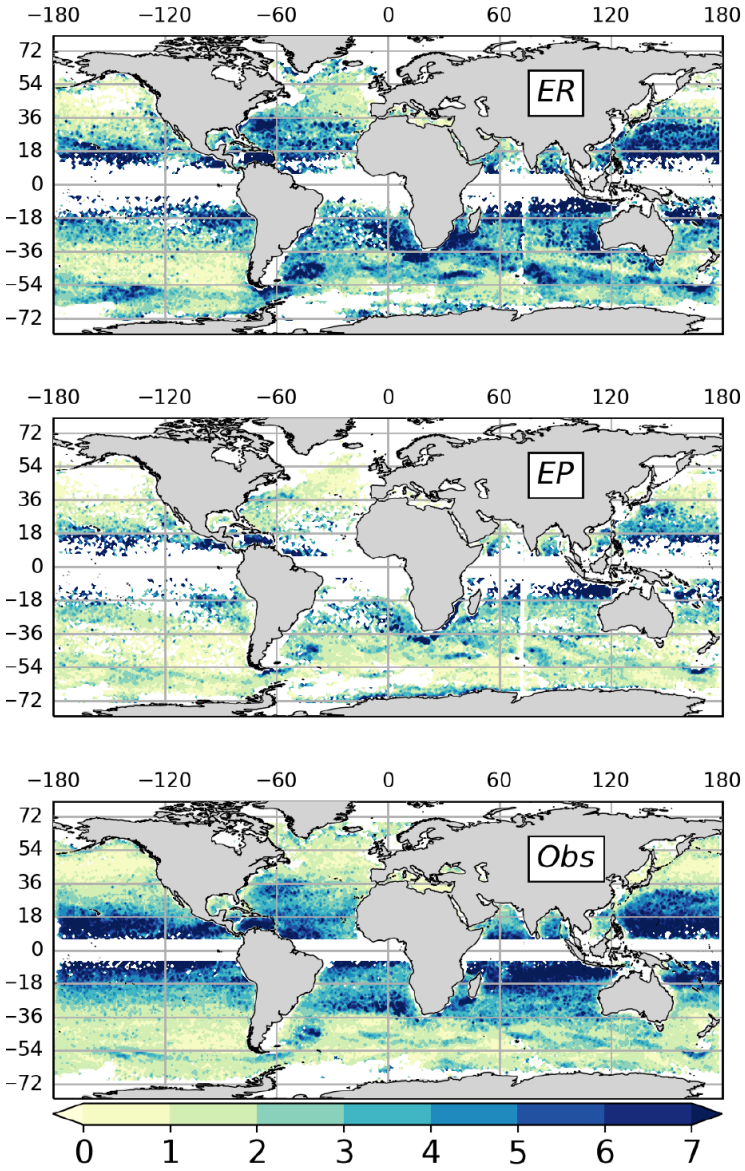

Figure 3.14: *20-year average of the ratio $D/\overline{L_{eff}}$ where D is net zonal zonal distance covered by an eddy and $\overline{L_{eff}}$ its lifetime-averaged effective radius. The ratios are mapped to genesis locations and binned to 1°× 1° boxes.*

EP_{sim} and ER_{sim} respectively. In the ER_{sim}, about a quarter (24%) of eddies have a radius L_{spd} equal to or smaller than 10 km while 90% of eddies have a radius L_{spd} equal to or smaller than 24 km (note that because of the convergence of the grid towards the poles, grid points can be significantly smaller than 10 km in ER_{sim}; see Fig. 3.17). Instead 23% of eddies in the EP_{sim} and no eddies in observations

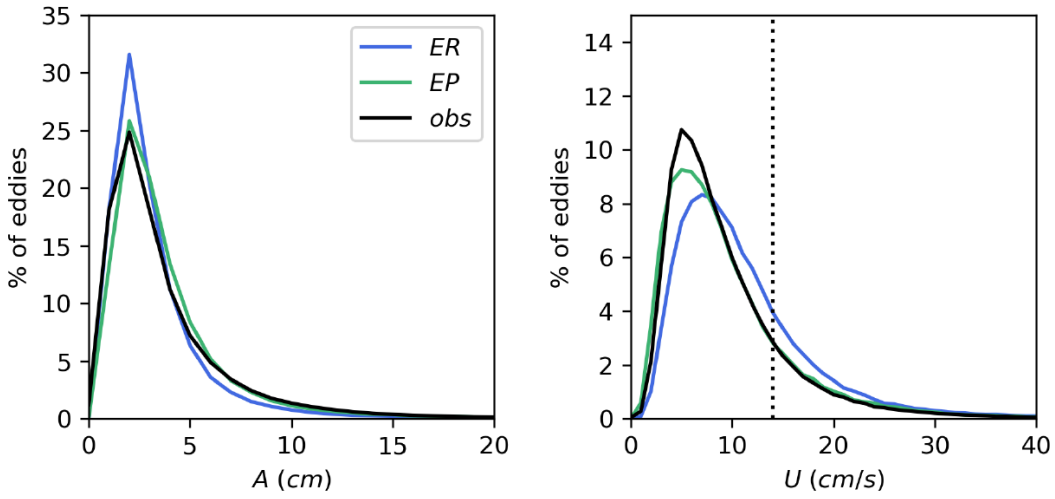

Figure 3.15: *Probability density functions of the lifetime-averaged amplitude A (left) and rotational velocity U (right) of eddies longer than 1 month (with 1 cm and 1 cm s^{-1} bins). The black dotted line is plotted at 14 cm s^{-1}.*

have a radius L_{spd} equal to or smaller than 24 km, which suggests an observational bias. Conversely, both the ER_{sim} and EP_{sim} do not capture many eddies with a large L_{spd}: while in observations about 50% of eddies have a radius L_{spd} equal to or larger than 48 km, only about 6% in the EP_{sim} and 0.5% in the ER_{sim} reach such values.

Differences are less striking, but still significant, in terms of the effective radius L_{eff} (Fig. 3.16). EP_{sim} and ER_{sim} share similar distributions with median values of 52 km and 39 km, respectively. The observed distribution for L_{eff} is centred around 50 km but it is narrower than in EP_{sim}. It is interesting to observe that L_{eff} and L_{spd} are more similar in observations than in the models (Fig. 3.16). While L_{spd} is only slightly smaller than L_{eff} in observations (as in (Chelton et al., 2011)), it is typically 2-2.5 times smaller than L_{eff} in the models.

L_{spd} is likely to be much smaller than L_{eff} for a Gaussian-shaped eddy whereas the two measures should be nearly equal for a quadratic-shaped eddy (e.g. Chelton et al., 2011). This may suggest that the profiles of observed eddies are closer to a quadratic shape (due to the post-processing bias) while the profiles of modelled

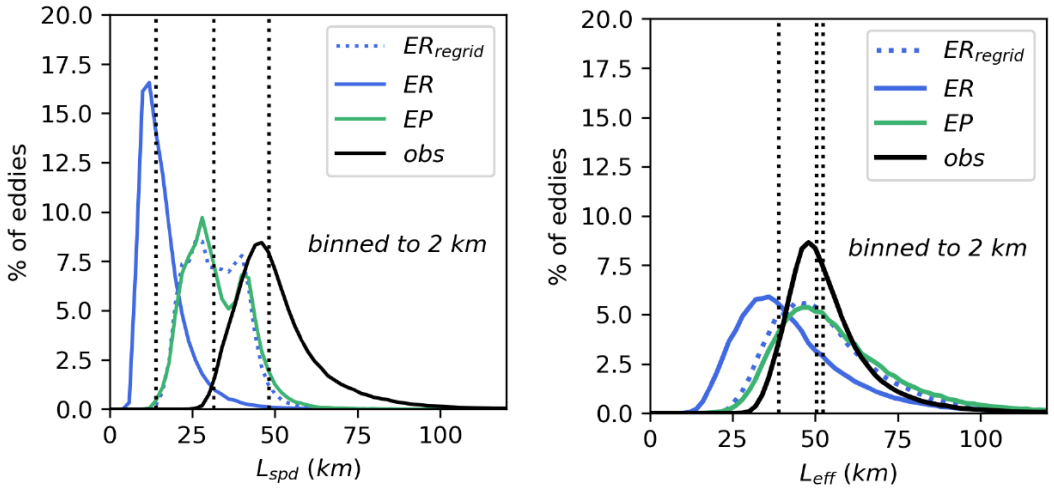

Figure 3.16: *Probability density functions (pdfs) of the lifetime-averaged L_{spd} and L_{eff}: a normalized pdf on a linear scale with 2 km bins. The black dotted lines are plotted at the medians for each resolution: the median values for L_{spd}/L_{eff} are 48 km/50 km, 32 km/52 km and 14 km/39 km for observations, EP_{sim} and ER_{sim}, respectively.*

eddies better match a Gaussian shape. More likely, this may reflect the large eddy radii found in observations. As the spatial scale grows in observations, closed SSH contours that satisfy the eddy algorithm criteria (e.g. no secondary extrema, shape test for circularity) are less likely to be found: L_{spd} is matched with L_{eff} (i.e. L_{spd} is reached at the edge of eddy).

3.5.4 Controls on eddy scales

Numerous studies have discussed processes that control the scale of ocean mesoscale eddies (Eden, 2007; Tulloch et al., 2011; Theiss, 2004; Stammer, 1997; Klocker et al., 2016). In this section, we discuss the eddy scales of coherent vortices in observations (based on an updated dataset compared to previous publications) and the EP_{sim} and ER_{sim} simulations in the light of these previous studies. The relationship between the size of eddies, the Rossby radius of deformation and the Rhines scale ($L_{Rhines} = \sqrt{\frac{U_{rms}}{2\beta}}$) is a recurring topic of investigation. A series of studies

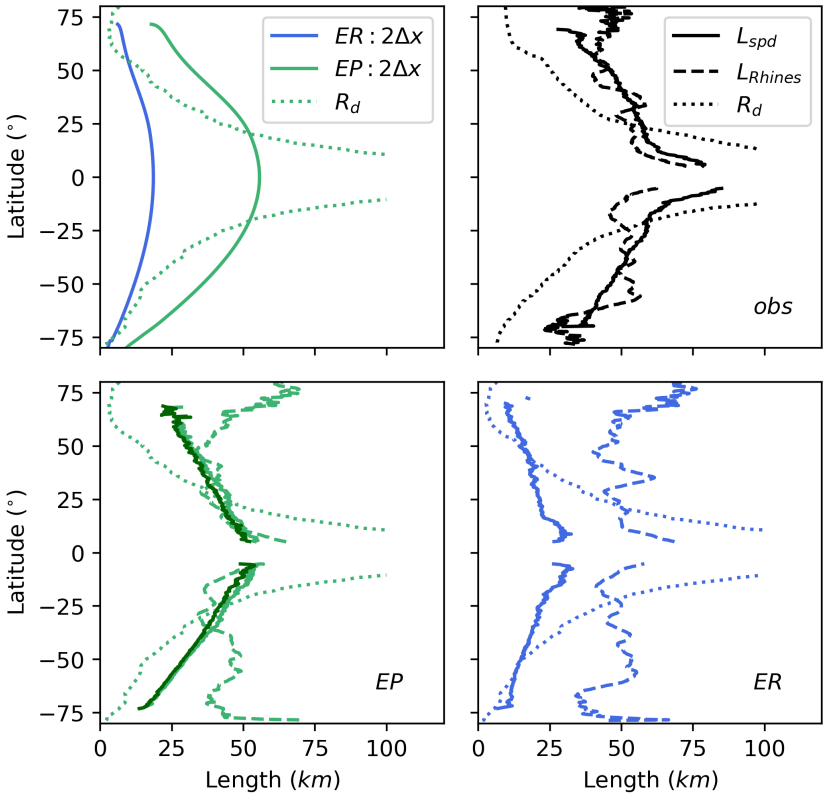

Figure 3.17: *(top left) Zonal average of the observed Rossby radius of deformation R_d and $2\Delta x$ for EP and ER. (top right and lower subplots) Zonal average of L_{spd} (solid lines), the Rossby radius of deformation (R_d, dotted line) and the Rhines Scale (L_{Rhines}, dashed line) for observations (black), EP_{sim} (green) and ER_{sim} (blue). The zonal average of L_{spd} for ER_{regrid} is plotted in dark green.*

(Theiss, 2004; Eden, 2007; Tulloch et al., 2009) have notably proposed that two regimes of ocean dynamics can be distinguished. They suggest that at low latitudes where L_{Rhines} is smaller than R_d, eddies scales with L_{Rhines} while at higher latitudes where L_{Rhines} is larger than R_d, eddies scales with R_d. The transition between the two regimes is found near 30°N/S (or $L_{Rhines} \simeq R_d \simeq 30$ km) equator-ward of which baroclinic eddies can transfer their energy to Rossby waves (Eden, 2007; Tulloch et al., 2009).

Starting with the models, it is interesting to note that the EP resolution allows eddy growth and propagation in high latitudes, as far as 60-70°N/S, where the EP

grid scale is larger than the Rossby radius R_d. Following Hallberg (2013), Fig. 3.17 (top left) compares R_d with twice the grid scale Δx for the EP and ER resolutions. This criteria is inspired by linear stability analysis of baroclinic systems (e.g. the Eady and Charney problems; see Vallis (2006) for a summary), which shows that maximum growth of linear waves is reached for wavelengths close to the Rossby radius of deformation. According to this simple criteria, eddies are expected to be found at nearly all latitudes in ER_{sim} but should be absent pole-ward of 30°N/S in EP_{sim} (Hallberg and Gnanadesikan, 2006). As evidenced by Figs. 3.2 and 3.5, this simple criteria does not apply in EP_{sim}. It is worth recollecting that although linear stability analysis predicts a maximum growth around the Rossby radius scale, it also predicts instability for a range of wavelength, including those larger than R_d. For example in the Eady problem, all wavelengths larger than 2.6 R_d are unstable while in Philip's two-layer model, which includes a large wavelength cut-off due to the β-effect, unstable wavelengths are found between 2.2 R_d and 2 π $\sqrt{U_s\ \beta^{-1}}$ (where U_s is the mean vertical shear). We speculate that in regions where the grid scale is larger than the Rossby radius, instability and eddy growth remain possible but occur on scales significantly larger than the Rossby radius (or than the scale of the maximum theoretical growth rate). Indeed, most eddies in EP_{sim} (81%) are larger than R_d, unlike in ER_{sim} where only 20% are. This suggests that in the models (notably in ER_{sim}) the eddy scale is partly set by the grid scale or the smallest multiple of Δx that allows the development of instabilities.

Further comparison reveals that the nominal and effective resolutions of these datasets, to be contrasted with the resolution of the underlying physics, also have a major influence on the estimated scales. To highlight this, the distribution of eddy scales for the ER resolution outputs are re-gridded to EP resolution (referred to as $ER_{sim}regrid$) as shown in Fig. 3.16 (dotted lines). Through the remapping, the peak of the distributions for L_{spd} in ER_{sim} increases from 12 km to 28 km. For L_{eff}, after remapping the distribution of ER_{sim} is shifted to larger values by 12 km. Sensitivity tests with the high-pass filtering of the SSH field does not alter significantly the eddy radius distributions (not shown). Not surprisingly, estimates

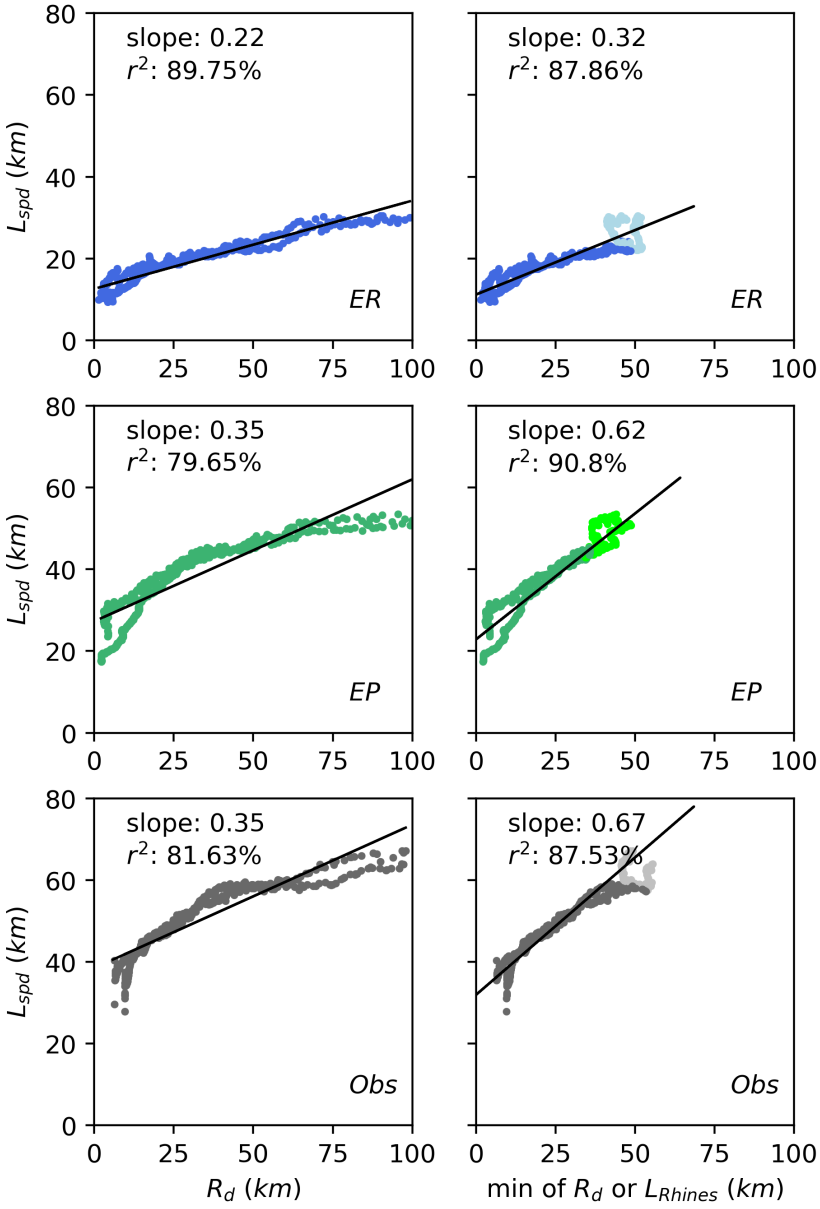

Figure 3.18: *L_{spd} compared to R_d (left) and to the minimum of R_d and L_{rhines} (right). The data is global after zonally averaging. The linear regression line is plotted in black. In the right panels, the shade of colour indicates whether the minimum is reached with R_d (darker shade) or L_{Rhines} (lighter shade). EP is plotted in blue, EP in green and observations are plotted in grey.*

of eddy scales are highly sensitive to the resolution of the dataset. It is however striking that the distributions of eddy radii for $ER_{sim}regrid$ are nearly identical to

those for EP_{sim}. This reinforces the argument above that eddies grow on a scale set by the grid scale. Despite having the same nominal grid resolution of 1/4°, observed eddy radii exhibit marked differences with those of EP_{sim} and $ER_{sim}regrid$, notably for L_{spd}. If the re-mapping of ER_{sim} to $ER_{sim}regrid$ is any guidance, this suggests that the effective resolution of the gridded observational dataset is larger than 1/4° and possibly closer to 1/2°, failing to capture the smaller eddies present in reality.

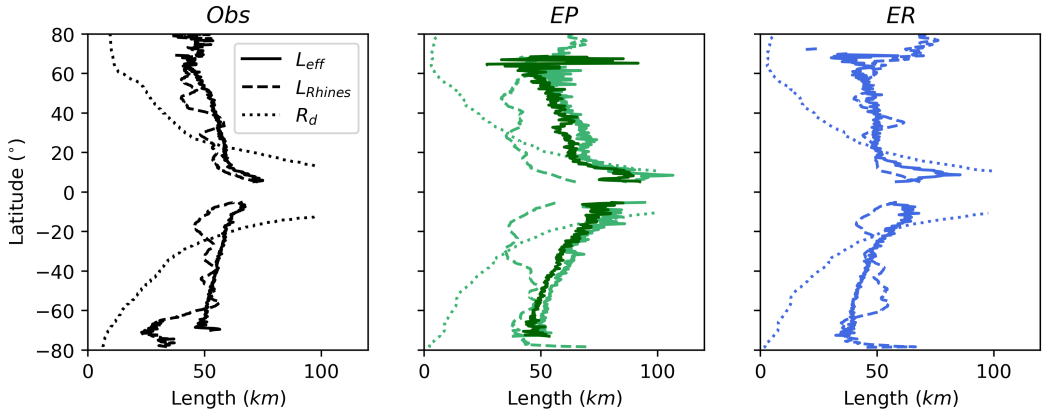

Figure 3.19: *A repeat of the zonal average shown in Fig. 3.17 for L_{eff} (solid lines) against the Rossby radius of deformation (R_d, dotted line) and the Rhines scale (L_{Rhines}, dashed line). Observations are plotted in black, EP is in green and ER in blue. The zonal average of L_{spd} for ER_{regrid} is plotted in dark green.*

A comparison of R_d, L_{Rhines} and L_{spd} is shown in Figs. 3.17 and 3.18. Equivalent plots for L_{eff}, which is more noisy than L_{spd}, are shown in Fig. 3.19 and 3.20. Here we use $U_{rms} = \sqrt{EKE_g}$ to compute L_{Rhines} where EKE_g is the surface geostrophic eddy kinetic energy (computed from 10 years of daily SSH anomalies for the EP_{sim} and observations and from 5 years for the ER_{sim}). Note that L_{Rhines} is not defined in a standard way in the literature. Eden (2007) uses the EKE associated with the barotropic flow. However, as the eddy velocity is surface-intensified, our calculation of the Rhines scale is very similar to that of Eden (2007) (their Fig. 6). Tulloch et al. (2009) define L_{Rhines} as $2\ \pi\ \sqrt{U_{rms}\ \beta^{-1}}$ and estimate U_{rms} as the root mean square of the eddy velocity from surface drifter data. Since their

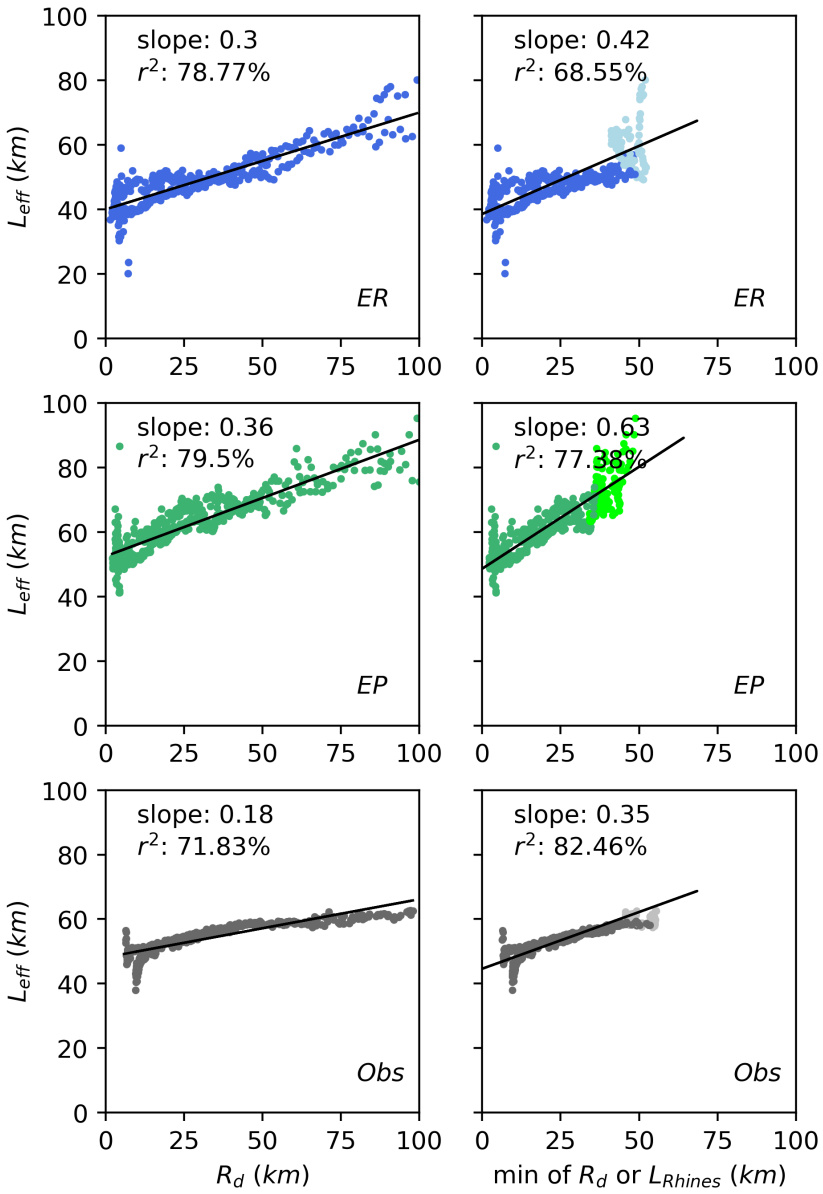

Figure 3.20: *Same as Fig. 3.18 but for the effective radius* L_{eff}.

U_{rms} and ours are similar (at least outside of the equatorial band, not shown), their estimate of the Rhines scale for observations differs from ours (Fig. 3.17, top right) by a factor 4 π. The Rhines scale is similar for models and observations, ranging between approximately 30 and 60 km (Fig. 3.17). Note that there is no contradiction with the fact that L_{spd} differs substantially between models and observations as the Rhines scale and L_{spd} are not directly related. L_{Rhines} depends on the square root of

the total geostrophic eddy kinetic energy while L_{spd} measures the distance between the eddy centre and the closed SSH contour with maximum averaged geostrophic velocity within an eddy. Compared to the Rossby radius R_d, L_{Rhines} exhibit a relatively flat, although noisy, meridional profile in all three datasets. As the Rossby radius is also similar in models and observations, the ocean is separated in two regimes, with $R_d \leq L_{Rhines}$ pole-ward of 30°N/S and $L_{Rhines} \leq R_d$ equator-ward of 30°N/S.

The eddy radii vary quasi-linearly with latitude, increasing toward the equator (Fig. 3.17). After zonally averaging, consistent with Fig. 3.16, eddy radii are smallest in ER_{sim} and largest in observations. Again, eddy radii in the regridded ER_{sim} is very similar to EP_{sim} (dark green line in Fig. 3.17). Note that the observed radii L_{eff} (Fig. 3.19) compare well with Fig. 11 in Tulloch et al. (2009) although our eddy radii are smaller. As the eddy detection algorithm used in this study is essentially based on Chelton et al. (2007), this difference may be attributed to the fact that we use a more recent altimeter product (with finer resolution and an increased number of satellites in more recent periods).

Scatter plots of L_{spd} versus R_d or the minimum of R_d and L_{Rhines} are shown in Fig. 3.18 (see Fig. 3.20 for L_{eff}). For observations and models, a good linear fit is found between L_{spd} (or L_{eff}) and R_d, although the slope of the best fit between L_{spd} and R_d is slightly weaker in the ER_{sim} than in observations and the EP_{sim}: for the ER_{sim}, EP_{sim} and observations slopes are 0.22, 0.35 and 0.35 with R^2 values of 90%, 80% and 82% respectively (Fig. 3.18, left column). For observations, this slope (0.35) is significantly smaller than the value of 0.8 found in Eden (2007) in the North Atlantic while the fit found here appears much better than that seen in Eden (2007). For both L_{spd} and L_{eff}, the relationship with R_d appears to break down (more scatter) for R_d larger than $\sim$ 100 km (not shown). The scatter plots shown here are taken globally but a similar relationship is found for the North Atlantic only (see Fig. 3.21). However note, Eden (2007) use a different measure of the eddy size (based on the first zero-crossing of the spatial auto-correlation function of SSH anomalies) as well a older version of the SSH altimeter product.

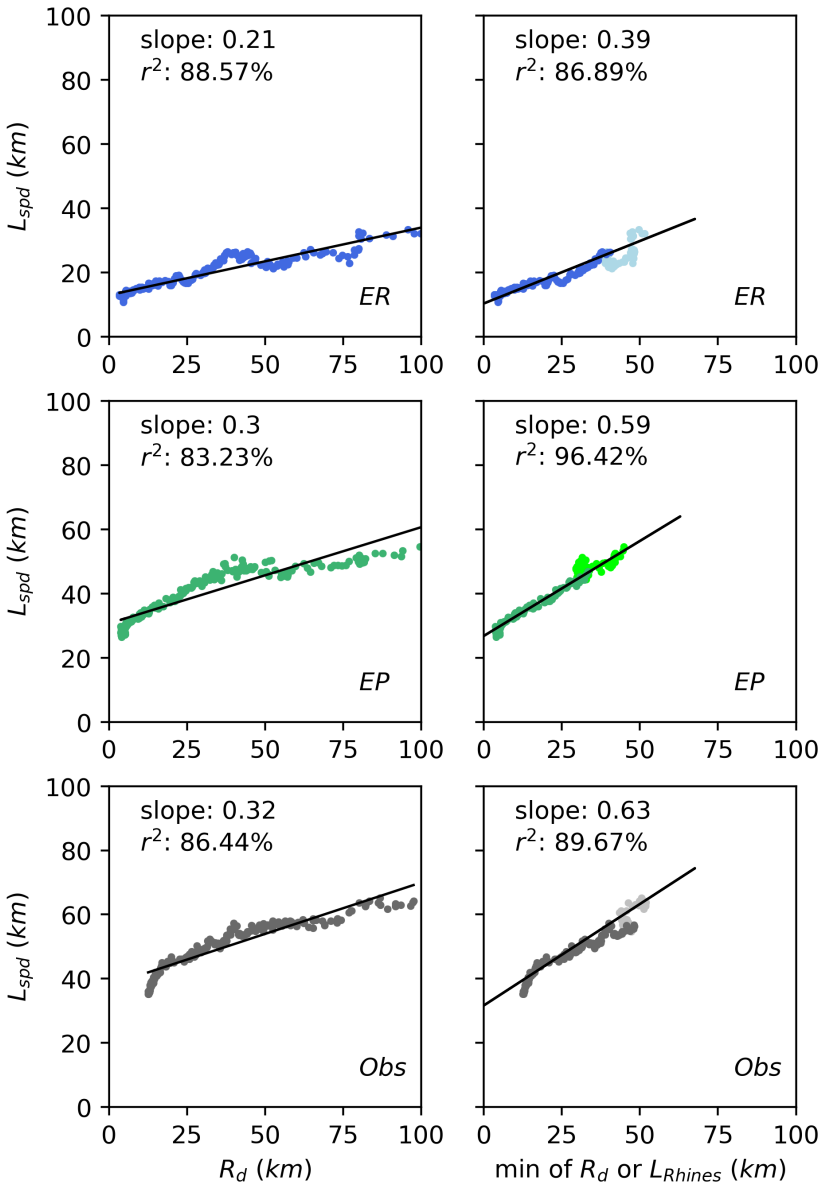

Figure 3.21: *Same as Fig. 3.18 but for the North Atlantic only (0 - 70°N, 80°W - 10°E) for comparison with Eden (2007).*

Following Eden (2007), we test the relationship between the eddy radii and the minimum of R_d and L_{Rhines} (Fig. 3.18, 3.20 and 3.21, right column). The shade of colour indicates whether the minimum is reached with R_d (darker shade) or L_{Rhines} (lighter shade). In observations and EP_{sim}, the link between eddy radii and $min(R_d, L_{Rhines})$ appears better than between eddy radii and R_d alone, as sug-

gested in previous studies (e.g. Eden, 2007; Tulloch et al., 2011). Replacing R_d by $min(R_d, L_{Rhines})$ clearly results in a more linear relationship to L_{spd}, as highlighted by the increased R^2 value, except from in ER_{sim}. However, this needs to be contrasted with the fact that the improvement of the fit (as measured by R^2) is often marginal and is sensitive to the choice of domain and of eddy radius definition (as shown for L_{eff} and for the North Atlantic in Figs. 3.20 and 3.21). Note that, as in Eden (2007), the slopes in EP_{sim} and observations are roughly double for $min(R_d, L_{Rhines})$ relative to R_d.

3.6 Additional Unpublished Results

In complement to the published work above, the following three sections present further unpublished investigations into the tracked eddy properties i.e. amplitude, velocity, radius (section 3.6.1), eddy kinetic energy (section 3.6.2) and eddy life cycles (section 3.6.3). In addition, section 3.6.3 discusses how mesoscale eddies in the ER_{sim}, EP_{sim} and observations compare to configurations with a different atmospheric component.

3.6.1 Relating eddy properties for Gaussian-shaped eddies

Although, in the paper we have discussed eddy amplitude, its rotational velocity and different radii, there is no obvious relationship between these three properties. For example, eddy radius is not linearly dependent on eddy amplitude, therefore an increased sea surface height anomaly does not directly translate to a larger eddy. Relating these properties is dependent on what we know of the shape, or spatial distribution, of an eddy and is fundamental to improve our estimates of eddy heat and material transport in the global ocean.

So far in literature, various studies examine eddy shape e.g. Chelton et al. (2011); Wang et al. (2015); Amores et al. (2017). After tracking observed eddies, Chelton et al. (2011) suggest a symmetrical Gaussian SSH structure occurs for the central 2/3 of an eddy, although the observed speed-based radius (L_{spd}) is artificially large and therefore they indicate the Gaussian approximation is inadequate. While a later study by Wang et al. (2015) suggest only about 50% of observational SSH anomalies (1-2 times eddy radius) are Gaussian-shaped. Amores et al. (2017) examine the spatial structure, beyond the coherent eddy interior, at the eddy periphery where secondary opposing anomalies are found as seen in averaged eddy composites in Hausmann and Czaja (2012). In this work, we investigate whether tracked coherent mesoscale eddies in the ER_{sim} and EP_{sim}, or observations using our slightly adapted algorithm, have a Gaussian shape and if so, whether eddy

amplitude, velocity and radius can be related.

By assuming mesoscale eddies have a symmetrical Gaussian structure, an original relation between eddy amplitude and spatial scale is provided in Appendix B.3 in Chelton et al. (2011). They estimate a relationship between the SSH anomaly, eddy amplitude (A) and spatial size of the eddy, using a new radius denoted as L, as shown in equation 3.1.

$$\eta = A \exp(\frac{-x^2}{2L^2}) \tag{3.1}$$

where x is the radial distance from the eddy centre, A is eddy amplitude and η is the height perturbation from a reference height i.e. the SSH anomaly. L is defined as the radius where the axial, or rotational, speed is at a maximum for a symmetrical Gaussian-shaped eddy i.e. the relative vorticity is zero. Essentially, L is equal to our previously defined variable, L_{spd} (the speed-based radius) when the shape of an eddy is a perfectly symmetrical Gaussian.

By assuming eddies do have a symmetrical Gaussian spatial structure, we expect to provide an estimate of the rotational velocity as a function of the speed-based eddy scale L_{spd} and amplitude, based on equation 3.1 as following. We reasonably assume an eddy is in both geostrophic (equation 3.2) and hydrostatic (equation 3.3) balance.

$$f\ V = \frac{1}{\rho_o}\frac{\partial P}{\partial x} \tag{3.2}$$

$$P = P_o - g\rho_o\eta \tag{3.3}$$

where f is the Corolis parameter, V is the surface geostrophic velocity (previously denoted as v_g), ρ_0 is the reference density, P is the pressure, P_0 is the reference pressure and x is the radial distance from the eddy center. By substituting equation 3.3 into equation 3.2 and rearranging, the geostrophic rotational velocity (V, now defined as U) becomes a function of the change in SSH with radial distance x as following.

$$U = -\frac{g}{f}\frac{\partial \eta}{\partial x} \tag{3.4}$$

Therefore, we can estimate the surface rotational velocity U as a function of eddy amplitude, eddy scale and the radial distance, by substituting equation 3.1 into equation 3.4 and assuming $L_{spd} = L$ i.e. all eddies have a symmetrical Gaussian shape, as following.

$$U = \frac{g\ A\ x}{f\ {L_{spd}}^2} \exp(\frac{-x^2}{2{L_{spd}}^2}) \tag{3.5}$$

Next, we need to identify the value of the radial distance x at which U is maximum. Knowing the surface velocity U has a maximum (and minimum) value when $\frac{\partial U}{\partial x} = 0$ (as illustrated in Fig. 3.23), we can differentiate equation 3.5, set equal to zero and find $x = \pm L_{spd}$. This means equation 3.5 reduces to the following:

$$U = \pm\frac{g}{f}\ e^{-\frac{1}{2}}\ \frac{A}{L_{spd}} \tag{3.6}$$

where f is estimated at 10^{-4} s^{-1} and gravity g is estimated as 981 cm s^{-1} to provide U in units of cm s^{-1}.

A comparison of how the theoretical relationship in equation 3.6 relates to the globally tracked eddies in the ER_{sim}, EP_{sim} and in observations is shown in Fig. 3.22. The estimated theoretical relationship (as an absolute value) is plotted in black, the binned eddy data in purple, and the scatter plots in either red (for anti-cyclonic eddies) or blue (cyclonic). Due to the very large number of global eddy snapshots a 10-day window is used in this plot, 1 year after the eddy tracking algorithm begun ($\sim 30,000$ eddy snapshots). The binned data is independent of the 10-day window chosen.

For observed eddies (lower subplots), the theoretical relationship approximately fits the binned eddy data suggesting the Gaussian approximation is valid. Whilst the theory does not fit the data for the modelled eddies, especially in the ER_{sim}. A scaling factor of L_{spd} is needed of 3 for ER_{sim} and 1.5 for EP_{sim} to fit the theory to the data (not shown).

Possible reasons for the discrepancy between the fit and the modelled data are first, the majority of modelled eddies do not have a Gaussian shape and so the theoretical relationship is not valid. Second, could our assumption of a constant Coriolis parameter (f) be the cause of the discrepancy? As a good fit is found for observations using a constant value for f, we suggest the discrepancy is likely to be related to differences in modelled eddy shape, compared to observations.

A 1D slice of the SSH anomaly from temporal- and spatial- averaged anti-cyclonic small-amplitude eddies in the ER_{sim} is shown in Fig. 3.23 (blue curve). This type of averaging uses 'eddy composite averaging', first introduced in Chapter 2.6. Small-amplitude eddies are chosen, where amplitude (A) is binned to 3$\pm$ 0.05 cm, due to their abundance in the global ocean (see Fig. 3.15). Using equation 3.5 and assuming the L_{eff} is 40 km (based on Fig. 3.16), we can estimate a 1D slice of the rotational velocity U (purple curve), which displays a magnitude similar to found in Fig. 3.15. The location of the two radii are displayed as vertical dotted lines, where the speed-based radius L_{spd} is situated at the maximum and minimum change in velocity.

These composite-averaged small-amplitude eddies clearly do not display a Gaussian structure within L_{eff}. In addition, the magnitude of the SSH anomaly is much larger relative to the tracked eddy amplitude. A comparison of the same 1D slice of composite-averaged SSH in largest-amplitude eddies (A=34$\pm$6 cm, SSH maximum is $\sim$ 50 cm), for each eddy polarity and in the EP_{sim} is shown in Fig. 3.24. The smaller amplitudes are shown with a maximum SSH magnitude of $\sim$ 10 cm, and cyclonic eddies are plotted as dashed lines. The largest-amplitude eddies do display a Gaussian structure in SSH, although the eddy tracking algorithm isolates approximately half the full SSH shape (i.e. only the area with L_{eff}, vertical black lines). Although small differences in the magnitude between anti-cyclonic and cyclonic eddies, the spatial structure is very similar.

There are still limitations to our estimate. Previous work has found the larger the amplitude of the eddy, the more likely the eddy is to be Gaussian-shaped (Wang et al., 2015). Are the smaller-amplitude eddies in the ER_{sim} biasing our estimates?

A later study finds the maximum eddy velocity L_{spd} can change throughout an eddy's lifetime, dependent on variations in eddy amplitude (Yang et al., 2019b). The band of maximum eddy velocity (L_{spd}) moves towards the eddy centre as eddy amplitude grows (i.e. as an eddy reaches maturity) and moves outwards towards L_{eff} as an eddy decays. The dependence of L_{spd} on eddy amplitude is not considered in our equation.

To conclude, eddies are often suggested to have a Gaussian shape so are simpler mathematically to understand and model, although there is no physical reason for them to be so. Here, we provide an estimate to relate the rotational velocity U to eddy amplitude A and eddy scale L_{spd} (equation 3.6) for Gaussian-shaped geostrophic eddies in observations, ER_{sim} and EP_{sim}. But we find that the majority of tracked eddies in models do not possess a Gaussian shape. In observations, we suggest the post-processing interpolation for the creation of the AVISO dataset may encourage eddies to form more of a Gaussian shape than found in reality.

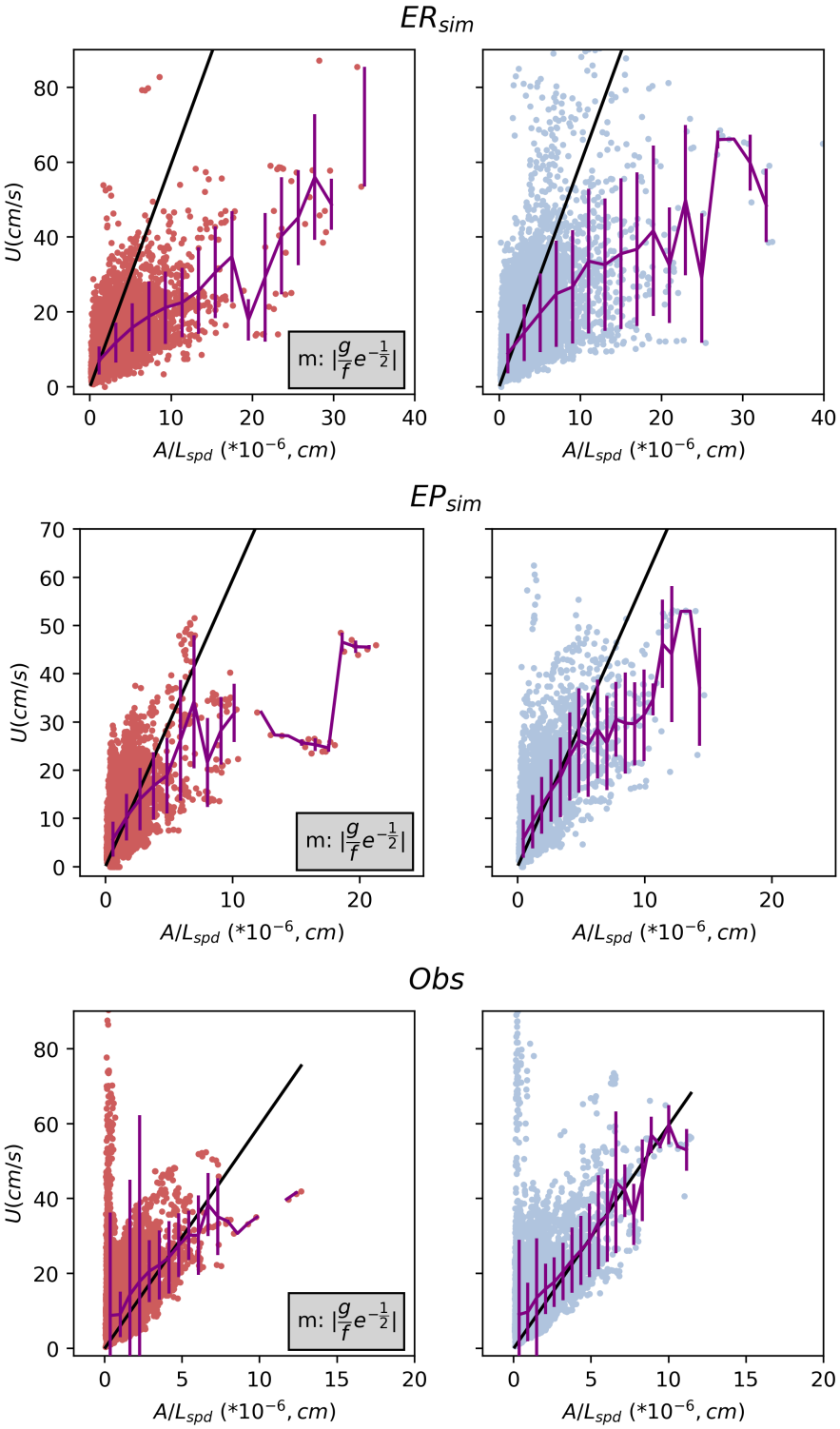

Figure 3.22: *A 10 day snapshot of global eddy properties after 1 year of eddy tracking. The original data shown as a scatter plot in red (anti-cyclones) or blue (cyclones). This data is binned where the width of each error bar is the standard deviation around the mean (purple). The theoretical prediction is plotted in black with gradient* m *(grey box).*

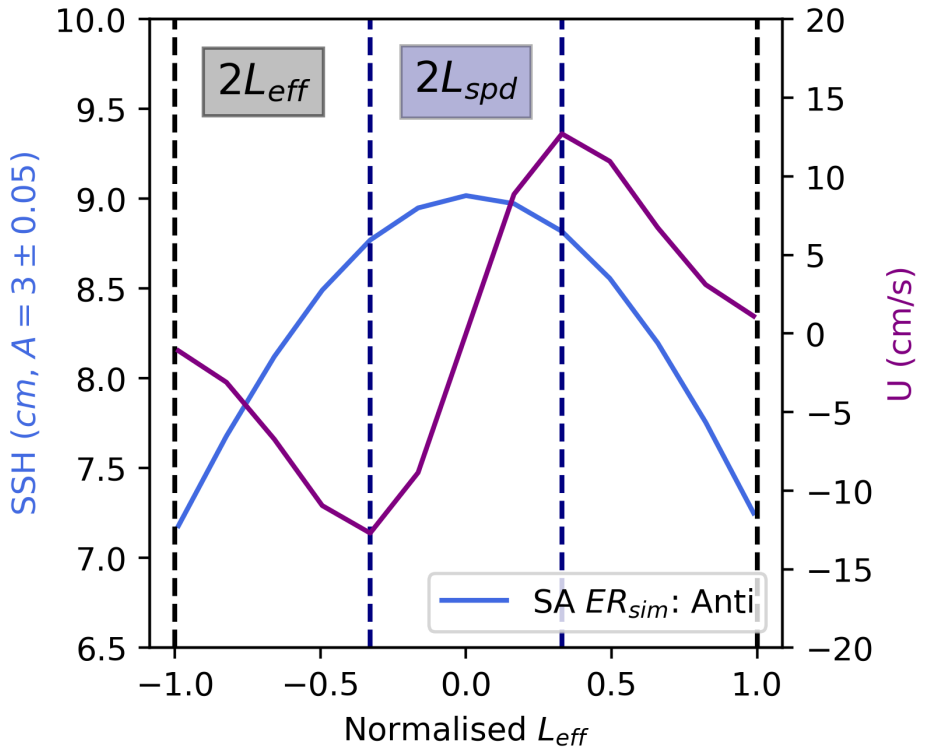

Figure 3.23: *A 1D slice of an anti-cyclonic small-amplitude (SA) eddy as an example. The spatial and temporal (1-yr) composite averaged SSH anomaly in small-amplitude eddies (A=3±0.05 cm) from the ER_{sim} (blue) is compared to estimated U (purple). Both the L_{spd} and L_{eff} are shown as vertical dotted lines. The eddy radii L_{spd} (navy) and L_{eff} (black) are plotted in vertical dotted lines where the distance in-between the coloured lines is twice the radius. The averaged L_{eff} is 40 km, and L_{spd} is 14 km.*

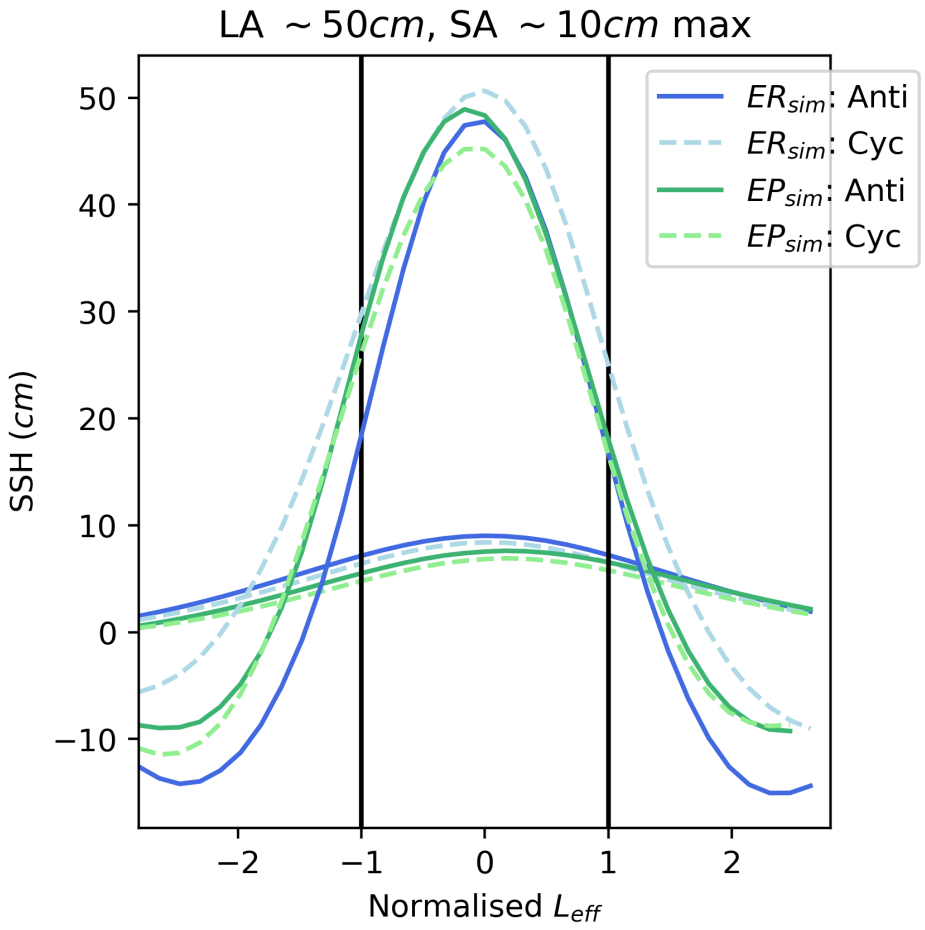

Figure 3.24: *1D slices of the composite-averaged SSH anomaly in tracked eddies in the ER_{sim} and EP_{sim} for large-amplitude eddies (binned to 34±6 cm, labelled as LA), and small-amplitude (binned to 3±0.05 cm, SA).*

3.6.2 How much EKE is found within closed coherent mesoscale eddies?

Eddy kinetic energy (EKE) is a fundamental quantity, often used to determine how well a model represents mesoscale eddy activity and is suggested to contribute as much as 80% of the total kinetic energy (Klein et al., 2019; Ding et al., 2020). High values of EKE are concentrated in eddy-rich regions, such as boundary currents and the Southern Ocean. Here the word 'eddy' in EKE is not just referring to closed coherent mesoscale eddies explored so far in this chapter; 'eddy' refers to all transient variations from the time mean. This includes eddies, filaments and meanders as well as large-scale Ekman processes, the El Nino Southern Oscillation and tropical instability waves. Therefore, EKE is often described as the kinetic energy of the time-varying component of the velocity field u, v as EKE_f:

$$EKE_f = \frac{1}{2}(\overline{u'}^{\,2} + \overline{v'}^{\,2}) \tag{3.7}$$

where $\overline{u'}^{\,2} = \overline{u^2} - (\overline{u})^2$, and u, v are the surface velocities in x- and y- directions.

EKE_f can be split into energy contained within either geostrophic (denoted as EKE_g) or ageostrophic features. Because mesoscale eddies are found in geostrophic balance, EKE contained within geostrophic features can be obtained directly as following.

$$EKE_g = \frac{1}{2}(\overline{{u_g}^2} + \overline{{v_g}^2}) \tag{3.8}$$

where $u_g = \frac{g}{f}\frac{\partial \eta'}{\partial x}$ and $v_g = -\frac{g}{f}\frac{\partial \eta'}{\partial y}$.

An active area of research is the quantification of how much of EKE_f is actually contained within closed coherent mesoscale eddies (denoted as EKE_e). This new research has only recently begun as a result of the availability of individually tracked eddies due to improved satellite altimeters. The study by Chelton et al. (2011) predicts between 40-60% of EKE is contained within coherent mesoscale eddies, while a more recent study by Martínez-Moreno et al. (2019) finds only 30% of EKE_f is found within coherent eddies in the Southern Ocean. Braby et al.

(2020) agree in the Agulhas region, most energy (2.5x) is found outside of coherent eddies. These results hold important implications to improve our understanding of where most EKE is held, and what needs to be resolved in ocean models.

Here we attempt to provide a global quantification of how much EKE_g is contained within coherent tracked eddies (EKE_e) in both the ER_{sim} and EP_{sim}, compared to observations. Both the geostrophic and full EKE are given as a 10-year mean, while the eddies are averaged over 20 years. The minimum eddy lifetime used in this section is 1 week. An important consideration is coherent mesoscale eddies are tracked in Lagrangian framework, while EKE_g (or EKE_f) are calculated for fixed Eulerian grid boxes. Here we take daily snapshots of EKE_e and do not consider variations in EKE with eddy lifetime.

EKE within mesoscale eddies EKE_e is not outputted directly from the tracking algorithm. Instead, the algorithm outputs the sum of EKE (here termed the total EKE, TEKE) within each tracked eddy within L_{eff}, at the location of the eddy centre. TEKE is initially not a useful quantity to compare to EKE_g; the magnitude of the sum is far larger than EKE_g, and does not take into account the distribution of energy over the size of the eddy. Instead, to find a more appropriate value of EKE_e, the following method is applied to TEKE.

- TEKE is converted to an area-average for each eddy, dependent on its effective radius L_{eff}.
- The averaged EKE is scaled by the percentage of the ocean occupied by mesoscale eddies i.e. to take into account where eddies are absent.

Further details of each process is given below. First, TEKE is converted to an area-average for each eddy (EKE_{av}) by dividing TEKE by the number of grid points (N_{circ}) within a fitted circle of radius L_{eff}. We know from the tracking algorithm criteria, the minimum number of grid points in a tracked eddy is at least 8. N_{circ} is calculated by knowing the number of grid points within the eddy radius (termed N_{rad}) using the theory of the 'Gauss circle problem'. This theory determines how many integer lattice points are present within a circle centered at the

origin and with a defined radius N_{rad}. For example, when $N_{rad} = 4$, the number of grid points in the circle $N_{circ} = 49$. N_{rad} is calculated by knowing L_{eff} and the grid box size dx.

$$EKE_{av} = \frac{TEKE}{N_{circ}} \tag{3.9}$$

$$N_{rad} = \frac{\overline{L_{eff}}}{\overline{dx}} \tag{3.10}$$

The over-line denotes a global and spatial mean, and we assume the variation in dx and L_{eff} is minimal relative to TEKE. It is too computationally expensive to vary L_{eff} and dx with each eddy snapshot, therefore a constant value was used.

Second, the eddy tracking algorithm provides values of EKE where eddies occur, and not does take into account values where eddies are absent. Therefore, we approximate the percentage of area covered by mesoscale eddies each day in the global ocean (P_{glob}), using equations 3.11 below. The final value of EKE_e shown in the figures below is $EKE_e = EKE_{av} * P_{global}$.

$$P_{glob} = \frac{\sum A_{eddy}}{A_{total} * n} \tag{3.11}$$

where $A_{eddy} = \pi {L_{eff}}^2$ which is the area covered by eddies, A_{total} is the approximated total area of the ocean and $n = 360 * 20$ which is the number of days in the temporal length of the dataset (20 years). By globally summing over all eddy areas, regional differences in the spatial size are averaged out.

Because the post-processing of TEKE and remapping Lagrangian variables to Eulerian is complex, there are many limitations and assumptions with our method. We assume the spatial structure of eddies forms a perfect circle (for area-averaging) and meridional and zonal variations in L_{eff} are small compared to the magnitude of EKE_e. Finally, our method only considers surface EKE as the eddies are only tracked at the surface.

Since performing this work, a more recent observational study by Ding et al. (2020) argues for the use of a metric (called LEKE) which combines both fixed Eulerian EKE and Lagrangian EKE following eddies, in the Northwest Pacific. Their method and limitations draw similarities to ours, which increases the confidence in

our results. Both methods use area-averaging as discussed above. Key differences are in the eddy radius used; we use the effective radius L_{eff} and Ding et al. (2020) use the speed-based radius. Second, they employ a coordinate to move with the eddy to consider variations of LEKE and the speed-based radius over the eddy's life cycle, while we use daily snapshots and do not consider the eddy evolution. Third, they manage to regrid LEKE into a regular $3^\circ \times 3^\circ$ grid, and we were unsuccessful attempting to do this whilst maintaining suitable magnitudes of EKE_e. Finally, they separate anti-cyclonic and cyclonic eddies, which is not our aim here.

Using equation 3.11, eddies in the EP_{sim} and ER_{sim} cover 5.77% and 5.79% of the global ocean each day. While the percentage cover of eddies in observational data is approximately double at 11.88%. The larger number of smaller eddies in the ER_{sim} covers a similar area of the ocean to the fewer, larger eddies found in the EP_{sim}.

A comparison of the different versions of EKE are plotted as global probability density functions in Fig. 3.25 for observations and each model resolution. Compared to TEKE, the magnitudes and distribution of EKE_e are more similar to both previous studies and to EKE_g (Ding et al., 2020). The bias in the large TEKE magnitudes in the ER_{sim} from a larger number of smaller eddies is removed in EKE_e. In observations, we find magnitudes of EKE_e are larger (1.6x) compared to EKE_g with medians of approximately 418 and 260 cm^2 s^{-2} respectively (shown by the vertical dotted grey lines in Fig. 3.25). This result could be a consequence of the over-estimate of L_{eff} within the observational dataset, as discussed earlier as a consequence of the post-processing bias. Perhaps, in reality the global area covered by mesoscale eddies is smaller, and therefore EKE_e should be smaller. Although, until a more accurate observational dataset is made available, it is difficult to validate this statement.

Similarly to our study, Ding et al. (2020) find EKE_g larger than EKE_e but our values of EKE_e are slightly smaller than the Lagrangian EKE calculated by Ding et al. (2020). The difference is expected because we are averaging over a global domain, rather than isolating the Kuroshio Current region. For both model

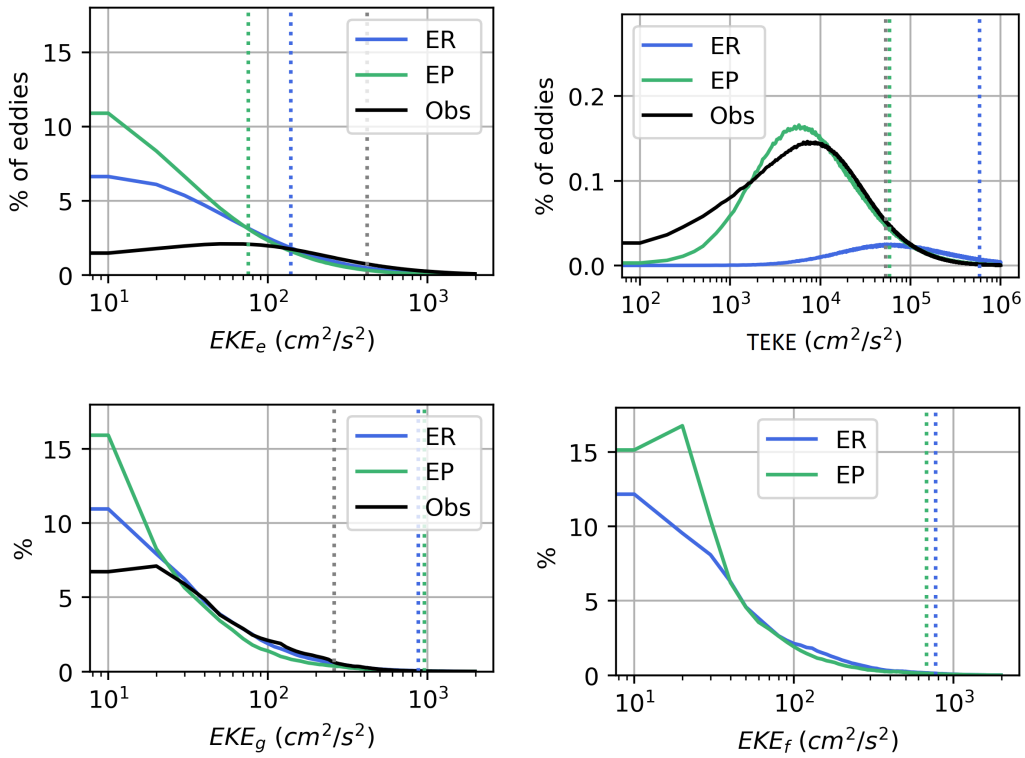

Figure 3.25: *Global probability density functions of EKE from coherent mesoscale eddies (EKE_e), the sum of EKE within an eddy (TEKE), geostrophic EKE (EKE_g) and the full EKE (EKE_f) for observations, and the ER and EP model resolutions. The vertical dotted lines represent the medians for each dataset. EKE_e, EKE_g and EKE_f are all binned with an interval of 10 cm^2 s^{-2} and a maximum of 2000 cm^2 s^{-2}.*

resolutions the medians of EKE_e are smaller than EKE_g: the medians of EKE_e for the EP_{sim} is 75 cm^2 s^{-2} and for the ER_{sim} is 139 cm^2 s^{-2}, compared to EKE_g medians of 955 and 874 cm^2 s^{-2} respectively. Using the medians, EKE_e makes up 7.8% of EKE_g in the EP_{sim} and 15.9% in the ER_{sim}.

In summary, we have successfully compared the quantity of mesoscale energy contained within closed coherent eddies, in comparison to the turbulent geostrophic field, consisting of meanders, jets and filaments. Although we have produced initial results and there are limitations to our method, we so far conclude less geostrophic EKE is contained within eddies in the two model resolutions, in comparison to

observations. Although the ocean comprises of a highly turbulent eddying field, tracked coherent mesoscale eddies only make up about 12% of the EKE in the observed ocean, about 8% in the EP_{sim} and 16% in the ER_{sim} (using the median values). Further analysis, beyond the scope of our initial analysis here, is needed to explore the reliability of the method in different geographical regions and to allow eddy size to vary with latitude. The final results section in this chapter discusses the variation of eddy properties, such as size, amplitude and EKE, over an eddy's lifetime.

3.6.3 The impact of mesoscale air-sea exchanges on eddy properties and life cycles

This section first introduces the impact of mesoscale air-sea exchanges on eddy properties by comparing configurations with either no atmosphere, or a higher atmospheric resolution, coupled to the same 1/12° ocean. Either removing or increasing the atmospheric resolution will directly alter the representation of air-sea heat and momentum fluxes at the mesoscale. How these fluxes impact the magnitude, distribution and life cycle of eddy properties, such as amplitude or size, is ambiguous. To gain an initial understanding, this section simply alters the atmospheric component and discusses the impact on eddy properties. A further diagnosis of the different mechanisms involved is provided in the following Chapters 4 and 5.

First, we rename the ER_{sim} back to N216-12, and compare to a higher resolution atmosphere (from 60 to 25 km, termed N512-12) and an ocean-only model (ORCA12, termed Nxx-12). The eddy tracking algorithm is run for 20 years for the N512-12 configuration and 10 years for Nxx-12.

The Nxx-12 ocean-only configuration has a reduction of 15% in eddy counts lasting longer than 1 month compared to the coupled N216-12 (ER_{sim}) configuration. Note re-running Nxx-12 with the coarse resolution (1/4°) bathymetry slightly reduces the number of eddies lasting longer than 1 month, however increases the number lasting longer than 4 months. This increase in longer-lasting eddies may be

associated with the increased formation of anti-cyclonic eddies from the Indonesian archipelago at 1/4° (EP) resolution, seen in Fig. 3.5. Increasing the atmospheric resolution in N512-12, from N216-12, slightly reduces the number of eddies identified, especially the percentage of longer lasting eddies.

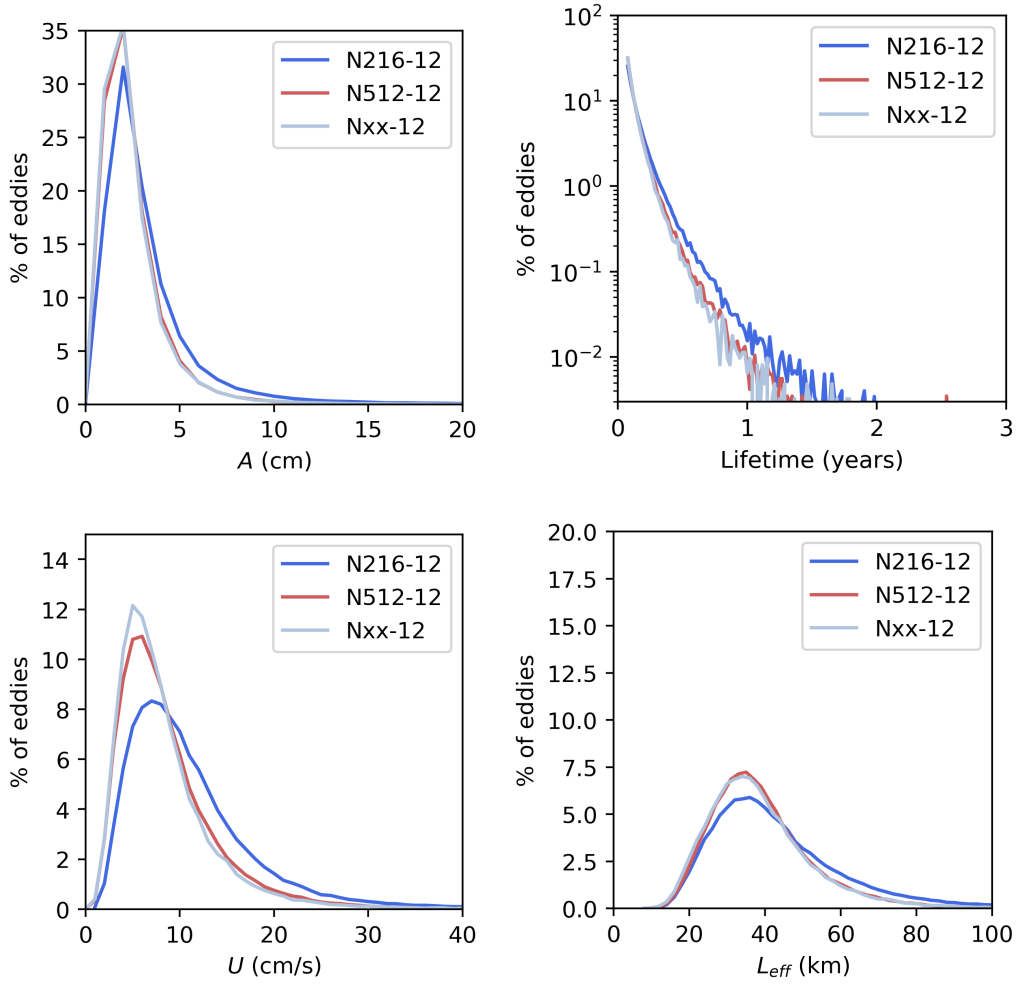

Figure 3.26: *Probability density functions of eddy amplitude (A), lifetime, rotational velocity (U) and effective radius (L_{eff}) when increasing the atmospheric resolution (N512-12, red curve) or in an ocean-only configuration (Nxx-12, light blue) compared to the ER_{sim} (N216-12, mid blue). These pdfs are repeats of Figures 3.9 (left), 3.15 and 3.16.*

A repeat of figures 3.15 and 3.16 is shown in Fig. 3.26 for Nxx-12 (light blue curve), N512-12 (red) and N216-12 (mid-blue). Both N512-12 and Nxx-12 reduce

the amplitude, rotational speed, radius and lifetime of mesoscale eddies, compared to N216-12, although different mechanisms occur for each configuration. Does increasing atmospheric resolution, so it is more similar to the ocean resolution, provide a better representation of mesoscale air-sea exchanges? We know these air-sea exchanges of heat and momentum, i.e. surface current or SST - wind stress coupling, induce eddy dampening deflecting energy to the atmosphere and slowing the eddy's rotational speed (U) as seen in the lower left subplot in Fig. 3.26 (Renault et al., 2016a; Gaube et al., 2015). This induced eddy dampening reduces eddy amplitude, lifetime and spatial scale (L_{eff}), as found in previous regional coupled model set ups in Renault et al. (2016b) and Oerder et al. (2018). The speed-based radius L_{spd} between the different configurations displays a similar distribution to L_{eff}, although at smaller scales.

Interestingly, the ocean-only configuration with no air-sea feedback and prescribed winds, has a very similar distribution of eddy properties to the higher-resolution N512-12 configuration (Fig. 3.26). Without air-sea feedback acting to dampen mesoscale eddies, one would expect eddy properties, e.g. amplitude or lifetime, to be unrealistically large. Instead, the distribution of eddy rotational velocity (U) and eddy lifetime is actually more realistic, e.g. more similar to observational U (Fig. 3.15) compared to N216-12, ER_{sim}. Coupling to a high-resolution atmosphere does not necessarily improve the representation of all eddy properties.

A further investigation into the differences in eddy lifetime with latitude is given in Fig. 3.27. Again N216-12 is a repeat of the ER_{sim} defined previously, and a relative dampening of eddy lifetime is observed in N512-12, especially at mid-latitudes. For example at 40°S a dampening of eddy lifetime in N512-12 of 15% is found, compared to N216-12. Oerder et al. (2018) argue it is the feedback from mesoscale surface current - wind stress coupling which shortens eddy lifetimes by 15%.

The meridional distribution of eddy lifetimes in both N512-12 and Nxx-12 do not provide an obvious better fit to observations, despite being shorter than N216-12 (Fig. 3.27). Whilst lifetimes in Nxx-12 in the Gulf Stream and Kuroshio Current ($\sim 30°N$) and at the highest latitudes ($\sim 50°S$ and $\sim 60°N$) are similar to N512-12,

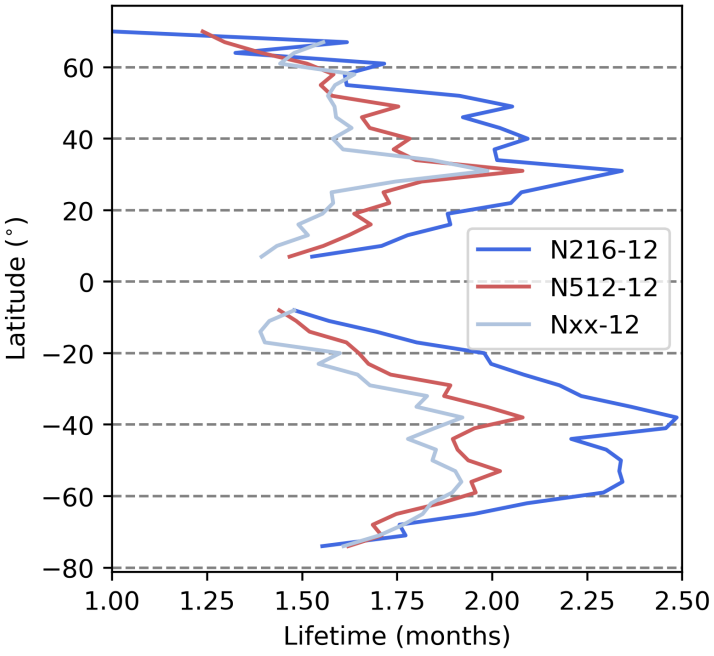

Figure 3.27: *Zonal average of eddy lifetime (in months) when increasing the atmospheric resolution (N512-12, red curve) or in an ocean-only configuration (Nxx-12, light blue) compared to the ER_{sim} (N216-12, mid blue). A repeat of Fig. 3.9 (right).*

generally lifetimes are slightly shorter in Nxx-12.

The relative dampening of an eddy in N512-12, compared to N216-12, is further explored by comparing how each eddy property varies over its life cycle. Oerder et al. (2018) argue eddy dampening reduces an eddy's growth and decay rate. Although this finding opposes previous work which is based on a different method of analysis Renault et al. (2016a). It remains unclear how mesoscale air-sea feedback influences the evolution (i.e. the growth, decay and lifetime) of individual eddies in different model configurations. As far as we know, this is the first study to compare life cycles of modelled eddy properties to observations.

To investigate how eddy evolution varies in different model configurations and observations, individual eddy tracks are normalized to remove differences in the magnitudes of the eddy properties. Following the notation and technique used by Samelson et al. (2014), eddy amplitude A for each eddy of number k is denoted

as A_k, where k varies from 1,2,3... etc. and combines both anti-cyclonic and cyclonic eddies. Each eddy's lifetime (denoted as J) is a function of the daily tracking timestep (Δt) and the number of days the eddy is tracked for (where time t is t_j with an index j of 1,2,3,... days) as following $J = t_j \Delta t$. In our case eddies are tracked every day so $\Delta t = 1$ and $J = t_j$. Note the original method by Samelson et al. (2014) uses a weekly timestep. Eddy amplitude trajectories can therefore be written as $A_k(t_j)$, varying in both eddy number (k) and the days tracked for (j).

First, each eddy amplitude trajectory is normalized by the time mean ($\overline{A_k}$) as following:

$$A_{norm} = \frac{A_k(t_j)}{\overline{A_k}} \tag{3.12}$$

where $\overline{A_k} = \frac{\sum A_k(t_j)}{J}$. For simplicity in the figures, eddy amplitude $A_k(t_j)$ is shortened to A, and J is referred to as lifetime. Exactly the same process is repeated for each eddy property: U, L_{spd} and the total EKE within an eddy, TEKE.

Second, each eddy amplitude trajectory is normalized by transforming the number of days an eddy is tracked for (t_j) into dimensionless time i.e. between 0-1.

$$t_{norm} = \frac{t_j - 0.5}{J} \tag{3.13}$$

The addition of the 0.5 value ensures t_{norm} is a mean over the Δt (1 day) interval, centred on the original time. Finally, t_{norm} is regridded so each eddy trajectory vector is of equal size, before calculating the mean across all trajectories.

Fig. 3.28 presents the normalized eddy properties (A, U, L_{spd} and TEKE) plotted against normalized time for the EP_{sim} (N216-025, green curve), the ER_{sim} (N216-12, blue), N512-12 (red) and observations (black). TEKE is the sum of all eddy kinetic energy within L_{eff}, which excludes all post-processing discussed in section 3.6.2 to form EKE_e. As the data is normalized, we can assume the difference in magnitudes between TEKE and EKE_e are irrelevant here. Finally, all eddies lasting longer than 1 month, and between 100,000-250,000 eddies are averaged, depending on the data source. The effective radius L_{eff} follows a very similar distribution to L_{spd} and is not shown.

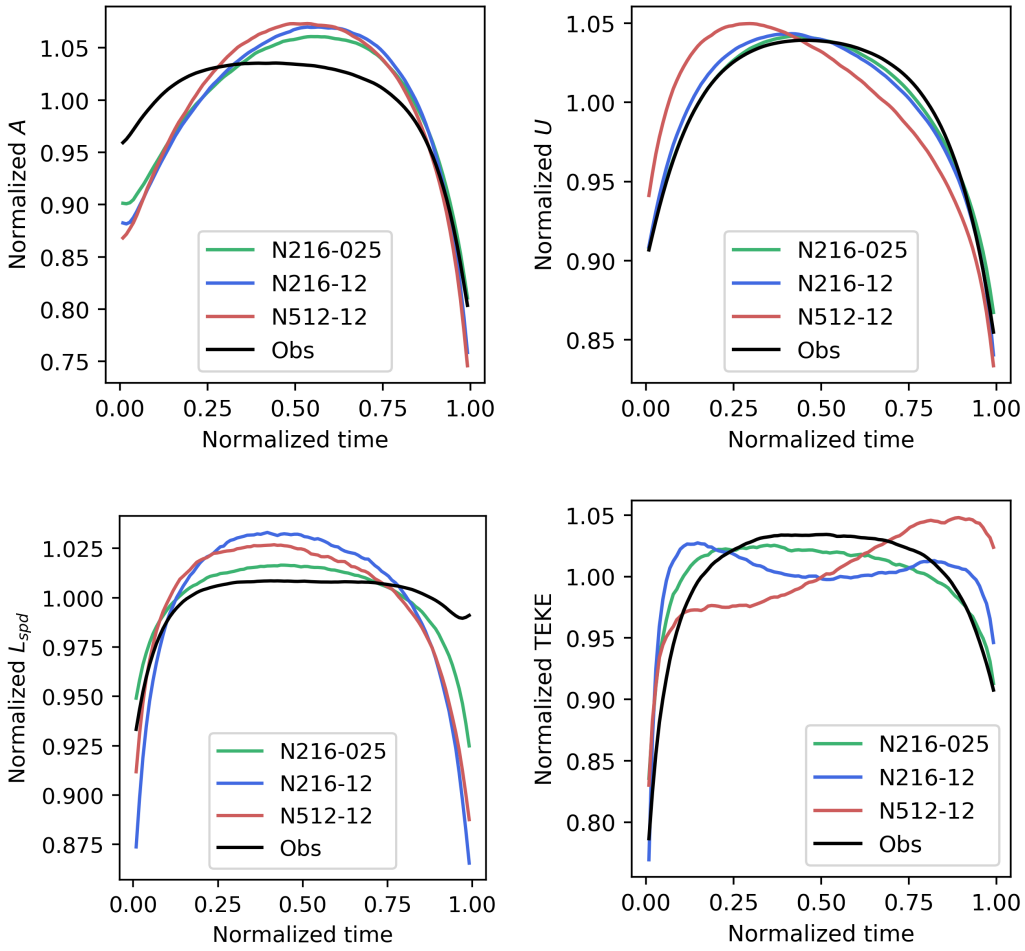

Figure 3.28: *Eddy life cycles for amplitude (A), the speed-based radius (L_{spd}), rotational velocity (U) and the total EKE within an eddy (TEKE). All eddies have a minimum lifetime of 1 month.*

At first glance, the growth and decay rate of modelled eddies, at all three resolutions, appears different to observations. The modelled eddies present a more bell-shaped, relatively symmetrical life cycle, particularly in terms of amplitude and rotational speed, i.e. a slower rate of growth and decay, compared to observed eddies. After modelled eddies reach their maximum value of either amplitude, radius or rotational velocity, they start to reduce, with a similar reduction rate as previous growth rate. The exception being the increase in TEKE over an eddy's life cycle in the eddy-rich ocean resolutions (N216-12 and N512-12). Instead, observed ed-

dies maintain a relatively constant amplitude, radius, rotational speed and energy (TEKE) over an eddy's life cycle between initial generation and its final reduction, as found in previous studies, despite changes in the number of satellites over time (Samelson et al., 2014; Ding et al., 2020; Zhang et al., 2020). Perhaps the increase in energy in N216-12 and N512-12 is related to why eddies live longer in these resolutions compared to observations.

The highest atmospheric resolution configuration, N512-12, presents slightly different life cycle profile, particularly for rotational velocity U and TEKE, compared to the other resolutions. N512-12 has the fastest growth rate for rotational velocity U, meaning the eddies speed up quicker then reduce their rotation at a slower rate, compared to observations, N216-12 and N216-025. This asymmetry in N512-12, compared to the other configurations or observations, is mirrored in TEKE where the energy increases over an eddy's lifetime, being considerably higher at the end of its life compared to the start.

Whether the generation or dampening of eddies (or both) are contributing to the differences between model resolutions, and observations is more complicated to evaluate than first thought. First, there are challenges to compare the observations with the model life cycles. The observational dataset is likely to struggle to capture the growth of eddies correctly, unlike the model. Therefore, if the growth of the eddies (particularly amplitude and L_{spd} in Fig. 3.28) in the models are cropped out to match observations, we suspect the normalised life cycle curve would look very similar between both observations and models. Instead, currently the observational life cycle appears 'stretched' by the normalisation in time. Second, the differences between the model resolutions for eddy amplitude, L_{spd} and U are not significant (in either Fig. 3.28 or 3.29). And third, the increase in TEKE in the 1/12° models over the life cycle is likely to be caused by an increase in L_{eff} as these smaller eddies get weaker (U reduces) over time, causing an inverse cascade of energy. Note TEKE is not scaled by radius and is the sum of TEKE across an eddy within L_{eff}.

Fig. 3.28 is then repeated in Fig. 3.29 for all eddies lasting longer than 1 year. Far less eddies are averaged compared to Fig. 3.28: the number of eddies ranges

between 116-706. This explains the increased variability seen in the life cycle, and implies the differences between the models and observations are not significant. Over longer-lasting eddies, the symmetrical bell-shape in modelled life cycles is absent, and a more linear trend is seen. The rate of change of eddy properties in the model configurations are more similar to each other than to observations. Modelled eddies (particularly N512-12) have both a faster rate of reduction of rotational velocity U and radius, and a faster rate of increase in TEKE, over their lifetime compared to observed eddies. We know eddies last longer in the model compared to observations, but why the rates of decay in size and rotational velocity increase in the model compared to observations (especially in the longest lasting eddies) is not obvious.

To conclude, these results convey the importance of both the atmospheric and oceanic resolution in coupled models to capture realistic mesoscale lifetimes and life cycles. At an increased atmospheric resolution, in N512-12, it is suggested a different representation of air-sea feedback alters the life cycle of mesoscale eddies, although it does not improve their realism. An understanding of how long mesoscale eddies live is fundamental to first, quantify the impact of eddy dampening from mesoscale air-sea exchanges and second on a larger scale, to parameterize the 'residence time' in oceanic heat and volume transport, such as recent work to be resubmitted by Marshall and Zhai (2021) (personal communication).

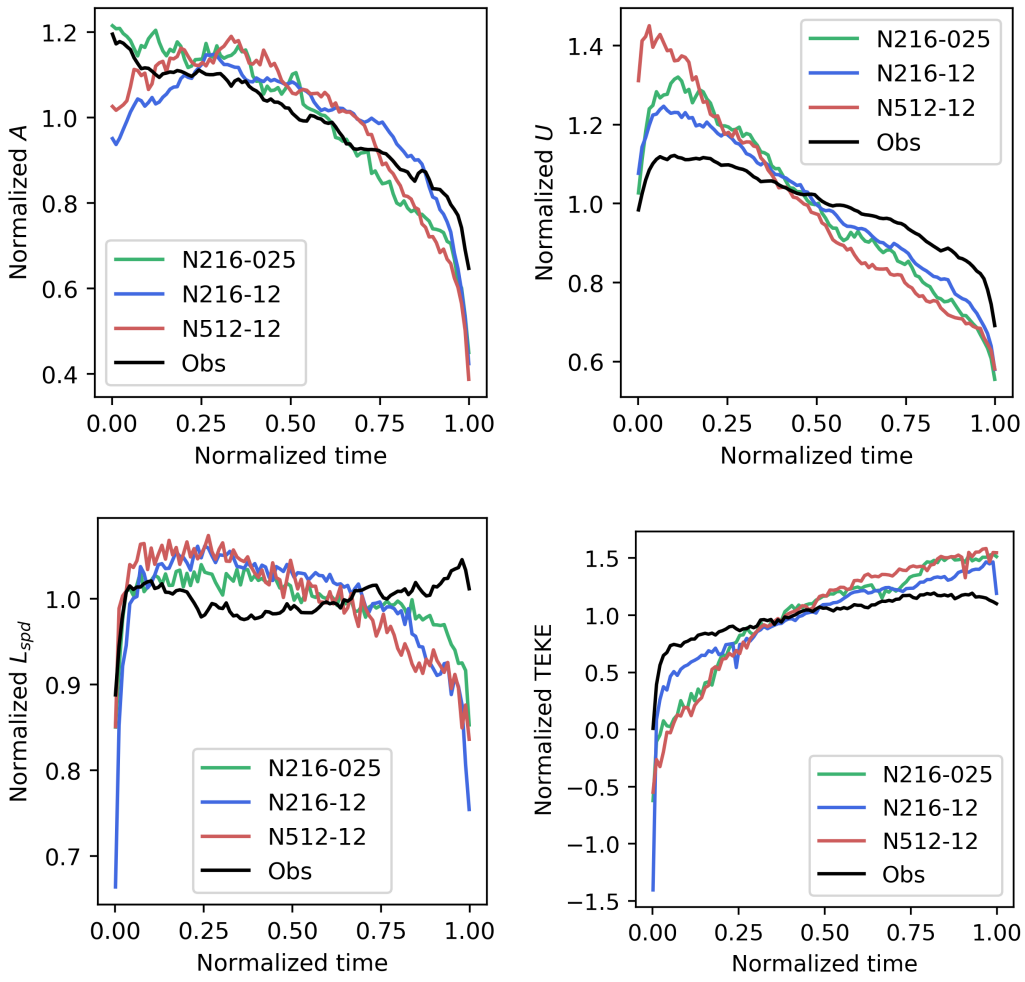

Figure 3.29: *A repeat of Fig. 3.28 for eddies with a minimum lifetime of 1 year.*

3.7 Conclusions

In alignment with our first thesis objective, strengths and limitations of ocean simulations at ER and EP resolution in the representation of mesoscale eddies are explored. We focus on the surface properties of eddies using an eddy tracking algorithm on SSH anomalies. Modelled properties are compared to observed properties evaluated from the satellite altimeter AVISO product. An ocean model's ability to better-represent eddies in eddy-energetic regions, such as the western boundary currents, the Agulhas retroflection and the Southern Ocean, has important implications for heat transport, global ocean stratification and eddy energy dissipation (Munday et al., 2013; Marshall and Zhai, 2021; Zhai et al., 2010).

The key findings are summarized below:

- Amplitude, rotational speed and propagation speed of eddies are very similar across observations and models.

- ER and EP resolutions generate only $\sim 63\%$ and 40% respectively as many eddies as in observations. A leading factor for this discrepancy is the low count (or sometimes complete absence in EP) of eddy generation in the mid-ocean gyres and in Eastern Boundary Currents.

- Eddy lifetime are biased low in the EP_{sim} compared to observations but biased high in the ER_{sim}, notably in the Southern ocean where the averaged eddy lifetime is about 30% larger than observed.

- Compared to EP_{sim} and observations, eddies are significantly smaller in ER_{sim}. This is true for both measures of eddy radius (speed-based and effective radius) although the differences are more striking for the speed-based radius.

- Eddy radii scale closely with the Rossby radius of deformation, R_d, in all three datasets. As suggested in previous studies, eddy sizes also relate well to the minimum of the R_d and the Rhines scale L_{Rhines}. The improvement in

the fit from R_d alone to $min(R_d, L_{Rhines})$ is particularly notable in the ER_{sim} and EP_{sim}.

- In contrast with suggestions from previous studies, EP_{sim} simulates a significant population of eddies up to the high latitudes where the model grid-scale is larger than the Rossby radius of deformation, R_d. These eddies likely grow on scales set by the smallest combination of grid-points that allows instability.

- Within $1L_{eff}$, we imply the majority of modelled mesoscale eddies tracked in this study do not possess a Gaussian structure.

- Less geostrophic EKE is contained within eddies in the two model resolutions, in comparison to observations. Although the ocean is a highly turbulent field, tracked coherent mesoscale eddies only make up about 12% of the observed ocean, and even less in the model, although there are limitations to calculation of EKE as discussed above.

For the number of metrics explored in this study, it is difficult to objectively evaluate whether ER resolution provides a significant improvement over EP resolution, in part due to concerns that observations may not provide a robust benchmark. Instead advantages of the ER_{sim}, compared to EP_{sim}, depend on the properties and region of interest. Benefits of the ER_{sim} include a similar number of eddies in the Southern Ocean, and globally a similar number of eddies living longer than 16 weeks, compared to observations. ER_{sim} eddies are less stationary and smaller eddies are able to develop, compared to the EP_{sim}. The genesis rate and size of the eddy populations are clear examples where the ER_{sim} improves upon EP_{sim}. This is likely the result of a better representation of the mean state in the ER_{sim} in eddy-energetic regions such as boundary currents and the ACC. Eddies generated in Eastern Boundary Currents are important for transferring heat and nutrients into the nutrient-poor open ocean (Frenger et al., 2018; Gaube et al., 2015). In that regard, the ER_{sim} clearly outperform the EP_{sim} where the basin interior are relatively empty of eddies.

In other aspects, outcomes of the model-observation comparison are more ambiguous. Our results suggest that the ER_{sim} over-estimates the survival rate of eddies. The dissipation of mesoscale eddies in the ocean remains an open question with a number of competing ideas being explored e.g. enhanced friction over rough bottom topography, the emission of internal waves, coupling to the atmosphere, the role of symmetric instability in the open ocean or interaction with WBCs (Zhai et al., 2010; Clément et al., 2016; Gula et al., 2016; Yu et al., 2019). It is not expected that such processes are captured in ER (nor EP) resolution models. Our analysis suggests that as resolution increases, allowing more vigorous eddies and a lower viscosity (for numerical stability), the absence of dissipation mechanisms may become problematic and introduce biases in the lifetime of the modelled eddies. However, we cannot rule out that eddy lifetime estimates are biased low in observations due to post-processing and smoothing of the SSH data that would limit the ability to track eddies.

The differences in eddy size are a particularly striking outcome of our analysis. Our results suggest that the eddy size is overestimated in observations by a factor 2 and possibly up to 4 depending on the considered measure, due to the post-processing of the observational dataset. The nominal resolution of the dataset is a key factor here and, consistent with previous studies, our analysis suggests that the effective resolution of the AVISO gridded dataset is coarser than 1/4° (Chelton and Schlax, 2003; Chelton et al., 2011; Sun et al., 2017; Arbic et al., 2013). Instead, the effective resolution in the ER_{sim} is much higher than in observations but the subsequent impact of the smaller eddies found in the ER_{sim} is unclear. Whether the total energy or heat contained within a greater number of smaller eddies in the ER_{sim} is similar to the fewer, larger eddies found in the EP_{sim} remains to be determined. However, initial insights show the area-averaged EKE (EKE_e) within coherent mesoscale eddies is similar in both the ER_{sim} and EP_{sim}.

Further studies are needed to explore the role of the tracked eddies in air-sea and surface-subsurface coupling within the climate system. An overestimation of eddy scales in observations could have implications for eddy parameterization and

interpretation of ocean dynamics. Mixing length arguments underlying many eddy parameterizations use the eddy scale as proxy for the mixing length (Klocker and Abernathey, 2013). Direct comparison of properties (e.g. wavenumber spectrum, see Scharffenberg and Stammer (2011)) along satellite tracks should help clarify to which extent differences between model and observations are robust or due to the post-processing necessary to generate the AVISO gridded product.

Finally, it must be noted that our model represents one set of parameter choices, for example the sensitivity to viscosity has not been tested, and only surface eddy properties are evaluated. Further studies should explore the 3-dimensional structure of eddies, the influence of eddies of air-sea exchanges and energy spectra to compare the redistribution of kinetic energy at larger scales for each resolution (Kjellsson and Zanna, 2017). Limitations of the eddy tracking algorithm should not be underestimated (Chelton et al., 2011). It is likely that some of our results (e.g. eddy counts) are dependent on our choice of eddy detection algorithm. However we have attempted to minimize its impact by applying the same algorithm to models and observations and focus our analysis on differences/similarities rather than the absolute values. This work lays the foundation for future studies at different resolutions and using different models as more high resolution data become available in which submesoscales start to be resolved. Observational SSH global datasets are likely to improve as satellite altimetry coverage is enhanced with the future launch of the SWOT altimeter.

Having performed a thorough analysis of globally tracked mesoscale eddy properties, within the state-of-the-art climate model HadGEM3-GC3.1, we can use this dataset, particularly the eddy amplitude and size metrics, to further evaluate the impact of air-sea feedback over these mesoscale eddies. In the following chapter we focus on feedback from air-sea turbulent heat fluxes on mesoscale eddies, and in Chapter 5 comparing to mesoscale SST-wind stress feedback, in order to investigate the impact on large-scale ocean circulation.

Chapter 4

Air-Sea Turbulent Heat Flux Feedback over Mesoscale Eddies

The chapter is structured, similarly to Chapter 3 as follows. Sections 4.1 to 4.5.2 present the published research paper, and additional complementary unpublished results are given in section 4.6. Section 4.7 concludes the chapter.

The publication details are: Moreton S., Ferreira D., Roberts M. and Hewitt H. (2021) Air-sea turbulent heat flux feedback over mesoscale eddies. Geophysical Research Letters, 48, e2021GL095407. https://doi.org/10.1029/2021GL095407

4.1 Abstract

Air-sea turbulent heat fluxes play a fundamental role in generating and dampening sea surface temperature (SST) anomalies. To date, the turbulent heat flux feedback (THFF) is well quantified at basin-wide scales ($\sim$20 W m^{-2} K^{-1}) but remains unknown at the oceanic mesoscale (10-100 km). Here, using an eddy-tracking algorithm in three configurations of the coupled climate model HadGEM3-GC3.1, the THFF over mesoscale eddies is estimated. The THFF magnitude is strongly dependent on the ocean-to-atmosphere regridding of SST, a common practice in coupled

models for calculating air-sea heat flux. Our best estimate shows that the mesoscale THFF ranges between 35 and 45 W m^{-2} K^{-1} when globally averaged, across different eddy amplitudes. Increasing the ratio of atmosphere-to-ocean grid resolution can lead to an underestimation of the THFF, by as much as 80% for a 6:1 resolution ratio. Our results suggest that a large atmosphere-to-ocean grid ratio can result in an artificially weak dampening of mesoscale SST anomalies.

4.2 Highlights

- Global turbulent heat flux feedback over coherent mesoscale eddies ranges between 35-45 W m^{-2} K^{-1}.
- Ocean to atmosphere SST regridding can underestimate turbulent heat flux feedback by up to 80%.
- Coupled models need a coordinated increase in ocean and atmosphere resolutions.

4.3 Introduction

The turbulent heat flux feedback (THFF, in W m^{-2} K^{-1}, denoted α hereafter) is a critical parameter, which measures the change in the net air-sea turbulent heat flux in response to a 1 K change in sea surface temperature (SST). It is a powerful tool to quantify the rate of dampening of SST anomalies. THFF can vary seasonally (largest in winter), geographically and with ocean spatial scale. Early studies estimate THFF at approximately 20 W m^{-2} K^{-1} for basin-scale mid-latitude SST anomalies, which, to first order, respond passively to atmospheric forcing (Bretherton, 1982; Frankignoul, 1985; Frankignoul et al., 1998, 2004; Small et al., 2020). More recent studies estimate that THFF increases to 40 W m^{-2} K^{-1} in the Gulf Stream, and decreases down to 10 W m^{-2} K^{-1} in the Antarctic Circumpolar Current (Hausmann and Czaja, 2012; Hausmann et al., 2017). To date, while THFF is

known to increase towards smaller scales, the smallest spatial scale used to quantify THFF is approximately 100 km.

The magnitude of THFF depends on the adjustment of the atmospheric boundary layer (ABL) to the SST anomaly. It is suggested that the removal of heat by surface winds is a key process (Bretherton, 1982; Hausmann et al., 2016). On smaller scales, atmospheric heat anomalies are quickly advected away from the SST anomaly, maintaining a large air-sea temperature contrast and strong heat flux damping. While on basin scales, heat advection becomes less efficient (slower), resulting in a small temperature contrast and reduced damping. On global scale, this adjustment completely disappears: the heat removal is controlled by radiation out to space and the THFF reaches only about 1-2 W m^{-2} K^{-1} (Gregory et al., 2004). However, how the THFF behaves at spatial scales below 100 km remains unknown.

Formed through intrinsic ocean variability, mesoscale eddy SST anomalies (of radius 10-100 km) drive distinct changes within the ABL through the so-called 'vertical mixing mechanism' (Frenger et al., 2013; Hayes et al., 1989; Putrasahan et al., 2013; Small et al., 2019; Wallace et al., 1989). A warm mesoscale SST anomaly transfers heat through turbulent heat fluxes up into the ABL. This heat addition reduces stability, enhances vertical mixing, and reinforces the downward transfer of momentum, strengthening surface winds. The opposite occurs over a cold SST anomaly. Past research on mesoscale air-sea exchanges largely focuses on momentum fluxes i.e. Renault et al. (2016b, 2019b) and Seo et al. (2016). However in eddy-rich regions, mesoscale-induced air-sea turbulent heat fluxes play an important role in altering eddy kinetic and potential energy and dampening SST anomalies (Ma et al., 2016; Bishop et al., 2020). Furthermore, mesoscale SST-turbulent heat flux exchanges can strengthen western boundary currents (WBC) by 20 to 40% and weaken thermal stratification in the upper ocean (Shan et al., 2020a; Ma et al., 2016; Small et al., 2020). It is therefore important to quantify THFF over transient mesoscale eddies.

Observational estimates of THFF at the oceanic mesoscale are restricted by the availability of high-resolution ocean and atmosphere data. First, the consistency

and effective resolution of global air-sea heat flux datasets are questionable, due to the different space-time resolutions from either atmospheric reanalysis or satellites (Villas Bôas et al., 2015; Leyba et al., 2016; Cronin et al., 2019; Li et al., 2017; Tomita et al., 2019). Second, the radii of observed mesoscale eddies maybe be overestimated by a factor of 2 due to the interpolation of along-track sea surface height measurements by satellite altimeters into regular grids (Moreton et al., 2020; Ducet et al., 2000; Chelton, 2013; Small et al., 2008; Minobe et al., 2008; Hausmann and Czaja, 2012; Xie, 2004; Cronin et al., 2019). As a result, this study uses a global coupled climate model with higher spatial ocean and atmospheric resolution than currently available in observations.

Current state-of-the-art climate models can provide global eddy-rich ocean simulations, with a horizontal resolution of approximately 1/12°. At this resolution, mesoscale eddies can be explicitly resolved globally, except in the highest latitudes with more, smaller and longer-lasting eddies compared to a 1/4° resolution (Haarsma et al., 2016; Roberts et al., 2019; Hewitt et al., 2017; Moreton et al., 2020). However, whether an eddy-rich ocean results in an improved representation of mesoscale SST-turbulent heat flux exchanges remains to be determined. The ratio of ocean-atmosphere horizontal resolution is likely to be an important factor (Jullien et al., 2020; Wu et al., 2019). In many current high-resolution coupled models with a NEMO ocean component, air-sea fluxes are computed on the atmospheric grid, which requires the interpolation of SST from the oceanic grid to the often coarser atmospheric grid through the OASIS3-MCT coupler (Williams et al., 2018; Valcke, 2013). The interpolation is likely to smooth out mesoscale features resolved on the ocean grid before calculation of the air-sea exchanges and if so, to introduce significant biases in non-linear air-sea feedbacks.

Therefore, our study has two goals: 1) to provide the first estimate of THFF over coherent mesoscale eddies globally at smaller spatial scales than previously evaluated and 2) to evaluate if THFF is dependent on the ratio of ocean-atmosphere resolution in coupled models. The estimates are obtained for coupled eddy-resolving and eddy-permitting simulations from the HadGEM3-GC3.1 model. The configura-

tions and methods are introduced in section 4.4. Section 4.5 presents the published results addressing the two goals, section 4.6 presents additional unpublished results and section 4.7 concludes and discusses implications for future research and model development.

4.4 Materials and Methods

4.4.1 Model data

We use output from the high-resolution global coupled climate model, HadGEM3-GC3.1 (Williams et al., 2018). The model simulations follow the CMIP6 High-ResMIP protocol, as part of PRIMAVERA (Haarsma et al., 2016; Roberts et al., 2019). Three configurations with a different ratio of ocean-atmosphere resolution are compared: N512-12 ($\sim$25 km atmosphere, 1/12° ocean), N216-12 ($\sim$60 km atmosphere, 1/12° ocean) and N216-025 ($\sim$60 km atmosphere, 1/4° ocean). Model outputs are obtained after a 20-year spin-up, and one year of daily data is used (the results are independent of the year chosen).

To compute air-sea latent and sensible heat fluxes, the OASIS3-MCT coupler passes the ocean model SST to the atmospheric grid using a second-order conservative interpolation (Valcke, 2013; Valcke et al., 2015; Hewitt et al., 2011). Here, we define the turbulent heat fluxes (THF) as the sum of latent and sensible heat fluxes, using the convention that positive THF denotes fluxes upwards from the ocean to the atmosphere. In the following, surface air temperature is taken at 1.5 m and the SST on the ocean grid (SST_O) is distinguished from the regridded SST on the atmospheric grid (SST_A).

4.4.2 Eddy tracking and compositing

From SSH outputs from the model simulations, closed coherent mesoscale eddies are identified and tracked daily in the global ocean for 20 years from SSH, using an eddy tracking algorithm adapted from Mason et al. (2014), which is originally based

on Chelton et al. (2011). Briefly, the algorithms detects closed SSH contours around SSH maximum/minimums. Eddy detection is also subject to certain criteria such as a shape test, i.e. how circular an eddy is. For further details of how the algorithm works, its adaptations and a model comparison to observations, the reader is referred to Chapter 3. The latter also provides a comparison with altimeter-based results (Ducet et al., 2000). It shows that the observational product likely overestimates the eddy radii because of the processing involved in generating a gridded dataset from the satellite tracks.

To isolate mesoscale anomalies, a 10-year climatological mean is removed from the fields, which are subsequently high-pass filtered, by removing a low-pass field obtained by a Gaussian filter of widths 20° (zonal) by 10° (meridional) (same filter as applied to the SSH for eddy tracking). Following Frenger et al. (2013); Hausmann and Czaja (2012); Villas Bôas et al. (2015), 'composite averaging' is used to remove high-frequency variability associated with weather. High-pass filtered anomalies centered on each eddy are first resized by the effective eddy radius L_{eff} before averaging. L_{eff} is defined as the radius of a fitted circle with the same area as the outermost closed SSH contour in each tracked eddy. Rotating the anomalies (to align with background SST or wind direction) before averaging makes little difference to our results.

Finally, the eddies and their associated fields are binned according to their eddy amplitude A, defined as the absolute difference between either the maximum (anticyclones) or minimum (cyclones) SSH and the value of the outermost closed SSH contour of the tracked eddy, from 3$\pm$0.05 cm (small-amplitude) to 34$\pm$6 cm (large-amplitude). This process selectively partitions the eddies to form a sample. A global map of the averaged absolute A per 1° squared is shown in Fig.4.1. As expected, larger amplitude eddies are concentrated in eddy-rich regions, such as WBCs and the Southern Ocean. Note eddy amplitudes are comparatively much smaller in the Eastern Boundary Upwelling Systems. The number of eddy snapshots in each amplitude bin is given in Table 4.1.

Fig. 4.2 shows composites of SST_O and THF from large-amplitude eddies,

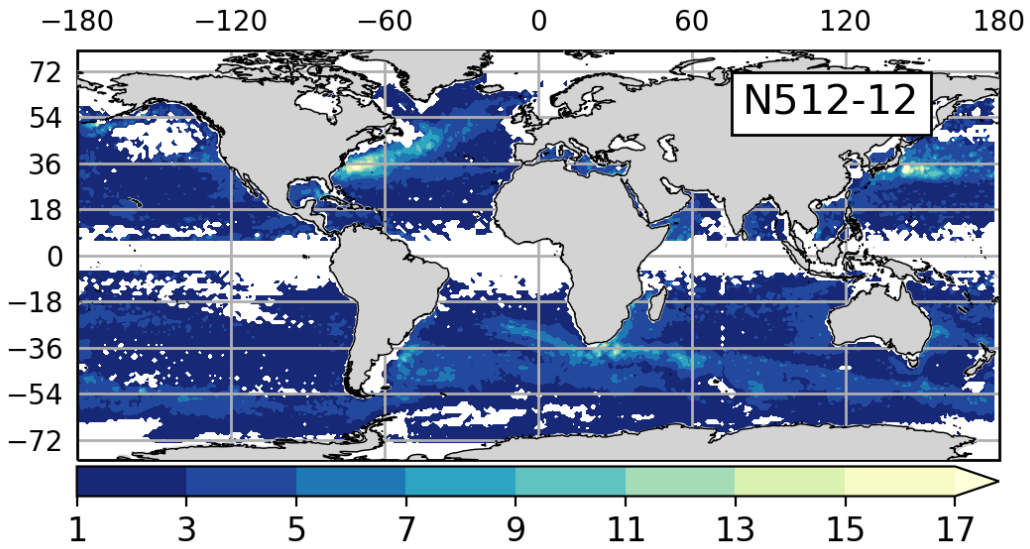

Figure 4.1: *The spatial distribution of eddy amplitudes in N512-12 for eddies lasting longer than 1 week (binned to 1°× 1° grid boxes).*

while a replica for small-amplitude eddies is found in Fig.4.3. Stippling indicates values which are not statistically significant from zero (using student's t-testing with a 99% confidence level). Note that closed contours of the composite anomaly are found beyond one L_{eff}: this is because L_{eff} is identified on individual eddies, while the composite averages remove much of the noise revealing close contours beyond L_{eff}. It is noted that eddy amplitude and eddy radius are not strongly related (Chelton et al., 2011; Moreton et al., 2020). Instead, eddy amplitude (A $\leq$25 cm) is linearly related to SST anomalies, as shown in Fig. S3 A and in previous studies (Villas Bôas et al., 2015).

An accurate comparison of eddy composites from the model to observations is difficult, due to the coarser resolution found in observations and differences in either how the SSH anomalies are isolated (i.e. by standard deviation of SSH anomalies or eddy tracking), the eddy tracking algorithm or the scales retained in the high-pass filtering. Despite this, the SST_O composites in the model have similar magnitudes and spatial distributions to previous observational case studies (Gaube et al., 2015; Hausmann and Czaja, 2012; Frenger et al., 2013; Sun et al., 2020). For all reso-

Eddy amplitude (cm)	Type	N216-025	N216-12	N512-12
3±0.05	A	5051	6732	6179
	C	4300	6084	5734
5±0.05	A	1891	2555	1709
	C	2232	2998	2367
7±0.1	A	1579	2215	1132
	C	2142	3119	2021
9±0.2	A	1513	2122	1020
	C	2142	3158	1793
11±0.5	A	1773	2582	1118
	C	3440	4702	2254
13±0.5	A	1153	1458	1015
	C	1926	2799	1349
15±1	A	1254	1909	1257
	C	2546	3556	1704
19±1	A	1212	1537	1247
	C	2151	2858	1308
24±4	A	1197	1224	1002
	C	1934	2427	1062
34±6	A	1068	1048	1380
	C	1299	1355	1848

Table 4.1: *Global number of eddy snapshots for each eddy amplitude bin in cm, for each model resolution and each polarity. The number of anticyclonic eddies (A) is listed above cyclonic eddies (C) for each bin.*

lutions, maximum SST anomalies of ∼0.6 K are found in eddies of amplitude of 15 cm (i.e. in eddy-energetic regions, Fig. S3A), close to the value of 0.75 K seen in observations (Hausmann and Czaja, 2012).

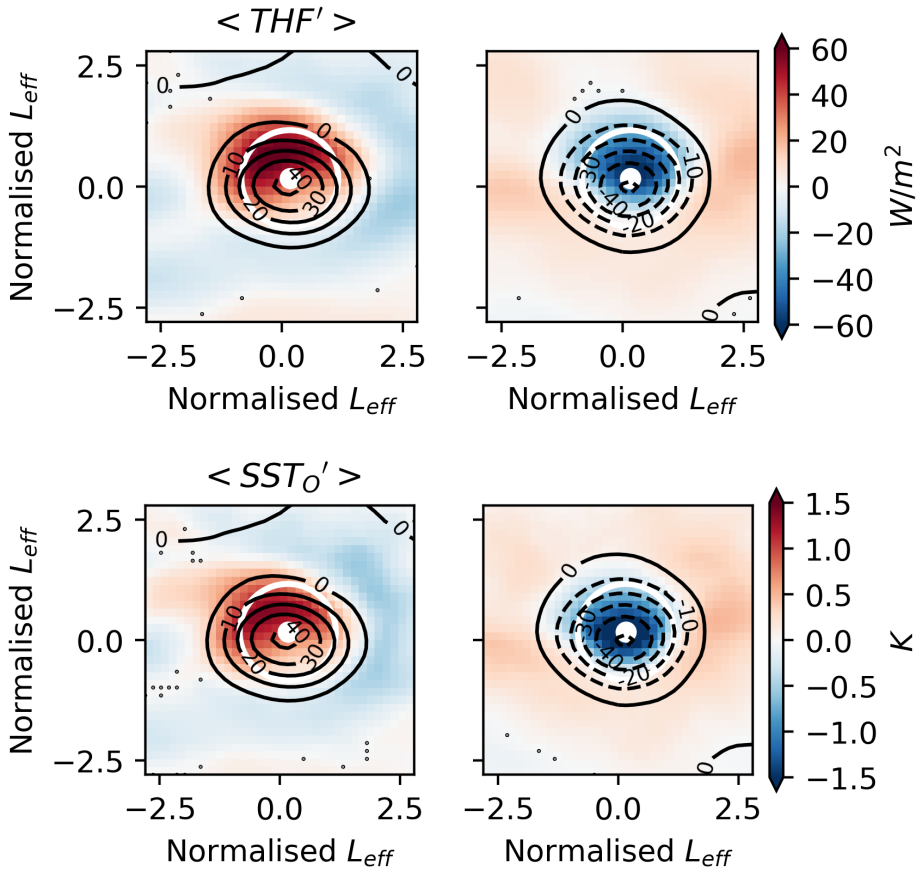

Figure 4.2: *Composite maps of turbulent heat flux THF in* $W\ m^{-2}$ *and SST on the ocean grid* SST_o *in* K *(both in colour) and SSH (black lines, in* cm*) for large-amplitude (A=34±6 cm) eddies from N512-12. Anti-cyclonic warm-core eddies are displayed with a red centre (left), and cyclonic cold-core eddies in blue (right). Solid (dashed) lines indicate positive (negative) values of SSH. The white dot is the centre of each tracked eddy and the white circle is 1 effective eddy radius* L_{eff}*. Values shown with a black dot are not significantly different from zero at the 99% confidence level based on a T-test.*

4.4.3 Decomposition of the turbulent heat flux feedback

The THFF α is defined as:

$$< THF' >= \alpha < SST' > \tag{4.1}$$

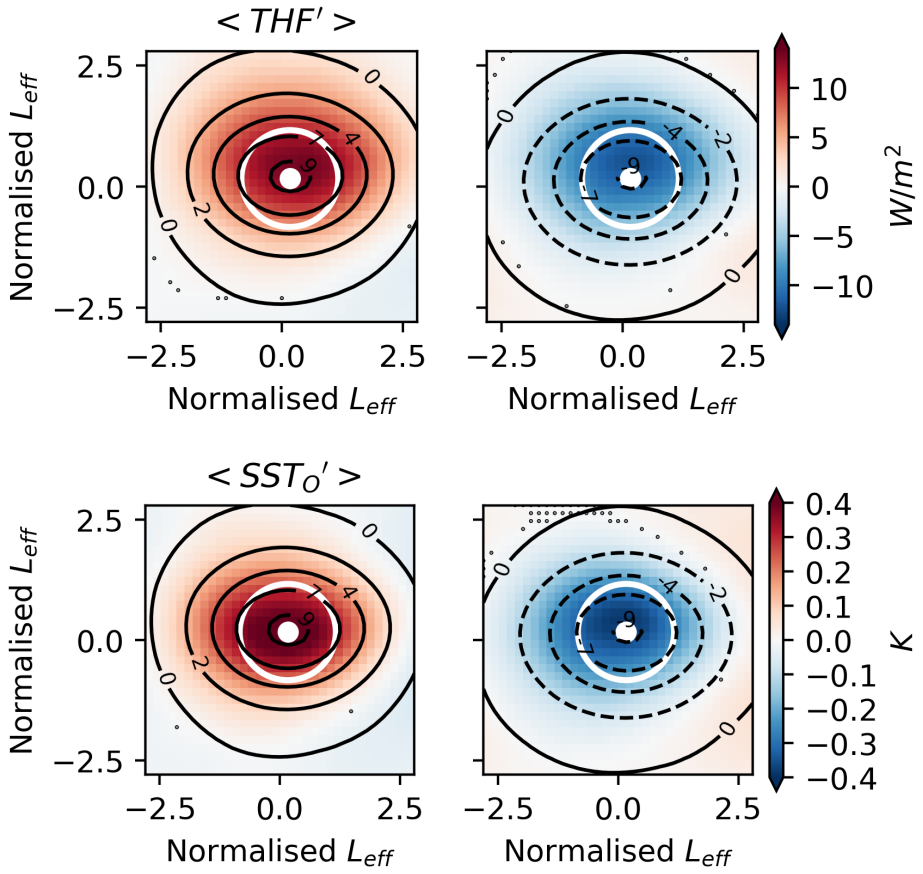

Figure 4.3: *A repeat of Fig. 4.2 for the smallest amplitude eddies from N512-12. Please refer to Fig. 4.2 for plot description.*

where primes indicate the high-pass filtered anomalies, and $< \ . \ >$ indicates the eddy-centric composites computed for all eddies tracked in the SSH model outputs. A positive value of α represents a negative heat flux feedback, i.e. a dampening of the SST anomaly by the THF.

Due to the regridding of SST to calculate air-sea heat fluxes in the coupled model, two THFFs can be computed from either SST_A or SST_O:

$$< THF' > \ = \ \alpha_O < SST'_O > \tag{4.2}$$

$$< THF' > \ = \ \alpha_A < SST'_A > . \tag{4.3}$$

The THFF α_O relates the THF anomalies to the prognostic SST anomalies in the ocean component, while α_A represents the THFF after re-gridding the ocean grid

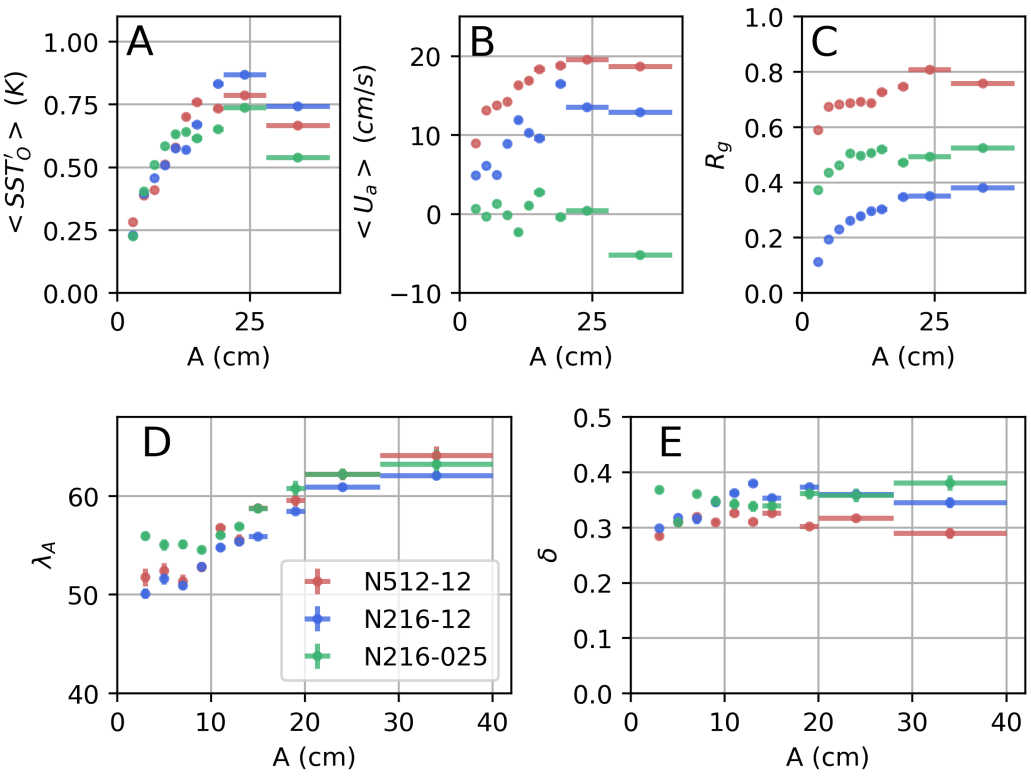

Figure 4.4: *Scatter plots of the absolute SST_O (A, K) and wind speed (B, cm/s) from the averaged eddy composites for each binned eddy amplitude (A, cm). The value plotted is the average within 1 L_{eff}. The regridding R_g, λ_A and δ coefficients are shown in subplots C,D and E respectively (calculated using 1 L_{eff}). Results are shown for each configuration: N512-12, N216-12, and N216-025. Anti-cyclonic and cyclonic eddies are combined using weighted averaging, relative to the number of composites.*

SST to the atmospheric grid (SST_A). Note that α_A does not directly affect the prognostic state of the simulation.

To understand the behaviour of the THFFs α_O and α_A, it is useful to introduce three coefficients λ_A, δ and R_g (Eqs. 4.4-4.6).

$$< THF' > \;=\; \lambda_A(< SST'_A > - < T'_{air} >) \tag{4.4}$$

$$< T'_{air} > \;=\; \delta < SST'_A > \tag{4.5}$$

$$< SST'_A > \;=\; R_g < SST'_O > . \tag{4.6}$$

First, the THF restoring coefficient λ_A is a simplification of the latent and sensible heat flux (LHF and SHF) bulk formulae used in the model (Large and Yeager, 2004). Following Frankignoul et al. (1998) and Hausmann et al. (2017), we assume that the LHF can be linearized to be expressed in terms of the air-sea temperature difference, $T_{air} - SST_A$ (see below). Second, δ measures the adjustment of the surface air temperature T_{air} to the regridded SST anomalies SST_A: when δ equals zero there is no ABL response or adjustment, whilst when δ equals one, a complete adjustment occurs resulting in a zero THF. Third, the R_g coefficient measures the impact of the ocean-to-atmosphere regridding on the SST magnitude. If R_g equals one, the magnitude of the SST anomaly peak is preserved during the regridding.

By isolating THFF based on SST_O (α_O) or based on re-gridded SST (α_A), we can provide an estimate for how the THFF is affected by the ratio of ocean-atmosphere resolution in coupled models. By re-arranging Eqs. (4.4) to (4.6), relationships between the coefficients can be derived, in order to trace changes from the THF restoring coefficient λ_A to α_O:

$$\alpha_A \;=\; (1-\delta)\,\lambda_A \tag{4.7}$$

$$\alpha_O \;=\; R_g\,\alpha_A \tag{4.8}$$

The THFF α_A is scaled down from λ_A by the air temperature adjustment in the ABL (Eq. 4.7). When the ABL temperature adjustment is weak (i.e. $\delta \sim 0$), α_A is close to the restoring embedded in the THF bulk formulae (i.e. λ_A here). Whilst when the adjustment is strong, the THFF α_A, and subsequently the dampening of SST anomalies, is much smaller than predicted by λ_A (Frankignoul et al., 1998). In other words, the coefficient λ_A represents an upper bound for α_A, which is achieved when air temperature adjustment (δ) is zero. This upper bound is the "fast limit" discussed by Hausmann et al. (2017).

The THFF using ocean model SST (α_O) is reduced from α_a by the SST regridding coefficient R_g (Eq. 4.8). It is anticipated that R_g is smaller than 1 and therefore that α_O is biased low compared to α_A.

In practice, the above coefficients are estimated over coherent mesoscale eddies through linear regressions between data from the composite maps. To remove variability occurring outside the detected eddies (Fig. 4.2), only data within a square of 2 $L_{eff}\times$ 2 L_{eff} is used in the linear regressions. Sensitivity to this choice will be discussed. Regressions for anti-cyclonic and cyclonic eddies are calculated separately, and a weighted average is calculated, using the number of anticyclonic and cyclonic eddies, to produce a total value (given as text in Fig. 4.5). The gradients of linear regression are dependent on $SST_{O/A}$ being on the x-axis. Assuming a normal distribution of data and using the student's t-test, 95% confidence intervals are supplied in Fig. 4.5 and 4.8.

4.5 Results

First the THFF coefficients, α_A and α_O, are discussed for the N512-12 configuration. This configuration is presented first because it is the least affected by regridding biases (section 4.5.1). A comparison to N216-12 and N216-025 configurations follows, to evaluate the impact of changes in the ratio of ocean-atmosphere resolutions on the THFF (section 4.5.2).

4.5.1 Estimating THFF over large-amplitude mesoscale eddies

Fig. 4.5 illustrates the relationships between the composite fields for the large amplitude eddies (A=34$\pm$6 cm) globally in N512-12. A repeat of the relationships for small-amplitude mesoscale eddies (A=3$\pm$0.05 cm) is shown in Fig. 4.6. The estimated coefficients $\alpha_{O/A}$, λ_A, δ and R_g from Eqs. 4.2-4.6 (rounded to 1 decimal place) are indicated in each panel with a corresponding 95% significance confidence interval.

There is a strong linear relationship between the composite anomalies of THF and air-sea temperature contrast (Fig. 4.5A). This supports the linearization of LHF underlying Eq. (4.4) (further supported is provided by a 0.98-0.99 correlation be-

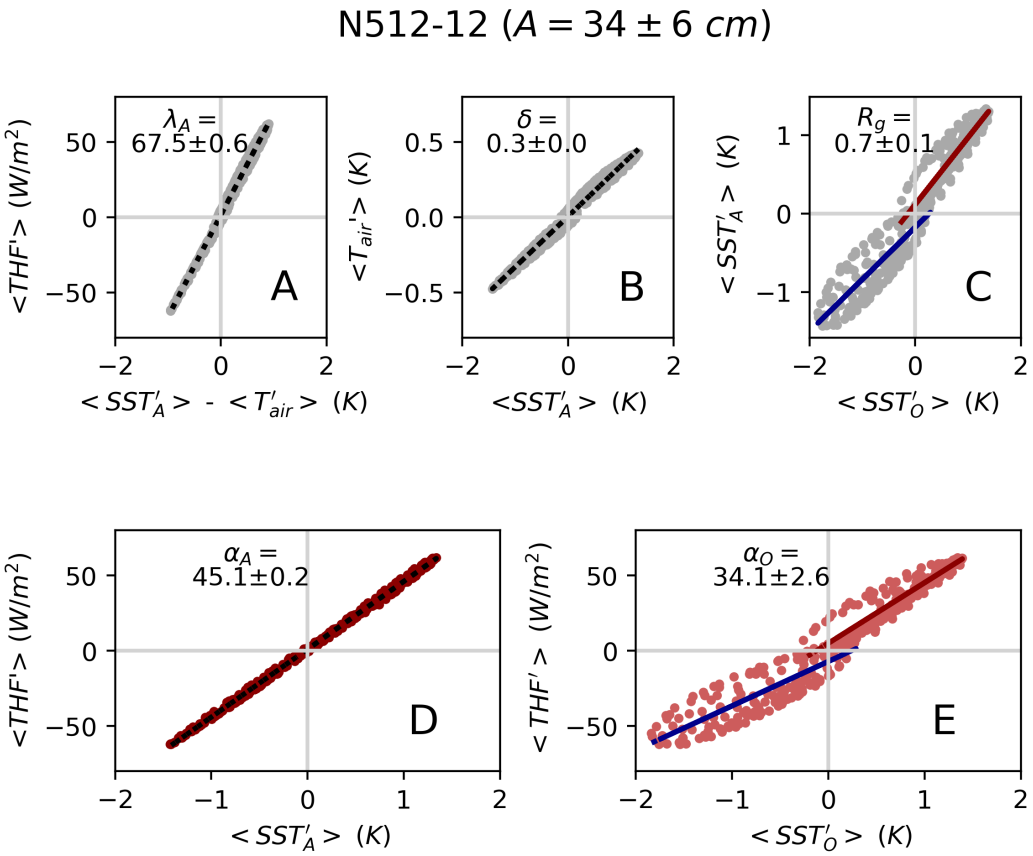

Figure 4.5: *Relationships between the composite fields of $SST_{O/A}$, THF and T_{air}, with the estimated coefficients ($\alpha_{O/A}$, λ_A, δ and R_g) rounded to 1 decimal place for the larger amplitude eddies (A=34±6 cm) globally in N512-12. The estimates indicated in each panel combined cyclonic and anticyclonic eddies as indicated in section 4.4. In subplots C and E, the regression lines for anticyclonic and cyclonic eddies are plotted in red and blue respectively.*

tween SST and the 1.5 m specific humidity Q_{air} over coherent eddies – not shown). The robust estimate of λ_A at 67.5 ± 0.6 W m^{-2} K^{-1} is larger than the $\sim$50 W m^{-2} K^{-1} estimate in Frankignoul et al. (1998) and Rahmstorf and Willebrand (1995) and the upper bound of 25-35 W m^{-2} K^{-1} of Hausmann et al. (2017). This discrepancy could reflect differences in the estimation methods. Published estimates are based on the linearization of bulk formulae using constant drag coefficients and monthly-mean large-scale winds. In contrast, our estimates (Fig. 4.5A) implicitly account

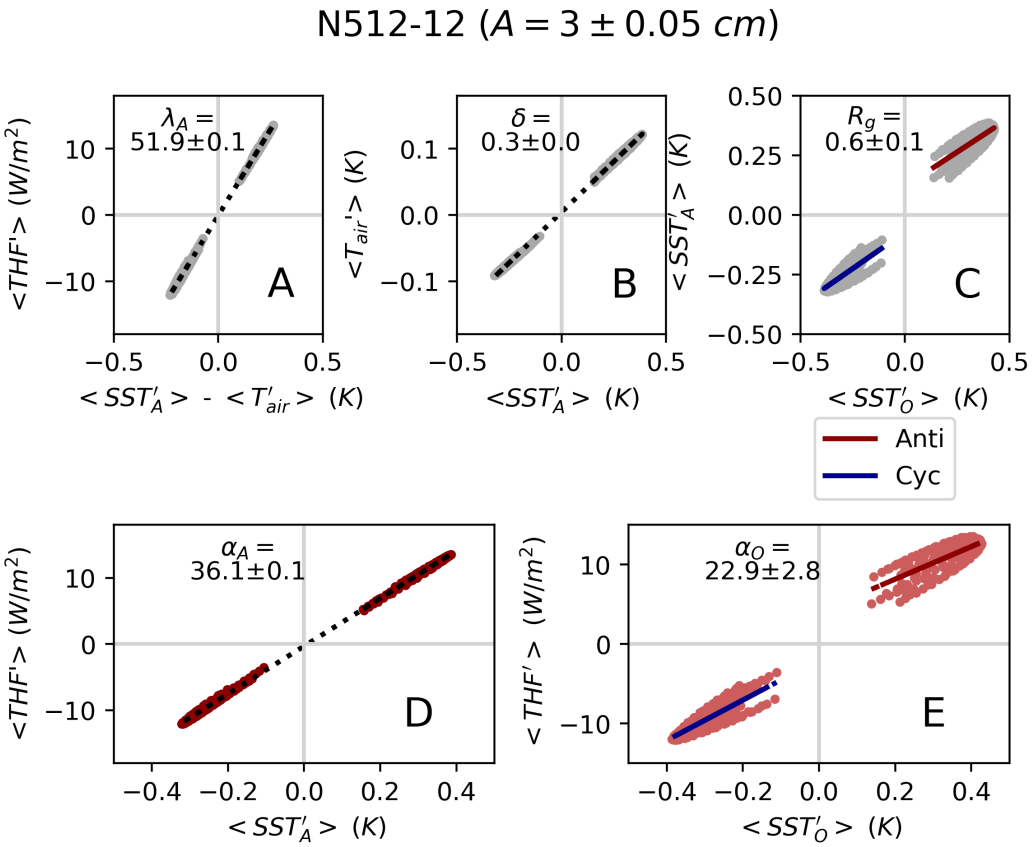

Figure 4.6: *A repeat of Fig. 4.5 for the smallest amplitude ($A = 3 \pm 0.05$ cm) eddies from N512-12.*

for 1) the full complexity of the bulk formulae implemented in HadGEM3-GC3.1 (see equation 2.8 and 2.9) where the drag coefficient is function of ABL stability and surface winds (Hewitt et al., 2011) and 2) dynamical adjustments in the ABL such as the modulation of surface winds by mesoscale eddy SST anomalies (Roberts et al., 2016; Frenger et al., 2013).

The atmospheric adjustment parameter δ is estimated at 0.34±0.01 for large amplitude eddies globally (Fig. 4.5B), i.e. the surface air temperature T_{air} anomaly is about a third of the mesoscale SST anomaly. Previous studies give 0.5 in the WBCs and the Antarctic Circumpolar Current (ACC) core, increasing to 0.9 in quiescent regions (Hausmann et al., 2017). However, these estimates are limited by the scale of ERA-I reanalysis (0.75×0.75°) and do not isolate coherent eddies. Although

the modelled large-amplitude eddies used in Fig. 4.5 are mostly found in WBCs (Fig. 4.1) our estimate suggests that T_{air} adjustments drop further below 0.5 over coherent mesoscale eddies.

The value of α_A ($\sim$45 W m^{-2} K^{-1}, Fig. 4.5D) can now be explained by combining estimates of λ_A and δ using Eq. (4.7): $\alpha_A \simeq$(1 - 0.34)$\times$67.5 $\simeq$ 44.5 W m^{-2} K^{-1}. As most large-amplitude eddies are found in the WBCs, our modelled estimate of α_A agrees well with previous observational estimates of 40-56 W m^{-2} K^{-1} in the Kuroshio region and 40 W m^{-2} K^{-1} in the Gulf Stream (Ma et al., 2015; Hausmann et al., 2016). Finally, the THFF on the prognostic SST, α_O, is about 25% smaller than α_A at 34.1$\pm$2.6 W m^{-2} K^{-1} (Fig. 4.5E). The reduction reflects the 25% decrease in the amplitude of mesoscale SST anomalies brought by the SST regridding ($R_g \simeq 0.74$, see Eq. (4.8); Fig. 4.5C).

Whilst the coefficients λ_A, δ and α_A exhibit a very small scatter, the scatter in α_O is significant, and can be attributed to the regridding between SST_A and SST_O, R_g (Fig. 4.5). This results in an uncertainty in α_O of about $\pm 2 - 3$ W m^{-2} K^{-1} (found consistently across all eddy amplitudes, and all resolutions). Interestingly, a small asymmetry between cyclonic and anticyclonic eddies in α_O can also be attributed to R_g (Figs. 4.5 and 4.6), potentially due to slight differences in magnitude of the eddy anomaly. It therefore appears that the regridding, even in the most favorable case of near matching resolutions, is a source of noise and non-linearities. Fig. 4.5 is repeated in Fig. 4.7 using data from the whole composited region shown in Fig. 4.2, i.e. a $5.6\ L_{eff} \times\ 5.6\ L_{eff}$ square. The asymmetry between polarities vanishes, which suggests this is not a robust feature, but possibly an artefact from the tracking algorithm and/or the regridding process. We do not investigate this asymmetry further.

The rationalization of the THFF α_A and α_O developed above for large-amplitude eddies applies equally well to small-amplitude eddies (see Fig. 4.6). We therefore present variations of α_A and α_O as a function of eddy amplitude A in N512-12 (Fig. 4.8A). To first order, the THFF increases with eddy amplitude (and hence with mesoscale SST anomalies, see Fig. 4.9). From a minimum THFF of $\sim$35-

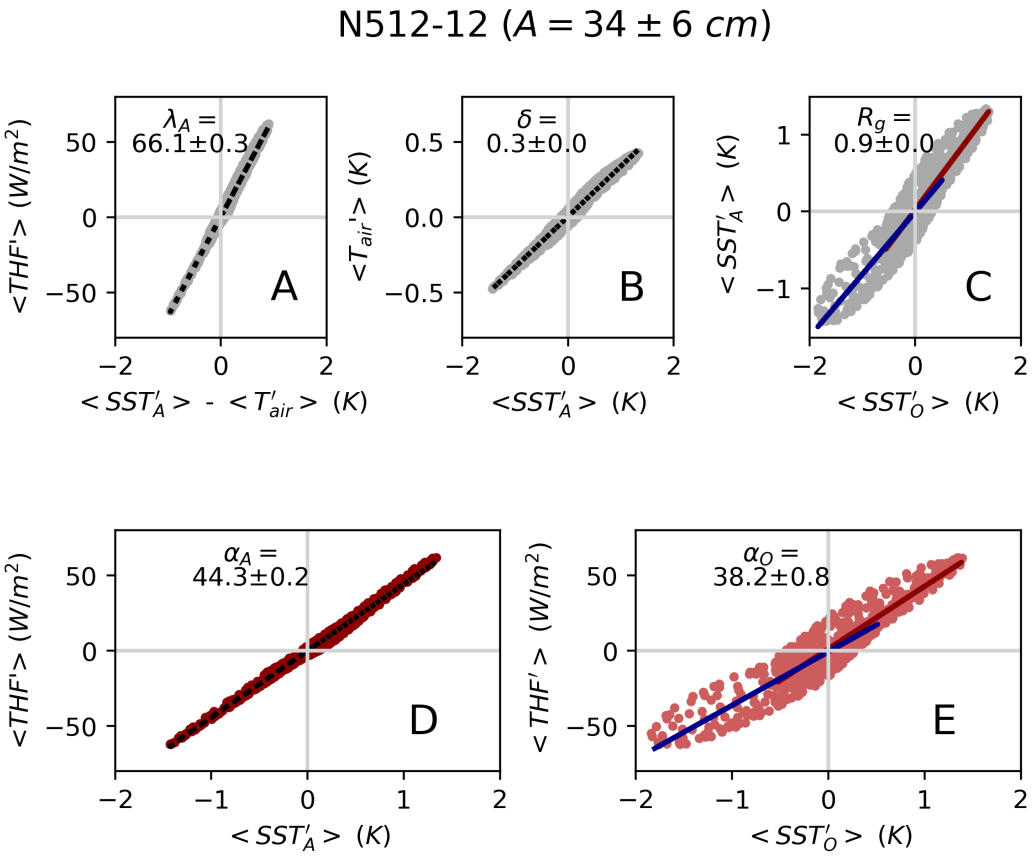

Figure 4.7: *A repeat of Fig. 4.5 for large-amplitude eddies from N512-12, using data from the whole composited region shown in Fig. 1, i.e. 2* $\times 2.8\ L_{eff} \times$ *2* $\times 2.8\ L_{eff}$ *square.*

38 W m^{-2} K^{-1} at 3-5$\pm$0.05 cm, α_A increases to around 45 W m^{-2} K^{-1} at 34$\pm$6 cm.

Referring to Eq. (4.7), variations in α_A are mainly driven by changes in the THF restoring λ_A whilst the atmospheric adjustment δ is relatively insensitive to eddy amplitude (compare Fig. 4.4 D and E). The restoring coefficient λ_A roughly increases with the eddy amplitude, or equally with the eddy SST anomaly as the two are strongly correlated (see Fig. 4.4 A). This likely reflects non-linearities embedded in the bulk formulae. One such non-linearity is the effect of the surface wind speed. As highlighted in previous studies (e.g. Roberts et al., 2016, and references therein), the ABL response to mesoscale SST anomalies includes a surface wind speed response proportional to the mesoscale SST anomalies. Here, we con-

firm that, as expected, the wind speed anomaly increases with the eddy amplitude (Fig. 4.4 B). This effect contributes to strengthen the air-sea exchanges λ_A over large eddies. However, it is likely that other non-linearities play a role (as suggested by results for other configurations, see below).

Variations in α_O generally follow those of α_A except at the smallest amplitudes where R_g decreases from 0.8 to about 0.6 (Fig 4.4 C in red for N512-12).

4.5.2 Impact of the ratio of ocean-atmosphere resolution on THFF

Fig. 4.8 summarizes estimates of α_A and α_O for each model configuration. For each configuration, the variation of α_A with amplitude are similar, which is unsurprising because the bulk formulae within α_A is the same in all atmospheric components, and both λ_A and δ are relatively insensitive to the resolution (see Fig. 4.4 D and E). However, in N216-12 and N216-025 the increase of α_A (through λ_A) with eddy amplitude is slightly smaller, compared to N512-12. This is consistent with a weaker surface wind response in N216-12 and N216-025 (Fig. 4.4 B). The near absence of a surface wind response in N216-025 suggests that other non-linearities such as the dependence of drag coefficient on temperature and ABL stability, contribute to the dependence of λ_A on the eddy amplitude/SST.

In contrast, α_O depends greatly on the difference between the oceanic and atmospheric grid resolutions: α_O is biased low relative to α_A by about 10, 20, and 25 W m^{-2} K^{-1} in N512-12, N216-025 and N216-12, respectively. In N216-12, the low bias reaches about 30 W m^{-2} K^{-1} for the small amplitude eddies ($<$5 cm).

Across all configurations and binned by eddy amplitude, the relative change between α_O and α_A exhibits a strong linear correlation with the regridding parameter R_g (Fig. 4.8D), with a slope of $\sim$1 as predicted by our simplified relationships (see Eq. 4.8). This reinforces our interpretation that the regridding of SST (captured by R_g) plays a fundamental role in determining α_O's low biases. The difference between α_O and α_A increases with R_g from 20-40% for N512-12, to 40-60% for N216-025 and to approximately 60-80% for N216-12. Crucially, the

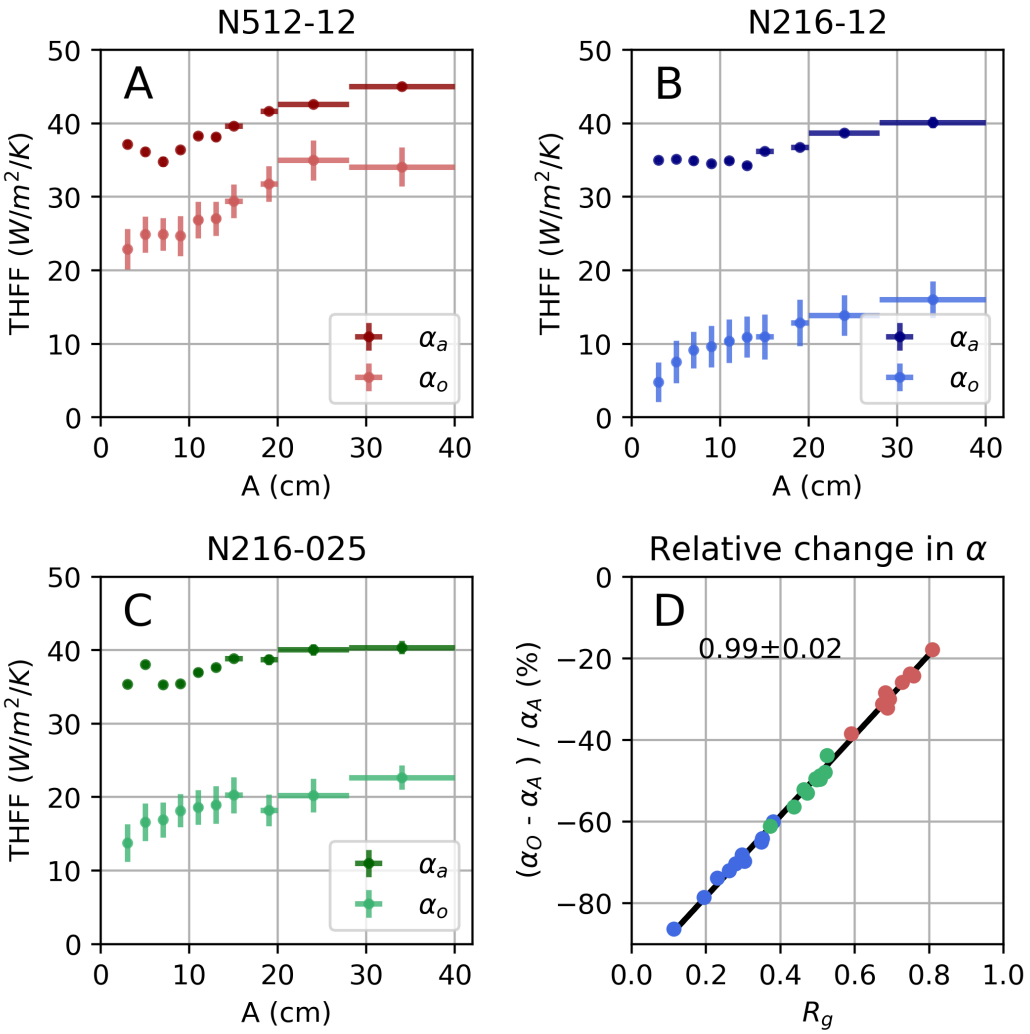

Figure 4.8: *THFF α_A and α_O (in W m^{-2} K^{-1}) as a function of the eddy amplitude (in cm) for A) N512-12, B) N216-12 and C) N216-025. THFF are calculated using data within a square of 2 L_{eff}× 2 L_{eff}. The horizontal bars indicate the width of the eddy amplitude bins, and the vertical error bars indicate the 95% confidence intervals (± 2.5 W m^{-2} K^{-1} for α_O averaged across all resolutions and amplitudes). D) The relative change between α_O and α_A (in %) as a function of R_g for all eddy amplitudes and all model configurations (the color coding indicates the configuration, as in panels A), B) and C). The gradient of the linear regression line is added as text, to be compared with the theoretical slope of 1 – see Eq. (4.8).*

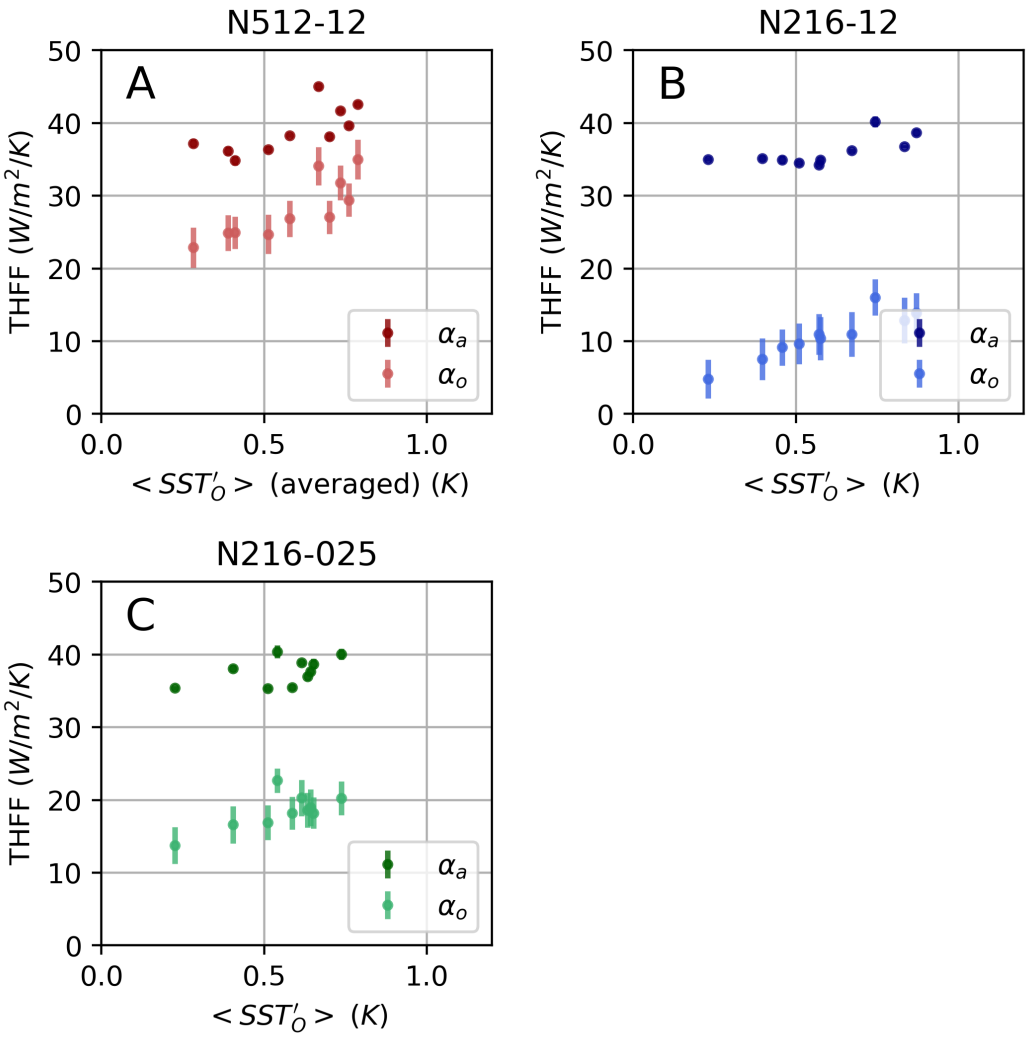

Figure 4.9: *A repeat of Fig. 4.8 plotting α_O and α_A as a function of the maximum SST_O anomaly, instead of eddy amplitude, for each configuration, N512-12, N216-12 and N216-025.*

low bias is the largest for the smaller amplitude eddies, which cover most of the global ocean in the configuration with the largest ratio between atmospheric and oceanic resolutions, N216-12. The typical eddy scale of small amplitude eddies (L_{eff} ≈40 km on average) is smaller than the atmospheric grid-scale in N216-12 (∼60 km), but larger in N512-12 (∼25 km), resulting in a minimal distortion from SST_O to SST_A (Fig. 4.8A). Regridding of SST_O reduces the amplitude of the mesoscale SST anomalies and creates an apparent spatial shift between SST_O

and SST_A (Fig. 4.10), creating a spatial mismatch between the heat flux (computed from SST_A) and the prognostic SST SST_O.

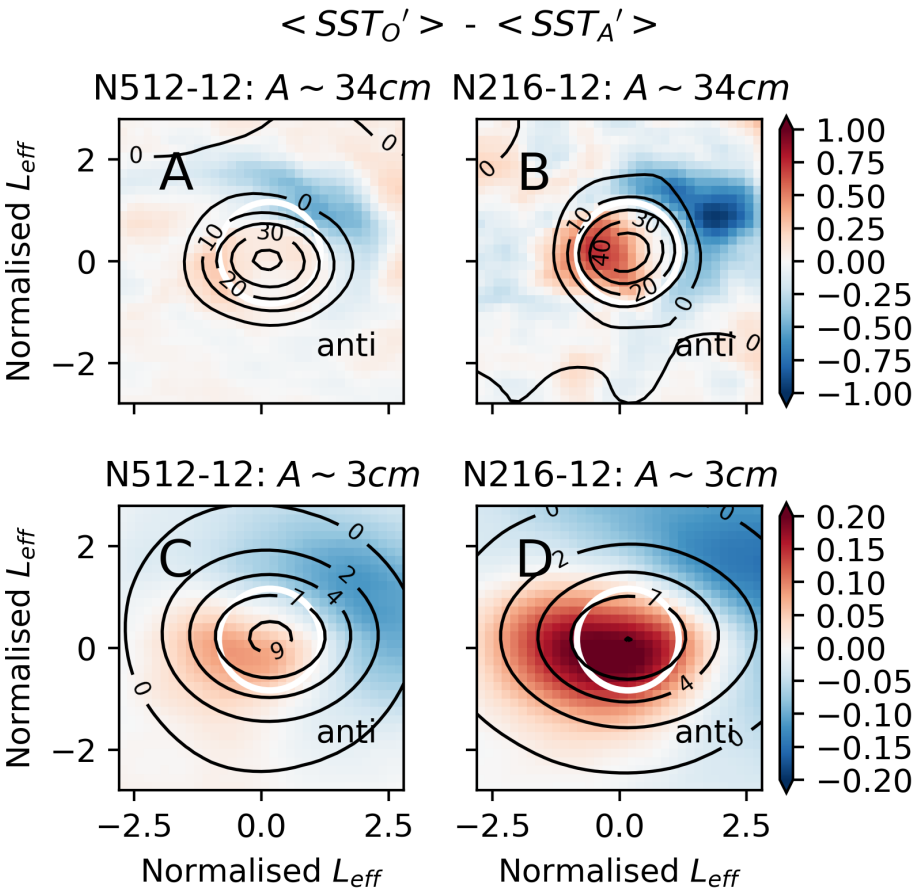

Figure 4.10: *The averaged difference in SST (K) for large- ($A \sim 34\ cm$) and small-amplitude ($A \sim 3\ cm$) anti-cyclonic eddies in N512-12 and N216-12, as labelled. Note a similar magnitude and spatial distribution is seen for cyclonic eddies, and the difference in SST is calculated first for each snapshot, then averaged.*

4.6 Additional Unpublished Results

In complement to the work above, the following five sections present additional unpublished results. Section 4.6.1 discusses the correlation between SSH and SST anomalies, which is fundamental to understanding the THFF, while section 4.6.2 demonstrates the impact of SST anomalies on the atmospheric boundary layer in N512-12 compared to observations. Section 4.6.3 compares LHFF and SHFF, including a discussion of the validity of LHFF in our coefficient λ_A, section 4.6.4 explains the statistical significance testing used throughout this chapter and finally, section 4.6.5 calculates the THFF using a Eulerian perspective i.e. fixed locations.

4.6.1 Relating SSTA, SSHA and eddy shape

The strong positive correlation between the SSH and SST anomalies is fundamental to understand why the THFF depends on eddy amplitude. The correlation between SST and SSH anomalies can be explained using the thermal wind equation (equation 4.9), where surface density fluctuations are compensated at a depth, H.

$$\frac{\partial U}{\partial z} = \frac{g}{f\rho_0}\frac{\partial \sigma}{\partial y} \tag{4.9}$$

where U is geostrophic velocity, f is the Coriolis parameter, ρ_0 is the reference density at a constant depth and σ is the horizontal density anomaly. Using the linear equation of state to make σ dependent on temperature changes ($\sigma = \rho_{ref} - \alpha_T\, T'$) and by assuming horizontal (y-direction) variations in the density anomaly are constant when integrating in across depth, equation 4.9 can be rearranged to:

$$\frac{U}{H} \approx \frac{g}{f\rho_0}\frac{-\alpha_T\, T'}{L} \tag{4.10}$$

where depth H is assumed to be at the main thermocline at 1000 m, α_T is a constant coefficient (2×10^{-4} K^{-1}), T' is the surface temperature anomaly and L is the horizontal length of the temperature anomaly.

By substituting the hydrostatic equation into the geostrophic balance equation, velocity (U) can be expressed as a function of the SSH anomaly (η' in metres) as

$U = \frac{g}{f}\frac{\eta'}{L}$, as shown in Chapter 3.6.1. By substituting this equation into equation 4.10, the relation between surface SSH and SST anomalies can be simplified to the following.

$$\frac{\eta'}{\alpha_T H} \approx T' \tag{4.11}$$

This approximation works well within composite-averaged coherent mesoscale eddies. For small-amplitude eddies (A $\approx$ 3 cm) a maximum SSH anomaly of 9 cm predicts a maximum SST anomaly of 0.45 K, as seen in Fig. 4.1 after globally and temporally averaging. Composite-averaged anti-cyclonic eddies provide a maximum SST anomaly of 0.43 K, while cyclonic eddies slightly underestimate at the prediction with a maximum absolute value of 0.39 K. Note the large discrepancy between the eddy amplitude and SSH anomaly, was discussed in Chapter 3.6.1, Fig. 3.24, and is a result of the eddy tracking algorithm not capturing the full eddy shape.

The close relationship between SST and SSH anomalies reduces slightly at the large-amplitude eddies, as seen in Fig. 4.4A between eddy amplitude and SST anomalies. For the largest-amplitude eddies (A $\approx$ 34 cm), a SSH anomaly of 40 cm predicts a SST anomaly of 2 K. Our spatial- and time- averaged composites slightly underestimate this value with a maximum SST anomaly of 1.39 K in anti-cyclones and an absolute maximum value of 1.84 K in cyclones. This slight underestimation is assumed to be a result of variability in the depth of the main thermocline globally and over the course of the year. In reality, dampening from air-sea interaction is likely to reduce the SST estimates, making them more similar to the magnitudes of the composites. Furthermore it should be highlighted these large- amplitude eddies are confined to a small region in the core of the WBC jets in either the Kuroshio Current or Gulf Stream (Fig. 4.9). Perhaps the background SST field plays a greater role in determining the SST anomaly in these small areas.

A very strong positive Pearson's correlation coefficient between SSH and SST anomalies is found at 0.99 (to 2 decimal places) within and around the tracked eddies (5.6 $\times L_{eff}$) for each polarity and amplitude size. Indeed the correlation co-

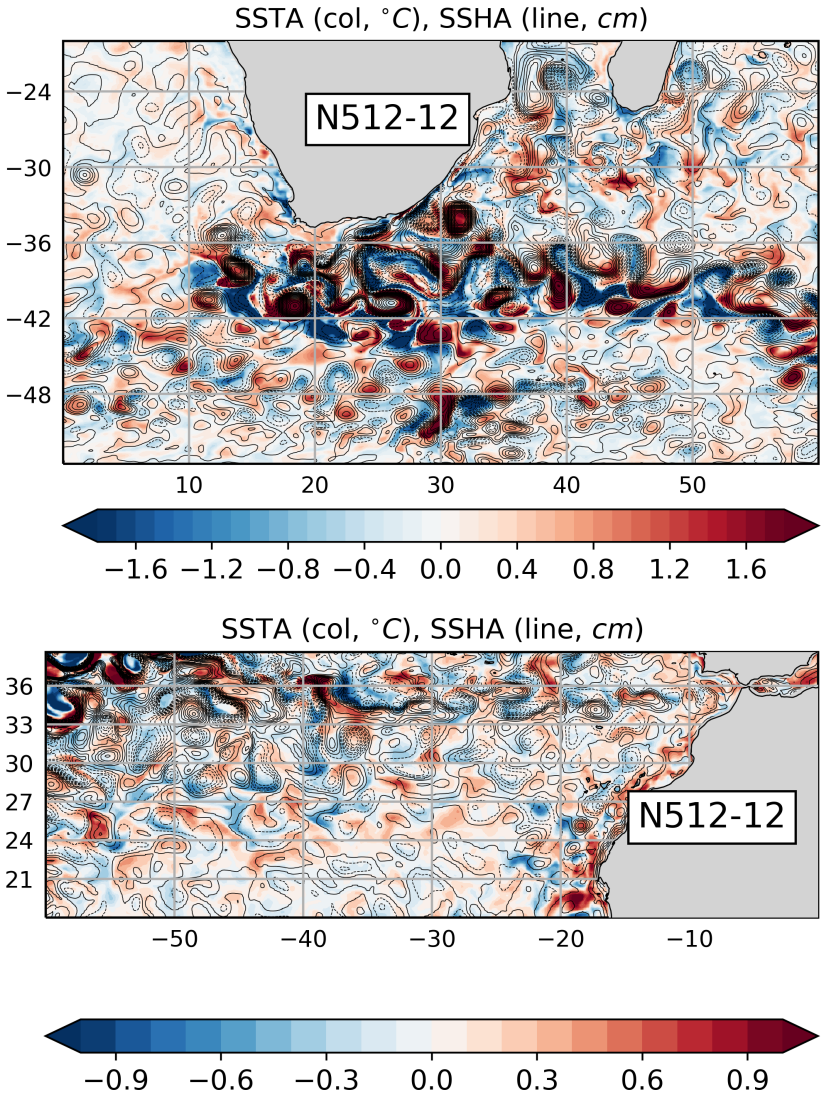

Figure 4.11: *An example of both SST anomalies (background colour) and SSH anomalies (black lines) in the Agulhas retroflection (upper subplot) and in the open ocean west of North Africa (lower subplot) from a daily snapshot in N512-12. The SSH contour line interval is 5cm and negative SSH anomalies are plotted as dotted lines.*

efficient between all mesoscale SST and SSH anomalies, beyond individual eddies, in the model is very strong at 0.99 in both the eddy-rich Agulhas region and in the open ocean west of Northern Africa. The spatial distribution of anomalies is shown in Fig. 4.11. The black lines are SSH anomalies and the background colour

represents SST anomalies.

Despite the strong correlation, it should be highlighted positive 'warm-core' eddy SST anomalies are not always within anti-cyclonic eddies (Ding et al., 2020; Liu et al., 2020). Leyba et al. (2016) argue that the anomalies are, instead, dependent on the SST background field (as shown in the south-west Atlantic). An example of this is seen in the open ocean (lower subplot in Fig. 4.11) where the polarity of SSH anomalies are not aligned with the polarity of SST anomalies. When sampling a small number of eddy snapshots, this has the potential to bias the THFF estimates too low. These mismatches in SST and SSH anomalies are rare and not significant when averaging globally, for any amplitude bin used in the study above.

A discussion of eddy shape begun in Chapter 3. Most eddies (especially at the smallest-amplitudes) were shown to differ from a Gaussian shape within 1 L_{eff}. Here, we extend this analysis to compare the spatial structure of the SST anomaly within and surrounding 1 L_{eff}.

As shown in Fig. 4.2, a mono-pole spatial structure is found within large-amplitude stable/ mature modelled eddies, similarly to previous observational studies (Hausmann and Czaja, 2012; Frenger et al., 2015). In most of the ocean, differences between the surface current and overlying wind stress control the net surface stress and drive Ekman pumping anomalies within the eddy interior, which act to dampen an eddy (Gaube et al., 2015). In addition, in eddy-energetic regions, such as at WBCs where the largest amplitude eddies are located, crosswind mesoscale SST gradients generate a curl of the surface stress, which competes against the surface wind to induce Ekman pumping anomalies, as explained in Chapter 1.3.1 (Chelton et al., 2004; O'Neill et al., 2010). This mechanism is sometimes called 'linear Ekman pumping', and produces the monopole structure of SST observed in Fig. 4.2.

Instead, for small-amplitude eddies a dipole spatial structure with a phase shift emerges (Hausmann and Czaja, 2012). Within small-amplitude eddies, the surface stress curl induced by mesoscale eddies, opposes the surface current vorticity gradient to create a dipole of Ekman upwelling and downwelling (Gaube et al., 2015; Dewar and Flierl, 1987). This is referred to 'non-linear' Ekman pumping. (Gaube

et al., 2015) argue both 'linear' and 'non-linear' Ekman pumping velocities are comparable in magnitude, but differ in spatial structure as described.

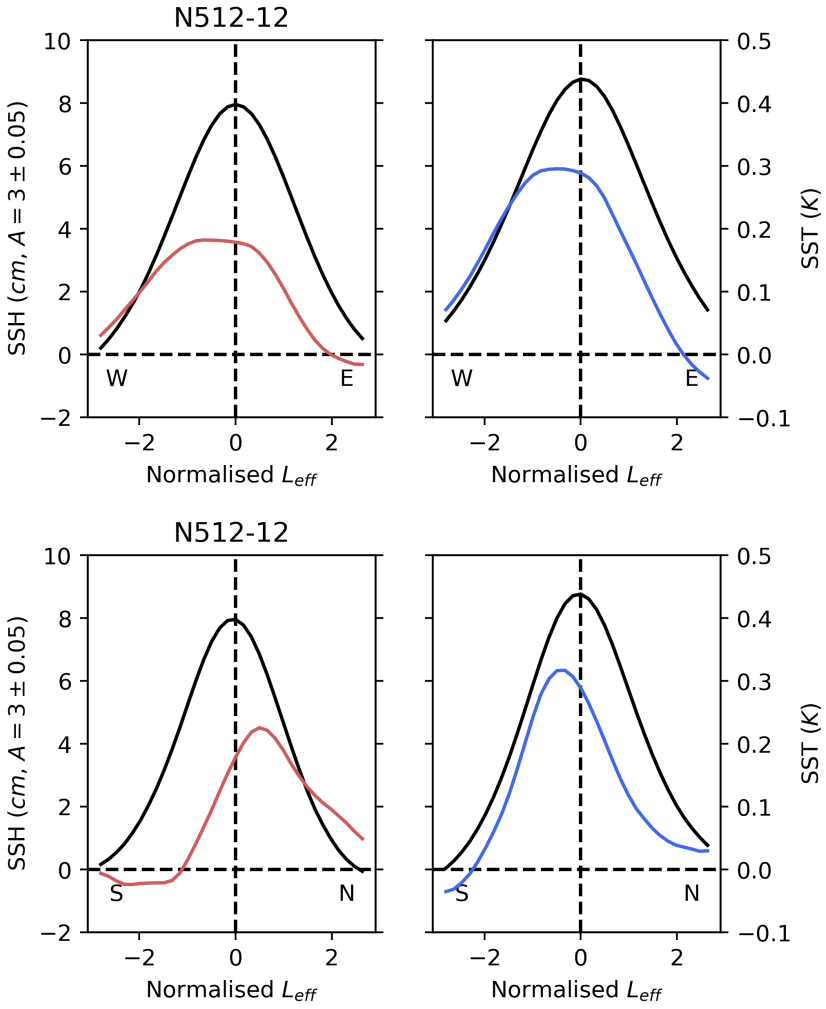

Figure 4.12: *1D slices from composite-averaged small-amplitude eddies in the Northern Hemisphere in N512-12. The solid black line represent SSH anomalies (cm) and coloured lines represent SST anomalies (K) for either anti-cyclones (red) or cyclones (blue). The upper subplots present a 1D slice at the eddy centre in the zonal direction, west to east, while the lower subplots are a slice at the eddy centre in the meridional direction, south to north (as indicated by the black letters in each subplot).*

Despite the strong correlation between SST and SSH, when globally averaging,

it is difficult to observe both the dipole of SST associated with small-amplitude eddies, and the phase shift between the maximum SSH and SST anomaly (Fig. 4.3). Instead, when isolating small-amplitude eddies from the Northern Hemisphere only, a phase shift between the SSH and SST peak does occur. Note, separating each hemisphere is necessary because the dipole spatial structure is opposite in either hemisphere. We assume a similar magnitude of the phase shift is found in the Southern Hemisphere.

Fig. 4.12 presents a 1D slice of small-amplitude eddy composites of SST (colour) and SSH (black solid line) in N512-12 in either the West-East (upper subplots) or South-North (lower subplots) direction across the whole Northern Hemisphere. Anti-cyclonic eddies are plotted in red (left column) and cyclonic eddies in blue (right column). The figure shows the maximum SST anomaly is shifted west of the maximum SSH anomaly, for both polarities, and SST anomalies are shifted either north in anti-cyclones and south in cyclones. These spatial shift between the anomalies in the small-amplitude modelled eddies match shifts in observations (Hausmann and Czaja, 2012), their Fig.5. Although, the magnitudes of SST and SSH anomalies in anti-cyclonic and cyclonic eddies differ slightly between the model and observations, likely because of different spatial filtering techniques. It is suggested the SSH-SST phase difference is explained because the small-amplitude eddies are in a growing mode of baroclinic instability produced by the surface SST gradients, which differ from the flow through depth, which determines the SSH.

Finally, by taking 1D slice of the eddy composite the extension of the SST anomaly outside of the tracked eddy radius (L_{eff}) is obvious. Although the SST peak remains within $1L_{eff}$, this spatial extension suggests the full impact from SST anomalies for small-amplitude eddies is larger than the estimated size of the eddy. A further breakdown and discussion of the impact of SST anomalies within coherent mesoscale eddies on the atmospheric boundary layer is supplied in the following section.

In conclusion, throughout most of the ocean SST is strongly correlated to SSH, which explains why THFF varies with eddy amplitude as shown above. A monopole

spatial structure with a small phase shift is found in large-amplitude modelled eddies, whilst a larger phase shift is found in small-amplitude eddies (after separating each hemisphere); both these spatial structures match previous observational studies. In addition, the spatial extent of SST within small-amplitude modelled eddies extends outside the tracked eddy radius, suggesting the spatial impact on the atmospheric boundary layer and THFF is larger than indicated by 1 L_{eff}.

4.6.2 Does a coupled climate model realistically represent the impact from mesoscale eddies within the local atmosphere ?

We have highlighted the importance of the ratio of ocean-atmosphere resolution in coupled climate models, regarding its impact on the THFF. In this section, we move a step further and evaluate how well variations in the local atmospheric boundary layer (ABL) in response to mesoscale eddies are represented in our highest-resolution coupled climate model available to us, N512-12 (Fig. 4.13). Numerous observational studies typically classify the impact on the local atmospheric boundary layer from mesoscale anomalies by the change in air-sea heat and freshwater fluxes, wind speed, boundary layer height and precipitation, through either the 'vertical mixing' or 'pressure adjustment' mechanisms, as discussed thoroughly in Chapter 1 (Frenger et al., 2013; Byrne et al., 2015; Putrasahan et al., 2013; Tsartsali et al., 2021). Here, we evaluate how well the ABL impact is represented in N512-12.

The composite of each variable, SST_O, THF, the freshwater flux (fwF), ABL height (H_{bl}), wind speed (U_a) and precipitation (P) are calculated using outputs from the N512-12 configuration. Each variable is high-pass filtered and composite-averaged using the same technique as described for SST_O and THF in section 4.4.2. The height of turbulent mixing is used as a proxy for the ABL height H_{bl}, and precipitation is calculated indirectly from the freshwater flux minus evaporation, itself from LHF.

The variables are shown in Fig. 4.13 for the N512-12 configurations for both anti-cyclonic (red centre) and cyclonic (blue centre) large-amplitude (A=34$\pm$6) eddies. The black contour lines represent SSH (cm), and black dots are where the averaged value is not statistically significant at the 99% confidence level. The composite maps display a consistent response across different variables, within the ABL, from variations in SST_O as expected. On average, warm mesoscale SST anomalies (with a maximum of about 1.5 K) transfers heat through turbulent heat flux anomalies (maximum of 60 W m^{-2}) and freshwater fluxes (20 mg m^{-2} s^{-1}) up into the ABL. The heat addition increases local vertical mixing, reduces stability and extends the height of the ABL by over 100 m. The increase in mixing strengthens the transfer of momentum downwards and surface winds (by a maximum of about 40 cm s^{-1}), cloud cover and rainfall (by a maximum of 0.15 mm hour^{-1}). The opposite occurs over a cold SST anomaly.

The averaged response of each variable anomaly within 1 L_{eff} is shown in Table 2 for large-amplitude eddies, and compared to the smallest amplitudes (A=3$\pm$0.05 cm) for each polarity from N512-12. All variables are normalized to a SST anomaly of 0.1 K, and all data within 1 L_{eff} is statistically significant to 99%. Although the response in small-amplitude eddies reduces slightly, the response is surprisingly similar between both large- and small- amplitudes. Despite previous studies discussing the potential unimportance of short-lived, small-amplitude eddies, as they are not observed accurately, we show their impact within the ABL is significant as shown in Table 4.2 (Frenger et al., 2015).

Previous observational studies have compared the same variables over smaller regions, such as the Kuroshio Extension region and the Southern Ocean. The magnitudes of SST, wind stress and THF within large-amplitude eddies in the model are very similar to previous observational estimates in the Kuroshio Extension region (Sun et al., 2020), despite previous work suggesting THF is overestimated in WBC regions (Wu et al., 2019). In the model after globally averaging large-amplitude eddies, a 0.1 K SST anomaly corresponds to THF anomaly of between 4-4.8 W m^{-2} and a change in surface wind speed anomaly by about 2.8 cm s^{-1} for either polar-

ity. In observations in the Kuroshio, (Sun et al., 2020) find a 0.1 K SST anomaly corresponds to THF anomaly of 4.8 W m^{-2} and a change in wind speed anomaly by 3 cm s^{-1}.

Instead, when comparing the model to Southern Ocean observations by (Frenger et al., 2013) the magnitudes of most variables differ, perhaps unsurprisingly due to the averaging of different regions and eddy amplitudes, and the different filtering techniques used. In observations in the Southern Ocean, (Frenger et al., 2013) find a 0.1 K SST anomaly corresponds to a small change in surface wind speed by 0.06 cm s^{-1} and by 0.0008 mm $hour^{-1}$ for precipitation. In the model, a 0.1 K SST anomaly corresponds to a change in wind speed anomalies by between 2.6-3.3 cm s^{-1}, and in precipitation by about 0.01 mm $hour^{-1}$.

Variable	L-Amp.		S-Amp.	
	A	C	A	C
SST'_O (K)	0.1	0.1	0.1	0.1
THF' (W m^{-2})	4.8	4.0	3.3	3.3
fw F′ (mg m^{-2} s^{-1})	1.4	1.2	0.9	0.9
H'_{bl} (m)	11.6	9.6	9.0	9.7
U'_a (cm s^{-1})	2.8	2.8	3.3	2.6
P′ (mm $hour^{-1}$)	0.01	0.01	0.01	0.01

Table 4.2: *Absolute values of the averaged variable magnitude within 1 L_{eff} for large- (L) and small- (S) amplitude eddies for each polarity, either anti-cyclonic (A) or cyclonic (C) in N512-12. All variables are normalized to a SST anomaly of 0.1 K, and all data within 1 L_{eff} is statistically significant to 99%. The variables are SST_O, THF, freshwater flux (fw F), ABL height (H_{bl}), wind speed (U_a) and precipitation (P), with the displayed units.*

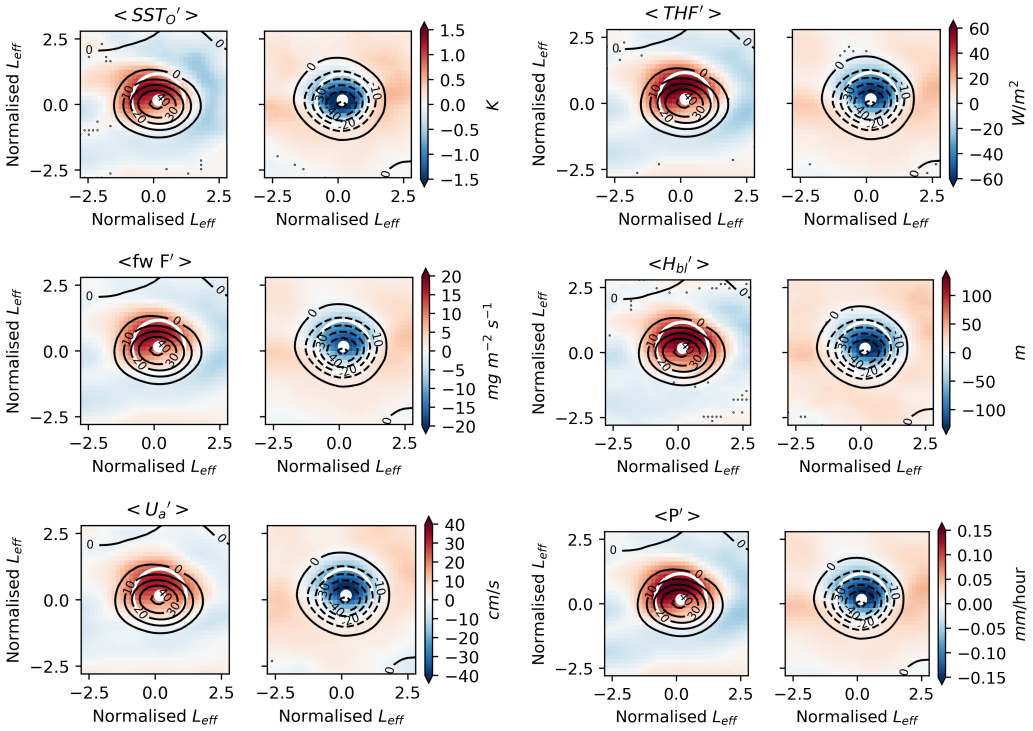

Figure 4.13: *The impact of SST_o anomalies in the local overlying atmosphere in large-amplitude (A=34±6 cm) eddies in N512-12. Composite maps of SST_O, THF, the upwards freshwater flux (fw F), wind speed (U_a), the boundary layer height (H_{bl}) and precipitation (P) (all in colour) and SSH (black contour lines, in cm). Anti-cyclonic warm-core eddies are displayed with a red centre (left), and cyclonic cold-core eddies in blue (right). Solid (dashed) lines indicate positive (negative) values of SSH. The white dot is the centre of each tracked eddy and the white circle is 1 effective eddy radius (L_{eff}). Values shown with a black dot are not significantly different from zero at the 99% confidence level based on t testing.*

4.6.3 The contribution of LHFF and SHFF to THFF

This section has two aims. First, we demonstrate that our linearization of latent heat flux (LHF) expressed as a function of the air-sea temperature difference, is valid. Second, the relative contributions of LHFF and sensible heat flux (SHFF) to the total turbulent heat flux (THFF) are compared to further understand variations in THFF with eddy amplitude.

The full latent (LHF) and sensible (SHF) heat flux equations are provided below.

$$Q_S = C_p\ \rho_{air}\ C_H\ U_{10}\ (SST - T_{air}) \tag{4.12}$$

$$Q_L = L\ \rho_{air}\ C_E\ U_{10}\ (Q_{sat} - Q_{air}) \tag{4.13}$$

where SST is SST_A defined previously, Q_{air} is the specific air humidity at 1.5 m, Q_{sat} is the saturation specific humidity at the sea surface, T_{air} is air temperature at 1.5 m, ρ_{air} is air density, U_{10} is the wind speed at 10 m relative to the ocean surface current, L is the latent heat of evaporation, C_E is the latent heat flux coefficient (Dalton number) and C_H is the sensible heat flux coefficient.

In this study, the full THF equations are reduced to a simplified equation between the heat flux and air-sea temperature difference, following work by Frankignoul et al. (1998). Wind speed, humidity and density from Eq.(4.12)-(4.13), are all assumed to be included in the λ_A coefficient.

A key assumption we make is the LHF can be linearized to be expressed in terms of the air-sea temperature difference, instead of the air-sea humidity difference. The linearization of LHF assumes the SST is proportional to Q_{sat}, and T_{air} is proportional to the 1.5 m specific humidity, Q_{air}. To test this assumption in large-amplitude eddies, the correlation between SST_A and T_{air} (δ in Fig. 4.5B) is compared to SST_A and Q_{air} in Fig. 4.14. Note all data points are taken after composite-averaging and are within 1 L_{eff} to exclude insignificant data (using a 95% confidence level) as seen in the dotted areas in the Q_{air} composite maps in Fig. 4.14.

A strong positive Pearson's correlation coefficient (0.98-0.99 for each polarity)

is found between $< Q'_{air} >$ and $< SST'_A >$ (or $< T'_{air} >$, not shown), which supports our assumption they are proportional to each other (Fig. 4.14). Despite a high coefficient, there is slightly more variance around the mean in Fig. 4.14, especially in warm-core anticyclonic eddies, in comparison to the T_{air}-SST_A relationship (δ) in Fig. 4.5. This scatter is assumed to be result of other processes, such as precipitation, affecting the specific humidity. The increase in the scatter of specific humidity over warm-core eddies could be related to the increased vertical mixing and turbulence in the local atmospheric boundary layer, unlike cold-core eddies which remain more stably stratified.

A recent study by Sun et al. (2020) calculate vertical profiles of Q_{air} over observed composite-averaged eddies, with the spatial distribution displaying a dipole and larger magnitudes of Q_{sat} ($\sim$ 40-80 mg kg^{-1}) than shown in N512-12 in Fig. 4.14 at 1.5 m height ($\sim$ 0.1 mg kg^{-1}). The difference between that study and ours is likely to be a result of the seasonal split of eddies into either winter or summer, and differences in the filtering.

When averaging over all mesoscale anomalies, the correlation is very low between Q_{air} and SST_A anomalies, as found in a study by Small et al. (2019) (their Fig.3) with a correlation between 0-0.4 outside eddy-rich regions in observations using monthly anomalies. However, over individual composite-averaged mesoscale eddies the correlation is high and our assumption is valid. Without high-pass filtering the anomalies, the correlation in the open ocean is weakened by large-scale atmospheric variability.

The relative contribution of LHFF (triangle markers) and SHFF (square markers) to the THFF (Fig. 4.8) is compared in Fig. 4.15 for each model resolution. As expected LHF dominates over SHF, although the difference between the two varies between models and over eddy amplitude. SHFF is relatively constant across all amplitudes, increasing by approximately 1 W m^{-2} K^{-1} between small- and large-amplitude eddies: between 4-5 W m^{-2} K^{-1} in N216-12, 5-6 W m^{-2} K^{-1} in N216-025 and 9-10 W m^{-2} K^{-1} in N512-12. This contrasts the LHFF which increases by between 6-10 W m^{-2} K^{-1} between small- and large- amplitudes: 4-11 W m^{-2} K^{-1}

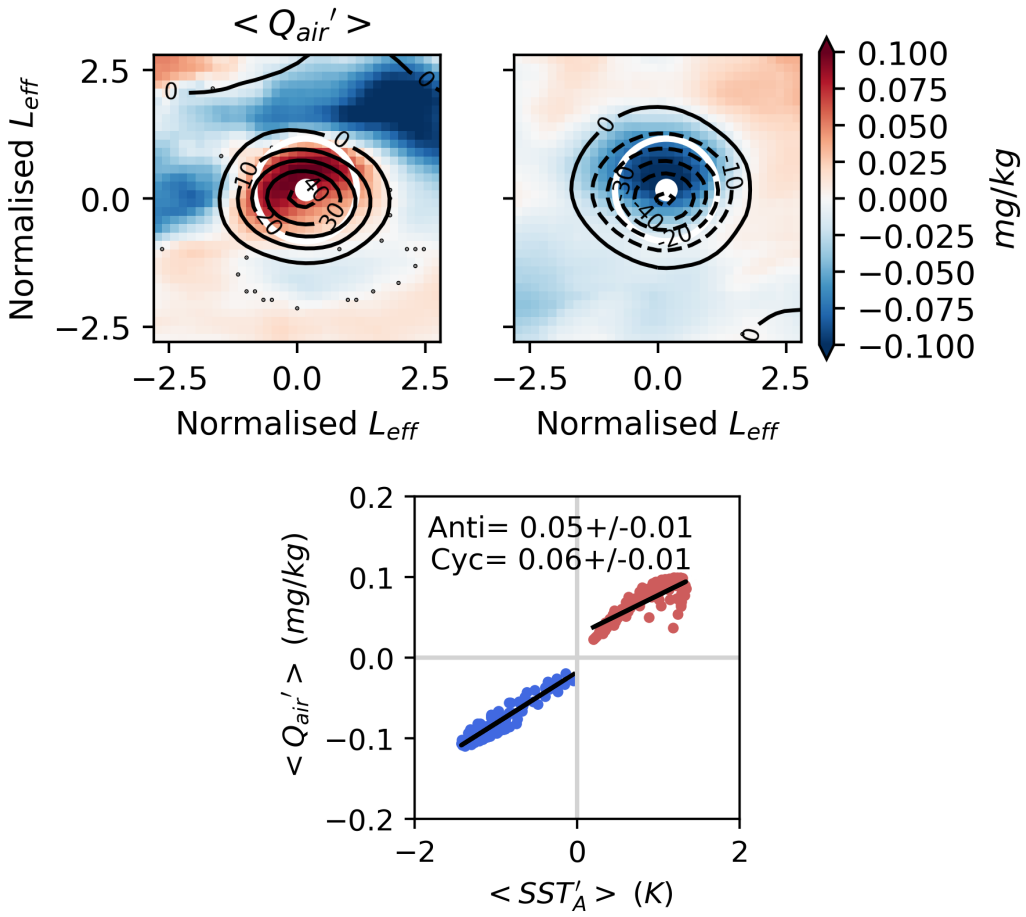

Figure 4.14: *Upper subplots: Specific humidity (Q_{air}, $mg\ kg^{-1}$) at 1.5m (colour) globally composite-averaged eddies for large-amplitude eddies in the N512-12 configuration. The black contour lines represent the SSH anomaly (cm). Anti-cyclonic warm-core eddies are displayed with a red centre, and cyclonic cold-core eddies in blue. The white circle represents 1 L_{eff}. Values shown with a black dot are not significantly different from zero at the 99% confidence level based on t testing. The scatter plot fits a linear regression line to the large-amplitude SST_O and Q_{air} eddy composites in N512-12. The gradient of the linear regression line (black) is given for anti-cyclones (red markers) and cyclones (blue).*

in N216-12, 10-16 W m^{-2} K^{-1} in N216-025 and 15-25 W m^{-2} K^{-1}in N512-12. The largest increase in LHFF with amplitude occurs in N512-12, which is reflected in the largest increase in THFF. This supports the argument that THFF increases

with eddy amplitude are dominated by changes in LHFF i.e. differences in surface and air humidity (and thus the air-sea temperature difference).

In conclusion, first, we demonstrate our linearization of latent heat flux (LHF), to be expressed as a function of the air-sea temperature difference instead of the air-sea humidity difference, in the study above is valid. Over mesoscale eddies, there is a strong positive linear correlation between SST and 1.5m specific humidity in 1 L_{eff}, although this correlation is small over all mesoscale anomalies. Second, variations in THFF are dominated by changes in LHF, relative to SHF where the latter remains relative constant between models and over increasing eddy amplitudes.

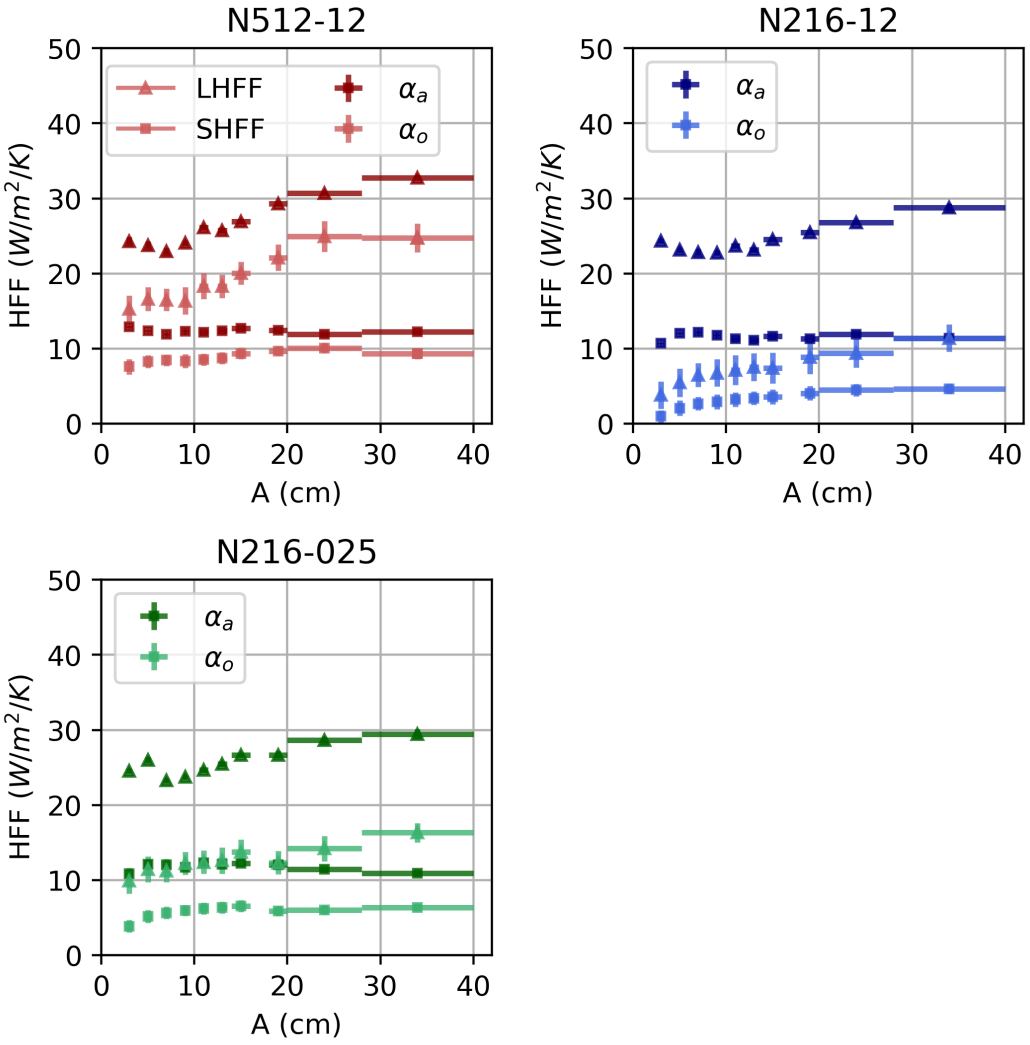

Figure 4.15: *A repeat of Fig. 4.8 where the variation of THF feedback with eddy amplitude is split into the feedback from LHF (triangle symbols) and SHF (squares). α_A is plotted in the darker colours, and α_O in the lighter colours for each resolution: N512-12 (red), N216-12 (blue) and N216-025 (green).*

4.6.4 A closer look at statistical significance

The degrees of freedom for statistical significance testing are calculated as the number of independent samples. Although eddy snapshots in each region globally are likely to be independent from one another, temporally the snapshots are dependent on the eddy conditions from the previous day. Therefore, the number of eddy snapshots composite-averaged, in each eddy amplitude bin, cannot be used as independent samples. Instead, eddy snapshots can be assumed independent samples by considering the median lifetime of the eddies in each bin and an air-sea de-correlation timescale of 7 days, as following.

$$N = n_{eddy}\frac{J}{\tau_{decorr}} \tag{4.14}$$

where N is the number of degrees of freedom, n_{eddy} is the eddy number in each amplitude bin, J is the median eddy lifetime (in days) and τ_{decorr} is the de-correlation timescale.

The de-correlation timescale of 7 days followed work by Frenger et al. (2013) who assumed the short 7 day de-correlation timescale of atmospheric quantities over the Southern Ocean. Their study compared their eddy composite results using a timescale of either 7 or 14 days (which reduced their sample size by more than half) which caused minor changes in the results and did not affect our conclusions. We assume this is valid globally.

As a proxy for the eddy number in each amplitude bin, we have to use the number of eddy births. Therefore a key assumption to our N estimate is the number of eddies born outside our chosen time period and amplitude bin is minimal. This is a more reasonable assumption for the largest-amplitude eddies (A $\sim$ 34 cm) as the time frame is four times as long as small-amplitude eddies. The reason the exact eddy number is not used is because it is difficult to distinguish after grouping the eddies by their amplitude. The eddy tracks are labelled by the number of days an eddy is tracked for. When isolating a specific amplitude, the eddies can be distinguished by their start (i.e. day 1). However, if the first day of the eddy track is not

captured in the chosen amplitude bin, the track is a list of numbers corresponding to the number of days tracked.

We can determine if an eddy in the binned subset has been tracked for 2 or more subsequent days: $\sim$ 16% in small-amplitude eddies and $\sim$ 85% in large-amplitude eddies (averaged for each polarity). This corresponds to the increased number of degrees of freedom for small-amplitude eddies because a larger number of isolated eddy snapshots (i.e. independent samples not from the same eddy) are present in subset, compared to large-amplitude eddies. A limitation that we have not accounted for whether the same eddy with an amplitude (A) of, for example, 3 cm grew to a larger amplitude and then shrunk back to an amplitude of 3 cm later in its lifetime: instead these two eddy snapshots (when at A=3 cm) would be treated as two independent snapshots. By assuming more than 7 days occurred between the two, these would be independent snapshots anyway.

Eddy amplitude (cm)	Type	N	n_{eddy}	J (days)
3$\pm$0.05	A	483	199	17
	C	577	311	13
34$\pm$6	A	135	86	11
	C	231	135	12

Table 4.3: *Number of degrees of freedom (N), eddy number (n_{eddy}) and median lifetime (J) in the small-amplitude (3$\pm$0.05) and large-amplitude (34$\pm$6) eddies in N512-12. The values from anticyclonic (A) eddies is listed first, then cyclonic (C) eddies.*

A key question closely related to the number of degrees of freedom is how many eddy snapshots are enough, in each amplitude bin, to provide a robust series of composites for averaging. After calculating the number of degrees of freedom, we can isolate values which are not statistically significant from zero (using student's t-testing with a 99% confidence level).

4.6.5 Eulerian perspective and seasonality

So far, using composite-averaging we average THFF in time and space i.e. using a Lagrangian perspective. Here, we evaluate how the THFF found within coherent mesoscale eddies compares to all mesoscale anomalies, i.e. from a Eulerian perspective. This includes all daily weather variability, seasonality and all eddy amplitudes. Finally, the Eulerian THFF is re-calculated separately for each month to explore seasonal variations in the THFF.

Previous work by Ma et al. (2016) evaluates an observed Eulerian THFF of 40.32 W m^{-2} K^{-1} between high-pass filtered SST and THF anomalies in the eddy-energetic Kuroshio Extension region, which is within our THFF (α_A) range of 35-45 W m^{-2} K^{-1} over eddies. Instead, we calculate Eulerian THFF globally, including both eddy-energetic and eddy-quiet regions. Here, we follow our previous work by calculating Eulerian λ_A and δ, and comparing how the regridding of SST impacts R_g and α_o. Are our estimates of THFF and the SST regridding errors consistent outside of closed mesoscale eddies ?

The creation of the mesoscale anomalies from the background field are the same mesoscale anomalies used for composite-averaging, i.e. a long-term mean has been removed and each daily snapshot is high-pass filtered by 20° x 10°. The temporal length of the data is 1 year. All coefficients λ, δ, R_g, α_a and α_o are calculated using global values for the 1st 5 days of every month for 1 year, to reduce computing time. All land values and high outlier anomalies are removed. These outliers are a consequence of the high-pass filtering technique at the highest NH latitudes and in the Baltic, Mediterranean, Black and Caspian Seas. To examine similar SST anomaly magnitudes as found within closed coherent eddies, mesoscale SST anomalies are capped at 1 K although the coefficients are consistent for larger SST anomalies (not shown).

The global Eulerian computation of the same coefficients from Fig. 4.5 and 4.3 (λ_A, δ, R_g, α_o and α_a) in N512-12 is shown in Fig. 4.16. Note the error bars of the coefficients are much larger over all mesoscale anomalies, compared to variance

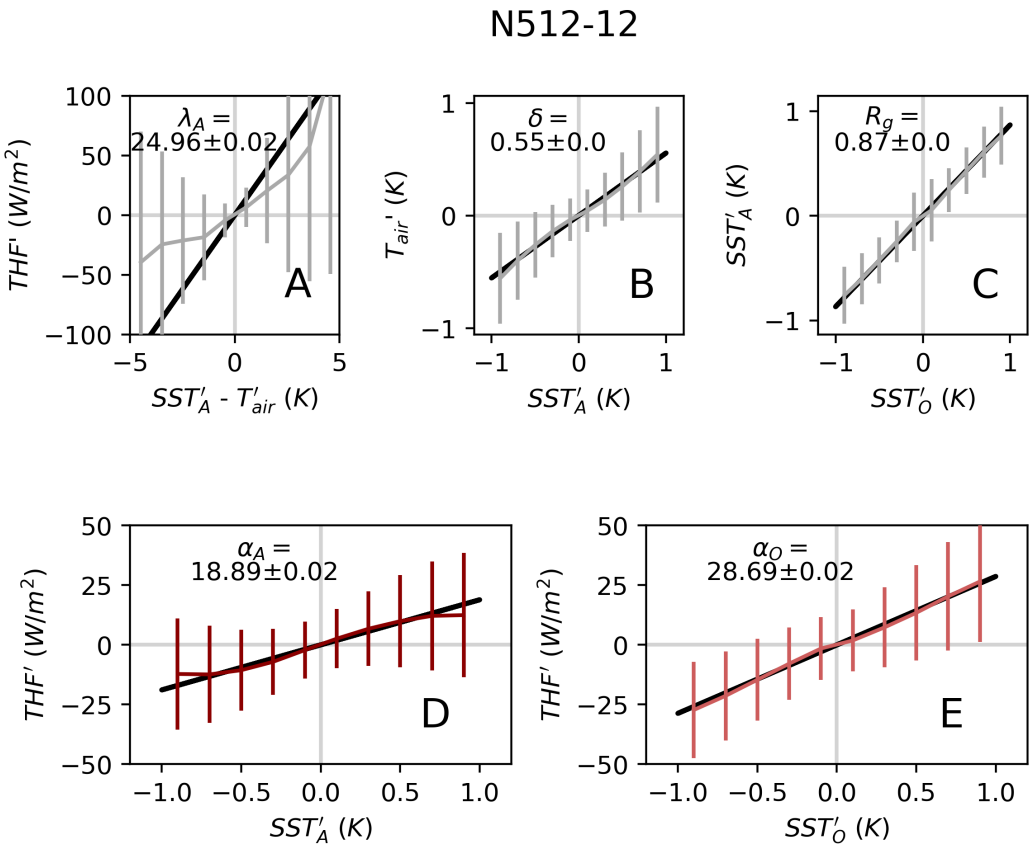

Figure 4.16: *A repeat of Fig. 4.5 for all Eulerian mesoscale anomalies, within 1 K (i.e. beyond coherent eddies) after high-pass filtering (20° × 10°) in N512-12.*

around the linear regression line found for coherent eddies (Fig. 4.5). First, the magnitude of the Eulerian THFF using the prognostic SST on the oceanic grid, α_O of 28.7 W m^{-2} K^{-1} lies within the range of THFF over mesoscale eddies [25-35] W m^{-2} K^{-1} (Fig. 4.16 E). Second, the Eulerian regridding parameter R_g is closer to 1 at 0.87 suggesting the effect of regridding SST is smaller over all mesoscale anomalies, compared to over individual eddies, as expected due to the larger spatial scales included in Fig. 4.16 C. Third, Eulerian α_A is smaller than α_O, as shown in Fig. 4.16 D, contrary to within mesoscale eddies (Fig. 4.8).

Over mesoscale eddies, α_A is approximated using the THF restoring coefficient (λ_A, Fig. 4.16 A) and atmospheric adjustment (δ, Fig. 4.16 B) using equation 4.7. However, this equation appears not valid when averaging over all mesoscale

anomalies [25(1-0.55) $\approx$ 11 W m^{-2} K^{-1}] and under-predicts the magnitude of α_A (19 W m^{-2} K^{-1}). Over all mesoscale anomalies, the atmospheric adjustment δ has a strong positive correlation and a gradient of about 0.5, which is within the upper bound given by Hausmann et al. (2017) for larger observed mesoscale anomalies (1°) in the Southern Ocean and North Atlantic. It is likely λ_A over all mesoscale anomalies is underestimated, due to the atmospheric variability captured within T_{air}. λ_A has a weak correlation with large error bars as shown in Fig. 4.16 A. We suggest finer spatial filtering is required to obtain a more accurate estimate of λ_A.

Unlike the eddy compositing method above, which removes all atmospheric variability, calculating the THFF over all mesoscale anomalies under a variety of atmospheric conditions e.g. weather systems means it is difficult to obtain a reliable estimate. Furthermore, we know from section 4.6.3, the strong correlation between the 1.5m specific humidity and SST found over coherent eddies is not consistent when expanded over all mesoscale anomalies, because the specific air humidity now contains weather variability. This again explains the weak correlation between the THF and temperature difference (λ_A) shown in Fig. 4.16 A. In other words, our assumption that LHF can be linearized to be expressed in terms of the air-sea temperature difference is not valid here.

A comparison of each coefficient for the three model configurations are given in Table 4.4. The restoring coefficient λ_A and atmospheric adjustment δ are similar between the resolutions, similarly to over eddies (Fig. 4.6 D,E). Instead, the regridding of SST R_g of SST is increased in N216-025, compared to N216-12 and N512-12.

The monthly variability of Eulerian α_O is shown in Fig. 4.17 for each hemisphere and each model resolution. Note that the SST anomalies are not capped to 1 K in these plots. THFF increases during the winter months, i.e. Nov-Jan in the Northern Hemisphere (NH) and in Jun-Aug in SH, and reduces in summer, similarly to a recent observational study in the Kuroshio Extension region (using J-OFURO flux data) (Sun et al., 2020; Tomita et al., 2019). Increases in THFF during winter

Variable	N512-12	N216-12	N216-025
λ_A	25.0	22.9	21.9
δ	0.55	0.59	0.61
R_g	0.87	0.76	0.74
α_A	18.9	17.1	15.9
α_O	28.7	24.0	22.4

Table 4.4: *Eulerian THFF coefficients for each model configuration.*

months correspond to an increase in both the magnitude of SST and THF anomalies, and in the background wind speed (Sun et al., 2020). In their study, THFF increases to 43 W m^{-2} K^{-1} in the winter months, and reduces to 33 W m^{-2} K^{-1} in the summer. In the model and averaged over the whole northern hemisphere (NH), the seasonal differences are doubled reducing from a maximum of about 34 W m^{-2} K^{-1} to 14 W m^{-2} K^{-1} in N512-12. Magnitudes of THFF are larger in the southern hemisphere increasing from about 26 W m^{-2} K^{-1} in the summer to about 37 W m^{-2} K^{-1} in the winter in N512-12, although with reduced seasonal differences, compared to the NH. The N512-12 configuration consistently increases the magnitude of THFF, compared to N216-12 and N216-025, however the distribution of seasonal variability remains similar in each hemisphere.

To conclude, first, can our work be easily replicated using Eulerian estimates? No, error bars over all mesoscale anomalies are much larger and the THFF restoring coefficient λ_A, and thus the α_A THFF is under-estimated. Second, are our estimates of THFF and the SST regridding errors consistent outside of closed mesoscale eddies ? The increase in the regridding of SST over the smaller amplitude eddies is not mirrored over all mesoscale anomalies, as the spatial scales are much larger. Finally, there are strong seasonal variations in the THFF, which further highlights the THFF calculated in this study is a global estimate and regionally, the THFF will vary considerably.

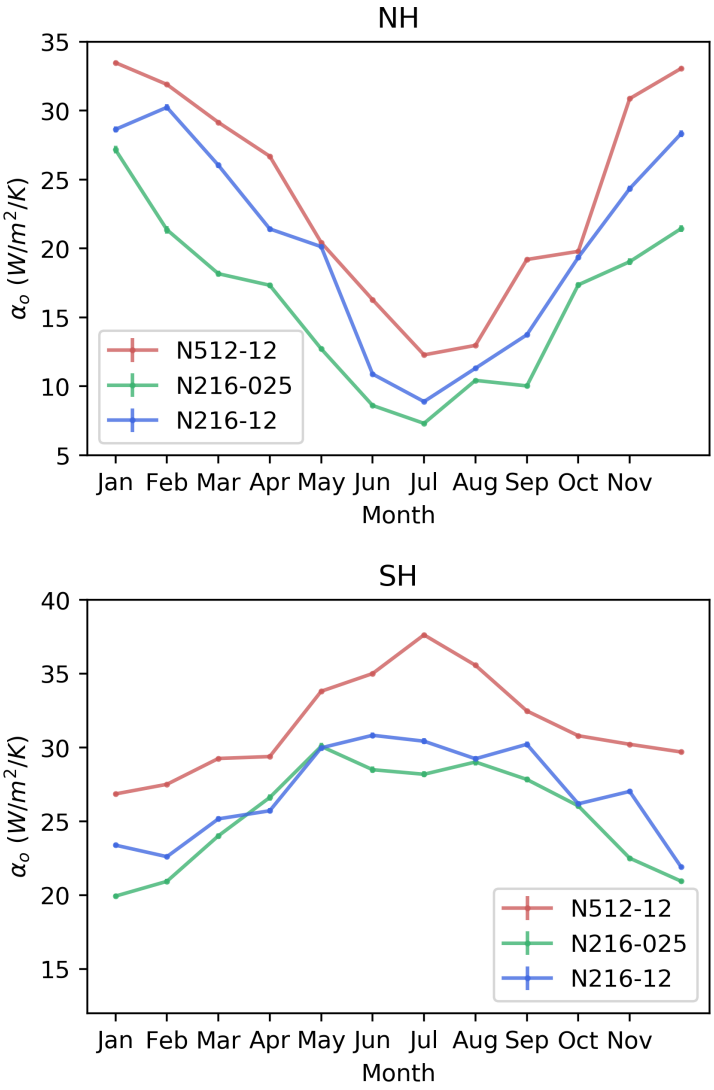

Figure 4.17: *The seasonality of Eulerian estimates of α_o for each resolution and each hemisphere. α_o is calculated for the 1st 5 days of every month for 1 year.*

4.7 Conclusions

In alignment with our second thesis objective, turbulent heat flux feedback over coherent mesoscale eddies is estimated globally in three configurations of a high-resolution coupled model HadGEM3-GC3.1. The key results of the chapter are summarised as following.

First, for the highest ocean-atmosphere resolution available (where the impact

of SST regridding from the ocean grid to the atmosphere grid is relatively minimal compared to the other configurations), the estimates of the THFF over mesoscale eddies range from 35 to 45 W m^{-2} K^{-1} where values roughly increase with eddy amplitude. Variations in THFF with amplitude are dominated by changes in latent heat flux, relative to the sensible heat flux. This is the first time such an estimate is provided as previous studies did not resolve such small scales nor attempt to isolate coherent eddies.

Second, we investigate configurations with a larger mismatch between oceanic and atmospheric resolutions. We find that the regridding of SST from the ocean to atmosphere grid can underestimate the eddy-induced THFF by 20 to 80%. Importantly, this low bias increases with the ratio between atmospheric and ocean resolutions, implying that increasing the oceanic resolution at constant atmospheric resolution can actually degrade the solution, at least in the representation of air-sea feedbacks.

The low bias in the THFF suggests that eddies are not dampened enough in the model. Eddies have a first order impact on the dynamics of WBCs and the ACC. However, small-amplitude eddies that dominate the eddy population cover the global open ocean, influencing the stratification, ocean heat uptake and biological processes. These eddies have a strong THFF of 35-40 W m^{-2} K^{-1} and are the most affected by the low biases due to regridding. Further work is needed to understand these biases, but it is likely to have range of impacts beyond eddy-rich regions: artificially large SST anomalies are likely to cause an artificially large local and large-scale ocean and atmospheric response (Bishop et al., 2020; Ma et al., 2016; Frenger et al., 2013).

Our findings should be tested with other high-resolution climate models, which adopted different coupling strategies (Yang et al., 2018). In addition, while our focus was on horizontal resolution, it is likely that the vertical resolution, in both the ocean and atmosphere, play a major role in the representation of mesoscale air-sea exchanges through its influence of the ABL adjustment (Stewart et al., 2017). We leave binning by eddy radii and exploring the effect of lags between SST and

THF on our THFF estimates for future work. Finally, we present a global estimate of THFF although geographical and seasonal variations in eddy amplitude, SST, air-sea heat fluxes, wind and ABL responses will cause large variations of the THFF. This is outside the scope of this work but will be interesting to evaluate in the future.

The results in this study hold implications for future model development. Similarly to HadGEM3-GC3.1, many current high-resolution coupled models (which use the OASIS coupler for example) compute air-sea turbulent heat fluxes on the atmospheric grid, using regridded SST (Roberts et al., 2019; Valcke et al., 2015). For the long spin-ups needed for climate simulations, it is unrealistic to expect the atmospheric resolution to match the oceanic resolution. Instead, it is suggested when resolving mesoscale eddies, that air-sea heat fluxes should be calculated on the finer-scale oceanic grid, as done by the Community Earth System Model (see Yang et al. (2018)). This method ensures that the high-resolution SST anomalies are maintained, although this requires a large logistical change for many coupled models and is computationally much more expensive.

Our results also indicate that the regridding introduces a noise and an asymmetry between cyclonic and anticyclonic eddies. Essentially, we need a 'better' regridding of SST_O to SST_A although it is inevitable that even the best regridding technique will degrade mesoscale SST anomalies in large ocean-atmosphere resolution difference. In ocean-only models, the ocean component is driven through bulk formulae and prescribed surface atmospheric fields, i.e. without ABL adjustment (i.e. $\delta = 0$ in our notations). In such setups, we expect mesoscale THFF to approach λ_A. However, the absence of an ABL adjustment also influences λ_A (e.g. neglecting the effect of dynamical adjustment on the drag coefficient). The net effect of these assumptions on the mesoscale THFF in ocean-only models remains to be quantified.

Having estimated the mesoscale THFF in the state-of-the-art climate model HadGEM3, we can now use these results to parameterize the air-sea heat flux feedback from mesoscale anomalies, within an ocean-only model, to explore the impact on large-scale ocean circulation in the following chapter.

Chapter 5

Thermal Mesoscale Air-Sea Feedback on Large-Scale Ocean Gyre Circulation

The chapter is structured as a traditional thesis chapter. Further details of the model set up are supplied in the Chapter Appendix in section 5.5.

5.1 Introduction

At mesoscales (10-100km) intrinsic ocean variability drives non-linear changes in the atmosphere, through air-sea heat and momentum fluxes. Warm mesoscale SST anomalies transfer heat, through turbulent heat fluxes, into the atmospheric boundary layer (ABL), reducing its stability, altering pressure gradients and strengthening surface winds. The opposite occurs over cold anomalies, where static stability in the ABL increases. Therefore, mesoscale thermal air-sea coupling can be separated into two relationships, the positive correlation between either SST and surface wind stress or between SST and air-sea heat fluxes, which both form the focus of this study.

In eddy-energetic frontal regions, previous studies suggest that these two thermal mesoscale air-sea interactions have significant competing consequences on the strength and position of WBCs. Mesoscale SST-wind stress coupling can destabilise the jet and reduce mid-latitude gyre strength by 30-40%, by generating a surface curl and eddy-induced Ekman pumping anomalies (Hogg et al., 2009; Gaube et al., 2015). In contrast, mesoscale SST-heat flux coupling strengthens the WBC jet by 20-40%, by reducing the conversion of eddy potential energy to eddy kinetic energy, and dampening mesoscale activity (Ma et al., 2016; Bishop et al., 2020). As most research to date focuses on the impact of mechanical dampening by mesoscale surface currents, no single study compares the relative importance of mesoscale SST-wind stress feedback compared to SST-heat flux feedback (Renault et al., 2019b; Seo et al., 2016; Oerder et al., 2018; Renault et al., 2019c). In this study, we investigate the relative and net impact of the two thermal mesoscale feedbacks on the WBC jet strength and position.

The local feedback from mesoscale SST-wind stress coupling has been extensively studied, i.e. Chelton et al. (2004); Chelton and Xie (2010); O'Neill et al. (2012), whilst a small number of modelled studies quantify the feedback on the large-scale circulation and WBC jet. Hogg et al. (2009) use a simple parameterization of mesoscale SST-wind stress coupling, using a double gyre set up within a quasi-geostrophic ocean model. It is currently unclear if a primitive equation model produces the same response.

Recent studies by Ma et al. (2016) and Bishop et al. (2020) show the importance of the mesoscale SST-heat flux feedback in the dissipation, or sink, of eddy potential energy (EPE) in mid-latitude WBC regions, accounting for over 50% of global EPE destruction. The dissipation of EPE reduces the conversion of EPE into eddy kinetic energy (EKE), dampening eddy activity and strengthening the mean jet. Ma et al. (2016) use a regional coupled model, in the Kuroshio Extension region, to essentially switch 'on' or 'off' the mesoscale SST-heat flux feedback. This is achieved by smoothing out mesoscale anomalies through low-pass spatial filtering, before passing the fields to the atmospheric component. Using a fully coupled model, Ma et al.

(2016) are unable to easily manually vary the intensity of the mesoscale feedback and investigate the sensitivity of the mean jet.

To date, a comparison of the relative importance of warm versus cold mesoscale anomalies within thermal air-sea feedback on the WBC jet is absent. Ma et al. (2016) find warm-core anti-cyclonic eddies have a stronger air-sea turbulent heat flux, compared to cold-core eddies which are less efficient, while Bishop et al. (2020) suggest cold-core eddies have a minimal impact on air-sea interaction as a sink of EPE in subtropical gyres, possibly due to the increased stability of the overlying ABL. In the Northwest Pacific, EKE within mesoscale warm-core anti-cyclonic eddies decays faster over an eddy's lifetime, compared to cold-core cyclonic eddies (Ding et al., 2020). This study aims to quantify whether warm mesoscale anomalies have a larger thermal air-sea feedback, and the implications for the WBC jet and the dampening rate of mesoscale anomalies.

WBCs are critical for global climate, weather patterns and the Atlantic meridional overturning circulation strength (Roberts et al., 2020b; Grist et al., 2021; Moreno-Chamarro et al., 2021). Although, current state-of-the-art climate models struggle to realistically represent the position, i.e. the separation from the coast, of WBCs even with a near-global representation of mesoscale activity and realistic topography (Grist et al., 2021; Renault et al., 2019b; Hewitt et al., 2020, 2017). Typical CMIP6 climate models, with a 1° ocean component, currently fail to resolve or parameterize mesoscale air-sea interactions. Could the representation of WBC separation in climate models be improved by the better simulation of thermal mesoscale air-sea feedback ?

In summary, the principal objective of this study is to investigate the relative and net feedback on WBC strength and position, and mesoscale dampening, from two distinct thermal air-sea coupling processes. We hypothesise the mesoscale SST-heat flux feedback dominates in controlling the WBC jet strength, relative to SST-wind stress feedback, as a result of the suggested dominating impact from the dampening of EKE. In other words, we hypothesise the strengthening of the jet induced by mesoscale heat flux feedback dominates over the destabilisation of the jet in-

duced by mesoscale SST-wind stress feedback. A secondary objective is to evaluate whether changes in thermal air-sea feedback are dominated by warm mesoscale SST anomalies, rather than cold anomalies and third, to address sensitivity of each feedback on the WBC jet.

To achieve our objectives, we use a primitive equation regional ocean model to parameterize and isolate the two thermal mesoscale air-sea fluxes and to evaluate their impact on the WBC separation and strength. The study is structured as follows: section 5.2 details the model set up, parameterization and coupling experiments, section 5.3 presents the results and section 5.4 concludes and discusses implications for future research and model development.

5.2 Data and Methods

5.2.1 MITgcm model set up

The MIT general circulation model (MITgcm) is a numerically efficient, simplified ocean-only model, which solves hydrostatic primitive equations on an Arakawa C-grid, using depth coordinates. The linear equation of state ($\rho = \rho_0(1 - \alpha_\theta\ \theta)$) is implemented in the model as a density anomaly dependent solely on ocean temperature (i.e. no salinity) as following: $\rho' = -\rho_0\ \alpha_\theta\ \theta'$ where the thermal expansion coefficient $\alpha_\theta = 2 \times 10^{-4}\ K^{-1}$ and ρ_0 is a reference density.

We create a wind-driven baroclinic double gyre circulation in a rectangular ocean basin to mimic the Kuroshio Current Extension region, a region of intense mesoscale activity and air-sea exchanges (Marshall et al., 1997; Munk, 1950; Stommel, 1948; Holm and Nadiga, 2003; Ma et al., 2016). The domain extends from $20°N$ - $63°N$ meridionially and 31° zonally, with a depth of 2780 metres, a flat bottom topography and no coastlines. The regular horizontal grid resolution is 1/10° in latitude and longitude with 25 unevenly spaced vertical layers (Δz): the top layer is 10m deep and the centre of each depth cell is plotted as a blue dot in Fig. 5.1, right. The region is mapped onto a sphere using spherical polar coordinates.

There are no eddy parameterizations as mesoscale eddies are explicitly resolved, while vertical mixing is parameterized through the 'kpp' parameterization scheme (Large et al., 1994). To maintain numerical stability, the high spatial resolution requires a minimum time step (Δt) of 15 minutes, as shown in equation 5.1. The maximum horizontal advection ($|c_{max}|$) is assumed to be 1 m/s, and the maximum longitudinal grid box size (Δx) at the Northern boundary at $63°N$ is approximately 5.2 km, where $\Delta x = a\cos(\lambda)\ \Delta\varphi$: a is the earth's radius, λ is latitude in degrees and $\Delta\varphi$ is around 11 km ($0.1°$).

$$S_a = 2(\frac{|c_{max}|\ \Delta t}{\Delta x}) < 0.5 \tag{5.1}$$

where $S_a \approx 0.346$.

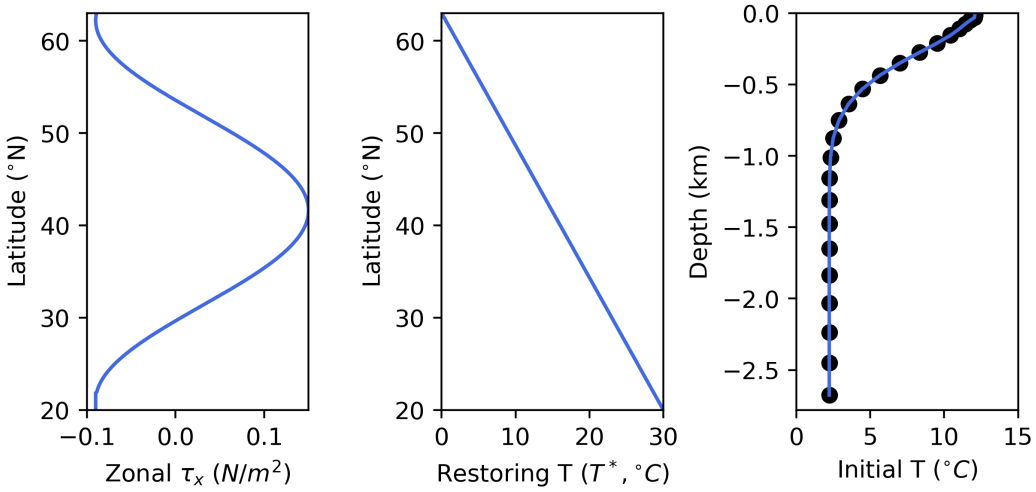

Figure 5.1: *Model forcings*

The lateral boundary conditions are set up as 'free-slip' i.e. the Stommel (1948) scheme is used and the tangential shear (or friction) at the domain boundaries is removed (Vallis, 2019). 'No-slip' conditions (zero velocities at the boundary) are found at the ocean floor, using a parameterized linear bottom drag. We aim to produce a strong jet penetration by narrowing the distance between the separation points in each gyre. Compared to 'no-slip' lateral boundary conditions, 'free-slip' decreases the distance between the points (Haidvogel et al., 1992). Although it can

be argued 'no-slip' lateral boundaries are the most appropriate, they are not needed for a finite-resolution model (Chassignet and Marshall, 2008).

Zonal wind stress forcing (τ) varies sinusoidally with latitude and is prescribed as following (plotted in Fig. 5.1, left):

$$\tau_x = -\tau_{max}\, cos(2\pi \frac{(\varphi - \varphi_0)}{L}) \tag{5.2}$$

where τ_{max} is 0.15 N m^2, φ is latitude, φ_0 is 20°N and L is the lateral (N-S) domain extent (43°). Note the negative wind stress is capped at -0.1 N m^2 for 2° at the bottom and top of the domain to prevent increased wind energy at the north and south boundaries (which generates too much/ unrealistic mesoscale activity). The large-scale wind stress remains constant in time (i.e. no seasonality), while meridional wind stress is zero. Note a positive value of τ corresponds to a downward surface momentum flux.

Buoyancy forcing (F_θ) is implemented as:

$$F_\theta = \frac{1}{\tau_{time}}(T - T^*) \tag{5.3}$$

Temperature T is restored to a defined fixed temperature (T^*) with a meridional gradient to mimic air temperature, using a constant restoring timescale (τ_{time}). Restoring temperature (T^*) for each latitude is shown in Fig. 5.1 (middle) alongside the spatially averaged initial temperature profile (Fig. 5.1, right).

Model outputs are obtained after a 80 year spin-up period. The large-scale SST and air-sea heat flux continue to drift at a rate of 0.01% and 0.92% per year respectively, when averaging over the last 10 years of the spin-up period (Fig. 5.2). As seen in the figure, although the rate of change of the heat flux is small, the spatially-averaged final magnitude does not converge to zero and is about minus 6.5 W m^{-2}, meaning heat is still entering the ocean. This is due to a leak associated with the linear free surface, and in this study we assume both the small drift in SST and heat flux, and the non-zero final value of the heat flux have a negligible impact on the results. Note in this study a positive air-sea heat flux (W m^{-2}) means heat is leaving the ocean, and a negative heat flux means heat is entering the ocean (contrary to the MITgcm default) to be consistent with Chapter 4.

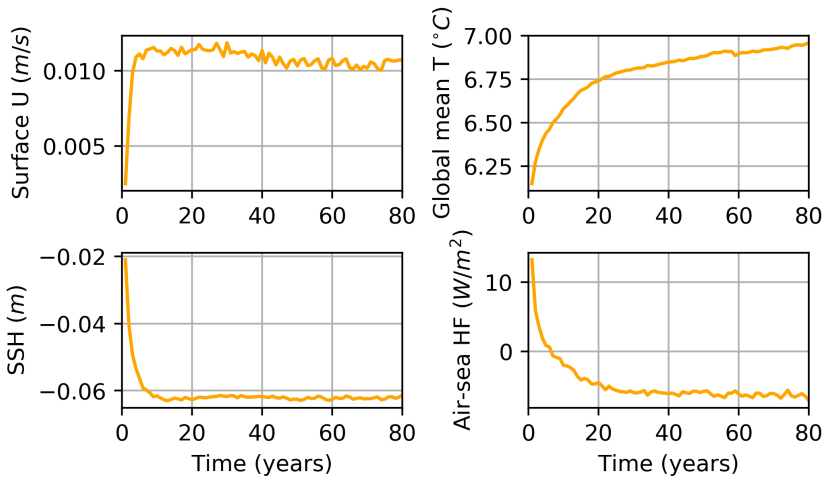

Figure 5.2: *Time series of surface zonal velocity (U), global mean temperature (T), sea surface height (SSH) and air-sea heat flux (HF) during the spin-up period. Note a positive HF means heat is leaving the ocean (i.e. entering the atmosphere), and a negative HF means heat is entering the ocean.*

Further details of the model time step, viscosity, lateral boundary conditions and the advection are provided in the Chapter Appendix in section 5.5, and details about the vertical mixing ('kpp') parameterization scheme are found in Chapter 2.3.

5.2.2 Comparison with previous studies

Fig. 5.3 provides a 3D view of the model domain overlaid with sea surface height (SSH, black contours), the zonal average of temperature with depth and a longitudinal profile of U-velocity, in the control experiment i.e. no air-sea mesoscale feedback exists. The zonal velocity profile is plotted at the latitude of the maximum velocity, i.e. around 40°N. As part of large scale ocean gyre circulation, Rossby waves transport energy westwards across the basin, causing a westward surface intensification, shown by increased SSH up to 80 cm, and a strong eddy-energetic WBC along the boundary (Stommel, 1948; Marshall and Plumb, 2008; Chassignet and Gent, 1991). While large-scale wind stress produces meridional Ekman transport. At zero wind stress curl, i.e. at the maximum zonal wind stress in Fig. 5.1,

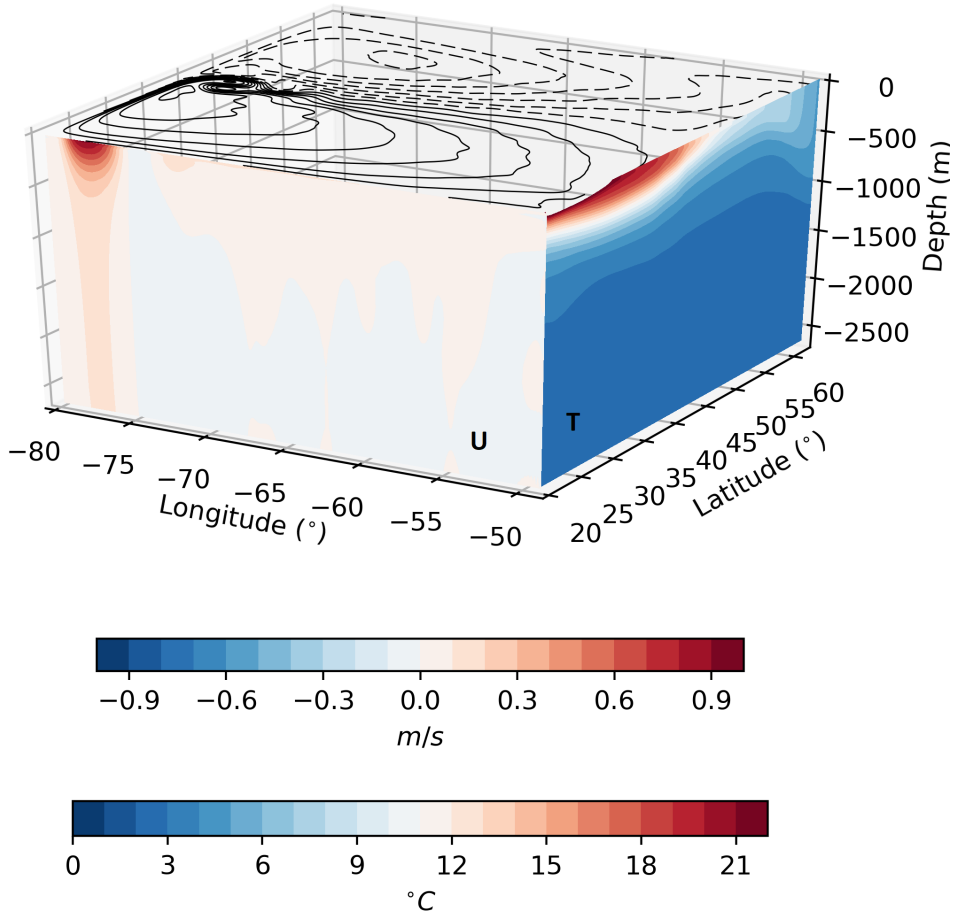

Figure 5.3: *The MITgcm domain (for the control experiment) in Cartesian coordinates for illustrative purposes. Note the model uses spherical coordinates and the diagram is not to scale. The black contour lines at the surface display SSH, where dashed lines are negative values and the contour interval is 10 cm. The latitude-depth face displays the zonal average of temperature (°C) and the longitude-depth face displays the zonal velocity (m s^{-1}) at the latitude of maximum velocity, at approximately 40°N.*

the current separates from the coast and penetrates into the ocean interior, forming the subpolar and subtropical gyre, as shown by the strong zonal velocity in Fig. 5.3. In reality, instabilities in the jet form intense localized regions of warm and cold anomalies, meanders in the current and intense air-sea interactions at the

mesoscale. In our set up the current remains close to the western boundary, compared to a quasi-geostrophic set up, where a strong jet extends much further into the ocean interior, as shown in Chassignet and Gent (1991) and Chassignet and Marshall (2008) for a similar double gyre set up. According to Özgökmen and Chassignet (2002), typically excess mesoscale activity at the separation point creates this unrealistic jet penetration and an energy sink is required. The ocean is stably stratified with a strong thermocline seen towards the south, with a shallow mixed layer depth of about 30 m. At the northern boundary, the water column is well-mixed and the mixed layer depth extends beyond 600 m.

Total kinetic energy is separated into time-mean and transient components. The time-varying component is commonly known as eddy kinetic energy (EKE). Spatial maps of both EKE and mean kinetic energy (MKE), vertically averaged from 240 m to the surface, are shown in Fig. 5.4 (upper plots) from the control experiment. EKE is computed from model snapshots of velocity using the equation EKE = $\frac{1}{2}(\overline{u'}^{\,2} + \overline{v'}^{\,2})$ where $\overline{u'}^{\,2} = \overline{u^2} - (\overline{u})^2$, $\overline{*}$ resembles a 20 year average, and u, v are the averaged velocities in the upper 240m in x- and y- directions respectively. As shown in Fig. 5.4, EKE in the jet region is about 0.1 extending to 0.9 $m^2\ s^{-2}$. In AVISO observations in the Gulf Stream, typical values of EKE are again about 0.1 $m^2\ s^{-2}$ but with a maximum of 0.38 $m^2\ s^{-2}$ (Chassignet and Xu, 2017; Thoppil et al., 2011). The peak of EKE in our set up is therefore slightly higher. In the open ocean, the EKE magnitudes of about 0.003 $m^2\ s^{-2}$ are similar to previous model simulations and observations in the North Atlantic (Jullien et al., 2020). As expected, MKE $(\frac{1}{2}(\overline{u}^2 + \overline{v}^2))$ is intensified in the WBC region, reaching maximum values of about 1.9 $m^2\ s^{-2}$. In the open ocean values reduce down to about 10^{-5} $m^2\ s^{-2}$.

To resolve mesoscale anomalies we require a stably stratified ocean, with small enough horizontal grid spacing to resolve the first baroclinic mode of the Rossby radius of deformation (R_d), so baroclinic instability can occur. Despite a small R_d in the northern latitudes between about [6-9] km (as shown for a snapshot in Fig. 5.4, lower left), mesoscale eddies still form across the full domain. This is shown in the spatial map of surface vorticity (ζ) in Fig. 5.4, lower right. The region around

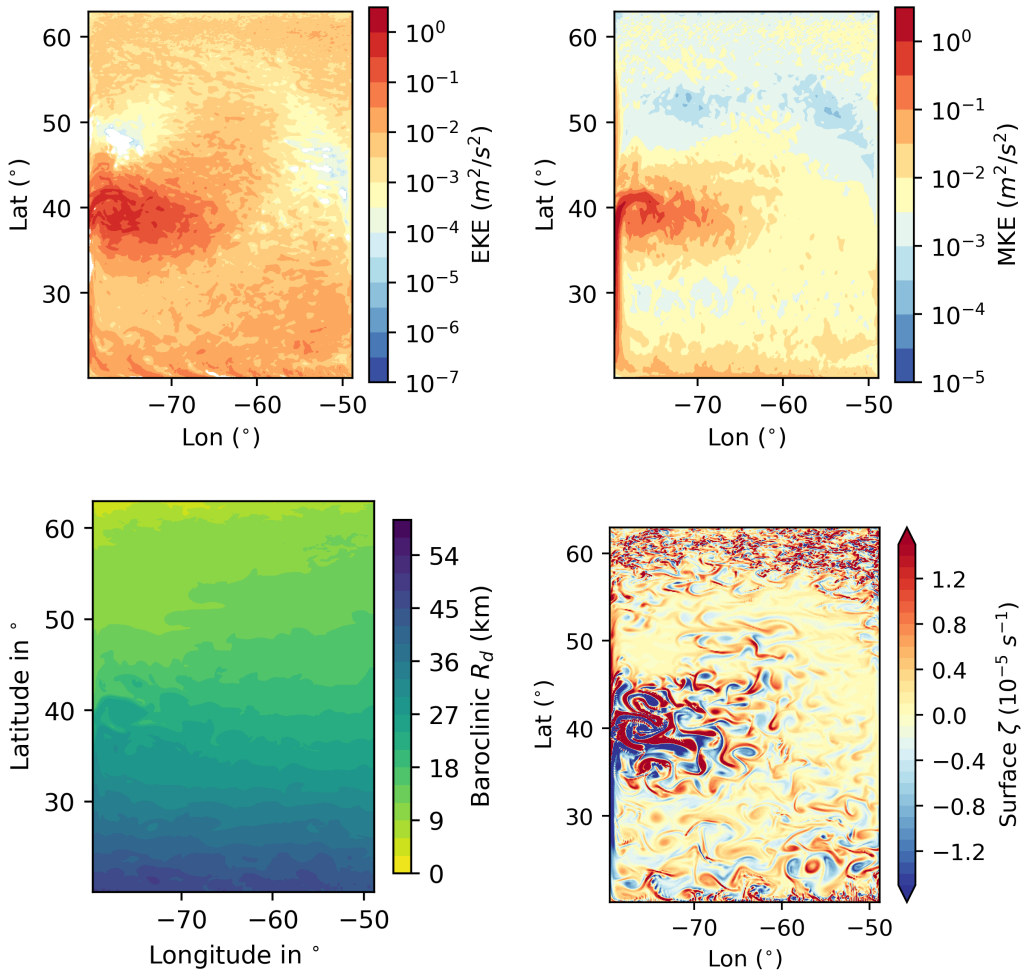

Figure 5.4: *Spatial maps of the time- and vertically- averaged (0-240 m) eddy kinetic energy (EKE, upper left) and the mean kinetic energy (MKE, upper right) with units of* $m^2\ s^{-2}$. *The lower subplots display a snapshot of the baroclinic Rossby radius of deformation (*R_d, *km) and surface vorticity (*ζ, s^{-1}*). All plots are from the control experiment, with no mesoscale feedback.*

the jet separation, where thermal mesoscale air-sea exchanges become important, is highly turbulent.

5.2.3 Extraction of mesoscale anomalies

To implement thermal air-sea feedback over mesoscale anomalies, first we isolate mesoscale anomalies from the background field using SST. As the model runs, mesoscale SST anomalies are isolated by removing the monthly mean of the previous month from the current SST field. Although the majority of the modelled SST anomaly magnitudes and distribution match observational SST anomalies, the maximum magnitudes in the model are higher, i.e. beyond 5 $^{\circ}C$. Often previous studies remove very high SST anomalies using high-pass spatial filtering on model output, although in this study this procedure is computationally expensive to implement, as the SST anomalies are calculated during the model simulation. For all experiments, mesoscale coupling is set to only occur over SST anomalies larger than 0.5° to isolate the larger mesoscale anomalies found within the WBC and to exclude very small anomalies in the gyre interior. The spatial mean of a snapshot of SST anomalies is close to zero (-0.008$^{\circ}C$), which means that at equilibrium, the monthly mean of the previous month is a good approximation of the large-scale SST of the current month.

5.2.4 Experiments

To address the aims of this study, we parameterize the SST-heat flux coupling and the SST-wind stress coupling at the oceanic mesoscale. As described above in the control experiment the wind stress and temperature restoring time scale are constant in time and space, which is typical of ocean-only models. Then for each experiment, the parameterizatons allow mesoscale wind stress and air-sea heat flux feedback to vary in time and space. Details of how each parameterization is implemented in the model are given below.

The magnitudes of each of the two parameterized feedbacks are doubled to evaluate their sensitivity, and SST-heat flux feedback is isolated into either warm- or cold- core anomalies. A summary of the eight simulations is provided in Table 5.1 below. Both the experiments and control are run for 20 years, after a 10 year spin

up period, and are both initialized from the 80-year run described above.

Experiment name	Label	HF feedback	WS feedback
Control	CTRL	x	x
SST-HF	$1\lambda_m$	✓	x
SST-HF 2x	$2\lambda_m$	✓	x
SST-HF (Warm SST′ only)	${\lambda_m}^A$	✓	x
SST-HF (Cold SST′ only)	${\lambda_m}^C$	✓	x
SST-WS	$1\tau_m$	x	✓
SST-WS 2x	$2\tau_m$	x	✓
Both feedbacks 2x	$2\lambda_m$ + $2\tau_m$	✓	✓

Table 5.1: *A summary of all the experiments, and its corresponding label used in the results, with or without mesoscale heat flux (HF) or wind stress (WS) feedback.*

Mesoscale SST-heat flux feedback

Within the model, the heat flux feedback HFF (here denoted as λ) is inversely proportional to the restoring timescale (τ_{time}). We relate the restoring timescale to the magnitude of the heat flux feedback (HFF, λ) for each experiment using the following formula.

$$\lambda = \frac{C_p\ \rho\ H}{\tau_{time}} \tag{5.4}$$

where ρ is the reference density (999.8 kg/m^3), C_p is the ocean specific heat capacity (4000 J kg^{-1} K^{-1}), H is the mixed layer depth (m) and τ_{time} is the restoring timescale in seconds (Frankignoul, 1985). The heat flux feedback is dependent on the depth of the well-mixed surface layer that SST-induced air-sea heat fluxes act upon where a reduction in the damping rate, or timescale, can be set by the mixed layer depth (especially seasonally) (Hausmann et al., 2016).

In order to increase the HFF over mesoscale anomalies, we simply reduce the restoring timescale over mesoscale anomalies. In the control experiment, the restor-

ing timescale is set to 22 days uniformly. It is reduced by about 2.4 times to 9 days over SST anomalies in the HF experiment, labelled $1\lambda_m$. Outside of SST anomalies, the restoring timescale remains at the control value of $\tau_{time} = 22$ days. In the $2\lambda_m$ experiment, the restoring timescale over SST anomalies is reduced from the control value by about 4.8 times to 4.5 days.

We attempt to estimate the HFF λ from the restoring timescale in each experiment, using a mixed layer depth of 10 m, the spatial distribution of estimates of λ_m are shown in Fig. 5.5, for either the $1\lambda_m$ or $2\lambda_m$ experiment. These estimates of 1λ are similar to the linear regression of SST and HF anomalies as performed in Chapter 4 (not shown) and to previous studies e.g. Frankignoul (1985). Although, in the model the median mixed layer depth is closer to 30 m, rather than 10 m, we suggest as a result of the limitations of using an ocean-only model. Regardless of the true magnitudes of the HFF, we focus our experiments on increasing HFF (by either 2.4 or 4.8 times) over mesoscale anomalies, relative to the background field.

Mesoscale SST-wind stress feedback

The positive linear relationship between SST and zonal wind stress anomalies at the mesoscale is given as following (O'Neill et al., 2003, 2010, 2012; Chelton et al., 2004; Chelton and Xie, 2010; Small et al., 2008):

$$\tau_m = \alpha \, SST' \tag{5.5}$$

where α is the coupling coefficient with a realistic magnitude of 0.014 N m^{-2} K^{-1} in the Kuroshio Extension region, according to the observational study by O'Neill et al. (2012) (note a magnitude of 0.012 is found in the Gulf Stream region). In their study, QuikSCAT wind stress and AMSR-E SST observed monthly-averaged fields were used to calculate this relationship, with a resolution of 1/4° and after high-pass filtering the variables. Their results were also validated against three other datasets.

We can use equation 5.5 to parameterize the variation in localized wind stress anomalies. Mesoscale wind stress anomalies (denoted as τ_m) are therefore temperature-dependent and vary spatially and temporally, unlike the background wind stress.

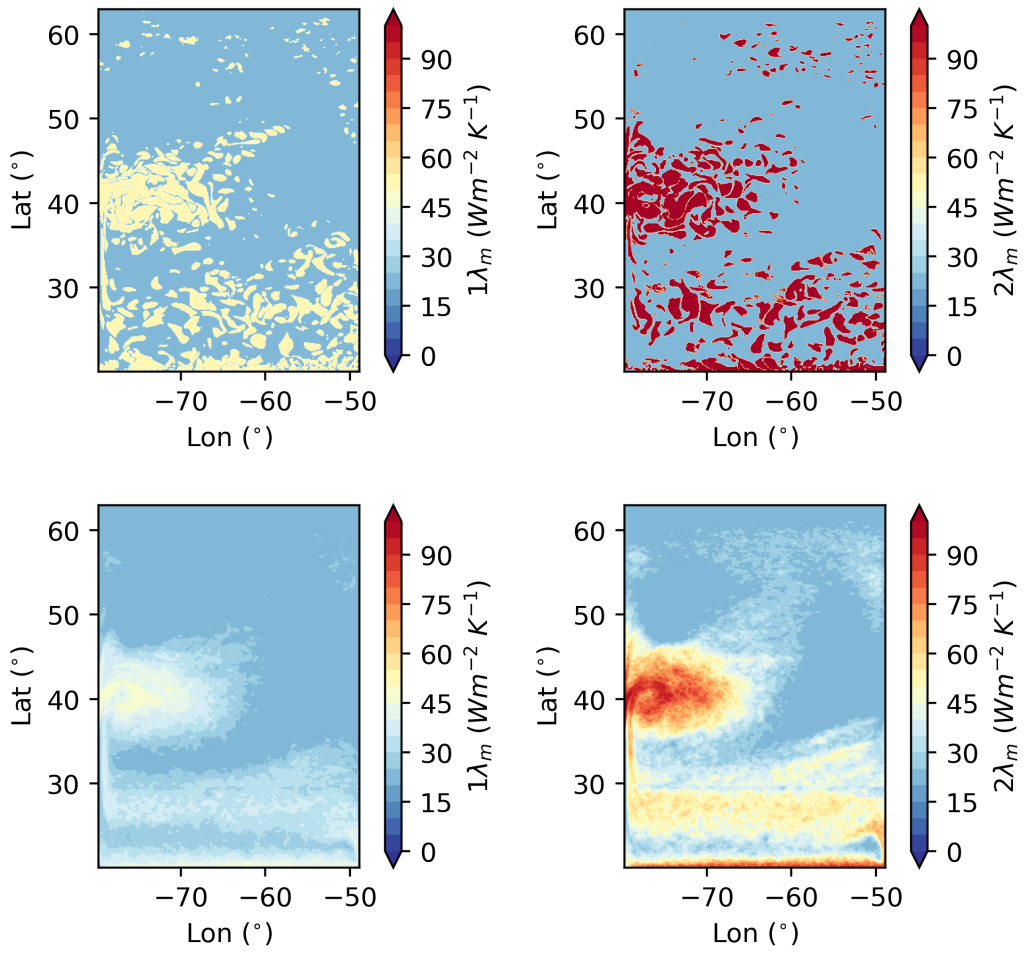

Figure 5.5: *The spatial distribution of estimates of λ (using a mixed layer depth of 10 m) for either the $1\lambda_m$ (left) or $2\lambda_m$ (right) experiment. The upper subplots are snapshots and the lower subplots present the time mean over the 20-year period.*

The direction of the background wind stress is also considered in the parameterization to ensure a positive SST-wind stress relationship is maintained for example, with a negative background wind stress.

In our set up, strong SST anomalies are capped at an absolute value of $5°C$ for the 2x τ_m experiment and $10°C$ for 1x τ_m to prevent unrealistically large values of τ_m. The wind stress error bars within the SST-wind stress relationship increase as the magnitude of the SST anomaly increases, and the maximum absolute SST anomaly in the observational study by O'Neill et al. (2012) is $2°C$. In real-

ity, seasonal variability increases the coupling coefficient α by up to 5 times in the Kuroshio region, although we exclude seasonal variability in our simplified set up.

Spatial maps of the anomalies of SST and mesoscale wind stress τ_m are shown in Fig. 5.6 at the final timestep. The addition of τ_m to the constant large-scale zonal wind stress forcing at the same final timestep is also displayed.

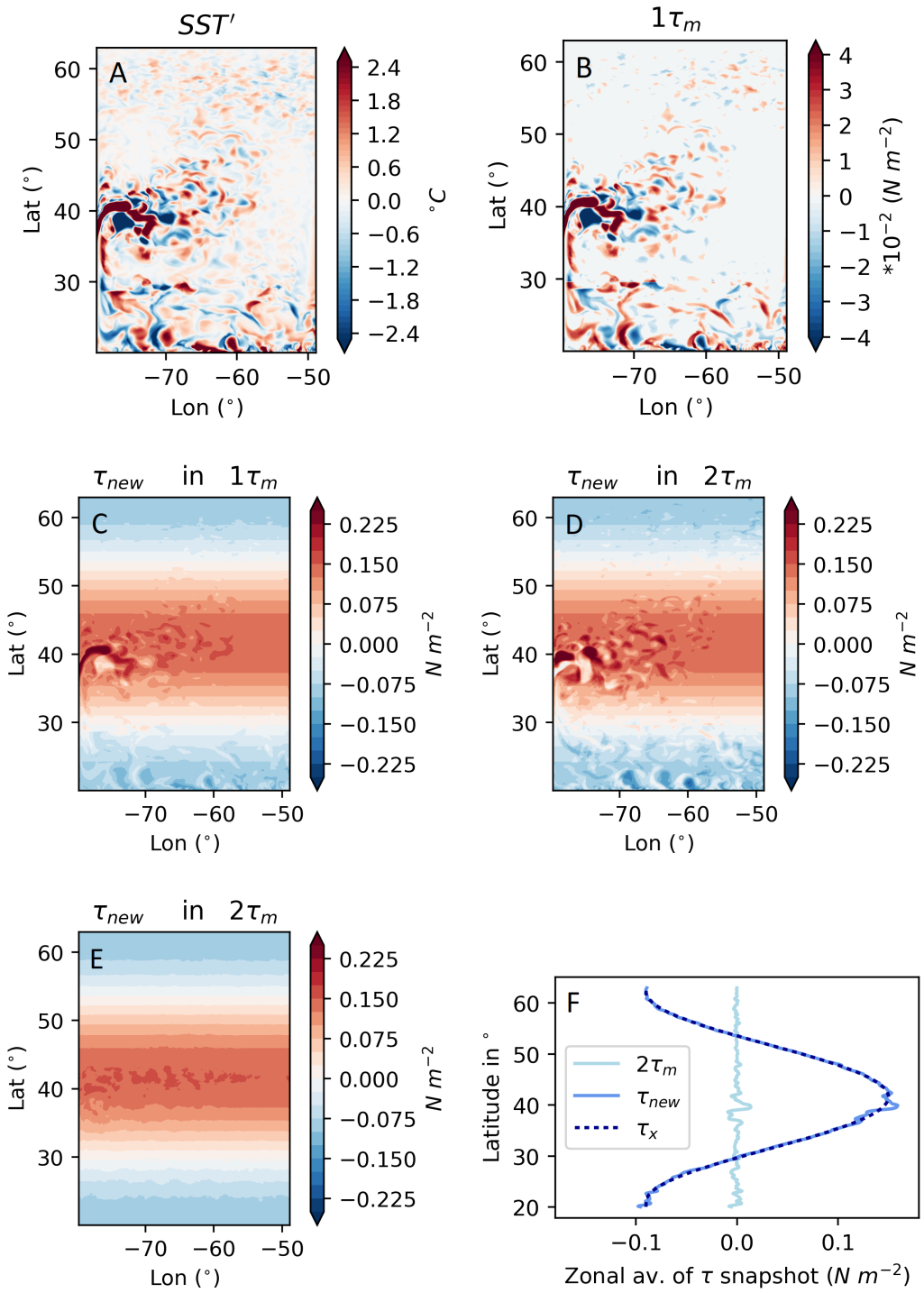

Figure 5.6: *Subplot (A) displays SST anomalies and (B) the corresponding wind stress over mesoscale anomalies in the "1τ_m" experiment at the final timestep. Subplots (C), (D) and (E) display the total wind stress (τ_{new}) combining both the background (τ_x) and mesoscale wind stress (τ_m). Subplot (C) displays τ_{new} in the "1τ_m" experiment and (D) in the "2τ_m" experiment, both plotted from the final timestep. Subplot (E) displays the time mean τ_{new} in the "2τ_m" experiment, and subplot (F) displays a zonal average of τ_{new} (solid dark blue line), τ_x (dotted) and τ_m (solid light blue) of snapshots in the "2τ_m" experiment at the final timestep.*

5.3 Results

First, we compare the impact of the two parameterizations of air-sea feedback over the local ocean, focusing on the dampening of EKE and SST anomalies (section 5.3.1). Second, the impact on the large-scale gyre circulation and WBC jet is evaluated (section 5.3.2), and followed by a comparison of the impact from either warm, or cold, SST anomalies only (section 5.3.3).

5.3.1 Impact on the local ocean

We begin by evaluating whether the local impact from the two thermal mesoscale air-sea feedbacks are consistent with previous studies. When including mesoscale wind stress feedback to the model, SST anomalies increase by a spatial and temporal average of 10% for $2\tau_m$ (16% for $1\tau_m$) relative to the control. When including mesoscale heat flux feedback (HFF) a decrease of 20% for the $2\lambda_m$ experiment (16% for $1\lambda_m$) in SST anomalies is found, commonly known as 'eddy dampening'. Similarly, the study by Hogg et al. (2009) identify an increase in localized Ekman pumping anomalies when increasing mesoscale wind stress feedback, and Ma et al. (2016) identify a localized reduction of eddy activity when increasing the HFF. As expected, by increasing mesoscale wind stress anomalies, the surface ocean becomes more energetic, while increasing small-scale heat flux feedback dampens SST.

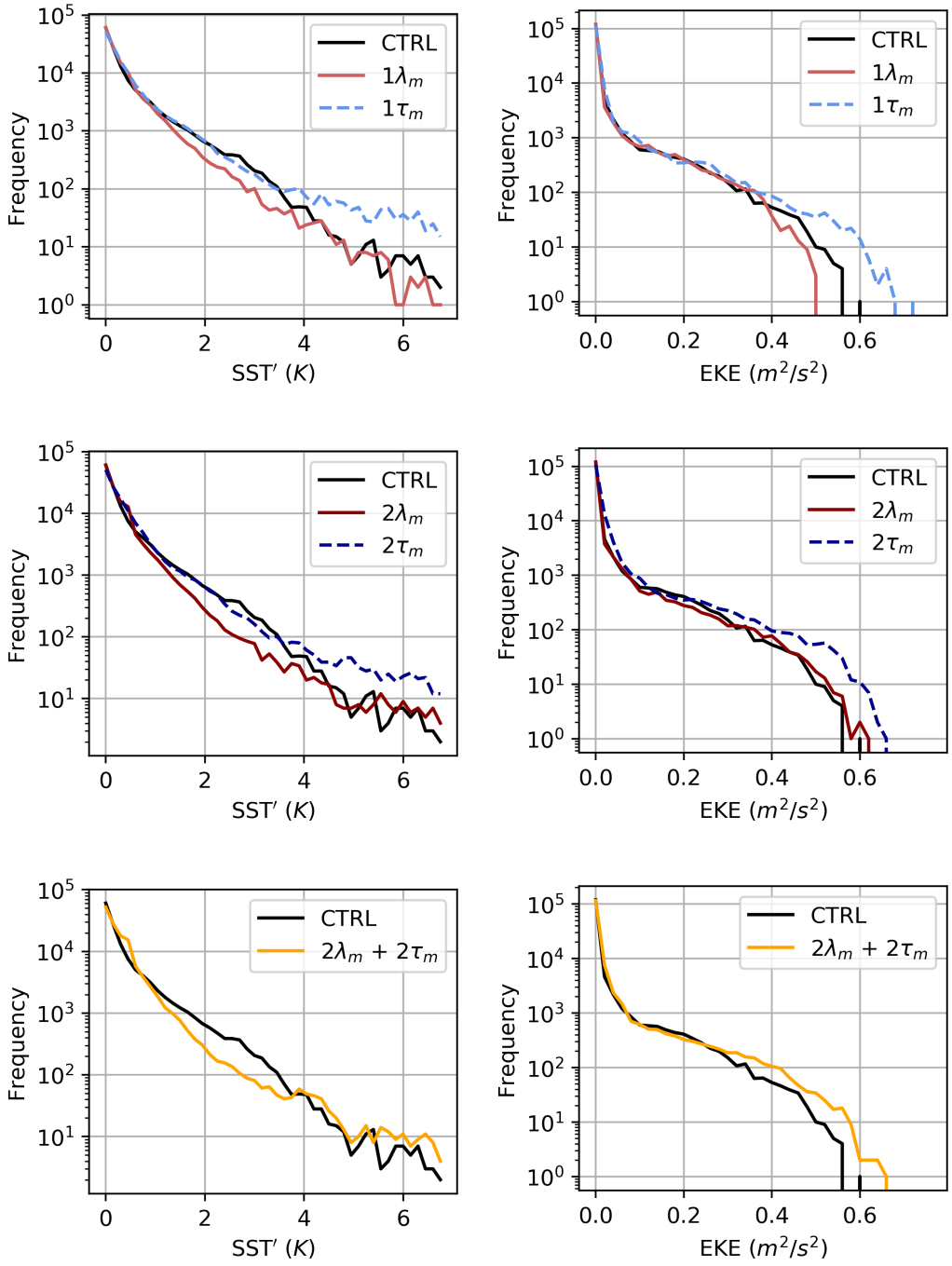

Figure 5.7: *Probability density functions of absolute values of SST anomalies (left column) and the vertically-averaged upper EKE, from surface to 240m depth (right) over the 20 year time period. The upper subplots display $1\tau_m$ (wind stress feedback, blue) and $1\lambda_m$ (HFF, red), the middle subplots display $2\lambda_m$ and $2\tau_m$ (darker corresponding colours) and the lower subplots displays both as marked (orange).*

The probability density functions of SST anomalies in each experiment in Fig. 5.7 (left column) shows the two feedbacks impact different SST magnitudes. HFF dampens most of the SST anomalies between about [1-4] K, found throughout the domain, with a maximum dampening of about 50% reduction in the number of eddies at 3 K for the $1\lambda_m$ experiment (63% for $2\lambda_m$) compared to the control. Instead, wind stress feedback mainly increases small number of large SST anomalies above about 4 K, found in the centre of the jet. There is a very small reduction in SST anomalies between about [2-3.5] K from wind stress feedback. When combining both effects ($2\lambda_m$ plus $2\tau_m$) the dampening of SST anomalies within [1-4] K dominates.

The dampening of mesoscale SST anomalies is reflected in changes in the upper EKE (here the EKE is vertically averaged from 240m to the surface) as shown in Fig. 5.7 (right). For the $1\tau_m$ experiment the increase in SST anomalies is reflected in a substantial increase in EKE by a spatial and temporal average of 29% for $2\tau_m$ (18.4% for $1\tau_m$). Similarly to SST anomalies, the largest EKE magnitudes above about 0.4 m^2 s^{-2} are increased, which are found around the jet extension (Fig. 5.4). Although, there is no clear distinction in the impact on EKE between the $1\tau_m$ and $2\tau_m$ experiments. Previous studies have debated the role of wind stress feedback on altering EKE, arguing surface current feedback plays a much more dominating role (Renault et al., 2019c). Instead, Byrne et al. (2015) and Jin et al. (2009) argue regionally, wind stress feedback does alter EKE magnitudes as found in our study. Similarly to our results, Hogg et al. (2009) identify an increase in EKE close to the jet separation when increasing wind stress feedback.

The impact of HFF on EKE is much smaller than the wind stress feedback, for the $1\lambda_m$ experiment and minimal when doubling the feedback for $2\lambda_m$ (Fig. 5.7). On average, EKE decreases by 13% for $2\lambda_m$ and 4% for $1\lambda_m$. These small changes in EKE in our set up do not reflect the 30% EKE reduction found in the global coupled Community Earth System Model (CESM), as a result of increased dissipation of eddy potential energy in Ma et al. (2016). Therefore, when combining both experiments there is a notable increase in larger EKE magnitudes as a result of wind

stress feedback.

In summary, mesoscale wind stress feedback has a dominant impact on EKE compared to mesoscale HFF. Contrary to previous studies, mesoscale wind stress feedback increases EKE, while mesoscale HFF dampens a wider range of SST anomalies found across the domain. We now go onto to evaluate the impact of these different localized changes on the mean WBC jet and gyre circulation.

5.3.2 Changes in gyre circulation and jet strength

The most striking impact of mesoscale feedbacks is the WBC jet separation latitude from the boundary. The vertically-averaged upper (0-240 m) mean kinetic energy (MKE) of the jet in the control experiment is shown in Fig. 5.8 (upper left), with the maximum zonal velocity of just under 1 m s^{-1} at 41.15°N. Despite small changes in mesoscale dampening locally when including HFF, the latitude of the maximum zonal velocity shifts northwards to 41.65°N in $1\lambda_m$ and further to 41.95°N in $2\lambda_m$, a maximum shift of about 88 km. The extent of the spatial shift is illustrated as a strong dipole when plotting the difference in MKE between $2\lambda_m$ and the control (Fig. 5.8, lower left). The northward shift is associated with a stronger narrower jet and a small increase in MKE near the boundary. The stronger jet is a consequence of the dampening of mesoscale activity. A stronger mean jet is required to balance the increased dissipation of eddy potential energy by air-sea heat fluxes (Ma et al., 2016; Small et al., 2020).

Further shifts in the latitude of the jet separation are found when including mesoscale wind stress feedback, although in the opposite direction. The increased EKE, i.e. eddy activity, appears to destabilise the jet by the increased transfer of energy from MKE to EKE, reducing its MKE near the boundary by a maximum of about 8%. This causes the jet separates from the boundary sooner, i.e. further south, and the maximum WSC to shift south (Fig. 5.8, middle right). A reduction in MKE along the jet is also found by Hogg et al. (2009) when increasing mesoscale wind stress coupling. The latitude of the maximum zonal velocity reduces to 40.15°N

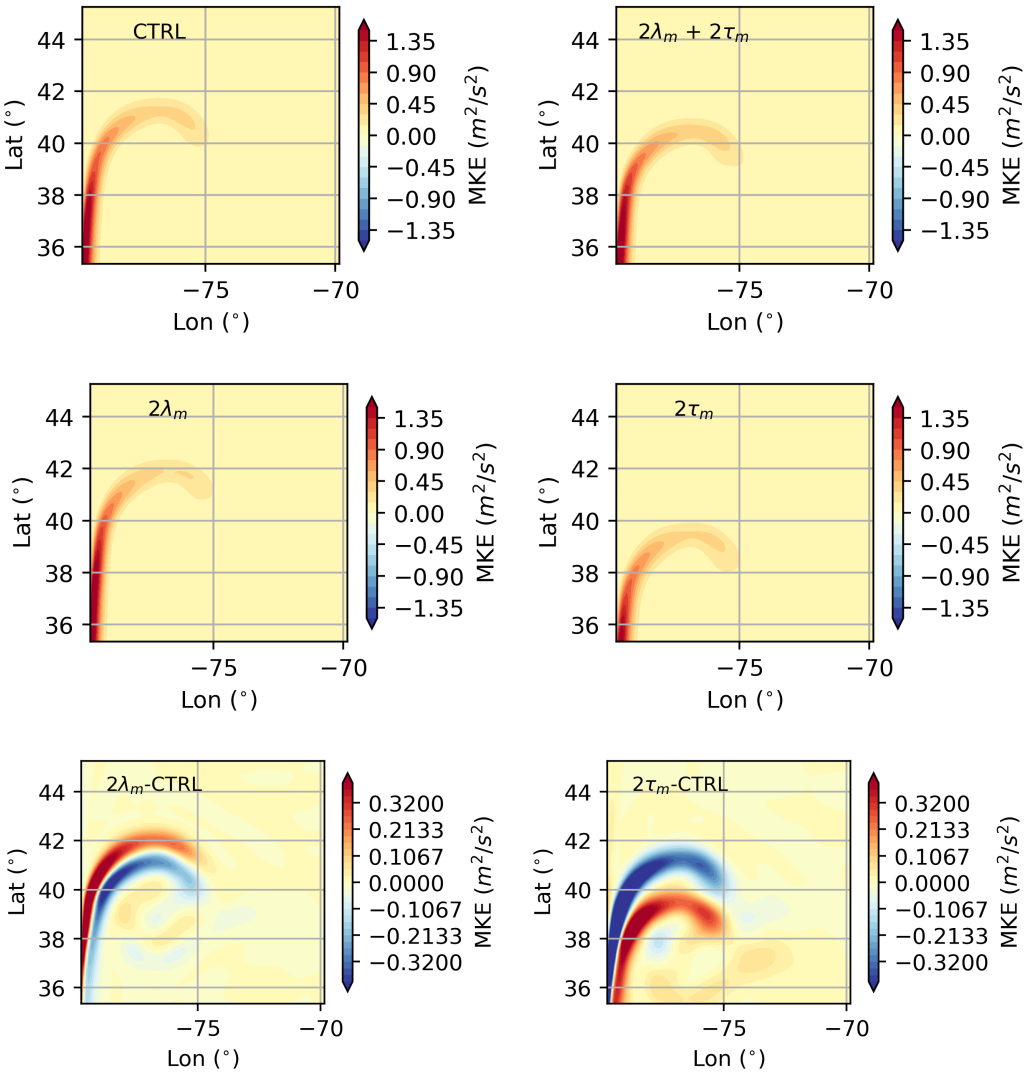

Figure 5.8: *Spatial maps of vertically-averaged upper (0-240m) mean kinetic energy (MKE, $m^2\ s^{-2}$) for each experiment as labelled, averaged over 20 years. The lower subplots present the difference where positive values mean the the addition of the mesoscale coupling coefficient increases MKE, compared to the control, and negative means the addition decreases MKE.*

in $1\tau_m$, and further to 39.65°N in $2\tau_m$, a shift of about 166 km, which is double the impact from HFF. This southward shift in the mean jet position is very similar to the southward shift in the peak of wind stress after adding mesoscale wind stress feedback ($\sim$ 189 km for $2\tau_m$), as shown in Fig. 5.6, lower right. Therefore,

when including both mesoscale feedbacks the large meridional shifts cancel out and the net jet separation shifts southwards by about 77 km (Fig. 5.8, upper right). The improvement in the jet separation in high-resolution models has been previous documented, but here we pinpoint the shift in the separation as a result of thermal mesoscale air-sea exchanges, and the role of HFF in preventing the jet shifting any further southwards (Chassignet and Marshall, 2008).

The increase in MKE in the jet after including mesoscale HFF is reflected further into the ocean interior (at about 66°W). At this longitude, mesoscale HFF (both in $1\lambda_m$ and $2\lambda_m$) causes a 50-60% strengthening of the jet velocity, after averaging over 20 years. This is shown in Fig. 5.9 where the relative change in the time-averaged U velocity (averaged $\pm$ 0.2° around the latitude with the maximum velocity) is plotted against longitude for each experiment. Note that increasing the latitudinal averaging (from $\pm$ 0.2°) slightly reduces in the percentage change, however the distribution of the curve is the same. The vertical grey lines in the upper left subplot display the zonal averaging region for the following subplots of U velocity in the figure. These subplots are centred on the maximum jet velocity in this region and display the increase in velocity of about 0.05 m s^{-1} in the $2\lambda_m$ experiment, compared to the control. Despite having no seasonality in our model, this is a similar magnitude of increase in velocity as found in Ma et al. (2016) in winter in the Kuroshio Extension region using the ensemble mean of the Coupled Regional Climate Model (CRCM) in their Fig. 2i. Note, this study only explores the impact on the jet in winter, when the mesoscale HFF is strongest in the Northern Hemisphere (shown in Chapter 4, Fig 4.17).

After including wind stress feedback, the jet velocity increases at this longitude as well, although to a smaller extent compared to HFF and with a wider structure (Fig. 5.9 middle and lower, right subplots). Therefore, when including both mesoscale feedbacks, the net effect is a strengthening of the jet of nearly 30% at this longitude (Fig. 5.9, orange curve). Similarly, the study by Ma et al. (2016) simulate a strengthening of the Kuroshio Current of between 20-40%.

Finally, mesoscale wind stress feedback causes a non-linear strengthening of

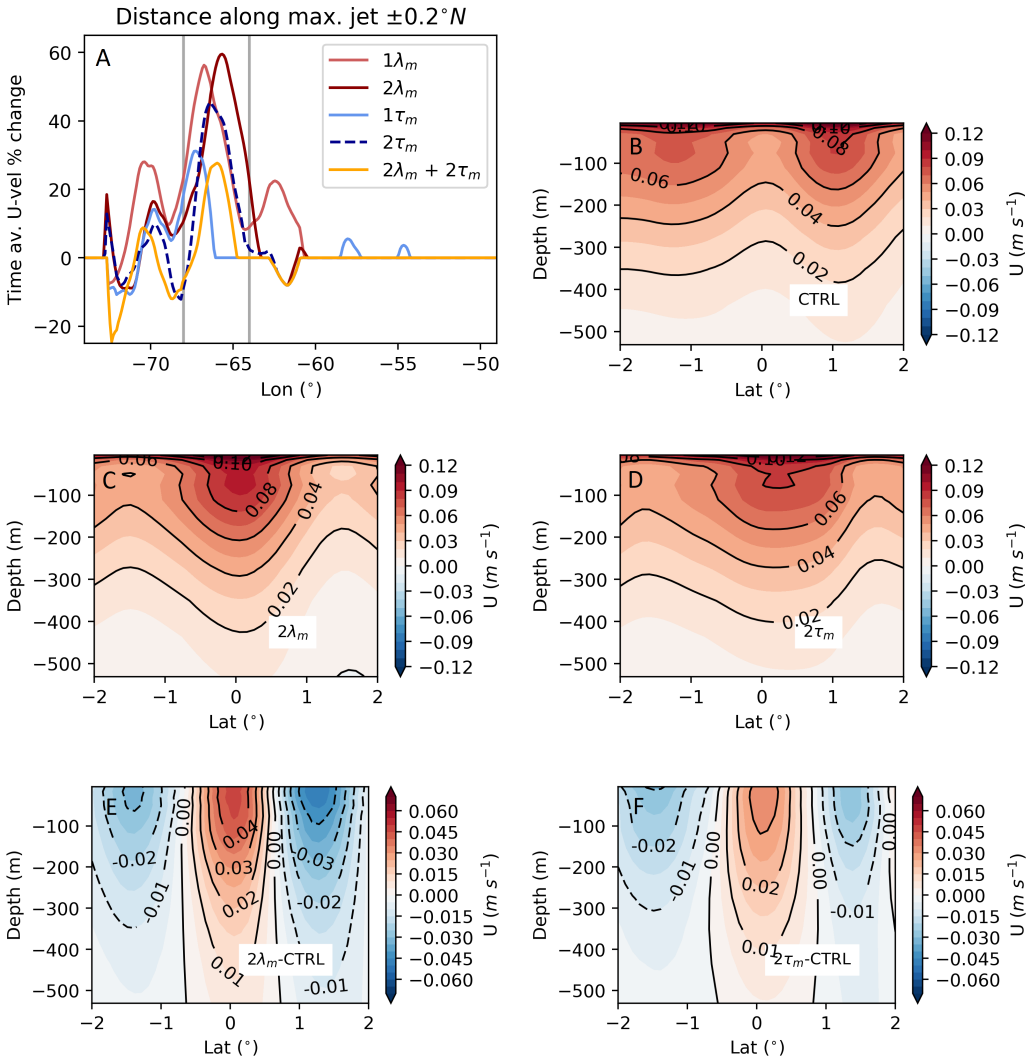

Figure 5.9: *Subplot (A) displays the relative change in the time-averaged U-velocity (± 0.2°N around the maximum value) against longitude for each experiment. The vertical grey lines indicate the zonal average used in the following subplots (B)-(F). Subplots (B), (C), and (D) display a vertical section of the zonal average of U-velocity (shm s^{-1}) centred on the latitude of the maximum jet velocity in the control, $2\lambda_m$ and $2\tau_m$ experiments respectively. Subplots (E) and (F) display the difference between each experiment and the control. All plots are time-averaged over the 20-year period.*

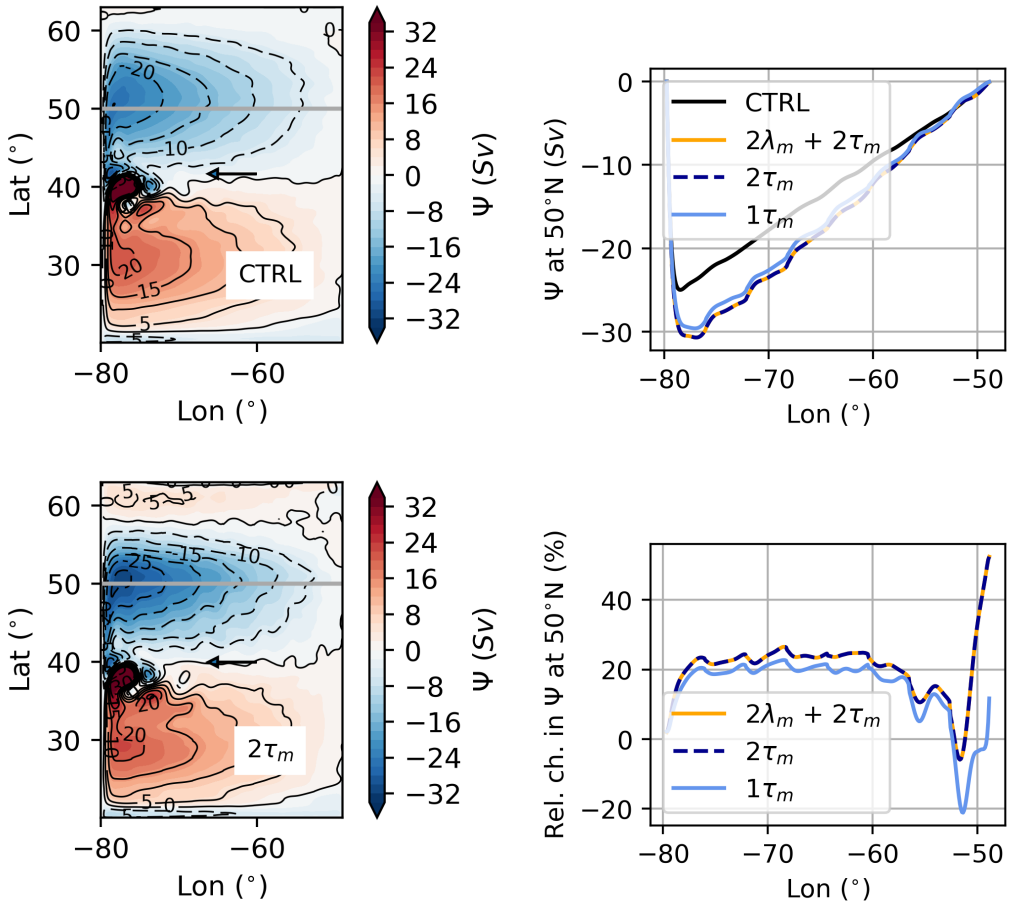

Figure 5.10: *Spatial maps of barotropic stream function (ϕ) in Sverdrups, with contours intervals of 5 Sv, over 20 years in the control experiment (upper left) and in $2\tau_m$ (lower left). The latitude of maximum zonal wind stress is shown by the black arrow. A longitudinal profile at 50°N is shown on the upper right (marked by the grey horizontal line on the maps) and the relative change in each experiment compared to the control is shown below.*

subpolar gyre circulation by about 5 Sverdrups at its maximum, and a consistent 20% increase across the subpolar gyre interior, when averaged over 20 years (Fig. 5.10). The increase in the subtropical gyre is about 1 Sverdrup, and may be related to the imbalance of vorticity across the domain, meaning the increased wind stress from mesoscale anomalies in the smaller region of the subpolar gyre has a larger impact on the circulation. Associated with the southward shift in wind stress

and mean jet, mesoscale wind stress feedback shifts the whole double gyre circulation southwards. The subpolar gyre strengthening seen is relatively insensitive to the strength of τ_m, as shown in the longitude profiles at 50°N in Fig. 5.10, right. This is potentially a result of the capping of the maximum values of τ_m for both experiments to stop τ_{new} becoming unrealistically large. The increase in gyre strength is contrary to the quasi-geostrophic (Q-G) model in Hogg et al. (2009), where decreases in MKE are associated with a 30-40% weakening of the circulation in both gyres. Here we show, although the MKE reduces and the jet destabilises close to the western boundary, there is no notable reduction in MKE across the gyre and instead the mean jet in the basin interior and gyre circulation both strengthen. In the study by Hogg et al. (2009) the symmetrical gyre response was likely to be a response of the symmetrical Q-G model and the lack of spatial shift in the circulation. Note that mesoscale HFF has no impact on the gyre circulation.

5.3.3 Warm vs cold anomalies

By isolating the mesoscale heat flux feedback (HFF) over either warm-core (λ_m^A) or cold-core (λ_m^C) anomalies, we find the impact of HFF increases slightly over cold-core anomalies. Cold-core anomalies provide a small increase in the dampening of SST anomalies (mainly between 1-4 K) compared to warm-core, as shown in the probability density function plot in Fig. 5.11. Here, the impact on EKE between either polarity is difficult to distinguish associated with the small impact from $1\lambda_m$, and cold-core anomalies produce a slightly stronger jet velocity at 66°W (not shown). This contrasts with previous work using coupled experiments, which highlight the importance of warm-core anomalies, associated with strong air-sea heat fluxes, and suggest cold-core anomalies have minimal impact, due to the enhanced stability of the atmospheric boundary layer (Ma et al., 2016; Bishop et al., 2020).

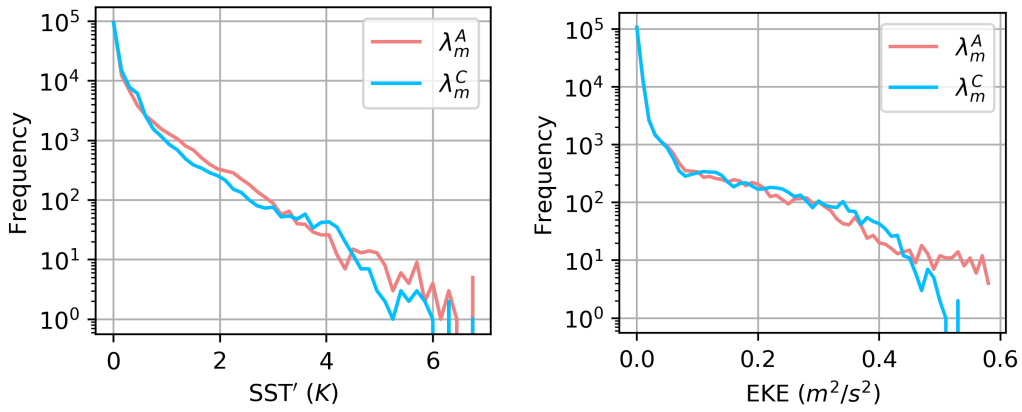

Figure 5.11: *Probability density functions of SST anomalies (left) and the vertically-averaged upper EKE, from surface to 240m depth (right) over 20 years, for warm-core (λ_m^A, pink) and cold-core (λ_m^C, blue) anomalies.*

5.4 Conclusions

In summary, we provide the first study to isolate and compare two thermal mesoscale feedbacks and their different impacts on the local and large-scale ocean, through the successful parameterization of each mesoscale feedback in the ocean-only MITgcm model. Our hypothesis that mesoscale SST-heat flux feedback (HFF) dominates in controlling the WBC jet velocity, relative to SST-wind stress feedback is supported. Mesoscale HFF dampens mesoscale SST anomalies by 20%, increases MKE in the jet close to the western boundary shifting the separation north, and causes an increase in the jet velocity up to nearly 60% further into the ocean interior. While the 20% strengthening of the subpolar gyre circulation is dominated by mesoscale wind stress feedback. Mesoscale wind stress feedback causes a significant 29% increase in eddy activity (EKE) and a large southern shift in the jet separation, due to a shift in the maximum wind stress. Therefore, both feedbacks are vital together because of their often competing influences.

An important distinction in this work compared to Hogg et al. (2009) is the 20% strengthening of the gyre circulation from mesoscale wind stress feedback,

rather than the weakening found in their quasi-geostrophic set up. The asymmetrical response between the subpolar and subtropical gyres is also unique.

We acknowledge the limitations of this study. Although it is simpler to isolate and parameterize the two mesoscale thermal air-sea feedbacks using an ocean-only model, because two feedbacks cannot impact each other this way, no doubt we exclude the two-way feedbacks and energy transfers between the ocean and atmosphere and any atmospheric variability. Ocean-only models typically have too much energy near the WBC separation point, and the jet penetration into the ocean interior is not realistic (Özgökmen and Chassignet, 2002). Furthermore, we exclude mesoscale surface current-wind stress interactions, which could compete against the thermal feedback response. Finally, further work could explore the sensitivity of the results to the choice of the minimum SST threshold (currently 0.5°C).

In our set up, we acknowledge there is a difference in the integrated vorticity across the domain causing an imbalance of vorticity. Although the wind stress input is symmetrical, its impact is larger in the subpolar gyre, due to a smaller integrated area associated with the spherical coordinates of the domain. Although our results did not extend to evaluate the impact of mesoscale SST-wind stress feedback on the vorticity imbalance, we suggest the existing vorticity imbalance could be important and is suggested for future work.

Although we show thermal mesoscale feedback has a significant impact on the strengthening of subpolar gyre circulation, whether mesoscale feedback is accountable for the subpolar gyre intensification found across a range of HighResMIP state-of-the-art climate models, compared to coarser resolutions, is difficult to conclude (Meccia et al., 2021; Jackson et al., 2020). Many other factors are present in coupled climate models, compared to our simplified set up, including improved convection in the Labrador Sea and improved bathymetry (Jackson et al., 2020). Instead, we can conclude that mesoscale feedback produces a clear southward shift of the WBC separation, as found in the improved Gulf Stream separation in a higher 1/12° resolution climate model, compared to eddy-permitting 1/4° (Grist et al., 2021). The shift in the jet has important implications for European weather and climate

(Moreno-Chamarro et al., 2021). Although, in climate models topography plays a significant role in the jet separation (Chassignet and Marshall, 2008).

It would be interesting to take this work further and to explore the role of topography in the jet separation for the different mesoscale feedbacks, and to extend to other geographical regions. Furthermore, the magnitude of the two mesoscale feedbacks varies dramatically depending on the season. In winter, in the Kuroshio region mesoscale HFF is more enhanced, and the mesoscale wind stress coupling coefficient increases up to 5 times (Ma et al., 2016; O'Neill et al., 2012). Previous work has shown in regions with a large seasonal cycle, the sink of eddy potential energy (EPE) from mesoscale anomalies is outweighed by seasonal generation of EPE, therefore the energy budget influencing the strength of MKE within the jet may change (Bishop et al., 2020). Finally, our parameterizations could be made more complex to mimic a coupled ocean-atmosphere system by coupling the ocean to a slab 1-layer atmosphere, to include air-sea adjustment between SST and surface air temperature. As it is still uncertain when mesoscale air-sea interactions will be able to be explicitly resolved in the current generation of CMIP climate models, our results hold important indications for what needs to be parameterized until then.

5.5 Chapter Appendix: MITgcm viscosity and advection scheme

The ability to resolve a realistic WBC depends on model viscosity (Chassignet and Gent, 1991). The viscosity operator used in this set up combines both the horizontal Laplacian eddy viscosity (A_h, with units of m^2 s^{-1}) with biharmonic viscosity (A_4, with units of m^4 s^{-1}). According to Chassignet and Marshall (2008), this combination produces the best WBC separation and penetration into the ocean, by combining the scale-selective feature of the biharmonic operator, with the dampening at larger scales (from the Laplacian operator). In addition, the combination allows a reduction of the Laplacian operator A_h by up to 50%, which is useful for high resolutions to reduce dissipation. Generally, viscosity is kept small enough so the model remains stable for horizontal friction at the given timestep, as shown in equation 5.6.

$$S_l = 2(\frac{4\ A_h \Delta t}{\Delta x^2}) < 0.6 \tag{5.6}$$

In our setup, $S_l \approx 0.01$ using the Laplacian operator A_h = 48 m^2 s^{-1}. Finally, the viscosity coefficient A_h plays an important role to ensure the width of the theoretical Munk frictional boundary layer width (M_w) is larger than the horizontal grid spacing to ensure it can be resolved correctly, according to:

$$M_w = \frac{2\pi}{\sqrt{3}} (\frac{A_h}{\beta})^{1/3} \tag{5.7}$$

where $\beta = 10^{-11}\ s^{-1}m^{-1}$, the variation of the Coriolis parameter with latitude. For our configuration where $A_h = 48$, the boundary layer width $M_w \approx 61$ km. At the southern boundary of our domain, where $\Delta x \approx 10.4$ km, the boundary layer is resolved across at minimum of 5 grid cells.

There is not one 'best' advection scheme to use in a high-resolution model. The scheme chosen is fundamental to determine how tracers (e.g. temperature) are advected (or transported) across each grid cell face in the Arakawa C-grid. A higher order advection scheme provides more accuracy however scale-selective diffusion

might be needed. If a solution has a propagating front, a flux limited scheme is needed. For this set up, we use the 'third order direct space-time flux limiter' advection scheme. It is multi-dimensional and non-linear. The 'limiter' feature removes false extrema, while 'multi-dimensional' means the stability is determined by the maximum Courant number of each dimension. Being non-linear means the scheme is stable at high Courant numbers (useful for small time-stepping) but at low Courant numbers, amplitude is kept in sharp peaks due to diffusion.

Chapter 6

Conclusions and Outlook

This thesis has met its overarching aims first, to improve current understanding of feedback on the local and large-scale ocean from mesoscale air-sea exchanges and second, to evaluate how well high-resolution models represent mesoscale eddies and their interaction with the atmosphere. In particular, the three key research gaps and thesis priorities, identified in Chapter 1, have been addressed to advance our understanding in this field. Here, we provide a summary of the key novel results identified in this thesis, and their significance for the wider field beyond mesoscale exchanges (section 6.1), an evaluation of the sensitivity of those results to the dataset and method chosen (section 6.2) and an indication of what questions remain and how these conclusions can shape future research (section 6.3).

The three completed thesis objectives are:

- How does the representation of coherent mesoscale eddy properties change with increased model ocean resolution ? (Chapter 3)
- What is the SST-THF feedback over coherent mesoscale eddies globally, and is it dependant on the ratio of ocean-atmosphere grid resolution ? (Chapter 4)
- How do mesoscale SST-induced air-sea exchanges (SST-wind stress and SST-heat fluxes) impact mid-latitude gyre circulation ? (Chapter 5)

To successfully evaluate each question, we first adapted an algorithm to isolate and track coherent mesoscale eddies in the state-of-the-art climate model HadGEM3-GC3.1. This provided a global dataset of individually tracked coherent mesoscale eddies, which was vital to Chapters 3 and 4, and provided an ideal set up for the rest of the thesis. In addition, the eddy tracking algorithm is now available (through M. Roberts) to evaluate the representation of eddy activity in future models, such as the next generation coupled 10 km ocean-atmosphere Met Office climate and numerical weather prediction (NWP) models scheduled for 2022. Next, a composite-averaging technique was chosen to efficiently identify corresponding ocean and atmospheric variables associated with these tracked eddies, across a range of resolutions. Finally, using the results from the high-resolution climate model gained in Chapter 4, we were able to set up and parameterize mesoscale air-sea heat flux feedback, alongside mesoscale SST- wind stress feedback. In the MITgcm ocean-only model, this set up was designed to allow evaluation of the impact from each feedback on the large-scale ocean circulation, something that would have been difficult to isolate from other feedbacks in HadGEM.

6.1 Key novel results

- As we move to higher ocean resolutions in state-of-the-art climate models (Hewitt et al., 2020), we provide a quantification of how well 1/12° ER_{sim} and 1/4° EP_{sim} represent mesoscale eddies. The ER_{sim} and EP_{sim} generate 63% and 40% of the eddies found in observations respectively, lacking in gyre interiors and at eastern boundary upwelling systems. Advantages of the ER_{sim}, compared to EP_{sim}, depend on the properties and region of interest. Genesis rate and size of the eddy populations are clear examples where the ER_{sim} improves upon EP_{sim}, likely because of a better representation of the mean state in eddy-energetic regions.

- Contrary to expectation, EP_{sim} simulates a significant population of eddies

up to the high latitudes where the model grid-scale is larger than the Rossby radius of deformation (Hallberg, 2013). These eddies likely grow on scales set by the smallest combination of grid-points that allows instability, and highlight the ability to perform polar mesoscale research using the EP_{sim}.

- Compared to EP_{sim} and observations, this work demonstrates eddies are significantly smaller in ER_{sim}, scaling well with the minimum of either R_d or the Rhines scale. Although, the spatial impact on the atmospheric boundary layer and mesoscale air-sea THF feedback is much larger in these eddies than indicated by the eddy radius. Therefore, correctly simulating the smaller eddies in ER_{sim} is still vital for air-sea exchanges.

- We suggest less EKE is contained within coherent mesoscale eddies in ER_{sim} and EP_{sim}, compared to observations, although eddy size is likely to be over-estimated in AVISO observations by a factor 2 which affects our estimates. EKE trapped within the smaller coherent eddies within ER_{sim} ($\sim$ 16 %) is doubled compared to EP_{sim} ($\sim$ 8 %) globally. Therefore, first, we suggest caution when evaluating eddy size using the observational AVISO and second, we highlight most EKE is found outside of coherent mesoscale eddies in the ER_{sim}, EP_{sim} and observations.

- An understanding of how long mesoscale eddies live is fundamental to represent the transport of heat, momentum and nutrients in the ocean and to parameterize the eddy residence time, such as recent work by Marshall and Zhai (2021) and Samelson et al. (2020). A significant result in this thesis is the over-estimation of the survival rate of eddies in the ER_{sim}, especially in the Southern Ocean. Our analysis suggests that as resolution increases, allowing more vigorous eddies and a lower viscosity, the absence of dissipation mechanisms may become problematic and introduce biases in eddy lifetime. In addition, when coupling the same ER ocean to a higher resolution atmosphere (N512-12) eddy lifetimes reduce, associated with an increase in mesoscale air-sea THF feedback.

- We produce the first estimate of THFF over coherent mesoscale eddies. For the highest ocean-atmosphere resolution available (N512-12), the THFF over mesoscale eddies is estimated at 35-45 W m^{-2} K^{-1} even in small-amplitude eddies, which are dominated by changes in LHF rather than SHF. Correctly simulating the THFF over mesoscale eddies is fundamental to represent realistic mesoscale SST anomalies within eddies and to replicate their interaction with the local and large-scale atmosphere, as well as the feedback onto the eddy itself.

- Choosing the optimal ratio of ocean-atmosphere resolution in coupled NWP and climate models is critically important for future research, especially as the atmospheric Met Office model core is proposed to change from the UM to LFRic by 2025 (Tim Graham, personal communication). We demonstrate how the regridding of SST from the ocean to atmosphere grid can underestimate the eddy-induced THFF by 20 to 80%. Importantly, this low bias increases with the ratio between atmospheric and ocean resolutions, implying that increasing the oceanic resolution at constant atmospheric resolution can actually degrade the solution, at least in the representation of air-sea feedbacks. The low bias in the α_O feedback, particularly in N216-12, suggests eddy SST anomalies are not dampened enough in the model, which may explain the artificially large eddy lifetimes found in N216-12 in Chapter 3. We advise, when fully resolving mesoscale air-sea exchanges, that air-sea heat fluxes should be calculated on the finer-scale oceanic grid to better carry SST variability on the ocean grid into the atmosphere. To conclude, the results have contributed to a proposal by Tim Graham at the Met Office in an attempt to run a high-resolution coupled NWP model at the same grid resolution.

- Finally, by producing the first study to parameterize two thermal mesoscale air-sea feedbacks in a single ocean-only model, we can isolate the different feedbacks on the large-scale ocean. We show mesoscale HFF dampens mesoscale SST anomalies by 20%, increases mean kinetic energy in the west-

ern boundary current (WBC) jet close to the boundary shifting the separation north, and causes an increase in the jet velocity up to nearly 60% further into the ocean interior. While the 20% strengthening of the subpolar gyre circulation is dominated by mesoscale wind stress feedback. Mesoscale wind stress feedback causes a significant 29% increase in eddy activity (EKE) and a large southern shift in the jet separation, due to a shift in the maximum wind stress. Therefore, both feedbacks are vital together because of their often competing influences. Together both mesoscale feedbacks produce a southward shift of the WBC separation, as found in the improved Gulf Stream separation in a higher 1/12° resolution climate model, compared to eddy-permitting 1/4° (Grist et al., 2021). The shift in the jet has important implications for European weather and climate. As it is still uncertain when mesoscale air-sea interactions will be able to be explicitly resolved in high-resolution coupled climate models, our results hold important implications for what needs to be parameterized until then.

The reduction in eddy SST dampening from mesoscale SST-THF feedback found in Chapter 4 may explain the overestimation of eddy lifetime and changes in the eddy life cycle found in Chapter 3, especially when the ratio of ocean-atmosphere grid resolution increases in N216-12 (labelled ER in Chapter 3). This is further supported by the reduction in eddy lifetime found in the N512-12 configuration, with a reduced ratio of ocean-atmosphere resolution. Although, the observational benchmark of eddy lifetimes may also be underestimated (specifically south of 40°S), due the post-processing of the dataset as discussed previously. The reduction in eddy SST dampening from mesoscale SST-THF feedback found in Chapter 4 appears to have little impact on the eddy amplitudes found in Chapter 3.

The southward shift in the WBC jet separation driven by mesoscale air-sea coupling (Chapter 5) may also be found in the coupled climate model HadGEM3-GC3.1, used in Chapters 3 and 4. Similarly, Grist et al. (2021) find a southward shift of the Gulf Stream separation in a higher 1/12° resolution configuration of

HadGEM3-GC3.1, compared to eddy-permitting 1/4° resolution. If true, the spatial distribution and properties (i.e. EKE, size and lifetime) of coherent mesoscale eddies found in Chapter 3 may be altered depending on the impact on the large-scale ocean from mesoscale air-sea coupling (Chapter 5). However, at this stage, our results from Chapter 5 use a simple ocean-only box model and it is difficult to compare directly to the much more complex earth system model of HadGEM3-GC3.1, for example topography will play a defining role in determining the WBC separation latitude.

6.2 Sensitivity of results to dataset and method

As with most scientific studies, there are limitations to the results. Here, we briefly discuss the sensitivity of the results to the quantity and quality of the datasets used, and the reliability of some of the methods used. Specifically, the limitations of the methods are addressed in terms of the eddy tracking algorithm and the spatial filtering applied for Chapters 3 and 4, and the mesoscale feedback parameterizations used in Chapter 5.

A major drawback of observational altimeter gridded SSH dataset is small-scale features can be smoothed out, during the interpolation and post-processing of the dataset, which reduces the effective resolution of the SSH dataset as explored in Chapter 3. We can be more certain eddy spatial sizes are biased too large (between a factor of 2 and 4) in observational data, and we speculate the peak eddy amplitudes, eddy lifetimes and EKE may be biased low due to the smoothing of SSH data. Along-track datasets are more realistic, as they are subjected to less post-processing, however do not have the spatial coverage to identify mesoscale eddies. It is a trade-off between resolution and data coverage. Resolution also reduces with latitude, causing geographical biases in the eddy properties, and throughout the 20 year time period we studied, as the number and quality of the satellite altimeters improved. So far, merging multiple satellites together (e.g. AVISO dataset) has improved the realism of the dataset, however the future release of the SWOT altimeter

will increase the global spatial resolution and reduce the post-processing and interpolation. Observational data is often used as a benchmark for model comparison, therefore should be a priority for future research. Some of the biases in the eddy properties (e.g. size, amplitude, lifetime, etc.) listed above could be quantified in future work, by regridding the model output using the same approach used by AVISO and evaluating its impact compared to if no regridding was performed, however it is outside the scope of this thesis.

Need to explain that you would then put the data back onto a grid using the same approach as used by AVISO and see what impact this has on the ”model based” results

Within climate models, we acknowledge no model is perfect and there are lots of biases and compensating errors in coupled ocean-atmosphere models. This thesis uses a single climate model, HadGEM3-GC3.1, and it would be useful in the future to replicate some of this work using other state-of-the-art climate models to explore their ability to represent the oceanic mesoscale and mesoscale air-sea feedbacks, particularly regarding the regridding of SST from the ocean to the atmosphere. However, HadGEM is a commonly used climate model and its ability to represent the mesoscale highlights its strengths and limitations. Finally, mesoscale air-sea heat flux feedback has large seasonal and geographical variations. For future research, it would be interesting to split the global estimates provided in Chapter 4 into different regions, and to repeat the experiments in Chapter 5 in the Southern Ocean and Agulhas retroflection.

It is likely that some of our results (e.g. eddy counts and size) are dependent on our choice of eddy detection algorithm. However we have attempted to minimize its impact by applying the same algorithm to models and observations and focus our analysis on differences/similarities rather than the absolute values. Furthermore, the magnitudes of the mesoscale anomalies are slightly dependent on the method of the spatial filtering. To circumvent this limitation the filtering varies with each ocean or atmosphere grid resolution however, the filtering does not take into account the variation of grid box size with latitude. This means variables at the highest latitudes

are slightly under filtered and remain larger (i.e not as well smoothed out) relative to lower latitudes. Although this causes small spatial biases in the filtered anomalies, the impact on the global results is minimal.

Finally, the MITgcm model is a simple ocean-only set up, and represents an important limitation for the realism of mesoscale modelling. Whether similar conclusions from Chapter 5 are found in a more realistic ocean model remains to be determined. Potential improvements would be to couple the ocean to an interactive slab ABL (e.g. 'cheapABL' for the MITgcm model). This provides a time lag allowing air temperature to respond to the air-sea heat fluxes. Increasing the ocean resolution, adding seasonality and adding a more realistic representation of the WBC, by either tilting the model boundary or adding realistic topography, may impact the shift in the WBC separation induced by mesoscale feedbacks.

In summary, it is important to interpret the results of this thesis relative to their sensitivity on the dataset and method used. Despite these limitations this body of work presents a range of original, robust research which makes a significant contribution to oceanic mesoscale research.

6.3 Outlook

To finish, the research presented here has answered the thesis objectives and advanced our understanding of first, how well mesoscale eddies, and their interaction with the atmosphere, are represented in a current state-of-the-art climate model and second, evaluated the impact of different mesoscale air-sea exchanges on the large-scale ocean.

The prospects for explicitly resolving mesoscale air-sea feedbacks in climate models are promising. In addition to an eddy-resolving ocean resolution of 1/12° (or higher) and an improved mean state, these results highlight a high corresponding atmospheric resolution is needed, to resolve the impact of the oceanic mesoscale in the ABL, to accurately represent mesoscale air-sea feedbacks, i.e. by reducing the ratio of ocean-atmosphere grid resolution as much as possible. It will be interesting

to rerun some of my results (especially from Chapter 4) on the latest state-of-the-art coupled climate model with an approximate 10 km atmosphere and ocean resolution, recently run by Malcolm Roberts (personal communication). Until those highly computationally expensive climate models become mainstream in upcoming CMIP projects, there is ample room to parameterize the mesoscale air-sea interactions, and their impact on the local and large-scale ocean, for coarser resolutions as found in Renault et al. (2019c) for mesoscale surface current-wind stress feedbacks.

Whether we can trust models or observational datasets more when evaluating mesoscale air-sea coupling and feedbacks remains debated. Reoccurring themes throughout this thesis are the limitations in the use of observational altimeter data and the sensitivity of numerical model results to resolution, which highlights there are still challenges in accessing the consistency of these datasets. In the future, a finer resolution observational dataset, to capture smaller mesoscale eddies with radii below about 40 km and potentially more realistic eddy lifetimes and life-cycles, will greatly aid this current research and produce a more reliable benchmark for state-of-the-art climate models to aspire towards.

We hope the conclusions presented in this thesis will shape future research, particularly with respect to what the optimal ocean-atmosphere resolution should be in coupled climate models to fully resolve the impact from mesoscale air-sea exchanges. As improved higher resolution observational datasets, i.e. Archer et al. (2020), and submesoscale resolving coupled models become available in the future, it would be interesting to progress and build on this work (Klein et al., 2019). To date, no study has explored air-sea exchanges over oceanic submesoscale features.

Bibliography

Abel, R., Greatbatch, R. J., Hewitt, H., and Roberts, M. J. (2017). Feedback of mesoscale ocean currents on atmospheric winds in high-resolution coupled models and implications for the forcing of ocean-only models. *Ocean Sci. Discuss*, Submitted(April):1–22.

Abernathey, R. and Haller, G. (2018). Transport by Lagrangian Vortices in the Eastern Pacific. *Journal of Physical Oceanography*, 48:667–685.

Abernathey, R., Marshall, J., and Ferreira, D. (2011). The Dependence of Southern Ocean Meridional Overturning on Wind Stress. *Journal of Physical Oceanography*, 41(12):2261–2278.

Altimetry, A. (2017). Mesoscale Eddy Trajectory Atlas Product Handbook. SALP-MU-P-EA-23126-CLS. Technical report, AVISO+ Satellite Altimetry Data, France.

Amores, A., Monserrat, S., Melnichenko, O., and Maximenko, N. (2017). On the shape of sea level anomaly signal on periphery of mesoscale ocean eddies. *Geophysical Research Letters*, 44(13):6926–6932.

Arbic, B. K., Polzin, K. L., Shriver, J. F., Scott, R. B., and Richman, J. G. (2013). On Eddy Viscosity, Energy Cascades, and the Horizontal Resolution of Gridded Satellite Altimeter Products*. *Journal of Physical Oceanography*, 43(2):283–300.

Archer, M. R., Li, Z., and Fu, L. L. (2020). Increasing the Space–Time Resolution of Mapped Sea Surface Height From Altimetry. *Journal of Geophysical Research: Oceans*, 125(6):1–18.

Banzon, V., Smith, T. M., Liu, C., and Hankins, W. (2016). A long-term record of blended satellite and in situ sea surface temperature for climate monitoring, modeling and environmental studies. *Earth System Science Data Discussions*, 8(2004):165–176.

Bars, D. L., Dijkstra, H. A., and Ruijter, W. P. M. D. (2014). Impact of the Indonesian Throughflow on the Atlantic Meridional Overturning Circulation. *Ocean Science*, 16(5):5470.

Bates, M., Tulloch, R., Marshall, J., and Ferrari, R. (2014). Rationalizing the Spatial Distribution of Mesoscale Eddy Diffusivity in Terms of Mixing Length Theory. *Journal of Physical Oceanography*, 44(6):1523–1540.

Bellucci, A., Athanasiadis, P. J., Scoccimarro, E., Ruggieri, P., Gualdi, S., Fedele, G., Haarsma, R. J., Garcia-Serrano, J., Castrillo, M., Putrahasan, D., Sanchez-Gomez, E., Moine, M.-P., Roberts, C. D., Roberts, M. J., Seddon, J., and Vidale, P. L. (2021). Air-Sea interaction over the Gulf Stream in an ensemble of High-ResMIP present climate simulations. *Climate Dynamics*, 56(634):2093–2111.

Biastoch, A., Lutjeharms, J. R., Böning, C. W., and Scheinert, M. (2008). Mesoscale perturbations control inter-ocean exchange south of Africa. *Geophysical Research Letters*, 35(20):2000–2005.

Bishop, S. P. and Bryan, F. O. (2013). A Comparison of Mesoscale Eddy Heat Fluxes from Observations and a High-Resolution Ocean Model Simulation of the Kuroshio Extension. *Journal of Physical Oceanography*, 43(12):2563–2570.

Bishop, S. P., Small, R. J., and Bryan, F. O. (2020). The Global Sink of Available Potential Energy by Mesoscale Air-Sea Interaction. *Journal of Advances in Modeling Earth Systems*, 12(10).

Bishop, S. P., Small, R. J., Bryan, F. O., and Tomas, R. A. (2017). Scale dependence of midlatitude air-sea interaction. *Journal of Climate*, 30(20):8207–8221.

Bjerknes, J. (1964). Atlantic Air-Sea Interaction. *Advances in Geophysics*, 10.

Braby, L., Backeberg, B., Krug, M., and Reason, C. (2020). Quantifying the Impact of Wind-Current Feedback on Mesoscale Variability in Forced Simulation Experiments of the Agulhas Current Using an Eddy-Tracking Algorithm. *Journal of Geophysical Research: Oceans*, 125(1):1–23.

Brannigan, L. (2016). Intense submesoscale upwelling in anticyclonic eddies. *Geophysical Research Letters*, 43(7):3360–3369.

Brannigan, L., Marshall, D. P., Naveira Garabato, A. C., George Nurser, A., and Kaiser, J. (2017). Submesoscale instabilities in mesoscale eddies. *Journal of Physical Oceanography*, pages JPO–D–16–0178.1.

Bretherton, F. P. (1982). Ocean climate modeling. *Progress in Oceanography*, 11(2):93–129.

Bryan, F. O., Tomas, R., Dennis, J. M., Chelton, D. B., Loeb, N. G., and Mcclean, J. L. (2010). Frontal scale air-sea interaction in high-resolution coupled climate models. *Journal of Climate*, 23(23):6277–6291.

Bryden, H. L. (1979). Poleward heat flux and conversion of available potentialenergy in Drake Passage. *J. Mar. Res.*, 37:1–22.

Byrne, D., Münnich, M., Frenger, I., and Gruber, N. (2016). Mesoscale atmosphere ocean coupling enhances the transfer of wind energy into the ocean. *Nature Communications*, 7.

Byrne, D., Papritz, L., Frenger, I., Münnich, M., and Gruber, N. (2015). Atmospheric Response to Mesoscale Sea Surface Temperature Anomalies: Assessment of Mechanisms and Coupling Strength in a High-Resolution Coupled Model over

the South Atlantic*. *JOURNAL OF THE ATMOSPHERIC SCIENCES*, 72:1872 – 1890.

Callies, J. and Ferrari, R. (2017). Baroclinic Instability in the Presence of Convection. *Journal of Physical Oceanography*, 48(1):45–60.

Carrier, M. J., Ngodock, H. E., Smith, S. R., Souopgui, I., and Bartels, B. (2016). Examining the potential impact of SWOT observations in an ocean analysis-forecasting system. *Monthly Weather Review*, 144(10):3767–3782.

Cayan, D. R. (1992). Latent and sensible heat flux anomalies over the northern oceans: driving the sea surface temperature.

Chaigneau, A., Gizolme, A., and Grados, C. (2008). Mesoscale eddies off Peru in altimeter records: Identification algorithms and eddy spatio-temporal patterns. *Progress in Oceanography*, 79(2-4):106–119.

Chang, P., Zhang, S., Danabasoglu, G., Yeager, S. G., Fu, H., Wang, H., Castruccio, F. S., Chen, Y., Edwards, J., Fu, D., Jia, Y., Laurindo, L. C., Liu, X., Rosenbloom, N., Small, R. J., Xu, G., Zeng, Y., Zhang, Q., Bacmeister, J., Bailey, D. A., Duan, X., DuVivier, A. K., Li, D., Li, Y., Neale, R., Stössel, A., Wang, L., Zhuang, Y., Baker, A., Bates, S., Dennis, J., Diao, X., Gan, B., Gopal, A., Jia, D., Jing, Z., Ma, X., Saravanan, R., Strand, W. G., Tao, J., Yang, H., Wang, X., Wei, Z., and Wu, L. (2020). An Unprecedented Set of High-Resolution Earth System Simulations for Understanding Multiscale Interactions in Climate Variability and Change. *Journal of Advances in Modeling Earth Systems*, 12(12).

Charnock, H. (1955). Wind stress on a water surface. *Quarterly Journal of the Royal Meteorological Society*, 81(349):320–332.

Chassignet, E. P. and Gent, P. R. (1991). The influence of boundary conditions on midlatitude jet separation in ocean numerical models.

Chassignet, E. P. and Marshall, D. P. (2008). Gulf stream separation in numerical ocean models. *Geophysical Monograph Series*, 177(January):39–61.

Chassignet, E. P. and Xu, X. (2017). Impact of horizontal resolution (1/12° to 1/50°) on Gulf Stream separation, penetration, and variability. *Journal of Physical Oceanography*, pages JPO–D–17–0031.1.

Chelton, D., Schlax, M., and AVISO (2017). New product: Mesoscale Eddy Trajectory Atlas.

Chelton, D. B. (2013). Ocean–atmosphere coupling: Mesoscale eddy effects. *Nature Geoscience*, 6(8):594–595.

Chelton, D. B., DeSzoeke, R. a., Schlax, M. G., El Naggar, K., and Siwertz, N. (1998). Geographical Variability of the First Baroclinic Rossby Radius of Deformation. *Journal of Physical Oceanography*, 28(3):433–460.

Chelton, D. B., Esbensen, S. K., Schalax, M. G., Thum, N., Frelich, M. H., Wintz, F. J., Gentemann, C. L., McPhaden, M. J., and Schopf, P. S. (2001). Observations of coupling between surface wind stress and sea surface temperature in the eastern tropical pacific. *Journal of Climate*, 14(7):1479–1498.

Chelton, D. B. and Schlax, M. G. (1996). Global Observations of Oceanic Rossby Waves. *Science*, 272(5259):234–238.

Chelton, D. B. and Schlax, M. G. (2003). The accuracies of smoothed sea surface height fields constructed from tandem satellite altimeter datasets. *Journal of Atmospheric and Oceanic Technology*, 20(9):1276–1302.

Chelton, D. B., Schlax, M. G., Freilich, M. H., and Milliff, R. F. (2004). Satellite Measurements Reveal Persistent Small-Scale Features in Ocean Winds. *Science*, 303:978–983.

Chelton, D. B., Schlax, M. G., and Samelson, R. M. (2011). Global observations of nonlinear mesoscale eddies. *Progress in Oceanography*, 91:167 – 216.

Chelton, D. B., Schlax, M. G., Samelson, R. M., and de Szoeke, R. A. (2007).

Global observations of large oceanic eddies. *Geophysical Research Letters*, 34(15):1–5.

Chelton, D. B. and Xie, S. P. (2010). Coupled ocean-atmosphere interaction at oceanic mesoscales. *Oceanography*, 23(4):54–69.

Cipollini, P., Cromwell, D., Jones, M. S., Quartly, G. D., and Challenor, P. G. (1997). Concurrent altimeter and infrared observations of Rossby wave propagation near 34° N in the Northeast Atlantic. *Geophysical Research Letters*, 24(8):889–892.

Clément, L., Frajka-Williams, E., Sheen, K. L., Brearley, J. A., and Garabato, A. C. N. (2016). Generation of Internal Waves by Eddies Impinging on the Western Boundary of the North Atlantic. *Journal of Physical Oceanography*, 46(4):1067–1079.

Craig, A., Valcke, S., and Coquart, L. (2017). Development and performance of a new version of the OASIS coupler, OASIS3-MCT-3.0. *Geoscientific Model Development*, 10(9):3297–3308.

Cronin, M. F., Gentemann, C. L., Edson, J., Ueki, I., Bourassa, M., Brown, S., Clayson, C. A., Fairall, C. W., Farrar, J. T., Gille, S. T., Gulev, S., Josey, S. A., Kato, S., Katsumata, M., Kent, E., Krug, M., Minnett, P. J., Parfitt, R., Pinker, R. T., Stackhouse, P. W., Swart, S., Tomita, H., Vandemark, D., Weller, A. R., Yoneyama, K., Yu, L., and Zhang, D. (2019). Air-Sea Fluxes With a Focus on Heat and Momentum. *Frontiers in Marine Science*, 6(July).

Cushman-Roisin, B., Chassignet, E., and Benyang, T. (1990). Westward Motion of Mesoscale Eddies. *Journal of Physical Oceanography*, 20:758 – 767.

Czaja, A., Frankignoul, C., Minobe, S., and Vannière, B. (2019). Simulating the Midlatitude Atmospheric Circulation : What Might We Gain From High-Resolution Modeling of Air-Sea Interactions ? *Current Climate Change Reports*.

Deremble, B., Dewar, W. K., and Chassignet, E. P. (2016). Vorticity Dynamics near sharp topographic features. *Journal of Marine Research*, 74:249–276.

Dewar, W. R. and Flierl, G. R. (1987). Some effects of the wind on rings.

Ding, M., Lin, P., Liu, H., Hu, A., and Liu, C. (2020). Lagrangian eddy kinetic energy of ocean mesoscale eddies and its application to the Northwestern Pacific. *Nature Scientific Reports*, 10(1):1–11.

Ducet, N., Le Traon, P. Y., and Reverdin, G. (2000). Global high-resolution mapping of ocean circulation from TOPEX/Poseidon and ERS-1 and -2. *Journal of Geophysical Research: Oceans*, 105(C8):19477–19498.

Eady, E. T. (1949). Long Waves and Cyclone Waves. *Tellus*, 1(3):33–52.

Eden, C. (2007). Eddy length scales in the North Atlantic Ocean. *Journal of Geophysical Research*, 112(C6):C06004.

Eden, C. and Greatbatch, R. J. (2008). Diapycnal mixing by meso-scale eddies. *Ocean Modelling*, 23(3-4):113–120.

Esmf Joint Specification Team:, Balaji, V., Boville, B., Cheung, S., Clune, T., Craig, T., Cruz, C., Silva, A., Deluca, C., Fainchtein, R. D., Eaton, B., Hallberg, B., Henderson, T., Hill, C., Iredell, M., Jacob, R., Jones, P., Kluzek, E., Kauffman, B., Larson, J., Li, P., Liu, F., Michalakes, J., Murphy, S., Neckels, D., Kuinghttons, R. O., Oehmke, B., Panaccione, C., Rosinski, J., Sawyer, W., Schwab, E., Smithline, S., Spector, W., Stark, D., Suarez, M., Swift, S., Trayanov, A., Vasquez, S., Wolfe, J., Yang, W., Young, M., and Zaslavsky, L. (2018). Earth System Modeling Framework ESMF Reference Manual Version 7.1.0r. Technical report, Earth System Modeling Framework ESMF.

Eyring, V., Bony, S., Meehl, G. A., Senior, C. A., Stevens, B., Stouffer, R. J., and Taylor, K. E. (2016). Overview of the Coupled Model Intercomparison Project Phase 6 (CMIP6) experimental design and organization. *Geoscientific Model Development*, 9(5):1937–1958.

Fang, F. and Morrow, R. (2003). Evolution, movement and decay of warm-core Leeuwin Current eddies. *Deep-Sea Research Part II: Topical Studies in Oceanography*, 50(12-13):2245–2261.

Ferrari, R. and Wunsch, C. (2009). Ocean Circulation Kinetic Energy: Reservoirs, Sources, and Sinks. *Annual Review of Fluid Mechanics*, 41(1):253–282.

Fox-Kemper, B., Adcroft, A., Böning, C. W., Chassignet, E. P., Curchitser, E., Danabasoglu, G., Eden, C., England, M. H., Gerdes, R., Greatbatch, R. J., Griffies, S. M., Hallberg, R. W., Hanert, E., Heimbach, P., Hewitt, H. T., Hill, C. N., Komuro, Y., Legg, S., Sommer, J. L., Masina, S., Marsland, S. J., Penny, S. G., Qiao, F., Ringler, T. D., Treguier, A. M., Tsujino, H., Uotila, P., and Yeager, S. G. (2019). Challenges and prospects in ocean circulation models. *Frontiers in Marine Science*, 6(FEB):1–29.

Fox-kemper, B. and Bachman, S. (2014). Principles and advances in subgrid modelling for eddy-rich simulations. *CLIVAR Exchanges: Special Issue: High Resolution Ocean Climate Modelling*, 19(65).

Frankignoul, C. (1985). Sea Surface Temperature Anomalies, Planetary Waves,. *Reviews of Geophysics*, 23(4):357–390.

Frankignoul, C., Czaja, A., and L'Heveder, B. (1998). Air-sea feedback in the North Atlantic and surface boundary conditions for ocean models. *Journal of Climate*, 11(9):2310–2324.

Frankignoul, C., Kestenare, E., Botzet, M., Carril, A. F., Drange, H., Pardaens, A., Terray, L., and Sutton, R. (2004). An intercomparison between the surface heat flux feedback in five coupled models, COADS and the NCEP reanalysis. *Climate Dynamics*, 22(4):373–388.

Frenger, I., Bianchi, D., Stührenberg, C., Oschlies, A., Dunne, J., Deutsch, C., Galbraith, E., and Schütte, F. (2018). Biogeochemical Role of Subsurface Coherent

Eddies in the Ocean: Tracer Cannonballs, Hypoxic Storms, and Microbial Stewpots? *Global Biogeochemical Cycles*, 32:1 – 24.

Frenger, I., Gruber, N., Knutti, R., and Münnich, M. (2013). Imprint of Southern Ocean eddies on winds, clouds and rainfall. *Nature Geoscience Letters*, 6:608 – 612.

Frenger, I., M.Munnich, Gruber, N., and Knutti, R. (2015). Southern Ocean eddy phenomenology. *Journal of Geophysical Research : Oceans*, pages 1–15.

Gaube, P., Barceló, C., McGillicuddy, D. J., Domingo, A., Miller, P., Giffoni, B., Marcovaldi, N., and Swimmer, Y. (2017). The use of mesoscale eddies by juvenile loggerhead sea turtles (Caretta caretta) in the southwestern Atlantic. *PLoS ONE*, 12(3).

Gaube, P., Chelton, D. B., Samelson, R. M., Schlax, M. G., and O'Neill, L. W. (2015). Satellite observations of mesoscale eddy-induced Ekman pumping. *Journal of Physical Oceanography*, 45(1):104–132.

Gent, P. R. and McWilliams, J. C. (1990). Isopycnal Mixing in Ocean Circulation Models.

Gill, A. E., Green, J. S., and Simmons, A. J. (1974). Energy partition in the large-scale ocean circulation and the production of mid-ocean eddies. *Deep-Sea Research and Oceanographic Abstracts*, 21(7).

Gnanadesikan, A., Pradal, M. A., and Abernathey, R. (2015). Isopycnal mixing by mesoscale eddies significantly impacts oceanic anthropogenic carbon uptake. *Geophysical Research Letters*, 42(11):4249–4255.

Gordon, A. L. and Giulivi, C. F. (2014). Ocean eddy freshwater flux convergence into the North Atlantic subtropics. *Journal of Geophysical Research : Oceans*, 119.

Gregory, J. M., Ingram, W. J., Palmer, M. A., Jones, G. S., Stott, P. A., Thorpe, R. B., Lowe, J. A., Johns, T. C., and Williams, K. D. (2004). A new method for diagnosing radiative forcing and climate sensitivity. *Geophysical Research Letters*, 31(3):2–5.

Griffies, S. M., Winton, M., Anderson, W., Benson, R., Delworth, T. L., Dufour, C. O., Dunne, J. P., Goddard, P., Morrison, A. K., Rosati, A., Wittenberg, A. T., Yin, J., and Zhang, R. (2015). Impacts on ocean heat from transient mesoscale eddies in a hierarchy of climate models. *Journal of Climate*, 28(3):952–977.

Grist, J. P., Josey, S. A., Sinha, B., Catto, J. L., Roberts, M. J., and Coward, A. C. (2021). Future Evolution of an Eddy Rich Ocean Associated with Enhanced East Atlantic Storminess in a Coupled Model Projection. *Geophysical Research Letters*, 48(7):1–13.

Gula, J., Molemaker, M. J., and McWilliams, J. C. (2016). Topographic generation of submesoscale centrifugal instability and energy dissipation. *Nature Communications*, 7:1–7.

Guymer, T. H., Businger, J. A., Katsaros, K. B., Shaw, W. J., Taylor, P. K., Large, W. G., Payne, R. E., Harvey, J. G., Pollard, R. T., Charnock, H., and Pollard, R. T. (1983). Transfer processes at the air-sea interface. *Philosophical Transactions of the Royal Society of London. Series A, Mathematical and Physical Sciences*, 308(1503):253–273.

Haarsma, R. J., García-Serrano, J., Prodhomme, C., Bellprat, O., Davini, P., and Drijfhout, S. (2019). Sensitivity of winter North Atlantic-European climate to resolved atmosphere and ocean dynamics. *Scientific Reports*, 9(1):1–8.

Haarsma, R. J., Roberts, M. J., Vidale, P. L., Catherine, A., Bellucci, A., Bao, Q., Chang, P., Corti, S., Fučkar, N. S., Guemas, V., Von Hardenberg, J., Hazeleger, W., Kodama, C., Koenigk, T., Leung, L. R., Lu, J., Luo, J. J., Mao, J., Mizielinski, M. S., Mizuta, R., Nobre, P., Satoh, M., Scoccimarro, E., Semmler, T., Small, J.,

and Von Storch, J. S. (2016). High Resolution Model Intercomparison Project (HighResMIP v1.0) for CMIP6. *Geoscientific Model Development*, 9(11):4185–4208.

Haidvogel, D. B., McWilliams, J. C., and Gent, P. R. (1992). Boundary current separation in a quasigeostrophic, eddy-resolving ocean circulation model. *Journal of Physical Oceanography*, 22(8):882–902.

Hallberg, R. (2013). Using a resolution function to regulate parameterizations of oceanic mesoscale eddy effects. *Ocean Modelling*, 72:92–103.

Hallberg, R. and Gnanadesikan, A. (2006). The Role of Eddies in Determining the Structure and Response of the Wind-Driven Southern Hemisphere Overturning: Results from the Modeling Eddies in the Southern Ocean (MESO) Project. *Journal of Physical Oceanography*, 36(12):2232–2252.

Hausmann, U. and Czaja, A. (2012). The observed signature of mesoscale eddies in sea surface temperature and the associated heat transport. *Deep-Sea Research Part I: Oceanographic Research Papers*, 70:60–72.

Hausmann, U., Czaja, A., and Marshall, J. (2016). Estimates of air-sea feedbacks on sea surface temperature anomalies in the Southern Ocean. *Journal of Climate*, 29(2):439–454.

Hausmann, U., Czaja, A., and Marshall, J. (2017). Mechanisms controlling the SST air-sea heat flux feedback and its dependence on spatial scale. *Climate Dynamics*, 48(3-4):1297–1307.

Hayes, S. P., McPhaden, M. J., and Wallace, J. M. (1989). The influence of Sea Surface Temperature on Surface Wind in the Eastern Equatorial Pacific: Weekly to Monthly Variability. *Journal of Climate*, 2:1500–1506.

Hewitt, H., Roberts, M. J., Hyder, P., Graham, T., Rae, J., Belcher, S. E., Bourdallé-Badie, R., Copsey, D., Coward, A., Guiavarch, C., Harris, C., Hill, R., Hirschi,

J. J., Madec, G., Mizielinski, M. S., Neininger, E., New, A. L., Rioual, J. C., Sinha, B., Storkey, D., Shelly, A., Thorpe, L., and Wood, R. A. (2016). The impact of resolving the Rossby radius at mid-latitudes in the ocean: Results from a high-resolution version of the Met Office GC2 coupled model. *Geoscientific Model Development*, 9(10):3655–3670.

Hewitt, H. T., Bell, M. J., Chassignet, E. P., Czaja, A., Ferreira, D., Griffies, S. M., Hyder, P., McClean, J. L., New, A. L., and Roberts, M. J. (2017). Will high-resolution global ocean models benefit coupled predictions on short-range to climate timescales?

Hewitt, H. T., Copsey, D., Culverwell, I. D., Harris, C. M., Hill, R. S., Keen, A. B., McLaren, A. J., and Hunke, E. C. (2011). Design and implementation of the infrastructure of HadGEM3: The next-generation Met Office climate modelling system. *Geoscientific Model Development*, 4(2):223–253.

Hewitt, H. T., Roberts, M., Mathiot, P., Biastoch, A., Blockley, E., Chassignet, E. P., Fox-Kemper, B., Hyder, P., Marshall, D. P., Popova, E., Treguier, A.-M., Zanna, L., Yool, A., Yu, Y., Beadling, R., Bell, M., Kuhlbrodt, T., Arsouze, T., Bellucci, A., Castruccio, F., Gan, B., Putrasahan, D., Roberts, C. D., Roekel, L. V., and Zhang, Q. (2020). Resolving and parameterising the ocean mesoscale in Earth System Models. *Current Climate Change Reports*, submitted(October).

Hogg, A. M., Dewar, W. K., Berloff, P., Kravtsov, S., and Hutchinson, D. K. (2009). The effects of mesoscale ocean-atmosphere coupling on the large-scale ocean circulation. *Journal of Climate*.

Holm, D. D. and Nadiga, B. T. (2003). Modeling mesoscale turbulence in the barotropic double-gyre circulation. *Journal of Physical Oceanography*, 33(11):2355–2365.

Holt, J., Hyder, P., Ashworth, M., Harle, J., Hewitt, H. T., Liu, H., New, A. L., Pickles, S., Porter, A., Popova, E., Icarus Allen, J., Siddorn, J., and Wood, R.

(2017). Prospects for improving the representation of coastal and shelf seas in global ocean models. *Geoscientific Model Development*, 10(1):499–523.

Hurlburt, H. E., Metzger, E. J., Hogan, P. J., Tilburg, C. E., and Shriver, J. F. (2008). Steering of upper ocean currents and fronts by the topographically constrained abyssal circulation. *Dynamics of Atmospheres and Oceans*, 45(3-4):102–134.

Jackson, L. C., Roberts, M. J., Hewitt, H. T., Iovino, D., Koenigk, T., Meccia, V. L., Roberts, C. D., Ruprich-Robert, Y., and Wood, R. A. (2020). Impact of ocean resolution and mean state on the rate of AMOC weakening. *Climate Dynamics*, 55(7-8):1711–1732.

Jin, X., Dong, C., Kurian, J., McWilliams, J. C., Chelton, D. B., and Li, Z. (2009). SST–Wind Interaction in Coastal Upwelling: Oceanic Simulation with Empirical Coupling. *Journal of Physical Oceanography*, 39(11):2957–2970.

Jones, P. W. and Division, T. (1998). A User's Guide for SCRIP: A Spherical Coordinate Remapping and Interpolation Package.

Jullien, S., Masson, S., Oerder, V., Samson, G., Colas, F., and Renault, L. (2020). Impact of ocean-atmosphere current feedback on ocean mesoscale activity: Regional variations and sensitivity to model resolution. *Journal of Climate*, 33(7):2585–2602.

Kelly, K. A., Mcphaden, M. J., and Johnson, G. C. (2001). Ocean Currents Evident in Satellite Wind Data. *Geophysical Research Letters*, 28(12):2469–2472.

Kilpatrick, T., Schneider, N., and Qiu, B. (2014). Boundary layer convergence induced by strong winds across a midlatitude SST front. *Journal of Climate*, 27(4):1698–1718.

Kirtman, B. P., Bitz, C., Bryan, F., Collins, W., Dennis, J., Hearn, N., Kinter, J. L., Loft, R., Rousset, C., Siqueira, L., Stan, C., Tomas, R., and Vertenstein, M. (2012). Impact of ocean model resolution on CCSM climate simulations. *Climate Dynamics*, 39(6):1303–1328.

Kjellsson, J. and Zanna, L. (2017). The impact of horizontal resolution on energy transfers in global ocean models. *Fluids*, 2(3).

Klein, P., Lapeyre, G., Siegelman, L., Qiu, B., Fu, L. L., Torres, H., Su, Z., Menemenlis, D., and Le Gentil, S. (2019). Ocean-Scale Interactions From Space. *Earth and Space Science*, 6(5):795–817.

Klocker, A. and Abernathey, R. (2013). Global Patterns of Mesoscale Eddy Properties and Diffusivities. *Journal of Physical Oceanography*, 44(3):1030–1046.

Klocker, A. and Marshall, D. P. (2014). Advection of baroclinic eddies by depth-mean flow. *Geophysical Research Letters*, 41:3517 – 3521.

Klocker, A., Marshall, D. P., Keating, S. R., and Read, P. L. (2016). A regime diagram for ocean geostrophic turbulence. *Quarterly Journal of the Royal Meteorological Society*, 142(699):2411–2417.

Kurian, J., Colas, F., Capet, X., McWilliams, J. C., and Chelton, D. B. (2011). Eddy properties in the California Current System. *Journal of Geophysical Research: Oceans*, 116(8).

Large, W. and Yeager, S. (2004). Diurnal to Decadal Global Forcing The Data Sets and Flux Climatologies. Technical Report 2004, National Center for Atmospheric Research (NCAR).

Large, W. G., McWilliams, J. C., and Doney, S. C. (1994). Oceanic vertical mixing: A review and a model with a nonlocal boundary layer parameterization. *Reviews of Geophysics*, 32(4):363–403.

Laurindo, L. C., Siqueira, L., Mariano, A. J., and Kirtman, B. P. (2018). Cross-spectral analysis of the SST/10-m wind speed coupling resolved by satellite products and climate model simulations. *Climate Dynamics*, 0(0):0.

Lemarié, F., Samson, G., Redelsperger, J.-L., Giordani, H., Brivoal, T., and Madec, G. (2020). A simplified atmospheric boundary layer model for an improved repre-

sentation of air-sea interactions in eddying oceanic models: implementation and first evaluation in NEMO (4.0). *Geoscientific Model Development Discussions*, 2020(August):1–44.

Leyba, I. M., Saraceno, M., and Solman, S. A. (2016). Air-sea heat fluxes associated to mesoscale eddies in the Southwestern Atlantic Ocean and their dependence on different regional conditions. *Climate Dynamics*, 49(7-8):2491–2501.

Li, F., Sang, H., and Jing, Z. (2017). Quantify the continuous dependence of SST-turbulent heat flux relationship on spatial scales. *Geophysical Research Letters*, 44(12):6326–6333.

Li, Q. Y., Sun, L., and Lin, S. F. (2016). GEM: A dynamic tracking model for mesoscale eddies in the ocean. *Ocean Science*, 12(6):1249–1267.

Lin, P., Liu, H., Ma, J., and Li, Y. (2019). Ocean mesoscale structure–induced air–sea interaction in a high-resolution coupled model. *Atmospheric and Oceanic Science Letters*, 12(2):98–106.

Lindzen, R. S. and Nigam, S. (1987). On the Role of Sea Surface Temperature Gradients in Forcing Low-Level Winds and Convergence in the Tropics.

Liu, Y., Yu, L., and Chen, G. (2020). Characterization of Sea Surface Temperature and Air-Sea Heat Flux Anomalies Associated With Mesoscale Eddies in the South China Sea. *Journal of Geophysical Research: Oceans*, 125(4):1–19.

Luyten, J., Pedlosky, J., and Stommel, H. (1983). The Ventilated Thermocline. *Journal of Physical Oceanography*, 13:292–309.

Ma, L., Woollings, T., Williams, R. G., Smith, D., and Dunstone, N. (2020). How Does the Winter Jet Stream Affect Surface Temperature, Heat Flux, and Sea Ice in the North Atlantic? *Journal of Climate*, 33(9):3711–3730.

Ma, X., Chang, P., Saravanan, R., Montuoro, R., Nakamura, H., Wu, D., Lin, X.,

and Wu, L. (2017). Importance of resolving kuroshio front and eddy influence in simulating the north pacific storm track. *Journal of Climate*, 30(5):1861–1880.

Ma, X., Chang, P., Saravanan, R., Monturoro, R., Hsiesh, J., Wu, D., Lin, X., Wu, L., and Jing, Z. (2015). Distant Influence of Kuroshio Eddies on North Pacific Weather Patterns. *Nature Scientific Reports*.

Ma, X., Jing, Z., Chang, P., Liu, X., Montuoro, R., Small, R. J., Bryan, F. O., Greatbatch, R. J., Brandt, P., Wu, D., Lin, X., and Wu, L. (2016). Western boundary currents regulated by interaction between ocean eddies and the atmosphere. *Nature*, 535(7613):533–537.

Madec, G. (2008). NEMO ocean engine.

Maloney, E. D. and Chelton, D. B. (2006). An assessment of the sea surface temperature influence on surface wind stress in numerical weather prediction and climate models. *Journal of Climate*, 19(12):2743–2762.

Marshall, D. P., Ambaum, M. H., Maddison, J. R., Munday, D. R., and Novak, L. (2017). Eddy saturation and frictional control of the Antarctic Circumpolar Current. *Geophysical Research Letters*, 44(1):286–292.

Marshall, D. P. and Zhai, X. (2021). Southern Ocean eddy-induced overturning and circumpolar transport inferred from eddy energy and its residence time. *Ocean Dynamics*, submitted.

Marshall, J., Adcroft, A., Hill, C., Perelman, L., and Heisey, C. (1997). A finite-volume, incompressible navier stokes model for, studies of the ocean on parallel computers.

Marshall, J., Jones, H., Karsten, R., and Wardle, R. (2002). Can eddies set ocean stratification? *Journal of Physical Oceanography*, 32(1):26–38.

Marshall, J. and Plumb, R. (2008). *Atmosphere, Ocean and Climate Dynamics*. Elsevier Academic Press.

Marshall, J. and Radko, T. (2003). Residual-Mean Solutions for the Antarctic Circumpolar Current and Its Associated Overturning Circulation. *Journal of Physical Oceanography*, 33(11):2341–2354.

Martínez-Moreno, J., Hogg, A. M. C., Kiss, A. E., Constantinou, N. C., and Morrison, A. K. (2019). Kinetic Energy of Eddy-Like Features From Sea Surface Altimetry. *Journal of Advances in Modeling Earth Systems*, 11(10):3090–3105.

Marzocchi, A., Hirschi, J. J., Holliday, N. P., Cunningham, S. A., Blaker, A. T., and Coward, A. C. (2015a). The North Atlantic subpolar circulation in an eddy-resolving global ocean model. *Journal of Marine Systems*, 142:126–143.

Marzocchi, A., Hirschi, J. J., Holliday, N. P., Cunningham, S. A., Blaker, A. T., and Coward, A. C. (2015b). The North Atlantic subpolar circulation in an eddy-resolving global ocean model. *Journal of Marine Systems*, 142:126–143.

Mason, E., Pascual, A., and McWilliams, J. C. (2014). A new sea surface height-based code for oceanic mesoscale eddy tracking. *Journal of Atmospheric and Oceanic Technology*, 31(5):1181–1188.

McClean, J. L., Bader, D. C., Bryan, F. O., Maltrud, M. E., Dennis, J. M., Mirin, A. A., Jones, P. W., Kim, Y. Y., Ivanova, D. P., Vertenstein, M., Boyle, J. S., Jacob, R. L., Norton, N., Craig, A., and Worley, P. H. (2011). A prototype two-decade fully-coupled fine-resolution CCSM simulation. *Ocean Modelling*, 39(1-2):10–30.

McWilliams, J. C. (2008). The nature and consequences of oceanic eddies. *Geophysical Monograph Series*, 177:5–15.

McWilliams, J. C. (2016). Submesoscale currents in the ocean. *Proceedings in Royal Society*, 472:1 – 32.

McWilliams, J. C., Norton, N., Gent, P. R., and Haidvogel, D. B. (1990). A Linear Balance Model of Wind-Driven, Midlatitude Ocean Circulation. *Journal of Physical Oceanography*, 20(1349-1374).

Meccia, V. L., Iovino, D., and Bellucci, A. (2021). North Atlantic gyre circulation in PRIMAVERA models. *Climate Dynamics*.

Mertz, F., Rosmorduc, V., Maheu, C., and Faugere, Y. (2017). Product User Manual For Sea Level SLA products from Copernicus Marine Service. Technical Report 1.1, Copernicus Marine Service.

Minobe, S., Kuwano-Yoshida, A., Komori, N., Xie, S. P., and Small, R. J. (2008). Influence of the Gulf Stream on the troposphere. *Nature*, 452(7184):206–209.

Moreno-Chamarro, E., Caron, L. P., Ortega, P., Loosveldt Tomas, S., and Roberts, M. J. (2021). Can we trust CMIP5/6 future projections of European winter precipitation? *Environmental Research Letters*.

Moreno-Chamarro, E., L.-P. Caron, P. Ortega, S. L. Tomas, M. J. R. (2020). Is winter precipitation change over Europe underestimated in current climate projections? *Proceedings in National Science Academy*, submitted.

Moreton, S. M., Ferreira, D., Roberts, M., and Hewitt, H. (2020). Evaluating surface eddy properties in coupled climate simulations with 'eddy-present' and 'eddy-rich' ocean resolution. *Ocean Modelling*, 147.

Moreton, S. M. and Roberts, M. (2021). An eddy tracking dataset for N512-12, N216-12 and N216-025 model configurations of HadGEM3-GC3.1 .

Munday, D. R., Johnson, H. L., and Marshall, D. P. (2013). Eddy Saturation of Equilibrated Circumpolar Currents. *Journal of Physical Oceanography*, 43(3):507–532.

Munday, D. R., Johnson, H. L., and Marshall, D. P. (2014). Impacts and effects of mesoscale ocean eddies on ocean carbon storage and atmospheric pCO2. *Global Biogeochemical Cycles*, 28(8):877–896.

Munk, W. (1950). On the wind driven ocean circulation.

Oerder, V., Colas, F., Echevin, V., Masson, S., and Lemarié, F. (2018). Impacts of the Mesoscale Ocean-Atmosphere Coupling on the Peru-Chile Ocean Dynamics: The Current-Induced Wind Stress Modulation. *Journal of Geophysical Research: Oceans*, 123:1–22.

O'Neill, L. W., Chelton, D. B., and Esbensen, S. K. (2003). Observations of SST-induced perturbations of the wind stress field over the Southern Ocean on seasonal timescales. *Journal of Climate*, 16(14):2340–2354.

O'Neill, L. W., Chelton, D. B., and Esbensen, S. K. (2010). The effects of SST-induced surface wind speed and direction gradients on Midlatitude Surface vorticity and divergence. *Journal of Climate*, 23(2):255–281.

O'Neill, L. W., Chelton, D. B., and Esbensen, S. K. (2012). Covariability of surface wind and stress responses to sea surface temperature fronts. *Journal of Climate*, 25(17):5916–5942.

O'Neill, L. W., Chelton, D. B., Esbensen, S. K., and Wentz, F. J. (2004). High-resolution satellite measurements of the atmospheric boundary layer response to SST variations along the Agulhas Return Current. *Journal of Climate*, 18(14):2706–2723.

Özgökmen, T. M. and Chassignet, E. P. (2002). Dynamics of two-dimensional turbulent bottom gravity currents. *Journal of Physical Oceanography*, 32(5):1460–1478.

Putrasahan, D. A., Gutjahr, O., Haak, H., Jungclaus, J. H., Lohmann, K., Roberts, M. J., and von Storch, J. (2021). Effect of resolving ocean eddies on the transient response of global mean surface temperature to abrupt 4xCO 2 forcing . *Geophysical Research Letters*, pages 1–12.

Putrasahan, D. A., Kamenkovich, I., Le Hénaff, M., and Kirtman, B. P. (2017). Importance of ocean mesoscale variability for air-sea interactions in the Gulf of Mexico. *Geophysical Research Letters*, 44(12):6352–6362.

Putrasahan, D. A., Miller, A. J., and Seo, H. (2013). Isolating mesoscale coupled ocean-atmosphere interactions in the Kuroshio Extension region. *Dynamics of Atmospheres and Oceans*, 63:60–78.

Rahmstorf, S. and Willebrand, J. (1995). The Role of Temperature Feedback in Stabilizing the Thermocline Circulation. *Journal of Physical Oceanography*, 25:787–805.

Renault, L., Lemarié, F., and Arsouze, T. (2019a). On the implementation and consequences of the oceanic currents feedback in ocean–atmosphere coupled models. *Ocean Modelling*, 141(July):101423.

Renault, L., Marchesiello, P., Masson, S., and McWilliams, J. C. (2019b). Remarkable Control of Western Boundary Currents by Eddy Killing, a Mechanical Air-Sea Coupling Process. *Geophysical Research Letters*, 46(5):2743–2751.

Renault, L., Masson, S., Arsouze, T., Madec, G., and McWilliams, J. C. (2019c). Recipes for How to Force Oceanic Model Dynamics. *Journal of Advances in Modeling Earth Systems*, 12(2).

Renault, L., Masson, S., Oerder, V., Jullien, S., and Colas, F. (2019d). Disentangling the Mesoscale Ocean-Atmosphere Interactions. *Journal of Geophysical Research: Oceans*, 124(3):2164–2178.

Renault, L., McWilliams, J. C., and Masson, S. (2017a). Satellite Observations of Imprint of Oceanic Current on Wind Stress by Air-Sea Coupling. *Nature Scientific Reports*, 7(1):1–7.

Renault, L., Mcwilliams, J. C., and Penven, P. (2017b). Modulation of the Agulhas Current Retroflection and Leakage by Oceanic Current Interaction with the Atmosphere in Coupled Simulations. *JOURNAL OF PHYSICAL OCEANOGRAPHY*, 47(1):2077–2100.

Renault, L., Molemaker, M. J., Gula, J., Masson, S., and McWilliams, J. C. (2016a). Control and Stabilization of the Gulf Stream by Oceanic Current Interaction with the Atmosphere. *Journal of Physical Oceanography*, 46(11):3439–3453.

Renault, L., Molemaker, M. J., McWilliams, J. C., Shchepetkin, A. F., Lemarié, F., Chelton, D. B., Illig, S., and Hall, A. (2016b). Modulation of Wind-Work by Oceanic Current Interaction with the Atmosphere. *Journal of Climate*, 46:1685 – 1703.

Reynolds, R. W., Smith, T. M., Liu, C., Chelton, D. B., Casey, K. S., and Schlax, M. G. (2007). Daily high-resolution-blended analyses for sea surface temperature. *Journal of Climate*, 20(22):5473–5496.

Ridley, J. K., Blockley, E. W., Keen, A. B., Rae, J. G. L., and West, A. E. (2018). The sea ice model component of HadGEM3-GC3 . 1. *Geoscientific Model Development*, 11:713 – 723.

Roberts, C. D., Vitart, F., Balmaseda, M. A., and Molteni, F. (2020a). The time-scale-dependent response of the wintertime North Atlantic to increased ocean model resolution in a coupled forecast model. *Journal of Climate*, 33(9):3663–3689.

Roberts, M. (2017a). MOHC HadGEM3-GC31-MH model output prepared for CMIP6 HighResMIP. Version 20190901.

Roberts, M. (2017b). MOHC HadGEM3-GC31-MM model output prepared for CMIP6 HighResMIP Version 20190901.

Roberts, M. (2018). MOHC HadGEM3-GC31-HH model output prepared for CMIP6 HighResMIP Version 20190901.

Roberts, M. J., Baker, A., Blockley, E. W., Calvert, D., Coward, A., Hewitt, H. T., Jackson, L. C., Kuhlbrodt, T., Mathiot, P., Roberts, C. D., Schiemann, R., Seddon, J., Vannière, B., and Vidale, P. L. (2019). Description of the resolution hierarchy

of the global coupled HadGEM3-GC3.1 model as used in CMIP6 HighResMIP experiments. *Geoscientific Model Development Discussions*, 12:4999–5028.

Roberts, M. J., Hewitt, H. T., Hyder, P., Ferreira, D., Josey, S. A., Mizielinski, M., and Shelly, A. (2016). Impact of ocean resolution on coupled air-sea fluxes and large-scale climate. *Geophysical Research Letters*, 43(19):10,430–10,438.

Roberts, M. J., Jackson, L. C., Roberts, C. D., Meccia, V., Docquier, D., Koenigk, T., Ortega, P., Moreno-Chamarro, E., Bellucci, A., Coward, A., Drijfhout, S., Exarchou, E., Gutjahr, O., Hewitt, H., Iovino, D., Lohmann, K., Putrasahan, D., Schiemann, R., Seddon, J., Terray, L., Xu, X., Zhang, Q., Chang, P., Yeager, S. G., Castruccio, F. S., Zhang, S., and Wu, L. (2020b). Sensitivity of the Atlantic Meridional Overturning Circulation to Model Resolution in CMIP6 HighResMIP Simulations and Implications for Future Changes. *Journal of Advances in Modeling Earth Systems*, 12(8):1–22.

Rouault, M., Verley, P., and Backeberg, B. (2014). Wind increase above warm Agulhas Current eddies. *Ocean Sci. Discuss*, 11(July 1999):2367–2389.

Samelson, R. M., O'Neill, L. W., Chelton, D. B., Skyllingstad, E. D., Barbour, P. L., and Durski, S. M. (2020). Surface stress and atmospheric boundary layer response to mesoscale SST structure in coupled simulations of the Northern California current system. *Monthly Weather Review*, 148(1):259–287.

Samelson, R. M., Schlax, M. G., and Chelton, D. B. (2014). Randomness, Symmetry, and Scaling of Mesoscale Eddy Life Cycles. *J. Phys. Oceanogr.*, 44:1012–1029.

Samelson, R. M., Skyllingstad, E. D., Chelton, D. B., Esbensen, S. K., O'Neill, L. W., and Thum, N. (2006). On the coupling of wind stress and sea surface temperature. *Journal of Climate*, 19(8):1557–1566.

Sasaki, H., Klein, P., Qiu, B., and Sasai, Y. (2014). Impact of oceanic-scale interac-

tions on the seasonal modulation of ocean dynamics by the atmosphere. *Nature Communications*, 5:1–8.

Scharffenberg, M. G. and Stammer, D. (2011). Statistical parameters of the geostrophic ocean flow field estimated from the Jason-1-TOPEX/Poseidon tandem mission. *Journal of Geophysical Research: Oceans*, 116(12):1–14.

Schubert, R., Schwarzkopf, F. U., Baschek, B., and Biastoch, A. (2019). Submesoscale Impacts on Mesoscale Agulhas Dynamics. *Journal of Advances in Modeling Earth Systems*, 11(8):2745–2767.

Sein, D. V., Koldunov, N. V., Danilov, S., Wang, Q., Sidorenko, D., Fast, I., Rackow, T., Cabos, W., and Jung, T. (2017). Ocean Modeling on a Mesh With Resolution Following the Local Rossby Radius. *Journal of Advances in Modeling Earth Systems*, 9(7):2601–2614.

Seo, H. (2017). Distinct influence of air-sea interactions mediated by mesoscale sea surface temperature and surface current in the Arabian Sea. *Journal of Climate*, 30(20):8061–8080.

Seo, H., Miller, A. J., and Norris, J. (2016). Eddy – Wind Interaction in the California Current System: Dynamics and Impacts. *Journal of Physical Oceanography*, 46(1989):439–459.

Shan, X., Jing, Z., Gan, B., Wu, L., Chang, P., Ma, X., and Wang, S. (2020a). Surface Heat Flux Induced by Mesoscale Eddies Cools the Kuroshio - Oyashio Extension Region. *Geophysical Research Letters*, pages 1–9.

Shan, X., Jing, Z., Sun, B., and Wu, L. (2020b). Impacts of ocean current–atmosphere interactions on mesoscale eddy energetics in the Kuroshio extension region. *Geoscience Letters*, 7(1).

Sheldon, L., Czaja, A., Vannière, B., Morcrette, C., Sohet, B., Casado, M., and Smith, D. (2017). A 'warm path' for Gulf Stream-troposphere interactions. *Tellus, Series A: Dynamic Meteorology and Oceanography*, 69(1):1–15.

Small, R. J., Bryan, F. O., Bishop, S. P., Larson, S., and Tomas, R. A. (2020). What drives upper-ocean temperature variability in coupled climate models and observations? *Journal of Climate*, 33(2):577–596.

Small, R. J., Bryan, F. O., Bishop, S. P., and Tomas, R. A. (2019). Air-sea turbulent heat fluxes in climate models and observational analyses: What drives their variability? *Journal of Climate*, 32(8):2397–2421.

Small, R. J., DeSzoeke, S. P., Xie, S. P., O'Neill, L., Seo, H., Song, Q., Cornillon, P., Spall, M., and Minobe, S. (2008). Air-sea interaction over ocean fronts and eddies. *Dynamics of Atmospheres and Oceans*, 45(3-4):274–319.

Small, R. J., Tomas, R. A., and Bryan, F. O. (2014). Storm track response to ocean fronts in a global high-resolution climate model. *Climate Dynamics*, 43(3-4):805–828.

Small, R. J., Xie, S. P., and Hafner, J. (2005). Satellite observations of mesoscale ocean features and copropagating atmospheric surface fields in the tropical belt. *Journal of Geophysical Research C: Oceans*, 110(2):1–19.

Smirnov, D., Newman, M., and Alexander, M. A. (2014). Investigating the role of ocean-atmosphere coupling in the North Pacific ocean. *Journal of Climate*, 27(2):592–606.

Song, Q., Chelton, D. B., Esbensen, S. K., Thum, N., and O'Neill, L. W. (2009). Coupling between sea surface temperature and low-level winds in mesoscale numerical models. *Journal of Climate*, 22(1):146–164.

Spall, M. A. (2007a). Effect of sea surface temperature-wind stress coupling on baroclinic instability in the ocean. *Journal of Physical Oceanography*, 37(4):1092–1097.

Spall, M. A. (2007b). Midlatitude wind stress-surface temperature coupling in the vicinity of oceanic fronts. *Journal of Climate*, 20(15):3785–3801.

Stammer, D. (1997). Global Characteristics of Ocean Variability Estimated from Regional TOPEX POSEIDON Altimeter Measurements. *Journal of Physical Oceanography*, 27:1743–1769.

Stern, M. E. (1965). Interaction of a uniform wind stress with a geostrophic vortex. *Deep Sea Research and Oceanographic Abstracts*, 12(3):355–367.

Stewart, K. D., Hogg, A. M. C., Griffies, S. M., Heerdegen, A. P., Ward, M. L., Spence, P., and England, M. H. (2017). Vertical resolution of baroclinic modes in global ocean models. *Ocean Modelling*, 113:50–65.

Stommel, H. (1948). The westward intensification of wind-driven ocean currents. *American Geophysical Union*, 29(2):202–206.

Storkey, D., Blaker, A. T., Mathiot, P., Megann, A., Aksenov, Y., Blockley, E. W., Calvert, D., Graham, T., Hewitt, H. T., Hyder, P., Kuhlbrodt, T., Rae, J. G. L., and Sinha, B. (2018). UK Global Ocean GO6 and GO7: a traceable hierarchy of model resolutions. *Geoscientific Model Development*, 11(8):3187–3213.

Su, Z. and Ingersoll, A. P. (2016). On the minimum potential energy state and the eddy size-constrained ape density. *Journal of Physical Oceanography*, 46(9):2663–2674.

Su, Z., Wang, J., Klein, P., Thompson, A. F., and Menemenlis, D. (2018). Ocean submesoscales as a key component of the global heat budget. *Nature Communications*, 9(1):1–8.

Sugimoto, S., Aono, K., and Fukui, S. (2017). Local atmospheric response to warm mesoscale ocean eddies in the Kuroshio–Oyashio Confluence region. *Scientific Reports*, 7(1):11871.

Sun, J., Zhang, S., Nowotarski, C. J., and Jiang, Y. (2020). Atmospheric responses to mesoscale oceanic eddies in the winter and summer North Pacific subtropical countercurrent region. *Atmosphere*, 11(8).

Sun, M., Tian, F., Liu, Y., and Chen, G. (2017). An improved automatic algorithm for global eddy tracking using satellite altimeter data. *Remote Sensing*, 9(3):1–18.

Sun, W., Dong, C., Tan, W., Liu, Y., He, Y., and Wang, J. (2018). Vertical structure anomalies of oceanic eddies and eddy-induced transports in the South China Sea. *Remote Sensing*, 10(5).

Sverdrup, H. (1947). Wind-driven currents in a baroclinic ocean; with application to the equatorial currents of the Eastern Pacific. *Geophysics*, 33(1):318–326.

Sweet, W., Fett, R., Kerling, J., and Violette, P. L. (1981). Air-sea interaction effects in the lower troposphere across the north wall of the Gulf Stream.

Tarshish, N., Abernathey, R., Zhang, C., Dufour, C. O., Frenger, I., and Griffies, S. M. (2018). Identifying Lagrangian Coherent Vortices in a Mesoscale Ocean Model. *Ocean Modelling*, 130:15–28.

Taylor, K. E., Stouffer, R. J., and Meehl, G. A. (2012). An overview of CMIP5 and the experiment design. *Bulletin of the American Meteorological Society*, 93(4):485–498.

Theiss, J. (2004). Equatorward Energy Cascade, Critical Latitude, and the Predominance of Cyclonic Vortices in Geostrophic Turbulence. *Journal of Physical Oceanography*, 34:1663–1678.

Thomas, L. N., Tandon, A., and Mahadevan, A. (2008). Submesoscale processes and dynamics. *Journal of Geophysical Research*, pages 17 – 38.

Thoppil, P. G., Richman, J. G., and Hogan, P. J. (2011). Energetics of a global ocean circulation model compared to observations. *Geophysical Research Letters*, 38(15):12–17.

Tomita, H., Hihara, T., Kako, S., Kubota, M., and Kutsuwada, K. (2019). An introduction to J-OFURO3, a third-generation Japanese ocean flux data set using remote-sensing observations. *Journal of Oceanography*, 75(2):171–194.

Torres, H. S., Klein, P., Menemenlis, D., Qiu, B., Su, Z., Wang, J., Chen, S., and Fu, L. L. (2018). Partitioning Ocean Motions Into Balanced Motions and Internal Gravity Waves: A Modeling Study in Anticipation of Future Space Missions. *Journal of Geophysical Research: Oceans*, 123(11):8084–8105.

Tsartsali, E., Haarsma, R., Athanasiadis, P., Bellucci, A., de Vries, H., Drijfhout, S., de Vries, I., Putrahasan, D., Roberts, M. J., Sanchez-Gomez, E., and Roberts, C. D. (2021). Impact of horizontal resolution on atmosphere-ocean coupling along the Gulf stream in global high resolution models, supplementary material. *Climate Dynamics*, Submitted:1–6.

Tulloch, R., Marshall, J., Hill, C., and Smith, K. S. (2011). Scales, Growth Rates, and Spectral Fluxes of Baroclinic Instability in the Ocean. *Journal of Physical Oceanography*, 41(6):1057–1076.

Tulloch, R., Marshall, J., and Smith, K. S. (2009). Interpretation of the propagation of surface altimetric observations in terms of planetary waves and geostrophic turbulence. *Journal of Geophysical Research: Oceans*, 114(2):1–11.

Ubelmann, C., Klein, P., and Fu, L. L. (2015). Dynamic interpolation of sea surface height and potential applications for future high-resolution altimetry mapping. *Journal of Atmospheric and Oceanic Technology*, 32(1):177–184.

Valcke, S. (2013). The OASIS3 coupler: a European climate modelling community software. *Geoscientific Model Development*, 6(2):373–388.

Valcke, S., Craig, T., and Coquart, L. (2015). OASIS3-MCT User Guide.

Vallis, G. (2006). *Atmospheric and Oceanic Fluid Dynamics: Fundamentals and Large-scale Circulation*. Cambridge: Cambridge University Press.

Vallis, G. (2019). *Essentials of Atmospheric and Oceanic Dynamics*. Cambridge: Cambridge University Press.

Verveer, P. J. (2005). Source Code for gaussian filter.

Villas Bôas, A. B., Sato, O. T., Chaigneau, A., and Castelão, G. P. (2015). The signature of mesoscale eddies on the air-sea turbulent heat fluxes in the South Atlantic Ocean. *Geophysical Research Letters*, 42(6):1856–1862.

Von Storch, J. S., Eden, C., Fast, I., Haak, H., Hernández-Deckers, D., Maier-Reimer, E., Marotzke, J., and Stammer, D. (2012). An estimate of the Lorenz energy cycle for the World Ocean based on the 1/10 STORM/NCEP simulation. *Journal of Physical Oceanography*, 42(12):2185–2205.

von Storch, J. S., Haak, H., Hertwig, E., and Fast, I. (2016). Vertical heat and salt fluxes due to resolved and parameterized meso-scale Eddies. *Ocean Modelling*, 108:1–19.

Wallace, J. M., Mitchell, T. P., and Deser, C. (1989). The Influence of Sea-Surface Temperature on Surface Wind in the Eastern Equatorial Pacific: Seasonal and Interannual Variability.

Walters, D., Baran, A. J., Boutle, I., Brooks, M., Earnshaw, P., Edwards, J., Furtado, K., Hill, P., Lock, A., Manners, J., Morcrette, C., Mulcahy, J., Sanchez, C., Smith, C., Stratton, R., Tennant, W., Tomassini, L., Van Weverberg, K., Vosper, S., Willett, M., Browse, J., Bushell, A., Carslaw, K., Dalvi, M., Essery, R., Gedney, N., Hardiman, S., Johnson, B., Johnson, C., Jones, A., Jones, C., Mann, G., Milton, S., Rumbold, H., Sellar, A., Ujiie, M., Whitall, M., Williams, K., and Zerroukat, M. (2019). The Met Office Unified Model Global Atmosphere 7.0/7.1 and JULES Global Land 7.0 configurations. *Geoscientific Model Development*, 12(5):1909–1963.

Walters, D., Boutle, I., Brooks, M., Melvin, T., Stratton, R., Vosper, S., Wells, H., Williams, K., Wood, N., Allen, T., Bushell, A., Copsey, D., Earnshaw, P., Edwards, J., Gross, M., Hardiman, S., Harris, C., Heming, J., Klingaman, N., Levine, R., Manners, J., Martin, G., Milton, S., Mittermaier, M., Morcrette, C., Riddick, T., Roberts, M., Sanchez, C., Selwood, P., Stirling, A., Smith, C., Suri, D., Tennant, W., Luigi Vidale, P., Wilkinson, J., Willett, M., Woolnough, S., and

Xavier, P. (2017). The Met Office Unified Model Global Atmosphere 6.0/6.1 and JULES Global Land 6.0/6.1 configurations. *Geoscientific Model Development*, 10:1487–1520.

Wang, Z., Li, Q., Sun, L., Li, S., Yang, Y., and Liu, S. (2015). The most typical shape of oceanic mesoscale eddies from global satellite sea level observations. *Frontiers of Earth Science*, 9(2):202–208.

Wei, Y., Wang, H., and Zhang, R. H. (2019). Mesoscale wind stress-SST coupled perturbations in the Kuroshio Extension. *Progress in Oceanography*, 172(March):108–123.

White, W. B. and Annis, J. L. (2003). Coupling of extratropical mesoscale eddies in the ocean to westerly winds in the atmospheric boundary layer. *Journal of Physical Oceanography*, 33(5):1095–1107.

White, W. B. and Bernstein, R., L. (1979). Design of an Oceangraphic Network in the Midlatitude North Pacific. *Journal of Physical Oceanography*, 9:592–605.

Williams, K. D., Copsey, D., Blockley, E. W., Bodas-Salcedo, A., Calvert, D., Comer, R., Davis, P., Graham, T., Hewitt, H. T., Hill, R., Hyder, P., Ineson, S., Johns, T. C., Keen, A. B., Lee, R. W., Megann, A., Milton, S. F., Rae, J. G., Roberts, M. J., Scaife, A. A., Schiemann, R., Storkey, D., Thorpe, L., Watterson, I. G., Walters, D. N., West, A., Wood, R. A., Woollings, T., and Xavier, P. K. (2018). The Met Office Global Coupled Model 3.0 and 3.1 (GC3.0 and GC3.1) Configurations. *Journal of Advances in Modeling Earth Systems*, 10(2):357–380.

Wolfram, P. J. and Ringler, T. D. (2017). Computing eddy-driven effective diffusivity using Lagrangian particles. *Ocean Modelling*, 118:94–106.

Wu, P., Roberts, M., Martin, G., Chen, X., Zhou, T., and Vidale, P. L. (2019). The impact of horizontal atmospheric resolution in modelling air–sea heat fluxes. *Quarterly Journal of the Royal Meteorological Society*, 145(724):3271–3283.

Wunsch, C. (1999). The work done by the wind on the oceanic general circulation. *Journal of Physical Oceanography*, 28(11):2332–2342.

Wunsch, C. (2002). Ocean observations and the climate forecast problem. *International Geophysics*, 83(C):233–245.

Wunsch, C. and Ferrari, R. (2004). Vertical Mixing, Energy, and the General Circulation of the Oceans. *Annual Review of Fluid Mechanics*, 36(1):281–314.

Wunsch, C. and Stammer, D. (1998). Satellite Altimetery, the Marine Geoid and the Oceanic General Circulation. *Annual Review of Earth and Planetary Science: OCEAN CIRCULATION AND GEOID*, 26:219–253.

Xie, P., Ishiwatari, M., Hashizume, H., and Takeuchi, K. (1998). Coupled ocean-atmospheric waves on the equatorial front. *Geophysical Research Letters*, 25(20):3863–3866.

Xie, S. P. (2004). Satellite observations of cool ocean-atmosphere interaction.

Xu, C., Zhai, X., and Shang, X. D. (2016). Work done by atmospheric winds on mesoscale ocean eddies. *Geophysical Research Letters*, 43(23):12,174–12,180.

Yang, H., Chang, P., Qiu, B., Zhang, Q., Wu, L., Chen, Z., and Wang, H. (2019a). Mesoscale air–sea interaction and its role in eddy energy dissipation in the Kuroshio extension. *Journal of Climate*, 32(24):8659–8676.

Yang, P., Jing, Z., and Wu, L. (2018). An Assessment of Representation of Oceanic Mesoscale Eddy-Atmosphere Interaction in the Current Generation of General Circulation Models and Reanalyses. *Geophysical Research Letters*, 45(21):11,856–11,865.

Yang, Z., Wang, G., and Chen, C. (2019b). Horizontal velocity structure of mesoscale eddies in the South China Sea. *Deep-Sea Research Part I: Oceanographic Research Papers*, 149(June):103055.

Yu, X., Naveira Garabato, A. C., Martin, A. P., Evans, D. G., and Su, Z. (2019). Wind-forced symmetric instability at a transient mid-ocean front. *Geophysical Research Letters*, pages 1–11.

Zanna, L., Chassignet, E. P., Yeager, S. G., Fox-Kemper, B., Bozec, A., Castruccio, F., Danabasoglu, G., Kim, W. M., Koldunov, N., Yiwen, L., Lin, P., Liu, H., Sein, D., Sidorenko, D., Wang, Q., and Xu, X. (2020). Energizing turbulence closures in ocean models. *CLIVAR Exchanges/US CLIVAR Variations*, 18(February):3–8.

Zhai, X., Johnson, H. L., and Marshall, D. P. (2010). Significant sink of ocean-eddy energy near western boundaries. *Nature Geoscience*, 3(9):608–612.

Zhang, N., Liu, G., Liu, Q., Zheng, S., and Perrie, W. (2020). Spatiotemporal Variations of Mesoscale Eddies in the Southeast Indian Ocean. *Journal of Geophysical Research: Oceans*, 125(8):1–18.

Zhang, X., Ma, X., and Wu, L. (2019). Effect of Mesoscale Oceanic Eddies on Extratropical Cyclogenesis: A Tracking Approach. *Journal of Geophysical Research: Atmospheres*, 124(12):6411–6422.

Zhou, G., Latif, M., Greatbatch, R. J., and Park, W. (2015). Atmospheric response to the North Pacific enabled by daily sea surface temperature variability. *Geophysical Research Letters*, 42(18):7732–7739.